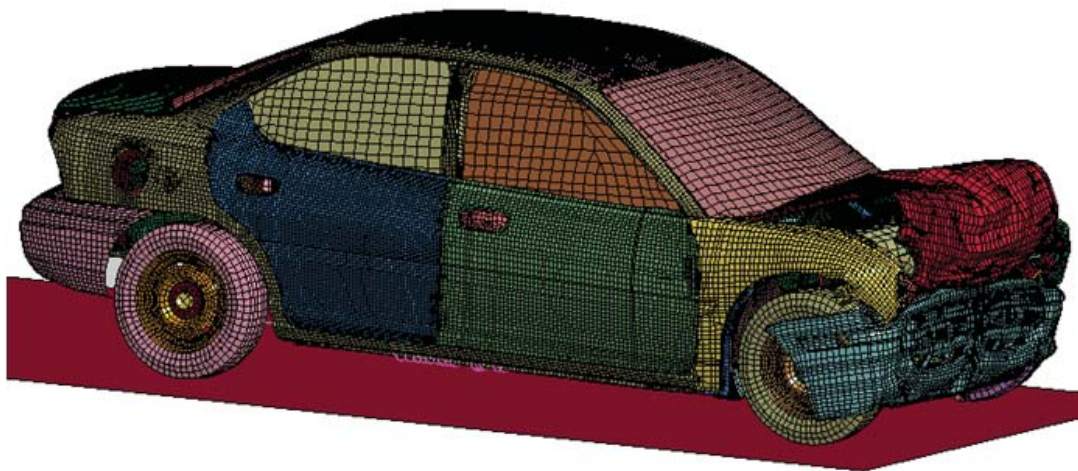


**Universität Stuttgart**



# Variational methods for consistent singular and scaled mass matrices

Anton Tkachuk





# **Variational methods for consistent singular and scaled mass matrices**

by

**Anton Tkachuk**

Bericht Nr. 60

Institut für Baustatik und Baudynamik der Universität Stuttgart

Professor Dr.-Ing. habil. M. Bischoff

2013



© Anton Tkachuk

*Berichte können bezogen werden über: / Reports are distributed by:*

Institut für Baustatik und Baudynamik

Universität Stuttgart

Pfaffenwaldring 7

70550 Stuttgart

Tel.: 0711 - 685 66123

Fax: 0711 - 685 66130

E-Mail: [sekretariat@ibb.uni-stuttgart.de](mailto:sekretariat@ibb.uni-stuttgart.de)

<http://www.ibb.uni-stuttgart.de/>

*Alle Rechte, insbesondere das der Übersetzung in andere Sprachen, vorbehalten. Ohne Genehmigung des Autors ist es nicht gestattet, diesen Bericht ganz oder teilweise auf photomechanischem, elektronischem oder sonstigem Wege zu kommerziellen Zwecken zu vervielfältigen.*

*All rights reserved. In particular, the right to translate the text of this thesis into another language is reserved. No part of the material protected by this copyright notice may be reproduced or utilized in any form or by any means, electronic or mechanical, including photocopying, recording or by any other information storage and retrieval system, without written permission from the author.*

D93 - Dissertation an der Universität Stuttgart

ISBN 978-3-00-044747-1

# **Variational methods for consistent singular and scaled mass matrices**

Von der Fakultät Bau- und Umweltingenieurwissenschaften  
der Universität Stuttgart zur Erlangung der Würde eines  
Doktor-Ingenieurs (Dr.-Ing.) genehmigte Abhandlung

vorgelegt von

**Anton Tkachuk**

aus Charkiw, Ukraine

Hauptberichter: Prof. Dr.-Ing. habil. Manfred Bischoff

Mitberichter: Prof. Dr. rer. nat. Barbara Wohlmuth

Mitberichter: Prof. Dr. Umberto Perego

Tag der mündlichen Prüfung: 23. Oktober 2013

Institut für Baustatik und Baudynamik der Universität Stuttgart

2013



## Kurzfassung

Singuläre und selektiv-skalierte Massenmatrizen sind für die Finite-Elemente Modellierung zahlreicher Probleme von großem Nutzen, zum Beispiel für die Niedriggeschwindigkeits-aufprall-, Tiefzieh- oder Falltestsimulation. Singuläre Massenmatrizen erlauben eine erheblich Verringerung der unerwünschten Oszillationen in der Kontaktkraft. Die Anwendung selektiver Massenskalierung für explizite Dynamiksimulationen führt zu einer Reduktion des Rechenaufwandes ohne maßgeblichen Verlust an Genauigkeit. Bekannte Methoden für singuläre und selektiv-skalierte Massenmatrizen basieren auf speziellen Quadraturregeln oder algebraischen Umformungen der Standardmassenmatrizen. Die vorliegende Arbeit widmet sich der Ableitung variationell streng konsistenter Massenmatrizen und deren Analyse. Die theoretische Grundlage dieser Arbeit ist ein neues parametrisches Hamiltonsches Prinzip mit unabhängigen Variablen für Verschiebung, Geschwindigkeit und Impuls. Die numerische Grundlage ist eine hybrid-gemischte Diskretisierung dieses neuen Prinzips und eine geschickte Auswahl von Ansatzräumen und freien Parametern. Die Qualität der neuen Massenmatrizen wird mit verschiedenen Benchmark-Tests gründlich analysiert und bewertet.

Die Arbeit gliedert sich in drei Teile. Im ersten Teil werden die wesentlichen Grundlagen und Notationen eingeführt. Es beinhaltet die zugrundeliegende Kontinuumsmechanik, die lokale Form des Anfangs-Randwertproblems für ein elasto-dynamisches Kontaktproblem, sowie dessen Lösung mit der Methode der finiten Elemente. Darüber hinaus werden die zentrale Differenzenmethode für nicht-diagonale Massenmatrizen und eine theoretische Abschätzung über die Reduktion der Rechenzeit mit selektiver Massenskalierung dargestellt. Außerdem wird auf die Motivation für die Implementierung alternativer Massenmatrizen eingegangen. Im zweiten Teil der Arbeit wird der neue variationelle Ansatz für elasto-dynamische Probleme vorgestellt. Der Grundstein der Arbeit ist die Herleitung des neuen Hamiltonschen Prinzips mit Penalty-Faktoren und eine Erweiterung des modifizierten Hamiltonschen Prinzips für kurze einseitige Gleitkontakte. Diese Formulierungen werden im Raum mit dem BUBNOV-GALERKIN-Ansatz diskretisiert. Als Ergebnis erhält man Familien singulärer und selektiv-skaliertes Massenmatrizen. Die entsprechenden Ansatzfunktionen werden für verschiedene Familien von Finiten Elementen gebildet. Diese Familien beinhalten Stab- und TIMOSHENKO-Balkenelemente für eindimensionale, sowie Kontinuumsselemente für zwei- und dreidimensionale Probleme. Die Ansatzfunktionen für singuläre Massenmatrizen werden für quadratische und kubische Elemente hergeleitet, für selektiv-skalierte Massenmatrizen bis zur dritten Ordnung. Im dritten Teil der Arbeit werden die neuen Massenmatrizen analysiert und bewertet und ein Ausblick für weitere mögliche Entwicklungen ist angeführt.

Zur Bewertung der neuen Massenmatrizen wurden die Ausbreitung harmonischer Wellen, freie und erzwungene Vibrationen, sowie Aufprallprobleme untersucht. Als erstes wird die Ausbreitung harmonischer Wellen mithilfe einer FOURIER-Analyse, angewendet auf die semi-diskrete Bewegungsgleichung, untersucht. Diese Analyse führt auf einen Satz von Dispersionsrelationen. Ein Vergleich der analytischen Dispersionsrelationen mit den dazugehörigen kontinuierlichen erlaubt eine effiziente Fehlerabschätzung. Auf diese Weise können die vorgeschlagenen Stab- und Balkenelemente analysiert werden. Als zweites werden Eigen-

wertprobleme für zwei- und dreidimensionale Probleme gelöst. Hierbei wird der Fehler in den niedrigen Frequenzen (Moden), sowie im gesamten Spektrum berechnet. Als drittes werden für die neuen Massenmatrizen spektrale Antwortkurven im interessanten Frequenzbereich für erzwungene Vibrationen ermittelt. Diese werden mit den Kurven für konsistente Massenmatrizen mithilfe des FRAC-Kriteriums (frequency response assurance criterion) verglichen. Die Werte des FRAC-Kriteriums zeigen den Fehler für lineare Probleme. Anschließend werden mehrere transiente Beispiele mit singulären und skalierten Massenmatrizen berechnet. Diese Beispiele bestätigen die erwartete Überlegenheit singulärer Massenmatrizen für Aufprallprobleme, d.h. die unerwünschten Oszillationen des Kontaktdrucks können erheblich reduziert werden. Variationell selektive Massenskalierung reduziert den Rechenaufwand für explizite dynamische Simulationen. Im Ausblick werden mögliche Weiterentwicklungen im Hinblick auf neue Elementtypen, alternative schwache Formen, sowie multi-physikalische Anwendungen vorgeschlagen. Als Nebenprodukt dieser Arbeit können Patch-Tests für Trägheitsterme, ein Überblick über parametrische und nicht-parametrische variationelle Prinzipien der Elastodynamik, sowie eine Herleitung des Hamiltonschen Prinzips mit einer halb-inversen Methode erwähnt werden. Die Anwendung der FE-Technologie für Massenmatrizen eröffnet neue Möglichkeiten in verschiedenen Bereichen der Dynamiksimulation, wie Falltest- und Automobilcrashsimulationen, sowie die Simulation phononischer Kristalle und Bauteile.

## Abstract

Singular and selectively-scaled mass matrices are useful for finite element modeling of numerous problems of structural dynamics, for example for low velocity impact, deep drawing and drop test simulations. Singular mass matrices allow significant reduction of spurious temporal oscillations of contact pressure. The application of selective mass scaling in the context of explicit dynamics reduces the computational costs without substantial loss in accuracy. Known methods for singular and selectively-scaled mass matrices rely on special quadrature rules or algebraic manipulations applied on the standard mass matrices. This thesis is dedicated to variationally rigorous derivation and analysis of these alternative matrices. The theoretical basis of this thesis is a novel parametric HAMILTON's principle with independent variables for displacement, velocity and momentum. The numerical basis is hybrid-mixed discretization of the novel mixed principle and skillful tuning of ansatz spaces and free parameters. The qualities of novel mass matrices are thoroughly analyzed by various tests and benchmarks.

The thesis has three main parts. In the first part of the thesis, the essential fundamentals and notations are introduced. This includes the basic continuum mechanics, the local form of an initial boundary value problem for an elasto-dynamic contact problem and its treatment with finite elements. In addition, an extension of the central difference method to non-diagonal mass matrices and a theoretical estimate of speed-up with selective mass scaling is given. Besides, a motivation for implementation of alternative mass matrices is given.

In the second part of the thesis, the novel variational approach for elasto-dynamic problems is presented. The corner stone of the thesis is the derivation of the novel penalized HAMILTON's principle and an extension of the modified HAMILTON's principle for small sliding unilateral contact. These formulations are discretized in space with the BUBNOV-GALERKIN approach. As a result, families of singular and selectively-scaled mass matrices are obtained. The corresponding shape functions are built for several families of finite elements. These families include truss and TIMOSHENKO beam elements for one-dimensional problems, as well as solid elements for two and three dimensions. Shape functions for singular mass matrices are derived for quadratic and cubic elements. Selectively-scaled mass matrices are given for elements up to the order three.

In the third part of the thesis, the novel mass matrices are analyzed and an outlook for future work is given. Propagation of harmonic waves, free and forced vibrations and impact problems are used for evaluation of the new mass matrices. First, the propagation of harmonic waves is studied with the help of a FOURIER analysis applied to the semi-discretized equation of motion. This analysis results in a set of dispersion relations. Comparison of the analytical expressions for discrete dispersion relations with the corresponding continuous ones allows efficient error estimation. In this way, the proposed truss and beam elements are analyzed. Secondly, eigenvalue problems are solved for two- and three-dimensional problems. The error in the lowest frequencies (modes) and in the whole spectrum is computed. Thirdly, spectral response curves for forced vibrations are obtained for the new mass matrices in ranges of interest. These curves are compared with the ones obtained with consistent mass matrices

via the frequency response assurance criterion. The values of the frequency response assurance criterion indicate the error for linear problems. Finally, several transient examples are solved with singular and scaled mass matrices. These examples confirm expected superiority of singular mass matrices for impact problems, i.e. spurious temporal oscillations of contact pressures are significantly reduced. Variational selective mass scaling reduces computational cost of explicit dynamic simulations. In the outlook, possible developments regarding new element types, alternative weak forms and several multi-physic applications are proposed.

As by-product of this thesis, patch tests for inertia terms, an overview of parametric and non-parametric variational principles of elasto-dynamics and a derivation of the penalized HAMILTON's principle with a semi-inverse method can be noted. Besides, the topic of finite element technology for mass matrices is posed. This can open new horizons for evolving branches of computational dynamics such as drop test and car crash simulations, phononic crystals and devices.

## Preface

This work was carried out at the Institute of Structural Mechanics of Stuttgart University within the project "Reduction of numerical sensitivities in crashsimulations on high performance computers (HPC-10)" funded by Baden-Württemberg Stiftung from December 2009 till November 2012. In this context, I gratefully acknowledge the financial support and the provided opportunity to work in close cooperation with German automotive industry. Further support of the Institute of Structural Mechanics from December 2012 till December 2013 is deeply appreciated.

First of all, I would like to thank my supervisor Prof. Dr.-Ing. habil. Manfred Bischoff. It has been an honor to be a PhD student at his institute. I have learned here a lot about structural mechanics: dynamics, contact, finite element technology, shells, stability, path-following etc., but what is more important, I have learned to enjoy structural mechanics despite long work days. This would have been impossible without the special scientific environment and friendly atmosphere, which he creates at the institute. Secondly, I would like to thank Prof. Dr. rer. nat. Barbara Wohlmuth and Prof. Dr. Umberto Perego for their willingness to co-referee the thesis and Prof. Dr.-Ing. Ullrich Martin for chairing the final exam. Furthermore, I want to thank Prof. Dr. rer. nat. Barbara Wohlmuth for hosting me for a week in March 2010 at TU München. The initial idea of this thesis was born during this stay.

The members of the institute contributed a lot to my professional and personal time in Stuttgart. The jokes during the coffee breaks brightened the work days. The excursions and the days of science inspired for diverse research. Moreover, I gratefully acknowledge the complete developer's team of the in-house finite element code *NumPro* and especially the team leader Dr.-Ing. Malte von Scheven. In this respect, I also want to thank Christoff Wilking for his initial implementation of the central difference scheme and basic 2D and 3D elements. I would also like to thank Anne Schäuble and Layla Koohi for careful proofreading this thesis.

Lastly, I would like to thank my family for their endless love and encouragement. My father, Prof. Dr. Mykola Tkachuk, introduced me the topic of contact mechanics and finite element analysis. My brother, Dr. Mykola Tkachuk, supported me a lot during my stay in Stuttgart. My mother, Dr. Anna Tkachuk, cares all the time and asks good questions. I thank my girlfriend, Anne Schäuble, for her help and patience during the final steps of the thesis.

Stuttgart, December 2013

Anton Tkachuk



---

# Contents

|  |             |
|--|-------------|
| <b>List of Figures</b>   | <b>xi</b>   |
| <b>List of Tables</b>  | <b>xv</b>   |
| <b>Nomenclature</b>  | <b>xvii</b> |
| <b>1 Introduction</b>  | <b>1</b>    |
| 1.1 Motivation . . . . .   | 1           |
| 1.2 Goals . . . . .  | 5           |
| 1.3 Overview . . . . .   | 5           |
| <b>2 State of the art</b>  | <b>7</b>    |
| 2.1 Basic Continuum Mechanics . . . . .                                    | 7           |
| 2.1.1 Kinematics and stress measures . . . . .                             | 8           |
| 2.1.2 Constitutive equations for hyperelastic materials . . . . .          | 11          |
| 2.1.3 Balance laws . . . . .   | 13          |
| 2.2 Large sliding frictionless contact . . . . .                           | 15          |
| 2.2.1 Motion, assumptions and notations . . . . .                          | 16          |
| 2.2.2 Contact gap and traction . . . . .                                   | 18          |
| 2.2.3 Boundary and initial conditions . . . . .                            | 20          |
| 2.2.4 Strong and weak form of contact IBVP . . . . .                       | 20          |
| 2.2.5 Linearized equations of elasto-dynamic contact . . . . .             | 21          |
| 2.2.6 Selected linearized models for thin-walled structures . . . . .      | 23          |
| 2.3 Discretization in space . . . . .                                      | 25          |
| 2.3.1 Residuum, algorithmic tangent and consistent mass matrices . . . . . | 26          |

|          |  |           |
|----------|--|-----------|
| 2.3.2    | Standard contact techniques . . . . .  | 28        |
| 2.3.3    | Mass lumping and mass customization . . . . .  | 29        |
| 2.3.4    | Singular mass matrices . . . . .   | 31        |
| 2.3.5    | Mass scaling . . . . .   | 33        |
| 2.4      | Integration in Time . . . . .  | 41        |
| 2.4.1    | Central difference method . . . . .  | 41        |
| 2.4.2    | An estimate for speed-up for SMS . . . . .   | 43        |
| 2.4.3    | Newmark $\beta$ method . . . . .   | 45        |
| 2.5      | Assessment of quality of space and time discretization . . . . .                                 | 47        |
| 2.5.1    | Temporal discretization . . . . .  | 47        |
| 2.5.2    | Spatial discretization . . . . .   | 48        |
| 2.5.3    | Assessment of dynamic behavior of semi-discretized equations using<br>Fourier analysis . . . . . | 48        |
| 2.5.4    | Participation factor for classification of load cases . . . . .                                  | 50        |
| 2.5.5    | Harmonic analysis . . . . .  | 50        |
| <b>3</b> | <b>Variational principles of elasto-dynamics</b>   | <b>53</b> |
| 3.1      | Penalized Hamilton's principle . . . . .   | 55        |
| 3.2      | Canonical two-field principles . . . . .   | 58        |
| 3.3      | Canonical three-field principle . . . . .  | 59        |
| 3.4      | A principle using an incompatible velocity field . . . . .                                       | 59        |
| 3.5      | Variational principles with contact conditions . . . . .   | 61        |
| 3.6      | Summary of variational methods for elasto-dynamics . . . . .                                     | 63        |
| <b>4</b> | <b>Spatial discretization of inertial terms</b>  | <b>65</b> |
| 4.1      | Three-parameteric template for mass matrix . . . . .   | 65        |
| 4.2      | Variational selective mass scaling . . . . .   | 67        |
| 4.2.1    | Case 1: one-parametric <b>u-v-p</b> -formulation . . . . .                                       | 67        |
| 4.2.2    | Case 2: two-parametric <b>u-v-p</b> -formulation . . . . .                                       | 68        |
| 4.2.3    | Case 3: one-parametric <b>u-v</b> -formulation . . . . .   | 68        |
| 4.3      | Hybrid-mixed mass matrices . . . . .   | 69        |
| 4.3.1    | Discretization of two-field canonical principles . . . . .                                       | 69        |
| 4.3.2    | Discretization of three-field canonical principle . . . . .                                      | 70        |
| 4.3.3    | Orthogonality and stability conditions . . . . .   | 72        |
| 4.4      | Incompatible velocity method for mass matrices . . . . .   | 73        |
| <b>5</b> | <b>Good ansatz spaces</b>  | <b>75</b> |
| 5.1      | Patch test for inertia terms . . . . .   | 75        |
| 5.2      | Shape functions for singular mass matrices . . . . .   | 77        |
| 5.2.1    | Derivation of shape functions in 1D . . . . .  | 77        |

|          |   |            |
|----------|---|------------|
| 5.2.2    | Special shape functions for three-node Timoshenko beam element . . .            | 83         |
| 5.2.3    | Shape functions for 2D . . . . .  | 84         |
| 5.2.4    | Shape functions for 3D . . . . .  | 85         |
| 5.3      | Variational selective mass scaling . . . . .                                    | 86         |
| 5.3.1    | Three-node triangle . . . . .   | 87         |
| 5.3.2    | Bilinear quadrilateral element . . . . .  | 89         |
| 5.3.3    | Quadratic Serendipity and Lagrange elements . . . . .                           | 89         |
| 5.3.4    | Linear tetrahedral element . . . . .  | 89         |
| 5.3.5    | Trilinear hexahedral element . . . . .  | 89         |
| 5.4      | Mass matrices using incompatible velocity formulations . . . . .                | 90         |
| <b>6</b> | <b>Spectral analysis</b>  | <b>91</b>  |
| 6.1      | Dispersion relations for selected hybrid-mixed singular mass matrices . . . . . | 91         |
| 6.1.1    | Three-node truss element: Tr2-0 . . . . .                                       | 91         |
| 6.1.2    | Four-node truss element: Tr3-1 . . . . .  | 93         |
| 6.1.3    | Quadratic Timoshenko element . . . . .  | 94         |
| 6.2      | Dispersion relations for selected SMS templates . . . . .                       | 96         |
| 6.2.1    | Truss elements . . . . .  | 96         |
| 6.2.2    | Two-node Timoshenko element . . . . .   | 100        |
| 6.2.3    | Three-node Timoshenko element . . . . .   | 102        |
| 6.3      | Eigenvalue benchmarks . . . . .   | 103        |
| 6.3.1    | NAFEMS FV32 . . . . .   | 103        |
| 6.3.2    | 2D square membrane with distorted mesh . . . . .                                | 106        |
| 6.3.3    | NAFEMS FV52 . . . . .   | 108        |
| 6.4      | Summary of spectral analysis . . . . .  | 110        |
| <b>7</b> | <b>Transient examples</b>   | <b>113</b> |
| 7.1      | Examples with hybrid singular mass matrices . . . . .                           | 113        |
| 7.1.1    | Wave propagation in truss . . . . .   | 113        |
| 7.1.2    | Projectile in rigid wall . . . . .  | 114        |
| 7.1.3    | Wave propagation in a Timoshenko beam . . . . .                                 | 116        |
| 7.1.4    | Lateral impact of a Timoshenko beam . . . . .                                   | 117        |
| 7.1.5    | Lateral impact of beam modeled with solid elements . . . . .                    | 118        |
| 7.1.6    | Impact of a disk onto rigid wall . . . . .                                      | 120        |
| 7.2      | Examples with selective mass scaling . . . . .                                  | 122        |
| 7.2.1    | Wave propagation in a Timoshenko beam . . . . .                                 | 122        |
| 7.2.2    | Tip loaded cantilever beam . . . . .  | 122        |
| 7.2.3    | Cantilever beam under a longitudinal load . . . . .                             | 125        |
| 7.2.4    | Arch bridge under point load . . . . .  | 126        |
| 7.2.5    | Six-throw crankshaft . . . . .  | 129        |

|          |   |            |
|----------|---|------------|
| 7.2.6    | Femur bone . . . . .  | 134        |
| 7.3      | Summary for transient examples . . . . .  | 137        |
| <b>8</b> | <b>Conclusions and outlook</b>  | <b>139</b> |
| 8.1      | Conclusions . . . . .   | 139        |
| 8.2      | Outlook . . . . .   | 142        |
|          | <b>Appendix</b>   | <b>145</b> |
| A        | Patch test for selected elements . . . . .  | 145        |
| B        | Derivation of the penalized Hamilton's principle of elasto-dynamics using a semi-inverse method . . . . . | 148        |
|          | <b>References</b>   | <b>151</b> |

---

# List of Figures

|      |   |    |
|------|---|----|
| 1.1  | Evolution of the total energy (left) and the history of the contact force (right) computed for a typical impact simulation (see Subsection 7.1.6) obtained with NEWMARK $\beta$ method, consistent mass matrix and LAGRANGE multipliers method for contact. . . . . | 2  |
| 1.2  | Contact force computed with different penalty factors (SPF) for example from Subsection 7.1.6. . . . .  | 2  |
| 1.3  | Deformation of a steel tube in a drop test, see OLOVSSON AND SIMONSSON (2006). . . . .  | 3  |
| 1.4  | Deformed shape of a <i>Neon</i> 1996 model after 40 ms for the initial velocity 15.6 m/s. . . . .   | 4  |
| 1.5  | History of the contact force for <i>Neon</i> 1996 model during the first 40 ms. . . .   | 4  |
| 2.1  | Mapping between the reference and the current configuration. . . . .  | 8  |
| 2.2  | Mapping of line and area elements. . . . .  | 10 |
| 2.3  | Internal traction vector $\mathbf{t}$ on virtual cut surface with normal $\mathbf{n}$ . . . . .   | 11 |
| 2.4  | Kinematic of two contacting bodies. . . . .   | 16 |
| 2.5  | Parametrization of a contact surface. . . . .   | 17 |
| 2.6  | Linearized kinematic on the contact surface. . . . .  | 23 |
| 2.7  | Truss model. . . . .  | 24 |
| 2.8  | TIMOSHENKO beam model. . . . .  | 25 |
| 2.9  | Element geometry. . . . .   | 26 |
| 2.10 | Locations and weights for optimally accurate nodal quadrature rules. . . . .  | 30 |
| 2.11 | Primary loop of TONTI diagram for linear elasto-dynamic contact problem (above) and its discrete counterpart (below). . . . .   | 33 |

|      |   |     |
|------|---|-----|
| 2.12 | Rigid body modes of a 3-node element with 2 DOFS per node. . . . .  | 37  |
| 2.13 | Characteristic distribution of eigenfrequencies for a thin-walled structure modelled with solid elements (black) and effect of mass scaling of thickness inertia (red). . . . .             | 39  |
| 2.14 | Classification of mass scaling methods. . . . .   | 40  |
| 2.15 | Flowchart for explicit time integration. . . . .  | 42  |
| 2.16 | Flowchart for calculations of acceleration vector with PCG. . . . .   | 43  |
| 2.17 | Tip loaded beam, problem setup (OLOVSSON ET AL. 2005). . . . .  | 43  |
| 2.18 | Flowchart for NEWMARK $\beta$ time integration. . . . .   | 46  |
| 2.19 | An infinite mesh of quadratic elements and a harmonic wave. . . . .   | 49  |
| 3.1  | Relations between variational formulations of elasto-dynamics. The novel principles are marked with an asterisk *. . . . .  | 63  |
| 4.1  | Linear two-parametric template of mass matrices obtained with equation (4.13)   | 69  |
| 4.2  | Approximation spaces for $\dot{\mathbf{u}}$ , $\mathbf{v}$ and $\mathbf{p}$ , quadratic forms for kinetic energy and discrete projection between approximation spaces. . . . .              | 71  |
| 5.1  | Hierarchical (left) and modified (right) shape functions for a quadratic truss element. . . . .   | 79  |
| 5.2  | Velocity shape function for quadratic truss element. . . . .  | 79  |
| 5.3  | Modified shape functions for the cubic 1D element. . . . .  | 82  |
| 5.4  | Shape function $N_1(\xi, \eta)$ of a nine-node quadrilateral element (Q2). . . . .  | 84  |
| 5.5  | Nine-node quadrilateral element (Q2). . . . .   | 85  |
| 6.1  | Dispersion for a quadratic truss element with constant velocities, Tr2-0. . . . .   | 92  |
| 6.2  | Dispersion for a cubic truss element with linear velocities, Tr3-1. . . . .   | 94  |
| 6.3  | Dispersion of a TIMOSHENKO Tr2-2-0-2 element vs. dispersion of continuum TIMOSHENKO beam model, $\Lambda = 1/4$ . . . . .   | 96  |
| 6.4  | Dispersion of Tr2MS1 element vs. continuum truss model. . . . .   | 97  |
| 6.5  | Dispersion of Tr3MS2 element vs. continuum truss model. . . . .   | 99  |
| 6.6  | Dispersion of Timoshenko Ti1-1-1-1MS2 element vs. continuum beam model, $\Lambda = 1/4$ . VSMS with constant ansatz for velocity. . . . .   | 101 |
| 6.7  | Dispersion of a Timoshenko Tr2-2-2-2MS2 element vs. continuum model, $\Lambda = 1/4$ . VSMS with a linear ansatz for translational velocity. . . . .  | 103 |
| 6.8  | Setup of FV32 NAFEMS benchmark. . . . .   | 104 |
| 6.9  | The six lowest modes for FV32 NAFEMS benchmark computed with Q1 element and CMM. . . . .  | 104 |
| 6.10 | Ratio of eigenfrequencies for different values of selective mass scaling parameters. $C_1$ - proposed in paper with $\Psi$ from (5.30), $\beta$ - method II OLOVSSON ET AL. (2005). . . . . | 106 |

|      |  |     |
|------|--|-----|
| 6.11 | The model of a square membrane (left) and sub-model (right) with mesh distortion $a = 0.5$ m (right). Material properties: $E = 207$ GPa, $\nu = 0.3$ , $\rho = 7800$ kg/m <sup>3</sup> . Mesh: $15 \times 15$ elements. . . . .     | 107 |
| 6.12 | Eigenmode four for a square plate computed with algebraic selective mass scaling with $\beta = 2$ , $f = 127.716$ Hz. . . . .  | 108 |
| 6.13 | Eigenmodes five (left) and six (right) for a square plate computed with algebraic selective mass scaling with $\beta = 2$ , $f_5 = 124.824$ Hz and $f_6 = 126.598$ Hz. . . . .   | 109 |
| 6.14 | Eigenmodes 256 for lumped mass matrix (left) and for algebraic selective mass scaling (right) with $\beta = 2$ , $f_{\max}^{\text{LMM}} = 1928.99$ Hz and $f_{\max}^{\text{ASMS}} = 873.97$ Hz. . . . .                              | 109 |
| 6.15 | Setup of FV52 NAFEMS benchmark. . . . .  | 109 |
| 6.16 | Ratio of eigenfrequencies for different values of selective mass scaling parameters. $C_1$ for element Hexa8MS6, $\beta$ for algebraic selective mass scaling. . . . .   | 110 |
| 7.1  | Wave propagation benchmark for trusses. . . . .  | 114 |
| 7.2  | Velocity profiles at different time points for a quadratic truss element with constant velocities, Tr2-0. . . . .  | 114 |
| 7.3  | Velocity profiles for a cubic truss element with linear velocities, Tr3-1, at different time points. . . . .   | 115 |
| 7.4  | Contact force at a rigid wall impact problem for a quadratic truss element, Tr2-0  | 115 |
| 7.5  | Contact force at a rigid wall impact problem for a cubic truss element with linear velocities, Tr3-1. . . . .  | 115 |
| 7.6  | Timoshenko beam wave propagation benchmark for 40 elements mesh. Constant velocity $v_0$ is prescribed at left end of the beam. . . . .  | 116 |
| 7.7  | Profiles of normalized transverse velocity $u_2/v_0$ for a wave propagation test for a Timoshenko beam at $t_{\text{end}} = 1.4 \cdot 10^{-3}$ . . . . .   | 117 |
| 7.8  | Setup of TIMOSHENKO bounce benchmark. . . . .  | 118 |
| 7.9  | Contact force at the center of the beam and evolution of the total energy. TIMOSHENKO bounce benchmark. . . . .  | 118 |
| 7.10 | Setup of bounce benchmark modeled with solid elements Q2P10V10. . . . .  | 119 |
| 7.11 | Contact force at the center of a beam (left) and total energy evolution (right) for impact problem of beam modeled with solid elements (Q2 vs. Q2P10V10). Results for $1 \times 8$ (above) and $1 \times 16$ (below) meshes. . . . . | 119 |
| 7.12 | Dependency of conditioning of algorithmic tangent on relative time-step for a beam modeled with solid elements Q2P10V10. . . . .   | 120 |
| 7.13 | Impact of a circular disk onto a rigid obstacle modeled with 125 solid elements Q2P10V10. . . . .  | 120 |
| 7.14 | Contact force and energy evolution for impact of a circular disk on a rigid obstacle (Q2 vs. Q2P10V10). $dt = 0.5$ $\mu$ s (above), $dt = 0.25$ $\mu$ s (middle) and $dt = 0.1825$ $\mu$ s (below). . . . .                          | 121 |

---

|      |   |     |
|------|---|-----|
| 7.15 | Profiles of normalized transverse velocity $u_2/v_0$ for wave propagation test for TIMOSHENKO beam at $t_{end} = 1.4 \cdot 10^{-3}$ . VSMS with constant velocity ansatz space (above) and linear ansatz space (below). . . . .   | 123 |
| 7.16 | The model of tip loaded beam (OLOVSSON ET AL. 2005). . . . .  | 124 |
| 7.17 | Tip deflection $w$ of a cantilever beam. . . . .  | 124 |
| 7.18 | Ratio of kinetic energy stored in artificially added mass to total energy. . . . .  | 125 |
| 7.19 | Axial tip displacement for the compression wave benchmark. . . . .  | 125 |
| 7.20 | Normalized mode participation factors. . . . .  | 126 |
| 7.21 | A model of an arch bridge. Material properties: $E = 30$ GPa, $\nu = 0.2$ , $\rho = 2400$ kg/m <sup>3</sup> , plane stress, thickness = 1 m. Mesh: 512 elements (eight- or nine-node quadrilaterals). Load: point force $F = 100$ kN applied in the middle of left arch. Duration: $t_{end} = 0.1$ s. . . . . | 127 |
| 7.22 | Displacement under external load. Results for S2 (above) and Q2 (below) element families. . . . .   | 127 |
| 7.23 | Dependence of the critical time-step size on mass scaling factor $C_1$ for S2 (left) and Q2 (right) element families. Computed values vs. fitted curve. . . . .   | 128 |
| 7.24 | Spectral response of the arch bridge evaluated at the excitation point computed with S2 (left) and Q2 (right) element families. . . . .   | 129 |
| 7.25 | Mesh of six-throw crankshaft. . . . .   | 130 |
| 7.26 | Crankshaft mesh built in GiD with target mesh size 7 mm. . . . .  | 131 |
| 7.27 | Spectral response of crankshaft evaluated at excitation point for different mass matrices (for range [15-45] Hz left and [150-180] Hz right). . . . .   | 132 |
| 7.28 | Absolute displacement amplitudes of crankshaft at excitation frequency 26 Hz (left) and 162 Hz (right). . . . .   | 132 |
| 7.29 | Absolute displacement of crankshaft at time 1 ms. Tetra4MS6, $C_1 = 300$ . . . . .  | 133 |
| 7.30 | Evolution of displacements at the tip of crankshaft (node 1) computed with Tetra4MS6, $C_1 = 300$ and LMM. . . . .  | 134 |
| 7.31 | Model of a femur bone. . . . .  | 134 |
| 7.32 | Mesh properties for the femur bone model. . . . .   | 135 |
| 7.33 | Absolute displacement amplitudes of femur at excitation frequency 223 Hz. . . . .   | 137 |
| 7.34 | Spectral response of crankshaft evaluated at excitation point for different mass matrices for range [100-150] Hz. . . . .   | 137 |
| A.1  | Setup for an inertia patch test. Q1 element. Density $\rho = 1.0$ . . . . .   | 146 |
| A.2  | Setup for an inertia patch test. S2 element. Density $\rho = 1.0$ . . . . .   | 146 |
| A.3  | Setup for the inertia patch test in 3D with Hexa8 element. Density $\rho = 1.0$ . . . . .   | 147 |

---

## List of Tables

|     |   |     |
|-----|---|-----|
| 1.1 | Speed-up for different methods in <i>RADIOSS</i> for the NUMISHEET2008 S-rail benchmark (ROY ET AL. 2011). . . . .  | 3   |
| 1.2 | Speed-up for different methods mass scaling strategies in a steel tube in a drop test benchmark (OLOVSSON AND SIMONSSON 2006). . . . .  | 3   |
| 2.1 | Element time-steps and mass scaling factors for BERNOULLI and TIMOSHENKO elements based on the maximum flexural and shear frequency. Exact stiffness is used for both elements. For TIMOSHENKO elements, a square cross-section with shear correction factor $\gamma_s = 5/6$ is assumed. . . . . | 35  |
| 6.1 | Comparison of dispersion properties of TIMOSHENKO beam element formulations (TKACHUK ET AL. 2013). . . . .  | 95  |
| 6.2 | Six lowest frequencies for FV32 benchmark computed with hybrid singular mass matrices. . . . .  | 104 |
| 6.3 | Comparison of different mass scaling formulations for FV32, $C_1 = 30$ . . . . .  | 105 |
| 6.4 | Six lowest eigenfrequencies $f_{1-6}$ computed with S2MS6 elements for FV32 benchmark. . . . .  | 106 |
| 6.5 | Critical time-step and conditioning of mass matrix for FV32 benchmark. S2 and Q2 element families. . . . .  | 107 |
| 6.6 | Comparison of different mass matrices for 2D square membrane example . . .  | 108 |
| 7.1 | Critical time-step and conditioning of mass matrix for the arch bridge model.   | 128 |
| 7.2 | Added mass and speed-up for conventional mass scaling applied the 7 mm crankshaft model. Value of added mass $\Delta m$ for SMS is given in sense of equation (2.88). . . . .   | 133 |

|     |   |     |
|-----|---|-----|
| 7.3 | Critical time-step size and average number of PCG iterations with JACOBI preconditioner for the mass matrix for the 7 mm crankshaft model. . . . .  | 133 |
| 7.4 | Added mass and speed-up for conventional mass scaling applied to the femur bone model, refinement 1. Value of added mass $\Delta m$ for SMS is given in the sense of equation (2.88). . . . . | 136 |
| 7.5 | Critical time-step and conditioning of mass matrix for the femur bone model.  | 136 |
| A.1 | Patch test for the inertia term with the Q1 family. . . . .   | 145 |
| A.2 | Patch test for the inertia term with the S2 family. . . . .   | 146 |
| A.3 | Patch test for the inertia term with the Q2 family. . . . .   | 147 |
| A.4 | Patch test for the inertia term with the Hexa8 element family. . . . .  | 147 |

---

# Nomenclature

The following abbreviations and symbols will be addressed several times throughout the thesis. Additionally, rarely occurring abbreviations and symbols are noted in the corresponding context.

## Abbreviations

|            |  |
|------------|--|
| IBVP       | Initial boundary value problem   |
| ODE        | Ordinary differential equation (system)                                      |
| DAE        | Differential algebraic equations   |
| FEM        | Finite element method  |
| LMM        | Lumped mass matrix   |
| RSL        | Row sum lumping scheme   |
| HRZ        | HINTON-ROCK-ZIENKIEWICZ lumping scheme, see HINTON ET AL. (1976)             |
| CMM        | Consistent mass matrix   |
| HMMM       | Hybrid-mixed (consistent) mass matrix  |
| HSMM       | Hybrid singular mass matrix  |
| CMS        | Conventional mass scaling  |
| SMS        | Selective mass scaling   |
| ASMS       | Algebraical selective mass scaling according to OLOVSSON ET AL. (2005)       |
| VSMS       | Variational selective mass scaling according to TKACHUK AND BISCHOFF (2013c) |
| EAS        | Enhanced assumed strain method   |
| FV32, FV52 | NAFEMS natural frequency benchmarks, see NAFEMS (1990)                       |

|                     |   |
|---------------------|---|
| BT                  | Boundary term   |
| MAC, or $\varphi_i$ | Mode assurance criterion (for $i^{\text{th}}$ mode)                             |
| FRAC                | Frequency response assurance criterion according to HEYLEN AND AVITABILE (1998) |

### Element notation convention

|            |  |
|------------|--|
| T1         | Triangular linear and quadratic FE   |
| Q1,Q2      | Quadrilateral bilinear and biquadratic FE with lumped or consistent mass matrices  |
| Q2VnPm     | Quadrilateral biquadratic FE with $n$ velocity and $m$ momentum parameters   |
| S2         | Quadratic serendipity FE with lumped or consistent mass matrix   |
| S2VnPm     | Quadratic serendipity FE with $n$ velocity and $m$ momentum parameters   |
| Tetra4     | Four-node tetrahedral element  |
| Hexa8      | Eight-node trilinear hexahedral FE   |
| Hexa27     | 27-node quadratic hexahedral FE  |
| Hexa27VnPm | 27-node quadratic hexahedral FE with $n$ velocity and $m$ momentum parameters  |
| Trn-m      | Truss FE with order $n$ and $m$ for displacement and velocity interpolation, respectively  |
| Tin-m-l-k  | Timoshenko beam FE with order $n, m, l, k$ for displacement, rotation, velocity and angular velocity interpolation, respectively |
| Ti*n-m-l-k | The same as previous, but with linked interpolation for displacement and rotations   |
| MS $n_v$   | Suffix at end of element name denoting variational selective mass scaling with $n_v$ modes                                       |
| Q2IVM8     | Quadrilateral element with mass matrix computed using incompatible velocity formulation with eight incompatible modes            |

### Symbols in the context of:

#### *Material body*

|                              |   |
|------------------------------|---|
| $\mathcal{O}$                | Origin of global Cartesian frame (inertial frame)   |
| $\mathcal{B}, \mathcal{B}_0$ | Material body in actual and reference configurations, respectively                            |
| $\mathbf{X}, \mathbf{x}$     | Reference and actual position of a material point   |
| $\rho$                       | Density of a material point   |
| $W$                          | Elastic energy density function   |
| $u$                          | Internal energy function  |
| $\partial\mathcal{B}_u$      | Part of the boundary of the body with prescribed displacement (DIRICHLET) boundary conditions |

|                                     |   |
|-------------------------------------|---|
| $\partial\mathcal{B}_t$             | Part of the boundary of the body with prescribed traction (NEUMANN) boundary conditions |
| $\partial\mathcal{B}_c$             | Part of the boundary of the body where contact may occur                                |
| $\hat{\mathbf{b}}$                  | Specific body force   |
| $\hat{\mathbf{t}}$                  | Boundary traction   |
| $\mathbf{t}_c$                      | Contact traction  |
| $\mathcal{I} = [0, t_{\text{end}}]$ | Time interval   |

*Kinematic measures*

|   |  |
|---|--|
| $\varphi$   | $\varphi(\mathbf{X}, t) : \mathcal{B} \times \mathcal{I} \rightarrow \mathcal{B}$ mapping from the reference to the actual configuration |
| $\mathbf{F} = \frac{\partial\varphi}{\partial\mathbf{X}}$ | Deformation gradient   |
| $\mathbf{C}$  | Right CAUCHY-GREEN deformation tensor  |
| $\mathbf{E}$  | GREEN-LAGRANGE strain tensor   |
| $\varepsilon$   | Linearized strain  |
| $\mathbf{u} = \mathbf{x} - \mathbf{X}$                    | Displacement   |
| $\mathbf{v} = \dot{\mathbf{u}}$                           | Velocity   |
| $\mathbf{a} = \ddot{\mathbf{u}}$                          | Acceleration   |
| $g_{\mathcal{B}}$   | Gap inside domain (for beams)  |
| $g_{\partial\mathcal{B}}$                                 | Gap at the boundary (for solid bodies and rods)  |

*Kinetic measures*

|  |  |
|--|--|
| $\mathbf{p} = \rho\mathbf{v}$  | Volume specific linear momentum                |
| $\mathbf{l} = \mathbf{x} \times \rho\mathbf{v}$                      | Volume specific angular momentum               |
| $\boldsymbol{\sigma}$  | True (CAUCHY) stress tensor                    |
| $\boldsymbol{\sigma}_{\text{PK1}}, \boldsymbol{\sigma}_{\text{PK2}}$ | First and second PIOLA-KIRCHHOFF stress tensor |
| $\boldsymbol{\sigma}_{\text{lin}}$                                   | Engineering stress tensor                      |
| $\mathbf{t} = \boldsymbol{\sigma}\mathbf{n}$                         | Stress vector (traction) field in the body     |

*Energetic measures*

|                    |  |
|--------------------|--|
| $T$                | Kinetic energy of a body $\mathcal{B}$   |
| $T^\circ$          | Kinetic energy computed with selectively scaled mass matrix or using template expression |
| $\Pi^{\text{int}}$ | Potential (internal) energy of a body  |
| $\Pi^{\text{ext}}$ | Potential of external forces   |
| $\Pi$              | Full potential energy  |
| $\delta W$         | Virtual work   |
| $L = T - \Pi$      | Lagrangian   |

|                                  |  |
|----------------------------------|--|
| $H = \int_{\mathcal{J}} L dt$    | Hamiltonian or action                              |
| $L^{\text{GEN}}, H^{\text{GEN}}$ | Generalized Lagrangian and generalized Hamiltonian |

*Standard model*

|                       |  |
|-----------------------|--|
| $E, \nu, \rho$        | YOUNG's modulus, POISSON's coefficient and density   |
| $l_e$                 | Element length in 1D   |
| $EA, GA_s, EI$        | Longitudinal, shear and flexural rigidity of a rod   |
| $\Lambda$             | Slenderness of a beam element $h/l_e$  |
| $r_g = \sqrt{I/A}$    | Radius of gyration   |
| <b>D</b>              | Material matrix (elasticity tensor or pre-integrated stiffness for thin-walled structures) |
| $dt$                  | Time-step  |
| $c$                   | Phase velocity (speed of sound)  |
| $f, \omega$           | Natural frequency and angular frequency  |
| $\omega_{\text{max}}$ | Maximal natural frequency  |
| $dt_{\text{crit}}$    | Critical time-step   |
| $\alpha$              | Mass scaling factor for conventional mass scaling  |
| $\beta$               | Mass scaling factor for ASMS   |
| $C_1, C_2, C_3$       | Mass scaling factors for VSMS  |
| $\Gamma_i$            | Modal participation factor for $\phi_i$  |

*FE vectors and matrices*

|                         |  |
|-------------------------|--|
| <b>F</b> <sup>int</sup> | Internal force vector                                    |
| <b>F</b> <sup>ext</sup> | External force vector                                    |
| <b>F</b> <sup>vbc</sup> | Nodal vector due to velocity boundary conditions         |
| <b>U, V, P</b>          | Displacement, velocity and momentum vectors              |
| <b>Z</b>                | Discrete contact forces (values of LAGRANGE multipliers) |
| <b>N</b>                | Shape function matrix for displacement                   |
| <b>Ψ</b>                | Shape function matrix for velocity                       |
| <b>χ</b>                | Shape function matrix for momentum                       |
| <b>Ñ</b>                | Shape functions for incompatible velocity                |
| <b>M</b>                | Mass matrix  |
| <b>M</b> <sup>*</sup>   | Hybrid singular mass matrix                              |
| <b>M</b> <sup>°</sup>   | Mass matrix after selective mass scaling                 |
| □ <sup>°</sup>          | Symbol referring to mass scaling                         |
| λ <sup>°</sup>          | Artificially added mass or mass augmentation             |
| $\mathcal{A}$           | Projection from velocity on displacement                 |
| $\mathcal{C}$           | Projection from momentum on displacement                 |

|  |   |
|--|---|
| $\mathcal{G}$                            | Projection from momentum on velocity  |
| $\mathcal{Y}$                            | Mass matrix w.r.t. velocity   |
| $\mathcal{H}$                            | Mass matrix w.r.t. momentum   |
| $\tilde{\mathbf{D}}, \tilde{\mathbf{L}}$ | Mass matrix and projection matrix for incompatible velocity                     |
| $\mathbf{B}_0$                           | Linear strain-displacement operator   |
| $\mathbf{G}$                             | Constraint matrix   |
| $\mathbf{K}$                             | Stiffness matrix  |
| $\boldsymbol{\phi}$                      | Eigenvector $\mathbf{K}\boldsymbol{\phi} = \omega^2\mathbf{M}\boldsymbol{\phi}$ |
| $\mathbf{o}_i$                           | Rigid body mode vector for an element   |
| $\mathbf{H}$                             | Frequency response function   |

*Spectral and dispersion analysis*

|   |  |
|---|--|
| $\lambda$                                       | Wavelength   |
| $k = 2\pi/\lambda$                              | Wavenumber   |
| $\kappa = k/l_e$                                | Dimensionless wavelength   |
| $\omega$  | Circular frequency of wave                                       |
| $\omega^\circ$                                  | Circular frequency after selective mass scaling                  |
| $\Omega = \omega l_e/c$                         | Dimensionless frequency  |
| $\square_{\text{aco}}, \square_{\text{opt}}$    | Subscript for acoustic and optical waves, respectively           |
| $\square^{\text{bend}}, \square^{\text{shear}}$ | Superscript for flexural (bending) and shear waves, respectively |

*Mathematical operators*

|                                |  |
|--------------------------------|--|
| Span                           | Linear envelope/hull/span for a given vector set                                       |
| ker                            | Kernel or null-space of a matrix/operator  |
| Tr                             | Trace of a matrix  |
| mod                            | Modulo operator that finds the remainder of division of one number by another          |
| cond                           | Condition number of matrix, $\text{cond}(\mathbf{A}) =  \mathbf{A} / \mathbf{A}^{-1} $ |
| $\delta$                       | Variation operator   |
| $\mathbf{L}, \mathbf{L}^*$     | Kinematic differential operator and its adjoint  |
| div, grad                      | Divergence and gradient operators  |
| $\overset{3}{\mathbf{E}}$      | Fundamental tensor of third order, LEVI-CIVITA permutation tensor                      |
| $\overset{23}{\mathbf{T}}$     | Transpose of 2nd and 3rd components of a high-order tensor                             |
| $\ni$                          | Differential inclusion   |
| $\cdot$                        | Scalar product of two vectors  |
| $\times$                       | Cross-product of two vectors in 2D and 3D or product of two spaces                     |
| $(,)$                          | Scalar product of two vector fields defined in a domain $\mathcal{B}$                  |
| $\mathbf{m}(,), \mathbf{a}(,)$ | Bilinear forms for kinetic and internal energy   |



---

# Introduction

## 1.1 Motivation

In the context of finite element simulation of structural dynamics, consistent or lumped mass matrices are not always the optimal choice from the point of view of accuracy, robustness or computational cost. It is known that the dispersion error of the weighted sum of the consistent and the lumped mass is smaller than for each of them (FELIPPA 2006). Standard mass matrices also lead to spurious oscillation of contact forces or divergent results for penalty treatment of contact with large values of contact penalty stiffness or for treatment of contact constraints using LAGRANGE multipliers. The usage of singular mass matrices significantly reduces such spurious oscillations (KHENOUS ET AL. 2008; HAGER ET AL. 2008). Application of Selective Mass Scaling (SMS) in explicit dynamics increases the critical time-step size and results in a substantial speed-up for many practical problems, like deep drawing and drop test simulations (OLOVSSON ET AL. 2005; BORRVALL 2011).

The reduction of the dispersion error using alternative mass matrices is a well studied subject, e.g. see KRENK (2001), FELIPPA (2001), IDESMAN ET AL. (2011), GUO (2012) and references therein. This question is not directly addressed in this thesis. This thesis is focused on singular and selectively-scaled mass matrices. In contrast to previous works on this subject, *a unified variational approach* is used to construct matrices with desired properties. The unified variational approach is based on a novel mixed parametric HAMILTON's principle, which provides the necessary flexibility in choosing ansatz spaces and free parameters. Consistent spatial semi-discretization of this principle results in *families* of consistent mass matrices. The most useful members of these families are selected, evaluated and reported in this thesis.

In the following, some examples are presented to illustrate the problems of the standard mass matrices and motivate the usage of singular and selectively-scaled mass matrices. As it is

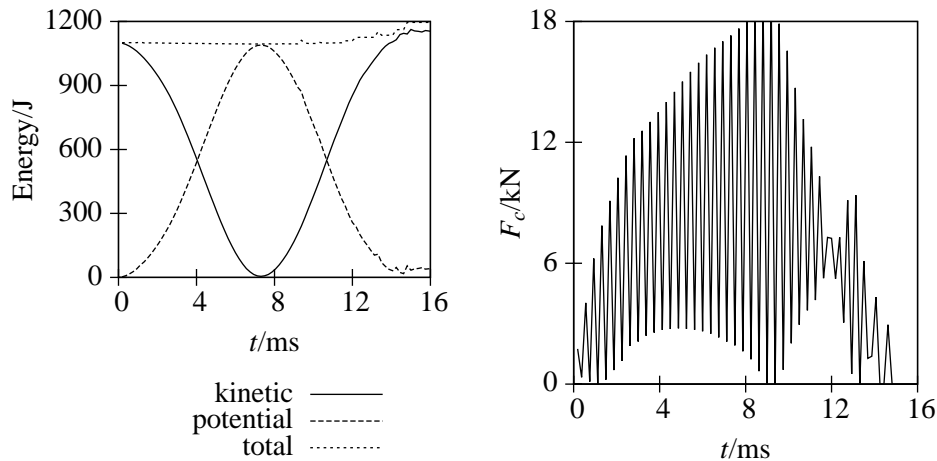


**Figure 1.1:** Evolution of the total energy (left) and the history of the contact force (right) computed for a typical impact simulation (see Subsection 7.1.6) obtained with NEWMARK  $\beta$  method, consistent mass matrix and LAGRANGE multipliers method for contact.

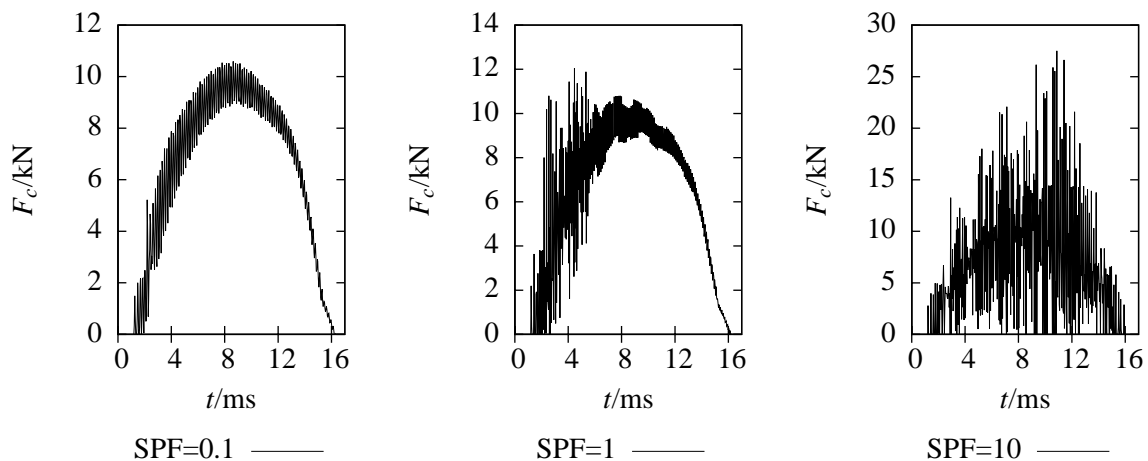


**Figure 1.2:** Contact force computed with different penalty factors (SPF) for example from Subsection 7.1.6.

mentioned above, the standard mass matrices may produce oscillation of contact forces, see Figure 1.1. Moreover, each release or activation of the contact constraint leads to an artificial gain or loss of the total energy. Using the penalty method for dynamic contact problems leads either to overpenetration, if the contact stiffness is small, or to highly oscillating contact forces, if the penalty factor is large, see Figure 1.2. In this thesis, these problems are substantially reduced using specially constructed singular mass matrices.

SMS is implemented in commercial codes and extensively used in industrial applications to reduce the computation time in explicit dynamics. There are also alternative methods to save computational time, like dynamic condensation or mesh adaptivity. SMS is competitive with

| Option                          | Simulation time, s | Speed-up w.r.t baseline |
|---------------------------------|--------------------|-------------------------|
| Baseline (fine mesh from start) | 5493               | 1                       |
| Mesh adaptivity                 | 599                | 9.2                     |
| Dynamic condensation            | 157                | 35                      |
| Selective mass scaling          | 119                | 46                      |

**Table 1.1:** Speed-up for different methods in *RADIOSS* for the NUMISHEET2008 S-rail benchmark (ROY ET AL. 2011).



**Figure 1.3:** Deformation of a steel tube in a drop test, see OLOVSSON AND SIMONSSON (2006).

| Option                               | Simulation time, s | Speed-up |
|--------------------------------------|--------------------|----------|
| No mass scaling (base model)         | 4268               | 1        |
| Double density                       | 3149               | 1.2      |
| Selective mass scaling, $\beta = 10$ | 1346               | 2.0      |
| Selective mass scaling, $\beta = 50$ | 621                | 3.4      |

**Table 1.2:** Speed-up for different mass scaling strategies in a steel tube in a drop test benchmark (OLOVSSON AND SIMONSSON 2006).

the alternative methods for reduction of computational time as a study for metal sheet forming shows, see Table 1.1. Here, SMS enables a speed-up of 46 times! More modest results are obtained in a drop test simulation, see Figure 1.3. A speed-up from 2.0 to 3.4 times is reported in OLOVSSON AND SIMONSSON (2006) for the explicit finite element code *KRYP*, see Table 1.2.

SMS can also be applied to a full-scale model of a car. In Figure 1.4, the deformed shape of a *Dodge Neon* model<sup>1</sup> is shown, which is computed after 40 ms of crash with the commercial code *LS-Dyna*. The history of contact forces is given in Figure 1.5. The base model uses time-step 1  $\mu$ s. Speed-up values of 1.13 and 1.17 are obtained with SMS for time-step sizes of 2  $\mu$ s and 3  $\mu$ s, respectively. The higher computational costs for contact treatment and solution of linear system of equation at each time-step<sup>2</sup> outweigh the benefits of larger time-step for this model.

<sup>1</sup>Available at <http://www.ncac.gwu.edu/vml/models.html>

<sup>2</sup>SMS leads to non-diagonal mass matrices.

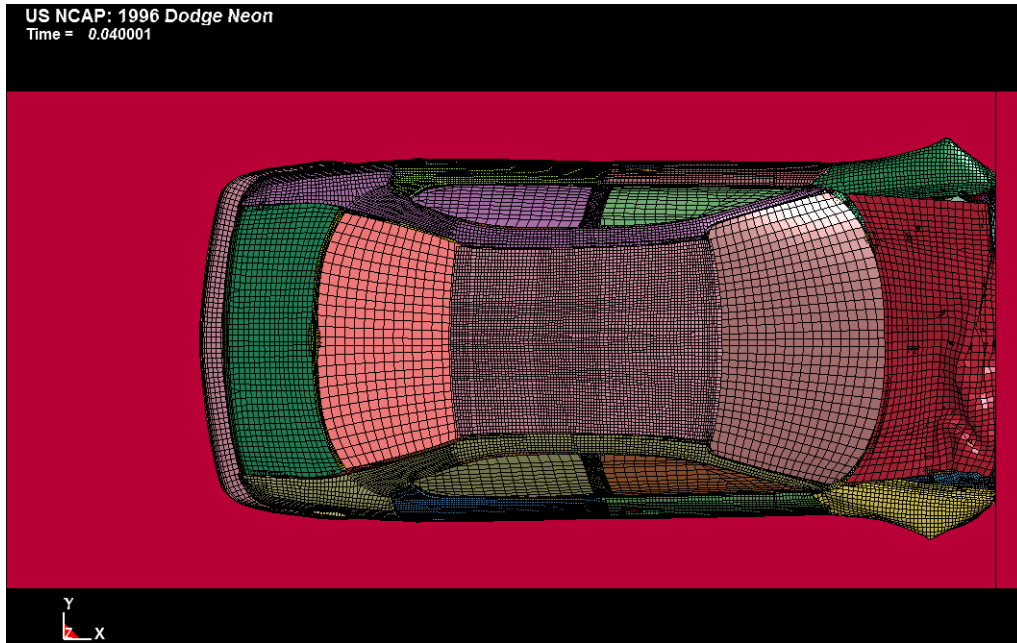


**Figure 1.4:** Deformed shape of a *Neon* 1996 model after 40 ms for the initial velocity 15.6 m/s.

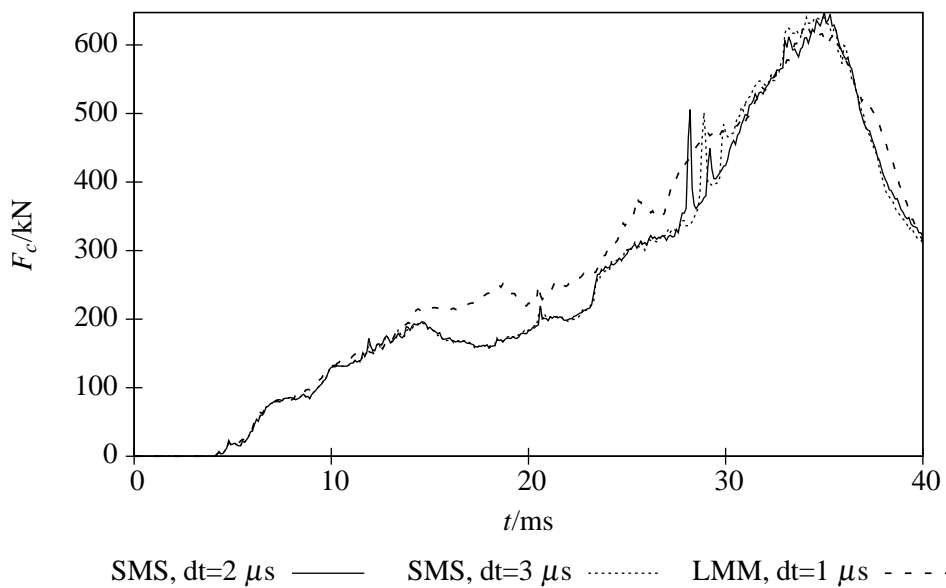


**Figure 1.5:** History of the contact force for *Neon* 1996 model during the first 40 ms.

These examples illustrate the range of applications of SMS and significant reduction of computational time for existing SMS techniques. However, there is a big potential for the improvement of the existing methods and for extending the range of applications.

## 1.2 Goals

This thesis follows the standard procedure for derivation of new finite elements: searching for appropriate weak formulation, setting the discretization procedure and approximation spaces, benchmarking and testing. In the context of singular and selectively scaled mass matrices, these steps are

- derive new parametric variational principles for elasto-dynamics with displacement, velocity and momentum as independent variables
- find appropriate discretization and approximation spaces for displacement, velocity and momentum
- evaluate critically the proposed discretization schemes and select the most efficient ones.

## 1.3 Overview

The thesis is organized in eight chapters and two appendices. In Chapter 2, a current approach to finite element discretization of dynamic structural problems is given. First, the basic continuum mechanics and the local form of an initial boundary value problem for an elasto-dynamic contact problem are given. The theories for selected thin-walled structures are also provided. Secondly, an overview over spatial finite element discretization of non-linear continuum and standard treatment of contact are given. Then, a topic of singular and scaled mass matrices is thoroughly investigated. The benefits of singular mass matrices for dynamic contact problems are explained and existing methods for construction of singular mass matrices are presented. Besides, methods for conventional and selective mass scaling for explicit dynamics are described. Furthermore, the standard time integration schemes are presented. This includes the central difference method<sup>3</sup> and NEWMARK  $\beta$  method, which are used later in the numerical examples. The methods for assessment of quality of the numerical solution conclude the Chapter 2.

Chapter 3 is devoted to the derivation of the novel penalized HAMILTON's principle and the modified HAMILTON's principle. The latter is extended for small sliding unilateral contact problems. The derived formulations can be directly discretized. In addition, the equivalence of the proposed penalized and modified HAMILTON's principles to the local formulation is shown by the derivation of the EULER-LAGRANGE equations.

---

<sup>3</sup>The standard procedure and a modification by OLOVSSON AND SIMONSSON (2006) for non-diagonal mass matrices needed for SMS. A theoretical estimate of speed-up for SMS is also derived.

In Chapter 4, different families of mass matrices are discussed. First, the family of consistent scaled mass matrices is built. Among the family three useful instances are chosen. Then the Hybrid-Singular consistent Mass Matrix (HSMM) is discussed, and its stability is considered. Moreover, the condition for the construction of a HSMM with zero components at certain nodes is derived. The latter condition requires special shape functions for the displacements. In Chapter 5, such functions for arbitrary line elements are built. On the basis of these functions, 2D and 3D extensions are proposed. Then good ansatz spaces for selectively-scaled mass matrices are proposed for truss, beam and solid elements.

The newly developed mass matrices are rigorously analyzed for three important applications, namely free vibrations, wave propagation and impact problems. The quality of the solution for the modal analysis is indirectly assessed for 1D examples using dispersion analysis. Accuracy of 2D and 3D elements is assessed by NAFEMS eigenvalue benchmarks. The results of such an analysis for the elements are presented in Chapter 6. Numerical examples for wave propagation and impact problems are presented in Chapter 7. Finally, the main results and the features of the new method and an outlook are given in Chapter 8.

In Appendices A and B the inertial patch tests for selected elements and an alternative derivation of the novel penalized HAMILTON's principle are considered.

---

## State of the art

In this Chapter, an current approach to FE discretization of dynamic structural problems is given. First, the basic continuum mechanics and the local form of an Initial Boundary Value Problem (IBVP) for an elasto-dynamic contact problem are given in Sections 2.1 and 2.2. The theories for selected thin-walled structures are also provided in Subsection 2.2.6. Secondly, an overview over spatial FE semi-discretization of non-linear continuum and standard treatment of contact is given in Section 2.3. Then, the question of singular and scaled mass matrices is thoroughly investigated in Subsections 2.3.4 and 2.3.5, respectively. The benefits of singular mass matrices for dynamic contact problems are considered and existing methods for construction of singular mass matrices are presented. Besides, methods for conventional and selective mass scaling for explicit dynamics are described. Furthermore, the standard time integration schemes are presented in Section 2.4. This includes the central difference method and NEWMARK  $\beta$  method, which are extensively used in later numerical examples in Chapter 7. The methods for assessment of quality of the numerical solution conclude the Chapter. These methods, i.e. dispersion analysis, frequency response assurance criterion and modal assurance criterion, allow evaluation of the influence of new mass matrices on eigenmodes and eigenfrequencies.

### 2.1 Basic Continuum Mechanics

In this section, a brief overview of continuum mechanics is given (for further reading cf. GURTIN (1981); MARSDEN AND HUGHES (1983); HOLZAPFEL (2000); BONET (2008)). First, basic notions of kinematics, strain and stress measures are introduced. Then, constitutive equations for hyperelastic material and balance laws are postulated. A statement of the initial boundary value problem and its weak form conclude the section.

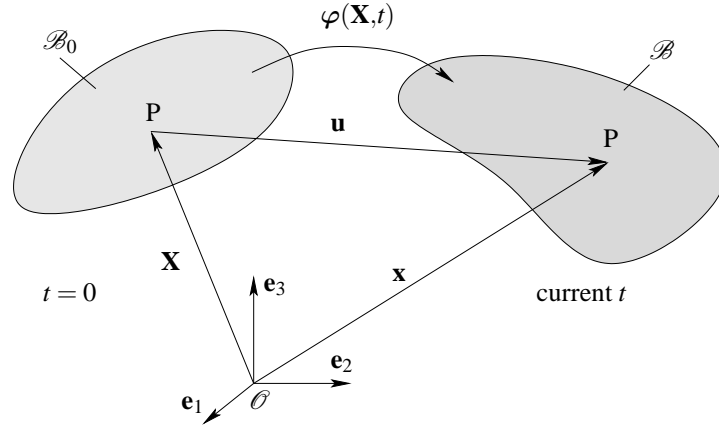


**Figure 2.1:** Mapping between the reference and the current configuration.

### 2.1.1 Kinematics and stress measures

Throughout the thesis, a Lagrangian description of motion relative to an inertial Cartesian frame is used. We denote with  $\mathcal{O}$  the origin of the coordinate system and with  $(\mathbf{e}_1, \mathbf{e}_2, \mathbf{e}_3)$  – the orthonormalized basis vectors. Let  $\mathcal{B}_0$  be a reference configuration of a body at time  $t = 0$  and  $\mathcal{B}$  be a current (deformed) configuration. Consider an arbitrary material point  $P$  given by its position vector  $\mathbf{X} \in \mathcal{B}_0$  at the reference configuration. We denote with  $\mathbf{x}$  a current position of a point  $P$ . The motion can be mathematically described by a time-dependent mapping  $\varphi$  between the reference and the current configuration

$$\mathbf{x} = \varphi(\mathbf{X}, t), \quad \varphi(\mathbf{X}, t) : \mathcal{B}_0 \times \mathcal{I} \rightarrow \mathcal{B}, \quad (2.1)$$

with  $\mathcal{I} = [0, t_{\text{end}}]$  being the time interval. We assume that the inverse mapping from the current to the reference configuration exists with

$$\mathbf{X} = \varphi^{-1}(\mathbf{x}, t), \quad \varphi^{-1}(\mathbf{x}, t) : \mathcal{B} \times \mathcal{I} \rightarrow \mathcal{B}_0. \quad (2.2)$$

We assume also that the mapping  $\varphi$  is sufficiently smooth, namely it is one time piecewise continuously differentiable in space and twice piecewise continuously differentiable in time. From now on, we use  $\mathbf{x}$  as a function of  $\mathbf{X}$  and  $t$ .

#### Displacement and deformation

The displacement of a material point  $P$  is the difference between its current and reference position vectors with

$$\mathbf{u} = \mathbf{x} - \mathbf{X}. \quad (2.3)$$

The velocity and the acceleration are defined as the first and the second time derivatives of the material point position vector with

$$\mathbf{v}(\mathbf{X}, t) = \frac{\partial \mathbf{x}}{\partial t} = \dot{\mathbf{x}}, \quad \mathbf{a}(\mathbf{X}, t) = \frac{\partial^2 \mathbf{x}}{\partial t^2} = \ddot{\mathbf{x}}. \quad (2.4)$$

Note, that the material coordinate  $\mathbf{X}$  is independent of time, thus the velocity and the acceleration can be expressed in terms of the displacement vector  $\mathbf{u}$  with

$$\mathbf{v}(\mathbf{X}, t) = \frac{\partial(\mathbf{u} + \mathbf{X})}{\partial t} = \frac{\partial \mathbf{u}}{\partial t} = \dot{\mathbf{u}}, \quad \mathbf{a}(\mathbf{X}, t) = \frac{\partial^2(\mathbf{u} + \mathbf{X})}{\partial t^2} = \ddot{\mathbf{u}}. \quad (2.5)$$

During the deformation process, the relative position of the material points in  $\mathcal{B}$  is changed. A material point is zero-dimensional object, and so it is impossible to define a deformation of a single point. The common approach considers an infinitesimal material fiber  $d\mathbf{x}$  intersecting the point  $P$ . A material fiber is defined as a smooth one-dimensional set of material points. Undergoing deformation, the fiber rotates and stretches. The total deformation of the fiber  $d\mathbf{x}$  is computed via mapping  $\varphi$  with

$$d\mathbf{x} = (\mathbf{x} + d\mathbf{x}) - \mathbf{x} = \varphi(\mathbf{X} + d\mathbf{X}, t) - \varphi(\mathbf{X}, t) = \mathbf{F} d\mathbf{X}, \quad (2.6)$$

with  $\mathbf{F} = \frac{\partial \mathbf{x}}{\partial \mathbf{X}}$  being the deformation gradient, see Figure 2.2. The volumetric deformation, or the ratio of initial infinitesimal material volume  $dV$  to an current volume  $dv$  around the material point  $P$ , can be computed using the Jacobian of the deformation gradient

$$\frac{dv}{dV} = \det(\mathbf{F}). \quad (2.7)$$

We regard here only proper mappings  $\varphi$  with  $\det(\mathbf{F}) > 0$ . This guarantees that the material volume does not turn inside out. The velocity gradient  $\dot{\mathbf{F}}$  is defined as the material gradient of the velocity vector with

$$\frac{\partial \mathbf{v}}{\partial \mathbf{X}} = \frac{\partial \dot{\mathbf{x}}}{\partial \mathbf{X}} = \dot{\mathbf{F}}. \quad (2.8)$$

Along the infinitesimal material fibers and volumes, infinitesimal material area elements may be introduced via cross-product of infinitesimal fibers  $d\mathbf{R}_1$  and  $d\mathbf{R}_2$ . The transformation of area elements  $d\mathbf{a}$  and  $d\mathbf{A}$  is governed by NANSON's formula with

$$d\mathbf{a} = \det(\mathbf{F}) \mathbf{F}^{-T} d\mathbf{A}. \quad (2.9)$$

The normal of the body surface follows the same transformation rules as the material area element, which is used for correct treatment of contact conditions.

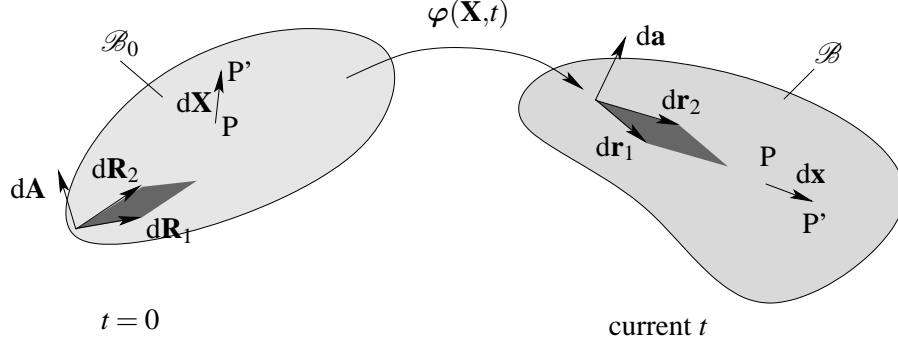


**Figure 2.2:** Mapping of line and area elements.

In the following, strain and deformation measures for finite deformations are introduced by the difference of the squares of the material fiber in current and reference configuration with

$$\begin{aligned} ds^2 - dS^2 &= d\mathbf{x} \cdot d\mathbf{x} - d\mathbf{X} \cdot d\mathbf{X} = d\mathbf{X} \cdot \mathbf{F}^T \mathbf{F} d\mathbf{X} - d\mathbf{X} \cdot d\mathbf{X} \\ &= d\mathbf{X} \cdot (\mathbf{C} - \mathbf{I}) d\mathbf{X} = d\mathbf{X} \cdot 2\mathbf{E} d\mathbf{X}, \end{aligned} \quad (2.10a)$$

where

$$\mathbf{C} = \mathbf{F}^{-T} \mathbf{F}, \quad \mathbf{E} = \frac{1}{2} (\mathbf{C} - \mathbf{I}), \quad (2.10b)$$

with  $\mathbf{C}$  being the right CAUCHY-GREEN deformation tensor and  $\mathbf{E}$  being the GREEN-LAGRANGE strain tensor. This completes the summary of kinematics.

### Stress measures

Internal forces are developed in deformable bodies as reaction to external action, which can be surface traction  $\hat{\mathbf{t}}$ , body forces  $\hat{\mathbf{b}}$  or contact traction with another body  $\mathbf{t}_c$ . The measure of intensity of the internal forces is stress. The CAUCHY stress theorem postulates that the stress state at a material point in the body can be defined by a second-order tensor  $\boldsymbol{\sigma}$ , called true stress tensor. The true stress tensor relates the stress vector  $\mathbf{t}$  on a plane with an arbitrary normal  $\mathbf{n}$  as

$$\mathbf{t} = \boldsymbol{\sigma} \mathbf{n}. \quad (2.11)$$

This relation is illustrated in Figure 2.3.

The normal vector  $\mathbf{n}$  and the stress vector  $\mathbf{t}$  belong to the current configuration. The first PIOLA-KIRCHHOFF stress  $\boldsymbol{\sigma}_{PKI}$  relates the reference normal vector to the current stress vec-

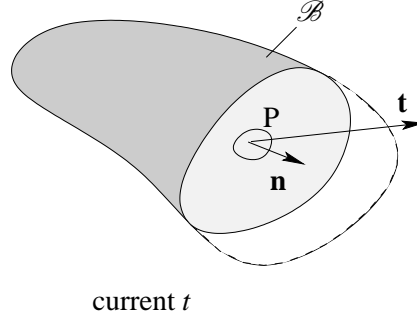


**Figure 2.3:** Internal traction vector  $\mathbf{t}$  on virtual cut surface with normal  $\mathbf{n}$ .

tor.  $\sigma_{PK1}$  is obtained from the true stress via transformation with

$$\sigma_{PK1} = (\det \mathbf{F}) \boldsymbol{\sigma} \mathbf{F}^{-T}. \quad (2.12)$$

This transformation results in a tensor with both reference and current basis components and it is called a *partial pull back*.

None of the stress tensors are energy conjugate with the strain tensors defined above. For this reason, the second PIOLA-KIRCHHOFF stress  $\sigma_{PK2}$  is introduced with

$$\sigma_{PK2} = (\det \mathbf{F}) \mathbf{F}^{-1} \boldsymbol{\sigma} \mathbf{F}^{-T}. \quad (2.13)$$

This transformation is a *complete pull back* to the reference configuration with an additional weighting factor  $\det \mathbf{F}$ . The partial push forward of the first PIOLA-KIRCHHOFF stress  $\sigma_{PK1}$  and the complete push forward of the second PIOLA-KIRCHHOFF  $\sigma_{PK2}$  read as follows

$$\boldsymbol{\sigma} = \frac{1}{\det \mathbf{F}} \sigma_{PK1} \mathbf{F}^T, \quad \boldsymbol{\sigma} = \frac{1}{\det \mathbf{F}} \mathbf{F} \sigma_{PK2} \mathbf{F}^T. \quad (2.14)$$

### 2.1.2 Constitutive equations for hyperelastic materials

Generally, the behavior of a solid material can be elastic and inelastic (plastic, viscoelastic or viscoplastic). It can depend on temperature and strength of electric and magnetic fields, etc. Even more complicated behavior is observed if the material undergoes phase transformation, e.g. for shape-memory alloys. Herein, only hyperelastic constitutive relations are used. Moreover, we neglect internal dissipation and thermal conduction, which means that no entropy is produced and the processes are isentropic. Thus, the constitutive equation used here relates the current stress only with a current value of strain.

Hyperelastic material is an ideal elastic material, for which the stress-strain relationship is derived from an elastic energy density function  $W$ . It is defined to be specific to the reference

volume and for the isentropic process it is related to the internal energy function  $W = \rho_0 u$ . Following standard derivations, the stress is obtained as the derivative of the elastic energy function  $W$  w.r.t. the GREEN-LAGRANGE strain tensor (see balance of energy below) with

$$\boldsymbol{\sigma}_{\text{PK2}} = \frac{\partial W}{\partial \mathbf{E}} = 2 \frac{\partial W}{\partial \mathbf{C}} = 2\rho_0 \frac{\partial u}{\partial \mathbf{C}}. \quad (2.15)$$

The material tangent  $\mathbf{D}$  relates infinitesimal increments of stress and strain. It can be computed as the second derivative of the free energy function

$$d\boldsymbol{\sigma}_{\text{PK2}} = d \frac{\partial W}{\partial \mathbf{E}} = \frac{\partial^2 W}{\partial \mathbf{E}^2} d\mathbf{E} = \mathbf{D} d\mathbf{E}, \quad (2.16a)$$

with

$$\mathbf{D} = \frac{\partial^2 W}{\partial \mathbf{E}^2} = \rho_0 \frac{\partial^2 u}{\partial \mathbf{E}^2}. \quad (2.16b)$$

The material tangent is a fourth-order tensor and in case of hyperelastic material, it possesses major and minor symmetries with

$$\mathbf{D}_{ijkl} = \mathbf{D}_{klij} = \mathbf{D}_{jikl}. \quad (2.17)$$

Now, we recall the elastic energy density function, stress-strain relations and the material tangent for most common materials, see OGDEN (1997); HOLZAPFEL (2000). The constitutive relation for the ST. VENANT-KIRCHHOFF material reads as follows

$$W = \frac{\lambda}{2} (\text{Tr}(\mathbf{E}))^2 + \mu \text{Tr}(\mathbf{E}^2), \quad (2.18a)$$

$$\boldsymbol{\sigma}_{\text{PK2}} = \lambda \text{Tr}(\mathbf{E})\mathbf{I} + 2\mu\mathbf{E}, \quad (2.18b)$$

$$\mathbf{D} = \lambda \mathbf{I} \otimes \mathbf{I} + 2\mu (\mathbf{I} \otimes \mathbf{I})^{\text{T}23}. \quad (2.18c)$$

For neo-Hookean material, the relations read

$$W = \frac{\mu}{2} (\text{Tr} \mathbf{C} - 3) - \mu \ln(\det \mathbf{F}) + \frac{\lambda}{2} (\ln(\det \mathbf{F}))^2, \quad (2.19a)$$

$$\boldsymbol{\sigma}_{\text{PK2}} = \mu (\mathbf{I} - \mathbf{C}^{-1}) + \lambda \mathbf{C}^{-1}, \quad (2.19b)$$

$$\mathbf{D} = \mu (\mathbf{C}^{-1} \otimes \mathbf{C}^{-1})^{\text{T}23} + 2(\mu - \lambda \ln(\det \mathbf{F})) \mathbf{C}^{-1} \otimes \mathbf{C}^{-1}. \quad (2.19c)$$

Note, that ST. VENANT-KIRCHHOFF and neo-Hookean materials are isotropic and their stored energy function depends only on the invariants of  $\mathbf{E}$  or  $\mathbf{C}$ .

### 2.1.3 Balance laws

As it was mentioned in the previous subsection, we limit ourselves to hyperelastic constitutive equations and we neglect internal dissipation and heat conduction. Therefore, the entropy balance inequality is omitted here (for a deeper description of thermodynamics of continua cf. GURTIN (1981); MARSDEN AND HUGHES (1983); HOLZAPFEL (2000); BONET (2008)).

We assume no mass production or influx. The action of the system is limited to an external body load  $\hat{\mathbf{b}}$  and an external surface load  $\hat{\mathbf{t}}$  and a flow of internal traction  $\mathbf{t}$  defined by the CAUCHY theorem. Now we can postulate the balance for basic mechanical quantities: mass, linear momentum, moment of momentum and energy. First, consider an open subset  $\mathcal{U} \supset \mathcal{B}$  with a sufficiently smooth boundary  $\partial\mathcal{U}$ . For this subset, we define the mass  $m$ , the linear momentum  $\mathbf{p}$ , the moment of momentum  $\mathbf{l}$ , the kinetic energy  $T$ , the internal energy  $U$  and the total energy  $E_{\text{tot}}$  as follows

$$m(\mathcal{U}) = \int_{\mathcal{U}} \rho \, dv, \quad \mathbf{p}(\mathcal{U}) = \int_{\mathcal{U}} \rho \mathbf{v} \, dv, \quad \mathbf{l}(\mathcal{U}) = \int_{\mathcal{U}} \mathbf{x} \times \rho \mathbf{v} \, dv, \quad (2.20a)$$

$$T(\mathcal{U}) = \int_{\mathcal{U}} \frac{\rho}{2} \mathbf{v} \cdot \mathbf{v} \, dv, \quad U(\mathcal{U}) = \int_{\mathcal{U}} \rho u(\mathbf{E}) \, dv, \quad E_{\text{tot}} = T + U, \quad (2.20b)$$

with  $\rho$  being the density. The balance of mass for the subset of material points  $\mathcal{U}$  postulates that in absence of mass production and mass influx, the rate change of the mass is zero. Application of the Transport theorem according to HOLZAPFEL (2000) and MARSDEN AND HUGHES (1983) results in

$$\frac{d}{dt} m(\mathcal{U}) = \int_{\mathcal{U}} \dot{\rho} \, dv = \int_{\mathcal{U}} (\dot{\rho} + \rho \operatorname{div} \mathbf{v}) \, dv = 0. \quad (2.21)$$

Using the Localization theorem for the latter integral and dividing it over  $\rho$ , one gets

$$\frac{\dot{\rho}}{\rho} + \operatorname{div} \mathbf{v} = \frac{\dot{\rho}}{\rho} + \frac{\partial \mathbf{v}}{\partial \mathbf{X}} \frac{\partial \mathbf{X}}{\partial \mathbf{x}} = \frac{d}{dt} (\ln(\rho) + \ln(\det \mathbf{F})) = 0. \quad (2.22)$$

The latter equation can be integrated in time. Substitution of the initial values of  $\det \mathbf{F}(t = 0) = \det \mathbf{I} = 1$  and  $\rho_0$ , yields the equation for the balance of mass

$$\rho \det \mathbf{F} = \rho_0 = \text{const.} \quad (2.23)$$

The balance of linear momentum postulates that the rate of change of linear momentum is equal to the total force from volume and surface loads, i.e.

$$\frac{d}{dt} \mathbf{p}(\mathcal{U}) = \frac{d}{dt} \int_{\mathcal{U}} \rho \mathbf{v} \, dv = \int_{\mathcal{U}} \rho \hat{\mathbf{b}} \, dv + \int_{\partial\mathcal{U}} \mathbf{t} \, da = \int_{\mathcal{U}} \rho \hat{\mathbf{b}} \, dv + \int_{\partial\mathcal{U}} \boldsymbol{\sigma} \mathbf{n} \, da. \quad (2.24)$$

The balance of mass together with the Transport theorem lead to the following statement  $\frac{d}{dt} \int_{\mathcal{U}} \rho \mathbf{v} dv = \int_{\mathcal{U}} \rho \dot{\mathbf{v}} dv$ . Application of the Divergence theorem to the term  $\int_{\partial \mathcal{U}} \boldsymbol{\sigma} \mathbf{n} da$  yields

$$\int_{\mathcal{U}} \rho \dot{\mathbf{v}} dv = \int_{\mathcal{U}} (\operatorname{div} \boldsymbol{\sigma} + \rho \hat{\mathbf{b}}) dv. \quad (2.25)$$

Finally, usage of the Localization theorem results in the local statement of the balance of linear momentum

$$\rho \dot{\mathbf{v}} = \operatorname{div} \boldsymbol{\sigma} + \rho \hat{\mathbf{b}}. \quad (2.26)$$

The balance of moment of momentum postulates that the rate of change of moment of momentum is equal to the total moment from volume and surface loads, i.e.

$$\frac{d}{dt} \mathbf{l}(\mathcal{U}) = \frac{d}{dt} \int_{\mathcal{U}} \mathbf{x} \times \rho \mathbf{v} dv = \int_{\mathcal{U}} \mathbf{x} \times \rho \hat{\mathbf{b}} dv + \int_{\partial \mathcal{U}} \mathbf{x} \times \mathbf{t} da = \int_{\mathcal{U}} \mathbf{x} \times \rho \dot{\mathbf{v}} dv + \int_{\partial \mathcal{U}} \mathbf{x} \times \boldsymbol{\sigma} \mathbf{n} da. \quad (2.27)$$

The terms  $\frac{d}{dt} \int_{\mathcal{U}} \mathbf{x} \times \rho \mathbf{v} dv$  and  $\int_{\partial \mathcal{U}} \mathbf{x} \times \boldsymbol{\sigma} \mathbf{n} da$  are recast using the balance of mass, vector algebra and the Divergence theorem

$$\frac{d}{dt} \int_{\mathcal{U}} \mathbf{x} \times \rho \mathbf{v} dv = \int_{\mathcal{U}} \mathbf{v} \times \rho \mathbf{v} dv + \int_{\mathcal{U}} \mathbf{x} \times \rho \dot{\mathbf{v}} dv = \int_{\mathcal{U}} \mathbf{x} \times \rho \dot{\mathbf{v}} dv, \quad (2.28a)$$

$$\int_{\partial \mathcal{U}} \mathbf{x} \times \boldsymbol{\sigma} \mathbf{n} da = \int_{\mathcal{U}} \operatorname{div} (\mathbf{x} \times \boldsymbol{\sigma} \mathbf{n}) dv = \int_{\mathcal{U}} \left( \mathbf{x} \times \operatorname{div} \boldsymbol{\sigma} + \overset{3}{\mathbf{E}} \boldsymbol{\sigma} \right) dv, \quad (2.28b)$$

with  $\overset{3}{\mathbf{E}}$  being the Fundamental tensor of 3rd order (LEVI-CIVITA permutation tensor). Substitution of the latter two expressions into the balance of momentum yields

$$\int_{\mathcal{U}} \left( \mathbf{x} \times (\rho \dot{\mathbf{v}} - \operatorname{div} \boldsymbol{\sigma} - \rho \hat{\mathbf{b}}) + \overset{3}{\mathbf{E}} \boldsymbol{\sigma} \right) dv = \mathbf{0}. \quad (2.29)$$

Using the balance of linear momentum and the Localization theorem, the local form of balance of momentum is obtained in a form

$$\overset{3}{\mathbf{E}} \boldsymbol{\sigma} = \mathbf{0} \Leftrightarrow \boldsymbol{\sigma}^T = \boldsymbol{\sigma}. \quad (2.30)$$

Thus, the balance of moment of momentum implies the symmetry of the CAUCHY stress tensor. The second PIOLA-KIRCHHOFF stress is also symmetric, which is easily checked using the transformation formula between  $\boldsymbol{\sigma}_{\text{PK2}}$  and  $\boldsymbol{\sigma}$ .

The balance of energy postulates that the rate of change of energy is equal to the total power from volume and surface loads, i.e.

$$\frac{d}{dt}E_{\text{tot}}(\mathcal{U}) = \frac{d}{dt}(T + U) = \int_{\mathcal{U}} \mathbf{v} \cdot \rho \hat{\mathbf{b}} \, dv + \int_{\partial\mathcal{U}} \mathbf{v} \cdot \mathbf{t} \, da = \int_{\mathcal{U}} \mathbf{v} \cdot \rho \hat{\mathbf{b}} \, dv + \int_{\partial\mathcal{U}} \mathbf{v} \cdot \boldsymbol{\sigma} \mathbf{n} \, da. \quad (2.31)$$

Recasting the terms  $\frac{d}{dt}(T + U)$  and  $\int_{\partial\mathcal{U}} \mathbf{v} \cdot \boldsymbol{\sigma} \mathbf{n} \, da$  yields

$$\frac{d}{dt}(T + U) = \int_{\mathcal{U}} \rho \mathbf{v} \cdot \dot{\mathbf{v}} \, dv + \int_{\mathcal{U}} \rho \frac{\partial u(\mathbf{E})}{\partial \mathbf{E}} : \dot{\mathbf{E}} \, dv, \quad (2.32a)$$

$$\int_{\partial\mathcal{U}} \mathbf{v} \cdot \boldsymbol{\sigma} \mathbf{n} \, da = \int_{\mathcal{U}} \text{div}(\boldsymbol{\sigma} \mathbf{v}) \, dv = \int_{\mathcal{U}} \left[ \left( \frac{\partial \mathbf{v}}{\partial \mathbf{x}} : \boldsymbol{\sigma} \right) + \mathbf{v} \cdot \text{div} \boldsymbol{\sigma} \right] \, dv. \quad (2.32b)$$

Substituting the latter expressions in the integral form of the energy balance given in equation (2.31), together with collecting terms, yields

$$\int_{\mathcal{U}} \left( \mathbf{v} \cdot (\rho \dot{\mathbf{v}} - \text{div} \boldsymbol{\sigma} - \rho \hat{\mathbf{b}}) + \left( \rho \frac{\partial u(\mathbf{E})}{\partial \mathbf{E}} : \dot{\mathbf{E}} - \frac{\partial \mathbf{v}}{\partial \mathbf{x}} : \boldsymbol{\sigma} \right) \right) \, dv = 0. \quad (2.33)$$

The first term in the integral is zero. The term  $\frac{\partial \mathbf{v}}{\partial \mathbf{x}} : \boldsymbol{\sigma}$  in equation (2.33) can be recast with

$$\begin{aligned} \frac{\partial \mathbf{v}}{\partial \mathbf{x}} : \boldsymbol{\sigma} &= (\mathbf{F} \dot{\mathbf{F}}^{-1}) : \frac{1}{\det \mathbf{F}} \mathbf{F} \boldsymbol{\sigma}_{\text{PK2}} \mathbf{F}^T = \frac{1}{\det \mathbf{F}} (\mathbf{F}^T \dot{\mathbf{F}}) : \boldsymbol{\sigma}_{\text{PK2}} = \frac{1}{\det \mathbf{F}} \text{sym}(\mathbf{F}^T \dot{\mathbf{F}}) : \boldsymbol{\sigma}_{\text{PK2}} \\ &= \frac{1}{\det \mathbf{F}} \dot{\mathbf{E}} : \boldsymbol{\sigma}_{\text{PK2}} = \frac{1}{\det \mathbf{F}} \boldsymbol{\sigma}_{\text{PK2}} : \dot{\mathbf{E}}. \end{aligned} \quad (2.34)$$

In the derivation, the symmetry (2.30) and the push-forward of the second PIOLA-KIRCHHOFF stress (2.14) are used. Substitution of equation (2.34), together with the local form of the mass balance (2.23) yield the local statement of energy balance w.r.t. the reference quantities

$$\rho_0 \frac{\partial u(\mathbf{E})}{\partial \mathbf{E}} : \dot{\mathbf{E}} = \boldsymbol{\sigma}_{\text{PK2}} : \dot{\mathbf{E}}. \quad (2.35)$$

## 2.2 Large sliding frictionless contact

In this section, a concise description of large sliding frictionless contact is given. A description of frictional contact with a rigorous derivation of tangential behavior is given in the classical textbooks WRIGGERS (2006) and LAURSEN (2002).

First, the motion of the contacting bodies is described and the basic assumptions and notations are introduced. Secondly, the impenetration condition and the traction contact condition are stated in a practical form. Finally, variation of the kinematic and traction values is given.

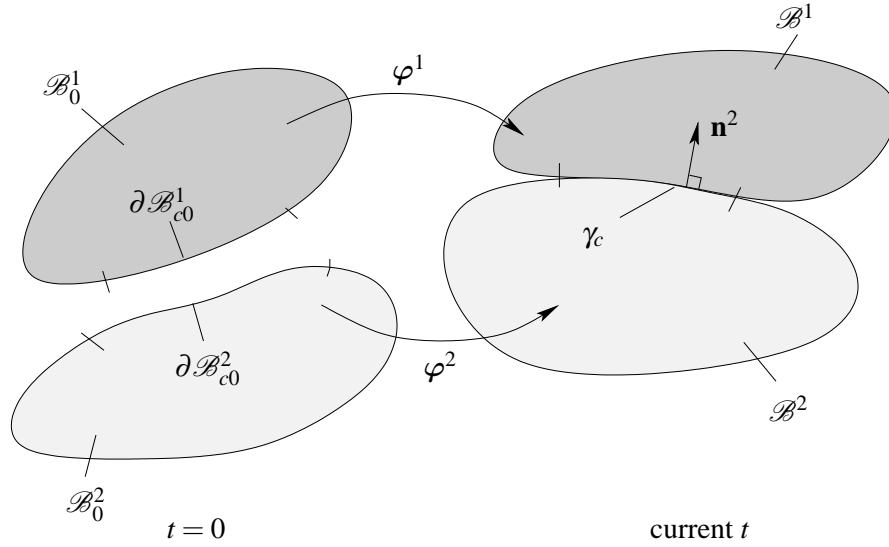


**Figure 2.4:** Kinematic of two contacting bodies.

### 2.2.1 Motion, assumptions and notations

Without loss of generality, a two-body contact is considered, see Figure 2.4. The bodies are defined by their reference positions  $\mathcal{B}_0^1$  and  $\mathcal{B}_0^2$ . The motion of the bodies is described by independent mappings  $\varphi^1$  and  $\varphi^2$  with

$$\varphi^1 : \mathcal{B}_0^1 \times \mathcal{I} \rightarrow \mathcal{B}^1, \quad \varphi^2 : \mathcal{B}_0^2 \times \mathcal{I} \rightarrow \mathcal{B}^2. \quad (2.36)$$

The superscripts 1 and 2 refer to bodies  $\mathcal{B}_0^1$  and  $\mathcal{B}_0^2$  throughout this section. At the current position at time  $t$ , the bodies occupy the configurations  $\mathcal{B}^1$  and  $\mathcal{B}^2$ . The DIRICHLET and NEUMANN boundary conditions are defined for the bodies analogously to the case without contact.

The parts of the boundary where contact may occur are denoted with  $\partial\mathcal{B}_c^1$  and  $\partial\mathcal{B}_c^2$  and the pull back of these boundaries to the reference configurations are denoted with  $\partial\mathcal{B}_{c0}^1$  and  $\partial\mathcal{B}_{c0}^2$ . For well-posedness consideration, it is necessary that the part of the boundary with DIRICHLET condition and the contact boundary do not overlap, i.e.

$$\partial\mathcal{B}_{c0}^1 \cap \partial\mathcal{B}_u^1 = \emptyset, \quad \partial\mathcal{B}_{c0}^2 \cap \partial\mathcal{B}_u^2 = \emptyset. \quad (2.37)$$

Moreover, we assume here that the contact part of the boundary belongs to the zero traction subset of the NEUMANN boundaries  $\partial\mathcal{B}_t^1$  and  $\partial\mathcal{B}_t^2$ , i.e.

$$\partial\mathcal{B}_{c0}^1 \supset \partial\mathcal{B}_t^{10} := \{\mathbf{X} \in \partial\mathcal{B}_t^1 : \hat{\mathbf{t}} = \mathbf{0}\}, \quad \partial\mathcal{B}_{c0}^2 \supset \partial\mathcal{B}_t^{20} := \{\mathbf{X} \in \partial\mathcal{B}_t^2 : \hat{\mathbf{t}} = \mathbf{0}\}. \quad (2.38)$$

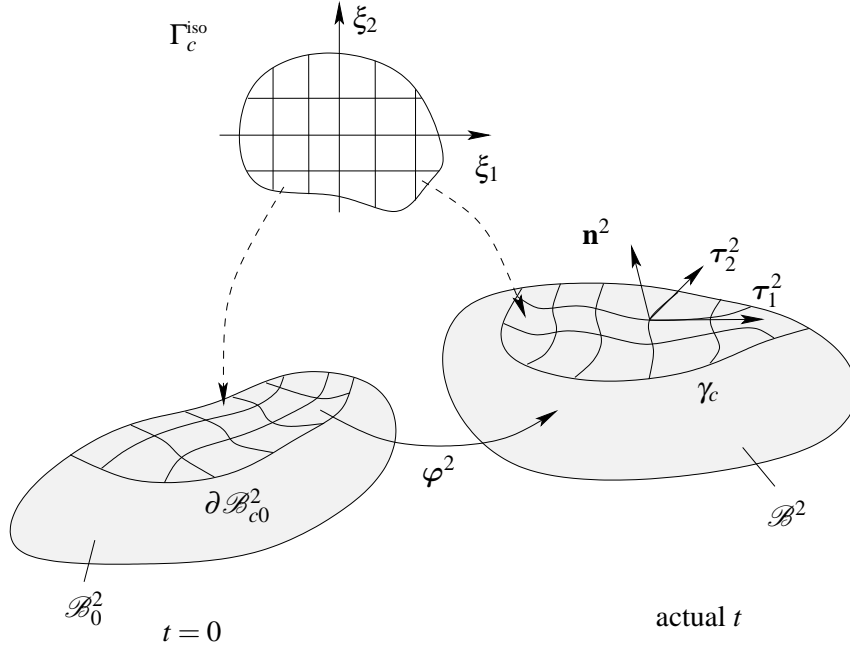


**Figure 2.5:** Parametrization of a contact surface.

The quantities relevant to contact require an appropriate coordinate system. It means that at least one of two adjacent surfaces is parametrized. Historically, it is the surface with superscript 1 and it is called the *slave* surface. The opposite surface with superscript 2 is called master surface. Here, we use convective covariant coordinates on the contact surface  $\partial\mathcal{B}_c^1$  defined as

$$\partial\mathcal{B}_c^1 = \{\mathbf{x}^1(\xi_1, \xi_2) : (\xi_1, \xi_2) \in \Gamma_c^{\text{iso}}\}, \quad (2.39)$$

where  $\Gamma_c^{\text{iso}}$  is some generic parametrization, see Figure 2.5. Now, we define the actual contact surface as the overlap between  $\partial\mathcal{B}_c^1$  and  $\partial\mathcal{B}_c^2$  with

$$\gamma_c = \partial\mathcal{B}_c^1 \cap \partial\mathcal{B}_c^2 \quad (2.40)$$

and the unit normal on  $\partial\mathcal{B}_c^1$  as

$$\mathbf{n}^1 = \frac{\boldsymbol{\tau}_1^1 \times \boldsymbol{\tau}_2^1}{|\boldsymbol{\tau}_1^1 \times \boldsymbol{\tau}_2^1|}, \quad (2.41)$$

with  $\boldsymbol{\tau}_\alpha^1$  with  $\alpha = 1, 2$  being the tangential vectors on a surface  $\gamma_c$ . As the actual contact surface is common (according to equation 2.40), the normal of the adjacent body must be the opposite to  $\mathbf{n}^1$  with

$$\mathbf{n}^2 = -\mathbf{n}^1. \quad (2.42)$$

Note, that the pull back images of the actual contact surface  $\gamma_c$  to the reference positions  $\partial\mathcal{B}_{c0}^1$  and  $\partial\mathcal{B}_{c0}^2$  do not coincide. The pull back of the normal vectors  $\mathbf{n}^1$  and  $\mathbf{n}^2$  is defined by NANSON's formula. It uses deformation gradients from two independent mappings  $\varphi^1$  and  $\varphi^2$ . Thus, this pull backs are generally not opposite, i.e.

$$\det \mathbf{F}^1 (\mathbf{F}^1)^{-T} \mathbf{n}^1 \neq \det \mathbf{F}^2 (\mathbf{F}^2)^{-T} \mathbf{n}^1 = -\det \mathbf{F}^2 (\mathbf{F}^2)^{-T} \mathbf{n}^2. \quad (2.43)$$

The tangential vectors can be computed by

$$\tau_\alpha^1 = \frac{\partial \mathbf{x}^1(\xi_1, \xi_2)}{\partial \xi_\alpha}, \quad \alpha = 1, 2. \quad (2.44)$$

The distance function between a point of the master surface  $\mathbf{x}^2$  and the slave surface  $\mathbf{x}^1$  is defined as

$$d(\xi_1, \xi_2) = \min_{\mathbf{x}^2 \in \partial\mathcal{B}_{c0}^2} |\mathbf{x}^2 - \mathbf{x}^1|. \quad (2.45)$$

The minimizer for the distance function is called the closest point projection or the proximity point  $\hat{\mathbf{X}}^2$  with

$$\hat{\mathbf{X}}^2(\hat{\xi}_1, \hat{\xi}_2) = \arg \min_{\mathbf{x}^2 \in \partial\mathcal{B}_{c0}^2} |\mathbf{x}^2 - \mathbf{x}^1|. \quad (2.46)$$

If the surface  $\partial\mathcal{B}_{c0}^2$  is smooth, the necessary condition for minimum of the distance reads as follows

$$\frac{\partial}{\partial \xi_\alpha} |\mathbf{x}^2 - \mathbf{x}^1| = \frac{\mathbf{x}^2 - \mathbf{x}^1}{|\mathbf{x}^2 - \mathbf{x}^1|} \cdot \tau_\alpha = 0, \quad \alpha = 1, 2. \quad (2.47)$$

This condition requires that the projection vector  $\mathbf{x}^2 - \mathbf{x}^1$  is orthogonal to the tangent plane and that it is parallel to the normal  $\mathbf{n}^1$ . Having this definition and assumption at hand, the contact gap and traction can be introduced.

## 2.2.2 Contact gap and traction

The normal gap is the main measure of impenetration. It is defined as

$$g_N = (\hat{\mathbf{x}}^2 - \mathbf{x}^1) \cdot \mathbf{n}^1. \quad (2.48)$$

The normal gap can be positive or negative. The impenetration condition requires that

$$g_N \geq 0. \quad (2.49)$$

Variation of the normal gap w.r.t mappings reads

$$\delta g_N = \delta(\mathbf{x}^2 - \mathbf{x}^1) \cdot \mathbf{n}^1 + (\mathbf{x}^2 - \mathbf{x}^1) \cdot \delta \mathbf{n}^1. \quad (2.50)$$

The variation of the unit normal vector is orthogonal to itself. Thus, the latter expression reduces to

$$\delta g_N = \delta(\mathbf{x}^2 - \mathbf{x}^1) \cdot \mathbf{n}^1. \quad (2.51)$$

Now, we consider the traction on the contact surface  $\gamma_c$ . First, they must satisfy the balance of momentum. For the massless interface this requires

$$\mathbf{t}_c^1 = -\mathbf{t}_c^2. \quad (2.52)$$

The contact tractions, which we assumed earlier, acting on the tractionless part  $\partial \mathcal{B}_i^{10}$  and  $\partial \mathcal{B}_i^{20}$ , are in coherence with the traction flux inside the bodies, defined by the CAUCHY stress field, i.e.

$$\mathbf{t}_c^1 = \boldsymbol{\sigma}^1 \mathbf{n}^1, \quad \mathbf{t}_c^2 = \boldsymbol{\sigma}^2 \mathbf{n}^2. \quad (2.53)$$

The contact traction vector is usually decomposed in a normal and a tangential part

$$\mathbf{t}_c^1 = t_{cN} \mathbf{n}^1 + t_{c\alpha} \boldsymbol{\tau}_\alpha. \quad (2.54)$$

We assume that there is no adhesion in normal direction between the bodies. Thus, the normal traction can be only compressive.

$$t_{cN} \leq 0. \quad (2.55)$$

Since the traction acts only when the gap is zero, the gap and the normal traction can not be simultaneously non-zero. Thus, the normal behavior can be stated in a form

$$g_N \geq 0, \quad t_{cN} \leq 0, \quad g_N t_{cN} = 0. \quad (2.56)$$

These relations are well-known SIGNIORINY's condition or KARUSH-KUHN-TUCKER conditions in mathematical programming, see KIKUCHI AND ODEN (1988) and CURNIER ET AL. (1995). The impenetration condition and non-negative traction condition are called

the primal and dual feasibility conditions, respectively. These conditions are inequality constraints. The equality  $g_{\text{N}t_{\text{cN}}} = 0$  is called the complementarity condition.

### 2.2.3 Boundary and initial conditions

For the closure of the problem of mechanical motion discussed above, boundary and initial conditions are required. The boundary conditions are DIRICHLET (for the prescribed motion) and NEUMANN (for the prescribed tractions) conditions with

$$\mathbf{u} = \hat{\mathbf{u}}(\mathbf{X}, t) \text{ in } \partial\mathcal{B}_u \times \mathcal{I}, \quad \mathbf{t} = \boldsymbol{\sigma}\mathbf{n} = \hat{\mathbf{t}} \text{ in } \partial\mathcal{B}_t \times \mathcal{I}. \quad (2.57)$$

The initial conditions describe the state of system at reference position  $t = 0$ . Here, it is assumed that the reference configuration is stress-free ( $\mathbf{F} = \mathbf{I}$ ,  $\boldsymbol{\sigma} = \boldsymbol{\sigma}_{\text{PK2}} = \mathbf{0}$ ). In addition, materials are hyperelastic and no initialization of the internal variables is required. Thus, the initial conditions impose the initial displacement and velocity with

$$\mathbf{u}|_{t=0} = \mathbf{u}_0, \text{ in } \mathcal{B}_0, \quad \mathbf{v}|_{t=0} = \mathbf{v}_0 \text{ in } \mathcal{B}_0. \quad (2.58)$$

### 2.2.4 Strong and weak form of contact IBVP

In the previous subsections, the individual field equations and conditions of a two-body contact are considered separately. Here, these equations are composed in an IBVP w.r.t. the unknown displacement. This IBVP is difficult to solve analytically and such attempts are not presented here. A detailed description of analytical solution of contact problems can be found in ALEXANDROV AND POZHARSKII (2002), JOHNSON (2003) and GALIN AND GLADWELL (2008). Some exact solutions for non-linear elasticity are given in OGDEN (1997) and FU AND OGDEN (2001). The presented IBVP is a possible starting point for the derivation of weak forms or variational formulations. A standard form based on the *Principle of virtual work* (PWV) and LAGRANGE multipliers treatment of normal contact concludes this subsection. Alternative variational formulations, which is one of the main foci of this thesis, are discussed in Section 3.

The IBVP is stated as follows:

Find  $\mathbf{u}^i : \mathcal{B}_0^i \times \mathcal{I} \rightarrow \mathcal{B}^i$  and  $t_{\text{cN}} : \partial\mathcal{B}_{\text{c0}} \times \mathcal{I} \rightarrow \mathbb{R}$  such that they satisfy the kinematic equations

$$\mathbf{F}^i = \mathbf{I} + \frac{\partial \mathbf{u}^i}{\partial \mathbf{X}}, \quad \mathbf{E} = \frac{1}{2}(\mathbf{F}^{i,\text{T}}\mathbf{F}^i - \mathbf{I}) \text{ in } \mathcal{B}_0^i \times \mathcal{I}, \quad (2.59a)$$

$$g_{\text{N}} = (\hat{\mathbf{x}}^2 - \mathbf{x}^1) \cdot \mathbf{n}^1, \quad (2.59b)$$

the balance of linear momentum

$$\rho \ddot{\mathbf{u}}^i = \operatorname{div} \boldsymbol{\sigma}^i + \rho^i \hat{\mathbf{b}}^i \quad \text{in } \mathcal{B}^i \times \mathcal{I}, \quad (2.59c)$$

the constitutive equation for given strain energy functions  $W^i(\mathbf{E})$

$$\boldsymbol{\sigma}^i = \frac{1}{\det \mathbf{F}^i} \mathbf{F}^i \frac{\partial W^i}{\partial \mathbf{E}} \mathbf{F}^{i,T} \quad \text{in } \mathcal{B}^i \times \mathcal{I}, \quad (2.59d)$$

the initial and boundary conditions

$$\mathbf{u}^i|_{t=0} = \mathbf{u}_0^i \quad \text{in } \mathcal{B}_0^i, \quad \dot{\mathbf{u}}|_{t=0} = \mathbf{v}_0 \quad \text{in } \mathcal{B}_0^i, \quad (2.59e)$$

$$\mathbf{u}^i = \hat{\mathbf{u}}^i(\mathbf{X}, t) \quad \text{in } \partial \mathcal{B}_u^i \times \mathcal{I}, \quad \mathbf{t}^i = \boldsymbol{\sigma}^i \mathbf{n}^i = \hat{\mathbf{t}} \quad \text{in } \partial \mathcal{B}_t^i \times \mathcal{I}, \quad (2.59f)$$

$$\boldsymbol{\sigma}^1 \mathbf{n}^1 = \mathbf{n}^1 t_{cN} \quad \text{in } \partial \mathcal{B}_c^1 \times \mathcal{I}, \quad \boldsymbol{\sigma}^2 \mathbf{n}^1 = -\mathbf{n}^1 t_{cN} \quad \text{in } \partial \mathcal{B}_c^2 \times \mathcal{I}, \quad (2.59g)$$

and the normal contact conditions

$$g_N \geq 0, \quad t_{cN} \leq 0, \quad g_N t_{cN} = 0 \quad \text{in } \partial \mathcal{B}_{c0} \times \mathcal{I}. \quad (2.59h)$$

Following the classical text books on computational contact mechanics WRIGGERS (2006) and LAURSEN (2002), the weak formulation using PWV is written as

$$\sum_{i=1,2} \left[ \int_{\mathcal{B}_0^i} \boldsymbol{\sigma}_{PK2}^i : \delta \mathbf{E}^i + \rho_0^i (\hat{\mathbf{b}}^i - \dot{\mathbf{v}}^i) \cdot \delta \mathbf{u}^i \, dv + \int_{\partial \mathcal{B}_t^i} \hat{\mathbf{t}} \cdot \delta \mathbf{u} \, da + \int_{\gamma_c} \delta \mathbf{u}^i \cdot \mathbf{n}^1 t_{cN} \, da \right] + G_c \geq 0, \quad (2.60)$$

with  $G_c$  being the term enforcing the contact constraint and  $\delta \mathbf{u}^i$  being the kinematically admissible variation of displacement. Here, the LAGRANGE multipliers form

$$G_c = \delta \int_{\gamma_c} \lambda_N g_N \, da. \quad (2.61)$$

For details about the discretization of this problem, see PUSO AND LAURSEN (2004a), YANG ET AL. (2005), HUEBER ET AL. (2006), HARTMANN ET AL. (2007) and POPP ET AL. (2009).

## 2.2.5 Linearized equations of elasto-dynamic contact

The linearization of the IBVP (2.59) or the weak form (2.60) are adequate if the deformations and rotations of the bodies are small ( $\mathbf{F} \approx \mathbf{I}$ ) and relative sliding of the bodies and change of normal is negligible. In this case, a linearized strains and a linearized material law can be used inside the domain. On the contact surface, the linearization of closest point projection and the

impenetration conditions are used. A concise derivation of this formulation is given below. For more detailed descriptions of standard treatment see WRIGGERS (2006) and LAURSEN (2002) and for an extensive study of the problem with use of *variational inequalities* see KIKUCHI AND ODEN (1988).

The linearized or engineering strain law reads

$$\boldsymbol{\varepsilon} = \mathbf{L}\mathbf{u}, \quad (2.62)$$

with  $\mathbf{L}$  being the differential operator for a given type of problem. In case of 2D and 3D elasticity, the differential operator is the symmetric part of the gradient, i.e.

$$\mathbf{L}\mathbf{u} = \text{sym grad } \mathbf{u} = \frac{1}{2} \left( \frac{\partial \mathbf{u}}{\partial \mathbf{X}} + \frac{\partial \mathbf{u}^T}{\partial \mathbf{X}} \right). \quad (2.63)$$

In Cartesian coordinates, the operator  $\mathbf{L}$  in the VOIGT notation reads

$$\mathbf{L} = \begin{bmatrix} \frac{\partial}{\partial X_1} & 0 \\ 0 & \frac{\partial}{\partial X_2} \\ \frac{\partial}{\partial X_2} & \frac{\partial}{\partial X_1} \end{bmatrix} \text{ in 2D,} \quad \mathbf{L} = \begin{bmatrix} \frac{\partial}{\partial X_1} & 0 & 0 \\ 0 & \frac{\partial}{\partial X_2} & 0 \\ 0 & 0 & \frac{\partial}{\partial X_3} \\ \frac{\partial}{\partial X_2} & \frac{\partial}{\partial X_1} & 0 \\ 0 & \frac{\partial}{\partial X_3} & \frac{\partial}{\partial X_2} \\ \frac{\partial}{\partial X_3} & 0 & \frac{\partial}{\partial X_2} \end{bmatrix} \text{ in 3D.} \quad (2.64)$$

Consistent notation for differential operators is used for the description of the kinematics in selected thin-walled structure theories. The adjoint operator to the operator  $\mathbf{L}$  is denoted as  $\mathbf{L}^*$ .

The constitutive equation in case of a linear material law reduces to HOOKE's law

$$\boldsymbol{\sigma}_{\text{lin}} = \mathbf{D}\boldsymbol{\varepsilon}. \quad (2.65)$$

Combination of the equation given above leads to the following statement of the IBVP

$$\begin{cases} \rho \ddot{\mathbf{u}} = \mathbf{L}^* \boldsymbol{\sigma}_{\text{lin}}(\mathbf{u}) + \hat{\mathbf{b}} & \text{in } \mathcal{I} \times \mathcal{B}_0 \\ \mathbf{u} = \mathbf{0} & \text{in } \mathcal{I} \times \partial \mathcal{B}_u \\ \boldsymbol{\sigma}_{\text{lin}} \mathbf{n} = \hat{\mathbf{t}} & \text{in } \mathcal{I} \times \partial \mathcal{B}_{t,0} \\ \mathbf{u}(0, \cdot) = \mathbf{u}_0 & \text{in } \mathcal{B}_0 \\ \dot{\mathbf{u}}(0, \cdot) = \mathbf{v}_0 & \text{in } \mathcal{B}_0. \end{cases} \quad (2.66)$$

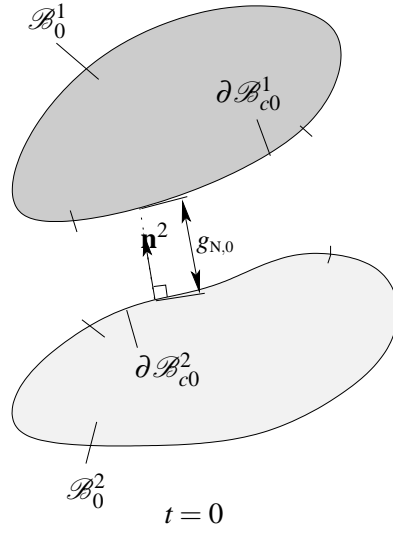


**Figure 2.6:** Linearized kinematic on the contact surface.

The contact conditions use a linearized gap function

$$g_N^{\text{lin}} = (\mathbf{x}^2 - \mathbf{x}^1) \cdot \mathbf{n} = (\mathbf{u}^2 - \mathbf{u}^1) \cdot \mathbf{n} - g_{N,0}, \quad (2.67)$$

with  $g_{N,0} = (\mathbf{X}^2 - \mathbf{X}^1) \cdot \mathbf{n}$  being the initial gap, see Figure 2.6.

### 2.2.6 Selected linearized models for thin-walled structures

In the theories discussed above, continuous domains are considered. In many applications, slender structures are used. For these structures, it is economically motivated to use assumptions and reduce the dimensionality of the problem. If two dimensions of a structural member are much smaller than the third one, it is called a *rod*. It is possible to reduce all quantities of a rod to the center line.

Straight rods are usually classified in subclasses by the carried loads. Trusses carry axial force, beams carry bending moments and transverse forces, shafts carry torque. There are special designations for members subjected simultaneously to a combination of forces, like axial and transverse forces and bending moments for a beam-column. Herein, two models are used: trusses and TIMOSHENKO beams. The matrix notation for the displacement vector  $\mathbf{u}$ , material matrix  $\mathbf{D}$ , differential operator  $\mathbf{L}$  etc. previously introduced for continuum models, is also used in the context of structural theories. The material matrix and density are understood here as quantities which are pre-integrated through the thickness .

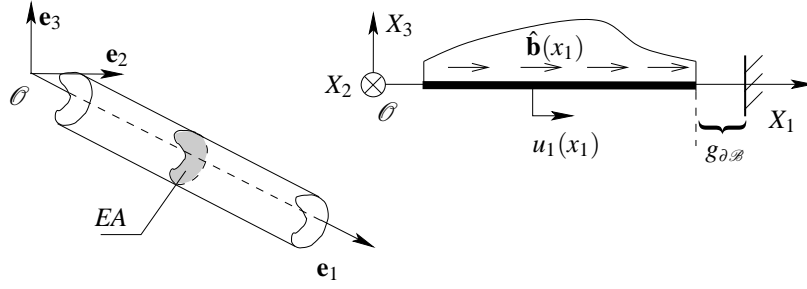


**Figure 2.7:** Truss model.

The primal kinematic unknown for the truss is the axial displacement  $u_1$ , see Figure 2.7. Following the matrix notation, the quantities defined within the truss model reads

$$\begin{aligned} \mathbf{u} &= [u_1], & \mathbf{v} &= [v_1], & \mathbf{p} &= [p_1], & \boldsymbol{\varepsilon} &= [\varepsilon_{11}], \\ \boldsymbol{\sigma}_{\text{lin}} &= [A\sigma_{11}], & \boldsymbol{\rho} &= [\rho A], & \mathbf{D} &= [EA], & \mathbf{L}^* = \mathbf{L} &= \left[ \frac{d}{dx_1} \right], \end{aligned} \quad (2.68)$$

with  $A$  and  $E$  being cross-sectional area and YOUNG's modulus, respectively.

For the truss, contact can occur only at the end points. The linearized impenetration conditions read

$$u_1(x=b) \leq g_{\partial\mathcal{B}}, \quad t_c(u_1 - g_{\partial\mathcal{B}}) = 0, \quad t_c \leq 0, \quad (2.69)$$

where  $b$  is the  $X_1$ -coordinate of the right end, see Figure 2.7.

The primal displacements for a two-dimensional TIMOSHENKO beam are the center line deflection  $u_2$  and the rotation of the cross-section  $\varphi_3$ , see Figure 2.8. The TIMOSHENKO beam model in matrix notation reads

$$\begin{aligned} \mathbf{u} &= \begin{bmatrix} u_2 \\ \varphi_3 \end{bmatrix}, & \mathbf{v} &= \begin{bmatrix} v_2 \\ \omega_3 \end{bmatrix}, & \mathbf{p} &= \begin{bmatrix} p_2 \\ l_3 \end{bmatrix}, \\ \mathbf{L} &= \begin{bmatrix} 0 & \frac{d}{dx_1} \\ \frac{d}{dx_1} & 1 \end{bmatrix}, & \mathbf{L}^* &= \begin{bmatrix} 0 & \frac{d}{dx_1} \\ \frac{d}{dx_1} & -1 \end{bmatrix}, & \mathbf{D} &= \begin{bmatrix} GA_s & 0 \\ 0 & EI \end{bmatrix}, \\ \boldsymbol{\sigma}_{\text{lin}} &= \begin{bmatrix} V \\ M \end{bmatrix}, & \boldsymbol{\varepsilon} &= \begin{bmatrix} \gamma \\ \varkappa \end{bmatrix}, & \boldsymbol{\rho} &= \begin{bmatrix} \rho A & 0 \\ 0 & \rho I_{33} \end{bmatrix}, \end{aligned} \quad (2.70)$$

with  $v_2$  and  $\omega_3$  being the linear and angular velocities,  $p_2$  and  $l_3$  being the linear and angular momenta,  $GA_s$  and  $EI$  being shear and bending stiffnesses,  $V$  and  $M$  being the transverse shear force and the bending moment,  $\gamma$  and  $\varkappa$  being the shear strain and the curvature of the center line,  $I$  being the effective momentum of the section in bending and  $I_{33}$  being the second moment of inertia, which might slightly differ from  $I$ . In this thesis, the possible

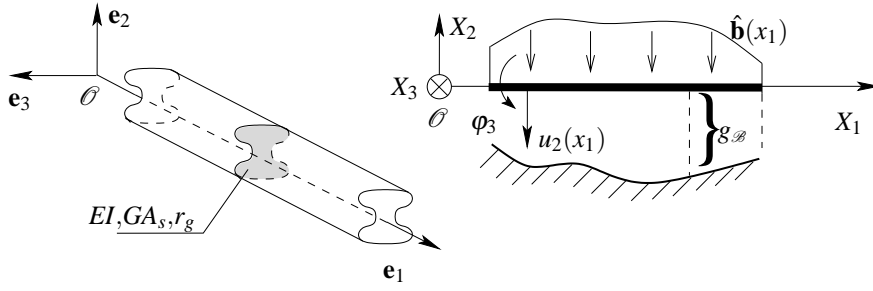


Figure 2.8: TIMOSHENKO beam model.

difference between the effective momentum and the second moment of inertia of a section is neglected. The gyration radius  $r_g$  is defined as  $\sqrt{I/A}$ . The shear correction factor is defined as  $\gamma_s = GA_s/GA$ .

For the beam model, contact may occur on the upper or lower surface along the whole length. Contact tractions on these surfaces lead to stresses and strains in thickness direction. These strains are usually neglected in standard beam models, but due to these strains the distance between a point where contact actually occurs and the center line changes. This effect qualitatively influences the distribution of the contact traction, see PELEH AND SUHOROLSKIY (1980) and GRIGOLYUK AND TOLKACHEV (1987). A shell theory that includes this effect may also be found in NAGHDI (1975). Moreover, the modern commercial codes include this effect as an option, see WHIRLEY AND ENGELMANN (1993). In this thesis, the effect of through-the-thickness strains on contact conditions is neglected. The contact conditions referring to the center line read

$$u_2 \leq g_{\mathcal{B}}, \quad t_c(u_2 - g_{\mathcal{B}}) = 0, \quad t_c \leq 0 \quad \text{in } \mathcal{B}. \quad (2.71)$$

## 2.3 Discretization in space

In the following section, a semi-discretization in space, which is used in this work, is presented. It is based on a total Lagrangian formulation using displacement parameters only, e.g. see ZIENKIEWICZ AND TAYLOR (2006); BONET (2008). Then, a brief description of the Node-to-Segment approach for unilateral and bilateral contact is given.

the focus of this thesis is discretization of inertial terms. A thorough overview of different mass matrices is given for beam, plate, solid and shell finite elements. This overview includes mass lumping techniques and mass matrix templates, singular mass matrices, conventional and selective mass scaling.

### 2.3.1 Residuum, algorithmic tangent and consistent mass matrices

Consider a quadrilateral parent finite element in parametric, reference and actual configuration, according to Figure 2.9. Let us denote the mappings from the parametric space to reference and actual configurations with  $\varphi^R$  and  $\varphi^a$ , respectively. These mappings can be written as the function between corresponding point positions  $\mathbf{x}$ ,  $\mathbf{X}$  and  $\xi$

$$\mathbf{X} = \varphi^R(\xi), \quad \varphi^R(\xi) : [-1,1] \times [-1,1] \rightarrow \mathcal{B}_0 \quad (2.72)$$

$$\mathbf{x} = \varphi^a(\xi, t), \quad \varphi^a(\xi, t) : [-1,1] \times [-1,1] \times \mathcal{I} \rightarrow \mathcal{B}. \quad (2.73)$$

Exploitation of the isoparametric approach means usage of equal approximation functions for

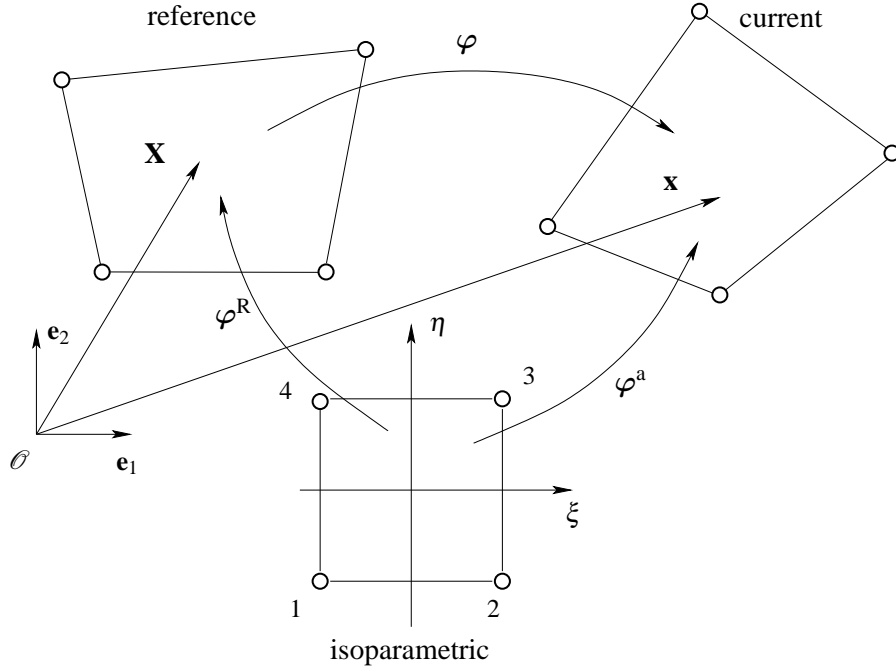


**Figure 2.9:** Element geometry.

the reference position vector  $\mathbf{X}$  and the displacement  $\mathbf{u}$

$$\mathbf{X}^h = \mathbf{N}\Xi, \quad \mathbf{u}^h = \mathbf{N}\mathbf{U}, \quad (2.74)$$

where  $\mathbf{N}$  is the matrix of shape functions,  $\Xi$  is the vector containing the reference positions of nodes and  $\mathbf{U}$  is the global displacement vector. First, we compute the Jacobian of the mappings  $\varphi^R$  and  $\varphi^a$  as

$$\mathbf{J}^R = \frac{\partial \mathbf{X}^h}{\partial \xi}, \quad \mathbf{J}^a = \frac{\partial \mathbf{x}^h}{\partial \xi} = \mathbf{J}^R + \frac{\partial \mathbf{u}^h}{\partial \xi}. \quad (2.75)$$

The deformation gradient  $\mathbf{F}$  can be expressed in tensor notation via the latter Jacobians with

$$\mathbf{F} = \mathbf{J}^a (\mathbf{J}^R)^{-1} = \left( \mathbf{J}^R + \frac{\partial \mathbf{u}^h}{\partial \boldsymbol{\xi}} \right) (\mathbf{J}^R)^{-1} = \mathbf{I} + \frac{\partial \mathbf{u}^h}{\partial \mathbf{X}^h} = \mathbf{I} + \frac{\partial \mathbf{N}\mathbf{U}}{\partial \mathbf{X}^h} \quad (2.76)$$

or in VOIGT notation with the help of the linear B-operator

$$\mathbf{F} = \mathbf{I} + \mathbf{B}_0 \mathbf{U}, \quad (2.77)$$

with  $\mathbf{B}_0$

$$\mathbf{B}_0 = \begin{bmatrix} \frac{\partial N_1}{\partial X_1} & 0 & \frac{\partial N_2}{\partial X_1} & 0 & \dots \\ 0 & \frac{\partial N_1}{\partial X_2} & 0 & \frac{\partial N_2}{\partial X_2} & \dots \\ \frac{\partial N_1}{\partial X_2} & 0 & \frac{\partial N_2}{\partial X_2} & 0 & \dots \\ 0 & \frac{\partial N_1}{\partial X_1} & 0 & \frac{\partial N_2}{\partial X_1} & \dots \end{bmatrix}. \quad (2.78)$$

With the deformation gradient at hand, other strain measures, stresses and internal forces may be computed using equations (2.10), (2.18) and (2.19).

The inertial forces are proportional to the accelerations. The standard approach uses equal approximations for velocity, acceleration and displacement described in equation (2.74). Moreover, the variation of the displacement  $\delta \mathbf{u}$  in the PVW expression is discretized with the same shape functions, leading to

$$\dot{\mathbf{u}}^h = \mathbf{N}\dot{\mathbf{U}}, \quad \ddot{\mathbf{u}}^h = \mathbf{N}\ddot{\mathbf{U}}, \quad \delta \mathbf{u}^h = \mathbf{N}\delta \mathbf{U}, \quad (2.79)$$

where  $\dot{\mathbf{U}}$ ,  $\ddot{\mathbf{U}}$  and  $\delta \mathbf{U}$  are the vectors of global velocities, accelerations and kinematically admissible displacements. Substitution of this discretization in the virtual work principle

$$\begin{aligned} \delta W^{\text{int,h}}(\mathbf{u}, \delta u) - \delta W^{\text{ext,h}}(\mathbf{u}, \delta u) + \delta W^{\text{kin,h}}(\mathbf{u}, \delta u) &= 0, \\ \delta W^{\text{int}}(\mathbf{u}, \delta u) &= \int_{\mathcal{B}_0} \delta \mathbf{E} : \mathbf{S} dV, \\ \delta W^{\text{ext}}(\mathbf{u}, \delta u) &= \int_{\mathcal{B}_0} \delta \mathbf{u} \cdot \rho_0 \hat{\mathbf{b}} dV + \int_{\partial \mathcal{B}_{t,0}} \delta \mathbf{u} \cdot \hat{\mathbf{t}} dA, \\ \delta W^{\text{kin}}(\mathbf{u}, \delta u) &= \int_{\mathcal{B}_0} \delta \mathbf{u} \cdot \rho_0 \ddot{\mathbf{u}} dV, \end{aligned} \quad (2.80)$$

results in the standard equation of motion

$$\mathbf{M}\ddot{\mathbf{U}} + \mathbf{F}^{\text{int}}(\mathbf{U}) = \mathbf{F}^{\text{ext}}, \quad (2.81)$$

with  $\mathbf{F}^{\text{int}}$  and  $\mathbf{F}^{\text{ext}}$  being the internal and external force vector.

Formulation (2.80) uses the pure displacement. More advanced formulations (mixed, enhanced assumed strain and assumed natural strain) are treated in detail in STEIN ET AL. (2004). Alternatively, an updated Lagrangian formulation (see BATHE (2006)) and arbitrary Lagrangian Eulerian formulation (see BELYTSCHKO ET AL. (2001)) may be used.

### 2.3.2 Standard contact techniques

During the last fifty years, many contact formulations for FEM have been proposed. They differ in many aspects, but we will focus on the type of spatial discretization of contact constraint (Node-to-Node, Node-to-Surface, Surface-to-Surface), the form of contact virtual work (pure LAGRANGE, penalty, etc.), the type of contacting bodies (bilateral contact of deformable bodies, unilateral contact) and the type of temporal discretization treatment of contact constraints for dynamics.

Initially, Node-to-Node (NTN) discretization of contact was proposed by FRANCAVILLA AND ZIENKIEWICZ (1975). This approach imposes an impenetration condition to pair initially adjacent nodes in normal and tangential direction. However, this method is restricted to small sliding contact and it requires matching meshes. Further, several variants of Node-to-Segment (NTS) discretizations were proposed in SIMO ET AL. (1985) and BENSON AND HALLQUIST (1990). They enable the solution of static and dynamic problems with large sliding and with non-matching meshes. It is possible to extend the formulation to self-contact<sup>1</sup>, see CARPENTER ET AL. (1991) and GEE (2004), which is important in post-buckling of shells and progressive folding in car crash simulation. Many commercial codes use them, because formulation and implementation are not complicated. Moreover, they allow explicit and implicit time integration.

However, NTS formulations possess several unavoidable drawbacks (see PUSO AND LAURSEN (2004a, b)):

- one-pass algorithms fail the contact patch test
- two-pass algorithms produce overconstraint
- non-smooth contact surfaces cause jumps in the tangent stiffness when slave nodes slide between adjacent master segments
- discrete constraints cause jumps in the contact forces when slave nodes slide off the boundaries of the master surface. This occurs even for flat surfaces.

Surface-to-Surface (STS) discretization allows to eliminate the aforementioned deficiencies. However, STS formulation needs more advanced techniques for contact detection, build-

---

<sup>1</sup>also called single surface contact algorithm in literature

ing contact segments, integration over the segments and calculation of a consistent tangent. For details see PUSO AND LAURSEN (2004b), GITTERLE ET AL. (2010), CICHOSZ AND BISCHOFF (2011) and POPP (2012).

Another important part of the contact formulation is its weak form  $G_c$ , see equation (2.60). Inequality constraints can be fulfilled either exactly by LAGRANGE multiplier form or approximately in terms of some regularization techniques according to WRIGGERS (2006) and LAURSEN (2002). The LAGRANGE multiplier method can not be used directly, as it is not known beforehand which of the constraints are active or inactive. Therefore, LAGRANGE multipliers are combined with an active set strategy, semi-smooth NEWTON methods or linear and non-linear complementarity functions, see HAGER (2010).

For dynamic contact problems, further issues are preservation of linear and angular momentum and energy, see LAURSEN AND CHAWLA (1997), BETSCH AND HESCH (2007), HAGER ET AL. (2008) and CICHOSZ AND BISCHOFF (2011). These algorithms usually impose conservation laws as additional constraints on a systems, modify treatment of internal form and lead to correction terms for loss or gain in contact events. The effort of implementation of these methods is substantial, nevertheless they are more and more widely used in commercial codes in the last decade.

Known dissipative algorithms are based on modified predictor-corrector schemes for NEWMARK, see PANDOLFI ET AL. (2002); DEUFLHARD ET AL. (2008) and ROTHE's method KRAUSE AND WALLOTH (2009). They are discussed in Subsection 2.3.4.

### 2.3.3 Mass lumping and mass customization

Diagonal or Lumped Mass Matrices (LMM) have many important applications. The most important usage is explicit dynamics, where the diagonal form of the mass matrix simplifies the calculation of the global acceleration vector. Moreover, the critical time-step for consistent mass matrices (CMM) is by factor two to three smaller than for a LMM. Other merits of LMM are better storage requirements, easier application of velocity boundary conditions and contact conditions.

There are three common methods for obtaining LMM

- Optimal or nodal quadrature,<sup>2</sup> proposed by FRIED AND MALKUS (1975)
- Special mass lumping or HINTON-ROCK-ZIENKIEWICZ (HRZ), proposed by HINTON ET AL. (1976)
- Row-sum-lumping, see HUGHES (2000) and COOK ET AL. (2007)

---

<sup>2</sup>sometimes called Spectral Finite Elements.

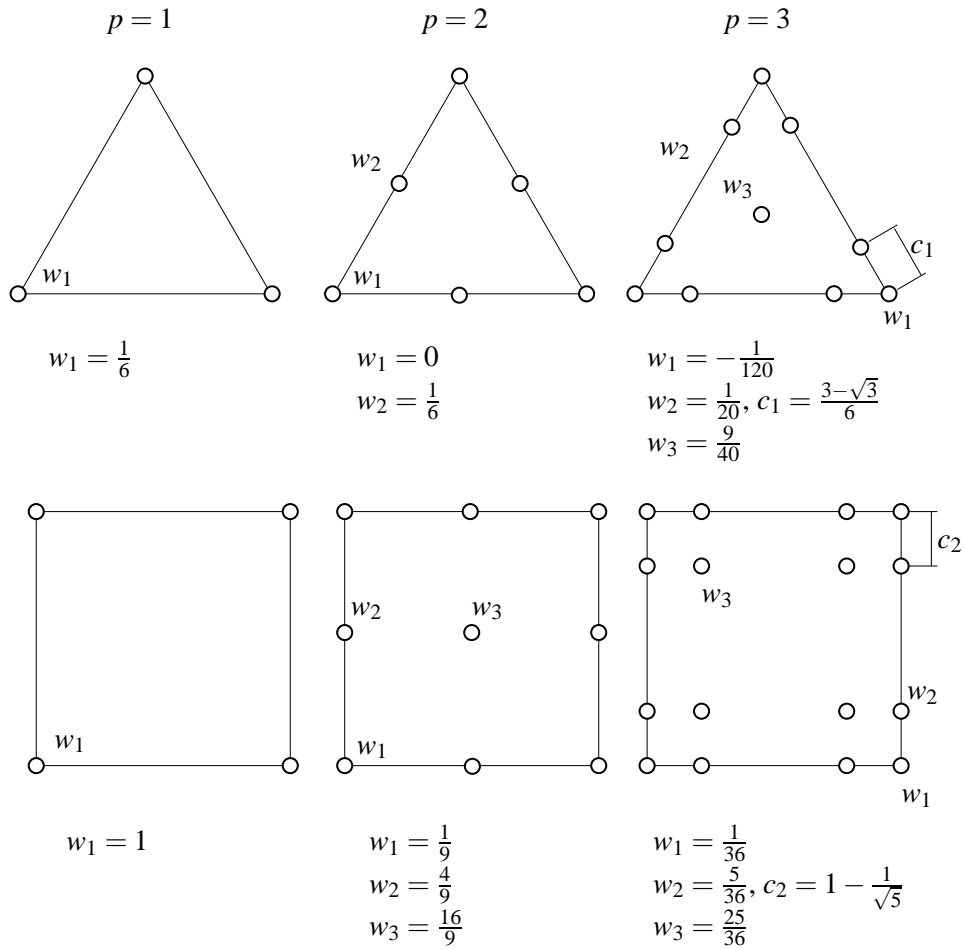


**Figure 2.10:** Locations and weights for optimally accurate nodal quadrature rules.

Optimal mass lumping is proposed in FRIED AND MALKUS (1975). The basic idea of this mass lumping is to place nodes at the location of a high order quadrature rule. Then, shape functions that fulfil interpolation conditions are used, which automatically yields a diagonal mass matrix. In case of line elements, the locations are the GAUSS-LOBATTO points. Tensor product of GAUSS-LOBATTO points is used for quadrilaterals and hexahedrals, see Figure 2.10. For these elements, the weights are always positive and the order of convergence for eigenfrequencies is preserved (FRIED AND MALKUS 1975). For triangular and tetrahedral elements, special locations are used which are tabulated in FRIED AND MALKUS (1975) and LUO AND POZRIKIDIS (2006). However, for high-order triangles and tetrahedrals, the weights may be negative. Alternatively, the nodes may be located at so-called FEKETE points. FEKETE points for a domain are those which maximize the determinant of the VAN-DEKONDE matrix for a given polynomial basis (PASQUETTI AND RAPETTI 2006). For triangles up to order 18 and tetrahedrals up to order nine, such points are tabulated in TAYLOR ET AL. (2001) and CHEN AND BABUŠKA (1996), respectively.

A diagonal mass matrix can also be obtained from CMM via a special procedure called mass lumping. Special mass lumping, or HRZ, scales the diagonal terms of CMM as follows

$$\mathbf{m}_{e,ii}^{\text{HRZ}} = \theta \mathbf{m}_{e,ii}, \quad \mathbf{m}_{e,ii} = \sum_{k=1}^{N_{GP}} \rho_0 N_i^2 w_k |J|_{\xi=\xi_k, \eta=\eta_k, \zeta=\zeta_k}, \quad (2.82a)$$

$$\theta = \frac{m_{\text{trans}}}{\sum_j \mathbf{m}_{e,jj}}, \quad m_{\text{trans}} = \int_{\mathcal{B}} \rho_0 d\mathcal{B} = \sum_{k=1}^{N_{GP}} \rho_0 w_k |J|_{\xi=\xi_k, \eta=\eta_k, \zeta=\zeta_k}. \quad (2.82b)$$

HRZ result in positive definite mass matrices by construction.

The other common procedure for mass lumping is Row Sum Lumping (RSL). The algorithm adds all entries of CMM in a row to diagonal. It can be efficiently applied for many elements. The problem is that for high-order elements, such as for eight-node quadrilateral or ten-node tetrahedral elements, RSL results in mass matrices with negative diagonal terms (COOK ET AL. 2007; BATHE 2006).

### 2.3.4 Singular mass matrices

The literature on singular mass matrices is not so rich, because they may only be obtained for a few cases. Initially, singular mass matrices were obtained for optimal mass lumping with zero nodal weights or row-sum lumping for special types of elements, e.g. the six-node triangle. Another source of SMM is mass matrix customization. Such a procedure allows avoiding stopping bands in semi-discrete FE lattices (FELIPPA 2006). Singular mass matrices are used in reduction methods for generalized eigenvalue problems, mass (dynamic) condensation and GUYAN reduction, see for details HUGHES ET AL. (1976), COOK ET AL. (2007) and VYSLOUKH ET AL. (1973).

A recent application of singular mass matrices is found in dynamic contact problems (HAGER ET AL. 2008; KHENOUS ET AL. 2008; HAURET 2010; RENARD 2010). The usage of singular mass matrices improves numerical stability of the semi-discrete problem: the differential index of the underlying differential-algebraic system is reduced from three to one, and spurious oscillations in the contact pressure, which are commonly reported for formulations with LAGRANGE multipliers, are significantly reduced. A more rigorous analysis is given below.

Standard spatial discretization of dynamic contact problems using LAGRANGE multipliers leads to systems of differential algebraic equations (DAE) with differential index of three (see ASCHER AND PETZOLD (1998))

$$\mathbf{M}\ddot{\mathbf{U}} + \mathbf{F}^{\text{int}}(\mathbf{U}, \dot{\mathbf{U}}, t) = \mathbf{F}^{\text{ext}}(t) + \mathbf{G}(\mathbf{U}, t)\mathbf{Z}, \quad (2.83a)$$

$$\mathbf{G}^T \mathbf{U} - \mathbf{g}_0 \geq 0, \quad \mathbf{Z} \leq 0, \quad \mathbf{Z}(\mathbf{G}^T \mathbf{U} - \mathbf{g}_0) = 0. \quad (2.83b)$$

We note that the non-penetration and complementary conditions given by (2.83b) do not act on all nodes but only on a proper subset. The numerical solution of such a system is challenging. Standard time integration schemes for ordinary differential equations (ODE) applied to System (2.83) may produce oscillating Lagrange multipliers and a substantial loss or gain in the total energy (LAURSEN (2002) and ASCHER AND PETZOLD (1998)). This type of spurious oscillations does not occur or is significantly reduced in case of DAE systems with smaller index. This observation motivates the combination of space and time discretization with the goal to reduce the index.

There are three principal approaches to reduce the index. The first is a modification of the algebraic constraints to a differential equation, e.g. BAUMGARTE stabilization one-index form (BAUMGARTE 1972) and GEAR-GUPTA-LEIMKUEHLER two-index form (GEAR ET AL. 1985). In the second approach, system (2.83) is solved directly in terms of predictor-corrector methods (see KRAUSE AND WALLOTH (2009); DEUFLHARD ET AL. (2008)). The third family makes use of a singular mass matrix  $\mathbf{M}^*$ . In case of linear elasto-dynamic systems, equation (2.83) can thus be reduced to

$$\begin{bmatrix} \mathbf{M}^i & \mathbf{0} \\ \mathbf{0} & \mathbf{0} \end{bmatrix} \begin{bmatrix} \ddot{\mathbf{U}}^i \\ \ddot{\mathbf{U}}^c \end{bmatrix} + \begin{bmatrix} \mathbf{K}^{ii} & \mathbf{K}^{ic} \\ \mathbf{K}^{ci} & \mathbf{K}^{cc} \end{bmatrix} \begin{bmatrix} \mathbf{U}^i \\ \mathbf{U}^c \end{bmatrix} = \begin{bmatrix} \mathbf{F}^i \\ \mathbf{F}^c \end{bmatrix} + \begin{bmatrix} \mathbf{0} \\ \mathbf{G}^c \end{bmatrix} \mathbf{Z}, \quad (2.84a)$$

$$(\mathbf{G}^c)^T \mathbf{U}^c - \mathbf{g}_0 \geq 0, \quad \mathbf{Z} \leq 0, \quad \mathbf{Z} \left( (\mathbf{G}^c)^T \mathbf{U}^c - \mathbf{g}_0 \right) = 0. \quad (2.84b)$$

with  $\mathbf{U}^i$  and  $\mathbf{U}^c$  referring to inner nodes and contact nodes, respectively.

As all equations that include the Lagrange multiplier  $\mathbf{Z}$  are now algebraic, the index of the system reduces to one. This is a much more suitable problem from the point of view of time integration. We follow this approach in this paper, which has been originally introduced for unilateral contact problems in KHENOUS ET AL. (2008).

A known complication of singular mass matrices is infinite eigenfrequencies in spectra, see BATHE (2006). First, initial conditions regarding velocity have no physical meaning at massless modes (displacement initial conditions are disputable). Second, phase velocity for part of short waves (modes) is infinity. This also leads to infinite (absent) branches in dispersion relations, see Section 6.1. Third, explicit time integration schemes can not be used.

Another motivation for singular mass matrices can be derived from the TONTI diagram, see Figure 2.11. Here, only the primary loop of the diagram is shown with displacements being the master field. All kinematic quantities, such as velocity, strain or contact gap are computed from the displacements. Then, the kinetic quantities, such as the stress, the linear momentum and the contact traction, are computed from the kinematic quantities. Finally, equilibrium in the domain is satisfied. In the discrete setting, the flowchart is very similar. However, the contact part of the boundary in the continuous setting has no inertia, whereas

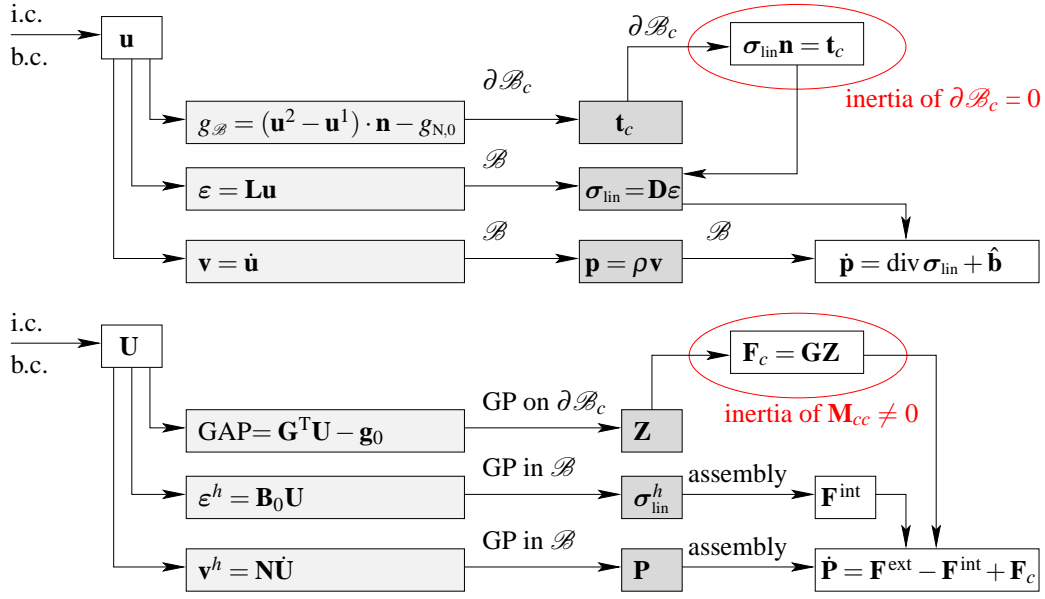


**Figure 2.11:** Primary loop of TONTI diagram for linear elasto-dynamic contact problem (above) and its discrete counterpart (below).

the contact nodes get some mass via CMM or LMM. Thus, removing the mass from the contact surface leads to recovery of the initial structure of the continuous equations.

A slightly different argumentation comes when the contact of thin-walled structures is considered. In this case, the potential contact domain and problem domain coincide. The removal of mass from whole contact domain then means removal of mass from the whole domain. Here, it is proposed to redistribute inertia inside the domain element-wise and to split all nodes in the massless and the inner nodes. Thus, this procedure just reduces the differential index from three to one.

### 2.3.5 Mass scaling

Scaling of inertia for explicit time integration is a common procedure since the 1970s. The aim of mass scaling in context of non-linear structural mechanics is to increase the critical time-step for explicit time integration without substantial loss in accuracy in the lower modes. Conventional Mass Scaling (CMS) adds artificial mass only to diagonal terms of the lumped mass matrix and thus, preserves the diagonal format of the mass matrix. It is usually applied to a small number of short or stiff elements, like spot-welds in car crash, whose high eigenfrequencies limit the time step size. CMS is also used for scaling of rotary inertia of beam and shell elements. This allows to increase the critical step size of these elements up to a corresponding critical step of truss or membrane elements. However, translational and rotational inertia of the structure increase, which may cause non-physical phenomena. Selective Mass

Scaling (SMS) adds artificial terms both to diagonal and non-diagonal terms, which results in non-diagonal mass matrices, but at least it allows preservation of translational mass. Thus, SMS can be used uniformly in the domain with less non-physical artefacts.

In this subsection, existing CMS and SMS methods for beam, shell and solid elements are described and their properties are discussed. The effect of mass scaling on the quality of the solution is discussed in Section 6.4.

### Conventional mass scaling

First, consider an EULER-BERNOULLI two-node column-beam element with cubic transverse and linear longitudinal displacements. For the time being, the influence of rotary inertia of the cross-section is neglected. The element critical time-step size for the row-sum diagonalized mass matrix is the minimum of the axial and flexural time-steps

$$dt_{\text{crit}}^e = \min \left( \frac{l_e}{c}, \frac{\sqrt{3}l_e^2}{12cr_g} \right), \quad (2.85)$$

with  $c$  being the phase velocity of longitudinal waves and  $r_g$  being the radius of gyration for the section. Analysis of this expression shows that for shorter elements with  $l_e/r_g < 4\sqrt{3}$ , the critical time-step is limited by flexural waves, see BELYTSCHKO ET AL. (2001). Therefore, the rotary inertia for these elements is artificially increased to match the axial critical time-step. This was proposed by KEY AND BEISINGER (1971) and leads for an element with constant cross-section to the mass matrix in the form

$$\mathbf{m}_e = \frac{\rho l_e A}{420} \begin{bmatrix} 210 & 0 & 0 & 0 \\ 0 & \alpha l_e^2 & 0 & 0 \\ 0 & 0 & 210 & 0 \\ 0 & 0 & 0 & \alpha l_e^2 \end{bmatrix}, \quad (2.86)$$

where  $\alpha = \max(17.5, 840r_g^2/l_e^2)$  is the mass scaling factor.

An appropriate scaling factor  $\alpha = 17.5(1 + 12r_g^2/l_e^2)$  is also obtained for a two-node TIMOSHENKO beam element with circular cross-section, cf. BELYTSCHKO AND MINDLE (1980). A short overview on scaling for these two types of beams is given in Table 2.1.

A similar procedure is applied for plate and shell elements, see HUGHES ET AL. (1978). The rotational inertia for a rectangular 'thick' plate element with isotropic material is scaled with the factor  $\alpha = l_e^2/(12t^2)$ , where  $l_e$  and  $t$  are the element size and the thickness of the plate. For a distorted element, a more precise estimate is made in BELYTSCHKO AND LIN (1985). In addition, such scaling leads to an isotropic nodal rotational inertia matrix  $\bar{M}_{xx} = \bar{M}_{yy} = \bar{M}_{zz} =$

| element type   | mass type | influence of rotary inertia | $dt_{\text{crit}}^{\text{flex}}$  | $dt_{\text{crit}}^{\text{shear}}$ | mass scaling $\alpha$                           |
|--|-----------|-----------------------------|---|-----------------------------------|---|
| two-node BERNOULLI column-beam; cubic transverse; axial linear | RLM       | no                          | $\frac{\sqrt{3}l_e^2}{12cr_g}$  | -                                 | $\max\left(17.5, 840\frac{r_g^2}{l_e^2}\right)$ |
|  | RLM       | yes                         | $\frac{\sqrt{3}l_e^2\sqrt{l_e^2+12r_g^2}}{12cr_g\sqrt{l_e^2+3r_g^2}}$               | -                                 | $\max\left(17.5, 630\frac{r_g^2}{l_e^2}\right)$ |
|  | CMM       | no                          | $\frac{\sqrt{21}l_e^2}{210cr_g}$  | -                                 | not used  |
|  | CMM       | yes                         | $\frac{\sqrt{21}\sqrt{l_e^4+180l_e^2r_g^2+1680r_g^4}}{210cr_g\sqrt{l_e^2+12r_g^2}}$ | -                                 | not used  |
| two-node linear TIMOSHENKO beam                                | CMM       | yes                         | $\frac{l_e\sqrt{5l_e^2+216r_g^2}}{c\sqrt{15l_e^2+180r_g^2}}$                        | $\frac{l_e}{\sqrt{3}c}$           | not used  |
|  | LMM       | no                          | $\frac{l_e\sqrt{75l_e^2+3240r_g^2}}{60cr_g}$  | $\frac{l_e^2}{2\sqrt{3}cr_g}$     | $\max\left(17.5, 210\frac{r_g^2}{l_e^2}\right)$ |

**Table 2.1:** Element time-steps and mass scaling factors for BERNOULLI and TIMOSHENKO elements based on the maximum flexural and shear frequency. Exact stiffness is used for both elements. For TIMOSHENKO elements, a square cross-section with shear correction factor  $\gamma_s = 5/6$  is assumed.

$\bar{M}_r = \rho A_e l_e^2 / 36$ , so that the rotary inertia is invariant under finite rotations. For a 3D 4-node shell element, such nodal mass matrix reduces to

$$\mathbf{m}_{\text{node}} = \frac{\rho t A_e}{4} \begin{bmatrix} 1 & 0 & 0 & 0 & 0 & 0 \\ 0 & 1 & 0 & 0 & 0 & 0 \\ 0 & 0 & 1 & 0 & 0 & 0 \\ 0 & 0 & 0 & \alpha t^3 & 0 & 0 \\ 0 & 0 & 0 & 0 & \alpha t^3 & 0 \\ 0 & 0 & 0 & 0 & 0 & \alpha t^3 \end{bmatrix}. \quad (2.87)$$

In case of truss, membrane and solid elements, the LMM is scaled by a factor of  $q$ . This reduces the element time-step size by the factor of  $\sqrt{q}$  and increases the translational and rotary inertia of the element by factor  $q$ . Usually, such scaling is applied to a small number of short or stiff elements with an overall increase of the mass of the model up to 1-3%. The amount of the added mass should be carefully controlled, see for recommendations WHIRLEY AND ENGELMANN (1993).

It is also possible to add artificial inertia to incompatible modes (MATTERN 2012; SCHMIED ET AL. 2013). In this way, static elimination of incompatible mode parameters can be avoided and at the same time, locking phenomena are circumvented. However, the stiffness of modes associated with the incompatible displacements is large and these modes provide the highest eigenfrequencies, which motivates the application of mass scaling to these modes.

### Selective mass scaling

Selective mass scaling was proposed in OLOVSSON ET AL. (2004, 2005). The original idea relies on the following *algebraic* construction of the scaled mass matrix  $\mathbf{m}_e^\circ$  of an individual element as

$$\mathbf{m}_e^\circ = \mathbf{m}_e + \lambda_e^\circ, \quad \text{with} \quad \lambda_e^\circ = \frac{\Delta m_e}{n} \left( \mathbf{I} - \sum_i \mathbf{o}_i^\top \mathbf{o}_i \right), \quad (2.88)$$

where  $\mathbf{m}_e$  and  $\lambda_e^\circ$  are LMM and Mass Augmentation (MA),  $n$  is the number of nodes per element,  $\Delta m_e$  is the artificially added mass and  $\mathbf{o}_i$  is some set of orthonormalized *rigid body modes*. Initially, it was proposed to include only translational rigid body modes (OLOVSSON ET AL. 2005). Herein, this method is referenced as Algebraic Selective Mass Scaling (ASMS). A later implementation includes also rigid body rotations (BORRVALL 2011). Hence, the properties of the algebraic SMS are defined by the linear hull of vectors  $\mathbf{o}_i$  and the amount of added mass  $\Delta m_e$ .

Example: 3-node 2D membrane element with constant density and nodal coordinates  $\Xi = [X_1, Y_1, X_2, Y_2, X_3, Y_3]$ . The LMM and two orthonormalized rigid body modes for such an element read

$$\mathbf{m}_e = \frac{m}{3} \begin{bmatrix} 1 & 0 & 0 & 0 & 0 & 0 \\ 0 & 1 & 0 & 0 & 0 & 0 \\ 0 & 0 & 1 & 0 & 0 & 0 \\ 0 & 0 & 0 & 1 & 0 & 0 \\ 0 & 0 & 0 & 0 & 1 & 0 \\ 0 & 0 & 0 & 0 & 0 & 1 \end{bmatrix}, \quad (2.89a)$$

$$\mathbf{o}_1 = 1/\sqrt{3} [1 \ 0 \ 1 \ 0 \ 1 \ 0]^\top, \quad (2.89b)$$

$$\mathbf{o}_2 = 1/\sqrt{3} [0 \ 1 \ 0 \ 1 \ 0 \ 1]^\top, \quad (2.89c)$$

where  $m = \rho A_e t$  is the translational mass of the element and  $A_e = \frac{1}{2}(Y_1 X_3 + Y_2 X_1 + X_2 Y_3 - Y_1 X_2 - Y_2 X_3 - Y_3 X_1)$  is the area of the element. Substitution of the two rigid body modes in equation (2.88) yields mass augmentation

$$\lambda_e^\circ = \frac{\Delta m_e}{6} \begin{bmatrix} 2 & 0 & -1 & 0 & -1 & 0 \\ 0 & 2 & 0 & -1 & 0 & -1 \\ -1 & 0 & 2 & 0 & -1 & 0 \\ 0 & -1 & 0 & 2 & 0 & -1 \\ -1 & 0 & -1 & 0 & 2 & 0 \\ 0 & -1 & 0 & -1 & 0 & 2 \end{bmatrix}. \quad (2.90)$$

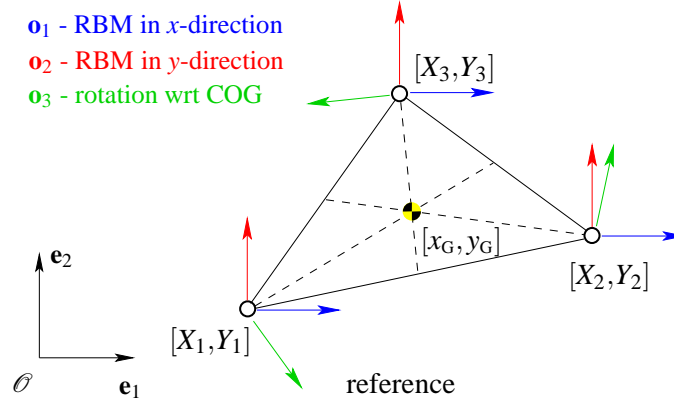


**Figure 2.12:** Rigid body modes of a 3-node element with 2 DOFS per node.

Thus, the translational mass  $m$  and the center of gravity  $[x_G, y_G]$  computed with ASMS has correct values. The values for moments of inertia w.r.t. the center of gravity  $[I_{XX}, I_{XY}, I_{YY}]$  are overestimated by the factor of  $4 + 6\Delta m/m$ . In order to get the correct value for the polar momentum ( $I_{XX} + I_{YY}$ ), the third rigid body mode vector should be also used in equation (2.88). Taking into consideration orthogonality with the vectors  $\mathbf{o}_{1,2}$ , the vector  $\mathbf{o}_3$  reads

$$\mathbf{o}_3 = \frac{\hat{\mathbf{o}}_3}{|\hat{\mathbf{o}}_3|}, \text{ with} \quad (2.91)$$

$$\hat{\mathbf{o}}_3 = \begin{bmatrix} Y_2 + Y_3 - 2Y_1 \\ 2X_1 - X_2 - X_3 \\ Y_1 + Y_3 - 2Y_2 \\ 2X_2 - X_1 - X_3 \\ Y_1 + Y_2 - 2Y_3 \\ 2X_3 - X_1 - X_2 \end{bmatrix}. \quad (2.92)$$

In this case, the local scaled matrix  $\mathbf{m}_e^\circ$  is fully occupied, i.e. it has entries coupling inertia in  $x$ - and  $y$ - direction.

In a total Lagrangian approach, assembly of the local scaled mass matrices is carried out once at the beginning of the computation. It leads to a global selective scaled mass matrix

$$\mathbf{M}^\circ = \bigcup_e \mathbf{m}_e^\circ. \quad (2.93)$$

Matrix  $\mathbf{M}^\circ$  has a non-diagonal structure. Therefore, calculation of the global acceleration vector  $\mathbf{a}_n$  requires at each time-step  $t_n$  a non-trivial solution of the linear system

$$\mathbf{M}^\circ \mathbf{a}_n = \mathbf{f}_n, \quad (2.94)$$

where  $\mathbf{f}_n$  is the global nodal force vector. It is proposed to use a preconditioned conjugate gradient method (PCG) with JACOBI preconditioner, see OLOVSSON AND SIMONSSON (2006).

SMS has the following effect on the structural behavior. The critical time-step roughly increases by the factor of  $\sqrt{1+\beta}$  with  $\beta$  being the ratio of the added mass to the element mass  $\Delta m/m$  (OLOVSSON AND SIMONSSON 2006). The eigenmodes of the structure are distorted and the order of the modes may be changed. The phase velocity for short waves is significantly reduced and the dispersive error for these waves is increased, see Subsection 6.2. In case of translational rigid body modes being taken, the rotary inertia of the structure is increased. If all rigid body modes are taken, then the rotary inertia is preserved. However in this case, the scaled mass matrix obtains coupled terms between inertia in x-, y- and z-direction (BORRVALL 2011). The condition number of the global mass matrix  $\mathbf{M}^\circ$  increases by factor approximately  $1+2\beta$  and the number of iterations needed for solving the system  $\mathbf{M}^\circ \mathbf{a}_n = \mathbf{f}_n$  grows proportionally to  $\sqrt{1+2\beta}$ .

ASMS is implemented in the commercial explicit FE codes *LS-Dyna*, *Impetus AFEA*<sup>3</sup> and *RADIOSS*<sup>4</sup>. It proved to be efficient for some applications such as deep drawing and cutting of metal sheets, car roof crash and drop tests (ARNAUDEAU 2010; BORRVALL 2011; PAGANI AND PEREGO 2013; ROY ET AL. 2011). The theoretical estimate of the speed-up that can be obtained with SMS is given in Subsection 2.4.2. The obtained speed-up in real-life application varies from two to forty, see also Chapters 1 and 7.

SMS for solid-shells and shells modelled with solid elements received in literature special attention. The typical spectrum of such structures is shown in Figure 2.13. Through-the-thickness modes limit the critical time-step size. However, these modes are not important for the global structural response and they may be suppressed via adding inertia for the stacks of the nodes, see OLOVSSON ET AL. (2004). A similar approach is given for dynamics of solid-shells in COCCHETTI ET AL. (2013) and PAGANI (2013). These works also include analytical estimates of the critical time-step and study on the distortion sensitivity of the proposed formulation.

MINDLIN's theory of elasticity with micro-inertia can be another possible starting point for derivation of SMS. This theory includes inertia for displacement and micro-rotations. After several simplifications of this general theory, the following equation of motion for isotropic media may be obtained:

$$\rho [\ddot{u}_i - (d_1^2 + d_2^2) \ddot{u}_{j,ij} - d_2^2 \ddot{u}_{j,ij}] = (\lambda + \mu) u_{j,ij} + \mu u_{i,jj}, \quad (2.95)$$

---

<sup>3</sup>LARS OLOVSSON is one of the active developers of *Impetus AFEA*. Some advanced mass scaling methods are implemented in the code, e.g. mass scaling for quadratic and cubic tetrahedral and hexahedral elements, mass scaling for clusters of nodes. However, the methods are not published (see <http://www.impetus-afea.com/>).

<sup>4</sup>Selective mass scaling is called *Advanced mass scaling* in *RADIOSS*.

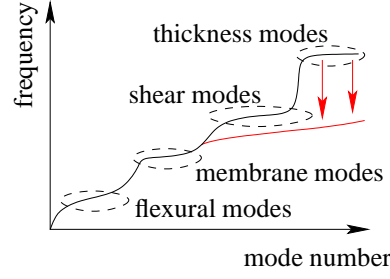


**Figure 2.13:** Characteristic distribution of eigenfrequencies for a thin-walled structure modelled with solid elements (black) and effect of mass scaling of thickness inertia (red).

with  $u_i$  being the displacement,  $\lambda$  and  $\mu$  being the LAMÉ constants.  $d_1$  and  $d_2$  are the length scale parameters related to the micro-structure, see ASKES ET AL. (2011). Finite element discretization of inertial terms leads to the element mass augmentation matrix  $\lambda^\circ$  with

$$\lambda^\circ = \int_{\mathcal{B}} \rho \mathbf{N}^T \mathbf{N} d\mathcal{B} + \int_{\mathcal{B}} (\mathbf{L}\mathbf{N})^T \hat{\rho} \mathbf{L}\mathbf{N} d\mathcal{B}, \quad (2.96)$$

$$\hat{\rho} = d_1^2 \mathbf{I} \otimes \mathbf{I} + d_2^2 (\mathbf{I} \otimes \mathbf{I})^{\text{T}23}. \quad (2.97)$$

Here,  $\hat{\rho}$  is the matrix of local micro-inertia properties and  $\mathbf{L}$  is the symmetric part of the gradient (2.64). Matrix  $\hat{\rho}$  reduces for the 2D case to

$$\hat{\rho} = \rho \begin{bmatrix} d_1^2 + d_2^2 & d_1^2 & 0 \\ d_1^2 & d_1^2 + d_2^2 & 0 \\ 0 & 0 & d_2^2 \end{bmatrix}. \quad (2.98)$$

A variation of equation (2.96) called Enhanced Selective Mass Scaling (eSMS) is given in GAVOILLE (2013). There, isotropic mass scaling is obtained for the length scale parameters  $d_1 = 0$  and  $d_2^2 \sim \beta$ . Moreover, the value for the scale parameter  $d_2$  is adjusted to the size of each element leading to a mass augmentation matrix in the form

$$\lambda^\circ = \beta_e m \frac{\int_{\mathcal{B}} (\mathbf{L}\mathbf{N})^T \mathbf{L}\mathbf{N} d\mathcal{B}}{\text{Tr} \int_{\mathcal{B}} (\mathbf{L}\mathbf{N})^T \mathbf{L}\mathbf{N} d\mathcal{B}}, \quad (2.99)$$

with  $\beta_e$  and  $m$  being the element scaling factor and mass, respectively, and Tr being the trace operator for a matrix.

Stiffness proportional mass scaling is recovered in equation (2.96), if the ratio of LAMÉ parameters  $\lambda/\mu$  and the squares of the scale parameters  $d_1^2/d_2^2$  are equal. Stiffness proportional scaling was proposed earlier in (MACEK AND AUBERT 1995; OLOVSSON ET AL. 2005), though. Positive features of stiffness proportional mass scaling are eigenmode preservation and controlled eigenfrequency reduction.

A variationally based method for SMS was proposed recently in TKACHUK AND BISCHOFF (2013c). The starting point of the proposed approach is a new parametrized variational principle of elasto-dynamics, which can be interpreted as penalized HAMILTON's principle. It uses independent variables for displacement, velocity and momentum in a three-field formulation. The penalized HAMILTON's principle imposes relations between velocity, momentum and displacement via the penalty method. Consistent discretization of the latter principle results in a parametric family of mass matrices. In this way, the translational inertia, center of gravity and polar momenta of individual elements may be preserved, which guarantees convergence of the method with mesh refinement. A distinctive feature of the method is variational rigorousness. Besides, the mass augmentation is prescribed via ansatz spaces for velocity and momentum. This method is discussed in detail in Sections 4.1, 6.2 and 7.2.

A classification of mass scaling methods the discussed above is given in Figure 2.14. The conventional mass scaling was extensively studied in the 1970s and 1980s. After the pioneering papers (MACEK AND AUBERT 1995; OLOVSSON ET AL. 2004, 2005; OLOVSSON AND SIMONSSON 2006), the selective mass scaling received a great deal of attention. New methods were proposed in ASKES ET AL. (2011); COCCHETTI ET AL. (2013); TKACHUK AND BISCHOFF (2013c, b); GAVOILLE (2013); SCHMIED ET AL. (2013). Besides, approximately 20 papers and conference talks describe speed-up of SMS for different applications.

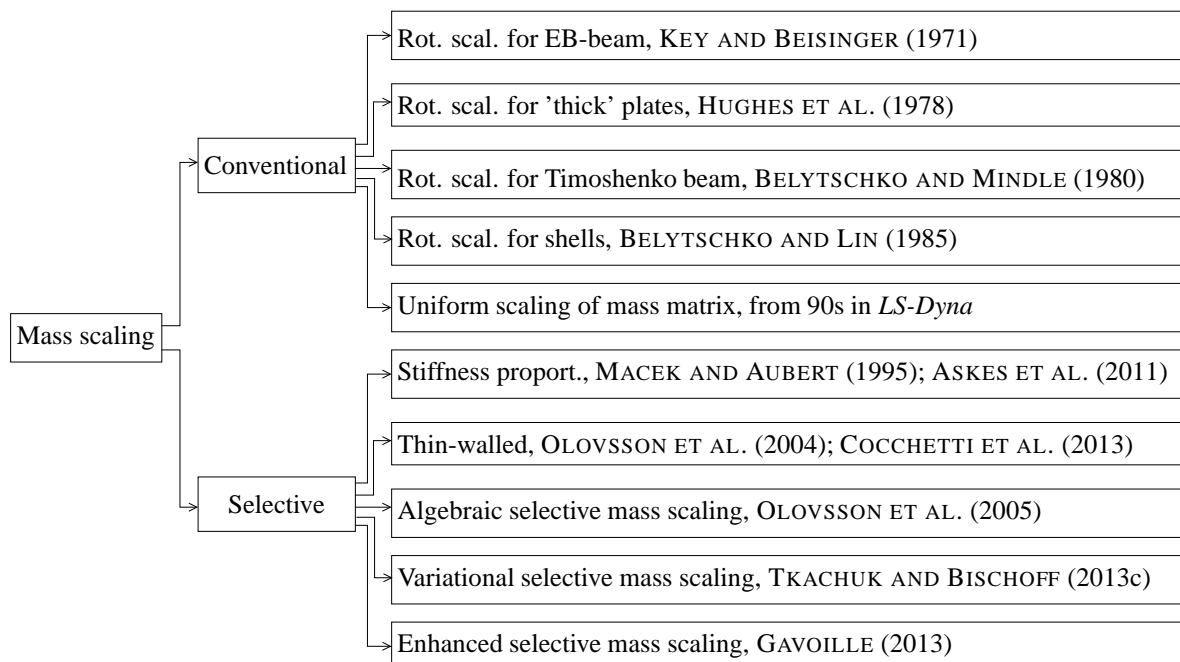


**Figure 2.14:** Classification of mass scaling methods.

## 2.4 Integration in Time

In this section, methods of solution for second order initial value problems are discussed. Here, the methods used in the thesis are presented, including central difference and NEW-MARK  $\beta$  methods. The description follows the notation used in BELYTSCHKO ET AL. (2001) with an extension of the central difference method to non-diagonal mass matrices presented in OLOVSSON AND SIMONSSON (2006).

### 2.4.1 Central difference method

The central difference method is a common method for explicit time integration. Its simplicity and robustness motivate the usage of the method for a broad range of applications. The most important applications include crash worthiness and manufacturing simulations. Another advantage is the structure of the algorithm allowing efficient parallelization and scalability on modern supercomputer architectures. For example, car crash simulation speed-up satisfactory up to 200 processors and 10 million DOFs for a hybrid *LS-DYNA* version (MENG ET AL. 2010; MAKINO 2008). Some applications on special computer architectures scale well up to 65K processors and 320 million DOFs (RAJAN 2007).

In the following, we consider for simplicity an algorithm with a constant time-step  $\Delta t$  (an algorithm with variable time-step can be found in BELYTSCHKO ET AL. (2001)). The initial time and the state of the system are denoted with  $t_0$ ,  $\mathbf{U}_0$  and  $\dot{\mathbf{U}}_0$ . The termination time is  $t_{\text{end}}$ . Displacements and accelerations are defined at full time-steps  $t_n$  as  $\mathbf{U}_n$  and  $\ddot{\mathbf{U}}_n$ , respectively. Velocities are defined in half-steps  $t_{n+1/2}$  as  $\dot{\mathbf{U}}_{n+1/2}$ . The central difference formulas for velocity and acceleration read

$$\dot{\mathbf{U}}_{n+1/2} = \frac{\mathbf{U}_{n+1} - \mathbf{U}_n}{\Delta t}, \quad \ddot{\mathbf{U}}_n = \frac{\dot{\mathbf{U}}_{n+1/2} - \dot{\mathbf{U}}_{n-1/2}}{\Delta t}. \quad (2.100)$$

Equations of motion are evaluated at the full time step  $t_n$

$$\mathbf{M}\ddot{\mathbf{U}}_n = \mathbf{F}_n = \mathbf{F}_n^{\text{ext}} - \mathbf{F}_n^{\text{int}} - \mathbf{F}_n^{\text{vbc}}. \quad (2.101)$$

The internal force vector  $\mathbf{F}_n^{\text{int}}$  is evaluated for the current displacement  $\mathbf{U}_n$  as described in Section 2.3. The force vector  $\mathbf{F}_n^{\text{vbc}}$  arises from velocity boundary conditions and the off-diagonal terms of the scaled mass matrix  $\mathbf{M}^\circ$ . It is assembled over all nodes with velocity boundary conditions to the vector

$$\mathbf{F}_n^{\text{vbc}} = \bigcup_{\text{vbc}} \mathbf{M}^\circ \ddot{\mathbf{U}}_n, \quad \text{with } \ddot{\mathbf{U}}_n = \frac{\dot{\mathbf{U}}_{n+1/2} - \dot{\mathbf{U}}_{n-1/2}}{\Delta t}, \quad (2.102)$$

1. Initialize  $t = t_0$ ,  $\mathbf{U} = \mathbf{U}_0$ ,  $\dot{\mathbf{U}} = \dot{\mathbf{U}}_0$
2. Compute LMM  $\mathbf{M}$  or SMS  $\mathbf{M}^\circ$  and preconditioner for mass matrix  $\mathbf{P}$
3. Get global force vector  $\mathbf{F}_n = \mathbf{F}_n^{\text{ext}} - \mathbf{F}_n^{\text{int}} - \mathbf{F}_n^{\text{vbc}}$
4. Compute acceleration  $\ddot{\mathbf{U}}_n = \mathbf{M}^{-1}\mathbf{F}_n$
5. Time update  $t_{n+1} = t_n + \Delta t$
6. Partial update of velocity  $\dot{\mathbf{U}}_{n+1/2} = \dot{\mathbf{U}}_n + \frac{\Delta t}{2}\ddot{\mathbf{U}}_n$
7. Enforce velocity b.c.  $\dot{\mathbf{U}}_{n+1/2} = \hat{\dot{\mathbf{U}}}_{n+1/2}$
8. Update nodal displacements  $\mathbf{U}_{n+1} = \mathbf{U}_n + \Delta t\dot{\mathbf{U}}_{n+1/2}$
9. Get global force vector  $\mathbf{F}_{n+1} = \mathbf{F}_{n+1}^{\text{ext}} - \mathbf{F}_{n+1}^{\text{int}} - \mathbf{F}_{n+1}^{\text{vbc}}$
10. Compute acceleration  $\ddot{\mathbf{U}}_{n+1} = \mathbf{M}^{-1}\mathbf{F}_{n+1}$
11. Partial update of velocity  $\dot{\mathbf{U}}_{n+1} = \dot{\mathbf{U}}_{n+1/2} + \frac{\Delta t}{2}\ddot{\mathbf{U}}_{n+1}$
12. Update time-step counter to  $n + 1$
13. Output
- 14 If  $t_{n+1} < t_{\text{end}}$  go to 5.

**Figure 2.15:** Flowchart for explicit time integration.

where  $\hat{\dot{\mathbf{U}}}$  are vectors of prescribed velocity. This term vanishes in case of LMM.

Thus, the update for velocity and displacement results in

$$\dot{\mathbf{U}}_{n+1/2} = \dot{\mathbf{U}}_{n-1/2} + \Delta t, \mathbf{M}^{-1}\mathbf{F}_n, \quad \mathbf{U}_{n+1} = \mathbf{U}_n + \Delta t\dot{\mathbf{U}}_{n+1/2}. \quad (2.103)$$

The algorithm for the central difference method is presented in Figure 2.15. Calculation of the global acceleration vector is performed at stages 4 or 10. If SMS is used, then the acceleration vector is computed with a direct solver for small systems or with a Preconditioned Conjugate Gradient method (PCG) with JACOBI preconditioner, see Figure 2.16. According to OLOVSSON AND SIMONSSON (2006), the acceleration vector from the previous step is used as starting value for the iterative solution. The tolerance for the iterative solver  $tol_a$  is usually in a range from  $10^{-3}$  to  $10^{-8}$  depending on the application.

The central difference method is conditionally stable. For linearized systems an the critical time-step size can be estimated on the basis of the maximum natural frequency  $\omega_{\text{max}}$  of the system, see HUGHES (2000) and BELYTSCHKO ET AL. (2001). Thus, the time-step size should satisfy the condition

$$\Delta t < \frac{2}{\omega_{\text{max}}}. \quad (2.104)$$

It is recommended to reduce the time-step further by the factor *SCFAC* from 0.67 to 0.9 depending on the application. The maximum natural frequency can be estimated from an iterative algorithm according to BENSON ET AL. (2010) or from an elementwise computation according to BELYTSCHKO ET AL. (2001).

1. Initialize acceleration with values from previous time-step  $\ddot{\mathbf{U}}_{n,0} = \ddot{\mathbf{U}}_{n-1}$
2. Compute initial residual  $\mathbf{r}_0 = \mathbf{F}_n - \mathbf{M}^\circ \ddot{\mathbf{U}}_{n,0}$
2.  $\mathbf{z}_0 = \mathbf{P}^{-1} \mathbf{r}_0$
3.  $\mathbf{p}_0 = \mathbf{z}_0$
4. while  $|\mathbf{r}_0| > tol_a |\mathbf{F}_n|$  do
5.  $\alpha_k = \frac{\mathbf{z}_k^\top \mathbf{z}_k}{\mathbf{p}_k^\top \mathbf{M}^\circ \mathbf{p}_k}$
6.  $\ddot{\mathbf{U}}_{n,k+1} = \ddot{\mathbf{U}}_{n,k} + \alpha_k \mathbf{p}_k$
7.  $\mathbf{r}_{k+1} = \mathbf{r}_k - \mathbf{M}^\circ \mathbf{p}_k$
8.  $\mathbf{z}_{k+1} = \mathbf{P}^{-1} \mathbf{r}_{k+1}$
9.  $\beta_k = \frac{\mathbf{z}_{k+1}^\top \mathbf{z}_k}{\mathbf{z}_k^\top \mathbf{r}_k}$
10.  $\mathbf{p}_{k+1} = \mathbf{z}_{k+1} + \beta_k \mathbf{p}_k$
- end do

**Figure 2.16:** Flowchart for calculations of acceleration vector with PCG.

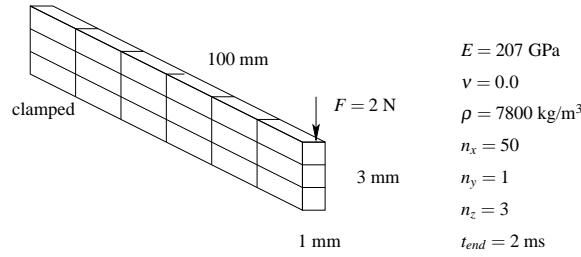


**Figure 2.17:** Tip loaded beam, problem setup (OLOVSSON ET AL. 2005).

## 2.4.2 An estimate for speed-up for SMS

The theoretical estimate of speed-up for SMS can be done comparing computational costs for LMM and SMS for the following simple example (OLOVSSON ET AL. 2005)<sup>5</sup>. The model for the example problem is shown in Figure 2.17. Initial zero displacements and velocities are assumed. The beam is loaded at the tip by an abrupt force  $F$ . The time-step scaling factor SCFAC is 0.67 for LMM and SMS. The model has  $n_{ele} = 50 \times 3 \times 1$  eight-node hexahedral elements,  $n_{node} = 400$  nodes and  $n_{dof} = 1200$  degrees of freedom.

The computational costs of explicit time integration with LMM can be roughly estimated as follows. The initialization steps 1 to 4 (Figure 2.15) result in costs of  $O(n_{dof})$ , which is small in comparison with discussed below costs. The most expensive part of the time integration loop (steps 5 to 14) is the computation of the global internal force vector (step 9)<sup>6</sup>. The global

<sup>5</sup>Two major drawbacks of this example are regular mesh and absence of contact. Distribution of element distortions and local critical time-steps have a significant influences on the efficiency of SMS. Treatment of contact usually takes 20 to 40% of the computational time in real life applications. However, the cost of treatment of the contact is proportional to the number of time-steps, which does not change the form of the final expression.

<sup>6</sup>The output (step 13) is never done at each step due to limitations of hard disk capacity and slowness of I/O operations. The number of output frames is usually by a factor of 1000 smaller than the total number of time-steps. The time spent on output is usually below 5 % and it is neglected here in the estimate.

internal force vector is assembled from  $n_{ele}$  local internal force vectors. Computation costs of a constant stress solid element with FLANAGAN AND BELYTSCHKO (1981) hourglass control and bilinear elasto-plastic material is  $\text{cost}_{ele} = 1388 \text{ FLOP}$ <sup>7</sup> (HALLQUIST ET AL. 2006). Thus, the computational cost for the global internal force vector is

$$\text{COST}_{ele} = \text{cost}_{ele} \times n_{step} = 1388 \times 150 = 208200 \text{ FLOP}. \quad (2.105)$$

The internal force vector is assembled at each time-step. The CFL criterion predicts the critical time-step of  $\Delta t_{crit} = l_e/c = 0.18\mu\text{s}$ . Taking in account a SCFAC of 0.67, this results in a time-step value  $\Delta t^{LMM} = 0.125\mu\text{s}$  and total number of time-steps  $n_{step} = 16000$  (for end time  $t_{end} = 2\text{ms}$ ). Thus, the computational cost estimate for LMM reads

$$\text{COST}^{LMM} \approx \text{COST}_{ele} n_{step} = \text{cost}_{ele} n_{ele} \frac{t_{end}}{\Delta t_{crit}^{LMM} \text{SCFAC}} = 208200 \times 16000 = 3.33 \text{ GFLOP}. \quad (2.106)$$

Explicit time integration (Figure 2.15) with SMS leads to several overheads: computation of the scaled mass  $\mathbf{M}^\circ$  and preconditioner  $\mathbf{P}$  (step 2), evaluation of the vector  $\mathbf{F}^{vbc}$  (step 3 and 9) and computation of the acceleration  $\ddot{\mathbf{U}}$  (step 4 and 10). The scaled mass  $\mathbf{M}^\circ$  and the preconditioner  $\mathbf{P}$  are computed in the beginning of the simulation. The computational cost for step 2 is  $O(n_{ele})$ . It is negligible in comparison with the costs for the internal force vector  $\text{COST}_{ele} n_{step}$ . The cost of evaluation of the vector  $\mathbf{F}^{vbc}$  is proportional to the number of nodes with prescribed velocity boundary conditions. This number is problem dependent (in the example, it is eight). In this estimate, it is assumed that the number of these nodes is small in comparison to the total number of nodes and the costs are negligible. The costs for computation of the acceleration  $\ddot{\mathbf{U}}$  is the costs of a single PCG iteration  $\text{COST}_{PCG}$  times the number of iterations  $n_{iter}$ , i.e.

$$\text{COST}_{solver} = \text{COST}_{PCG} \times n_{iter}. \quad (2.107)$$

The average number of iteration for the relative tolerance  $tol_a = 10^{-5}$  is eight. The costs for a single PCG iteration  $\text{COST}_{PCG}$  can be estimated as

$$\text{COST}_{PCG} = 2 \times \text{bandwidth} \times n_{dof} = 2 \times 5 \times 1200 = 12000 \text{ FLOP}. \quad (2.108)$$

This yields an estimate  $\text{COST}_{solver}$  of 108000 FLOP.

The number of time-steps for SMS depend on mass scaling  $\beta$  via a factor  $\sqrt{1+\beta}$ . For  $\beta = 8$ , the time-step is scaled by factor three to  $\Delta t^{SMS} = 0.375\mu\text{s}$  ( $\Delta t_{crit}^{SMS} = \sqrt{1+\beta} l_e/c = 0.54\mu\text{s}$ ). The total number of time-steps for the end time  $t_{end} = 2\text{ms}$  is 5333. Thus, the estimate for the

---

<sup>7</sup>Floating point operations.

computational costs of explicit time integration with SMS reads

$$\begin{aligned} \text{COST}^{SMS} &\approx (\text{COST}_{\text{ele}} + \text{COST}_{\text{solver}}) n_{\text{step}} = (\text{COST}_{\text{ele}} + \text{COST}_{\text{solver}}) \frac{t_{\text{end}}}{\Delta t_{\text{crit}}^{SMS} SCFAC} \\ &= (208000 + 108000) \times 5333 = 1.69 \text{ GFLOP}, \end{aligned} \quad (2.109)$$

Finally, it leads to the theoretical estimate of speed-up for SMS

$$\text{SPEED-UP} = \frac{\text{COST}^{LMM}}{\text{COST}^{SMS}} \approx \frac{\Delta t_{\text{crit}}^{SMS}}{\Delta t_{\text{crit}}^{LMM} (1 + \text{COST}_{\text{solver}}/\text{COST}_{\text{ele}})} = \frac{3.33}{1.69} = 1.97. \quad (2.110)$$

Note, that the speed-up is proportional to the ratio  $\Delta t_{\text{crit}}^{SMS} / \Delta t_{\text{crit}}^{LMM}$ . Besides, small ratios for  $\text{COST}_{\text{solver}}/\text{COST}_{\text{ele}}$  allow large theoretical values for the speed-up. In the example, the ratio is 0.52, which reduces the theoretical speed-up from three to 1.97. Fast iterative solution for accelerations requires good conditioning<sup>8</sup> and small bandwidth of the scaled mass matrix  $\mathbf{M}^\circ$ , which is discussed in Subsection 6.3.2. In addition, the computational costs  $\text{cost}_{\text{ele}}$  for other FE formulations may be up to 11000 FLOP, like *LS-Dyna* eight-node hexahedral element (ELFORM = -2 or 3) or ten-node tetrahedral element (ELFORM = 16 or 17). For these elements, the ratio  $\text{COST}_{\text{solver}}/\text{COST}_{\text{ele}}$  is less and SMS has larger potential. This example illustrates, that the efficiency of SMS is reached at good balance between the costs for global internal force calculation and iterative solution for acceleration.

### 2.4.3 Newmark $\beta$ method

The second most popular method in computational structural mechanics is the NEWMARK  $\beta$  method proposed in NEWMARK (1959). NEWMARK  $\beta$  is a one-step and self-starting method and it is available in most implicit commercial codes. It relies on the following update rules for displacement and velocity

$$\mathbf{U}_{n+1} = \mathbf{U}_n + \dot{\mathbf{U}}_n + \frac{\Delta t^2}{2} (2\beta \ddot{\mathbf{U}}_{n+1} + (1 - 2\beta) \ddot{\mathbf{U}}_n), \quad (2.111a)$$

$$\dot{\mathbf{U}}_{n+1} = \dot{\mathbf{U}}_n + \Delta t (\gamma \ddot{\mathbf{U}}_{n+1} + (1 - \gamma) \ddot{\mathbf{U}}_n), \quad (2.111b)$$

with  $\beta$  and  $\gamma$  being parameters of the method. The parameters  $\beta$  and  $\gamma$  determine accuracy and stability of the method, e.g. see HUGHES (2000).

<sup>8</sup>The number of PCG iteration should be less than 50.

1. Initialize  $t = t_0$ ,  $\mathbf{U} = \mathbf{U}_0$ ,  $\dot{\mathbf{U}} = \dot{\mathbf{U}}_0$
2. Compute mass matrix  $\mathbf{M}$
3. Get global force vector  $\mathbf{F}_n = \mathbf{F}_n^{\text{ext}} - \mathbf{F}_n^{\text{int}} - \mathbf{F}_n^{\text{vbc}}$
4. Compute acceleration  $\ddot{\mathbf{U}}_n = \mathbf{M}^{-1}\mathbf{F}_n$
5. Time update  $t_{n+1} = t_n + \Delta t$
6. Predictor  $\mathbf{U}_{n+1} = \tilde{\mathbf{U}}_{n+1} + \Delta t^2\beta\ddot{\mathbf{U}}_{n+1}$  and  $\dot{\mathbf{U}}_{n+1} = \dot{\tilde{\mathbf{U}}}_{n+1} + \Delta t\gamma\ddot{\mathbf{U}}_{n+1}$   
(Loop over NEWTON-RAPHSON iterations:)
7. Get global force  $\mathbf{F}_{n+1} = \mathbf{F}_{n+1}^{\text{ext}} - \mathbf{F}_{n+1}^{\text{int}} - \mathbf{F}_n^{\text{vbc}}$ , assemble global tangent  $\mathbf{K}_T$
8. Compute algorithmic right hand side and tangent (2.115)
9. Solve for  $\Delta\mathbf{U}_{n+1}^i$
10. Check for convergence
11. Update of velocity and acceleration
12. Update time-step counter to  $n + 1$
13. Output
- 14 If  $t_{n+1} < t_{\text{end}}$  go to 5.

**Figure 2.18:** Flowchart for NEWMARK  $\beta$  time integration.

The solution is split in predictor and corrector steps. The predictor step is written as

$$\tilde{\mathbf{U}}_{n+1} = \mathbf{U}_n + \Delta t\dot{\mathbf{U}}_n + \frac{\Delta t^2}{2}(1 - 2\beta)\ddot{\mathbf{U}}_n, \quad (2.112a)$$

$$\dot{\tilde{\mathbf{U}}}_{n+1} = \dot{\mathbf{U}}_n + \Delta t(1 - \gamma)\ddot{\mathbf{U}}_n. \quad (2.112b)$$

The corrector step reads as follow

$$\mathbf{U}_{n+1} = \tilde{\mathbf{U}}_{n+1} + \Delta t^2\beta\ddot{\mathbf{U}}_{n+1}, \quad (2.113a)$$

$$\dot{\mathbf{U}}_{n+1} = \dot{\tilde{\mathbf{U}}}_{n+1} + \Delta t\gamma\ddot{\mathbf{U}}_{n+1}. \quad (2.113b)$$

The unknown acceleration  $\ddot{\mathbf{U}}_{n+1}$  at the new time-step is expressed using the corrector equation

$$\ddot{\mathbf{U}}_{n+1} = \frac{1}{\Delta t^2\beta} \left( \mathbf{U}_{n+1} - \tilde{\mathbf{U}}_{n+1} \right). \quad (2.114)$$

Substitution of the acceleration in equilibrium equation (2.81) at  $t_{n+1}$  leads to the following equation with respect to the unknown displacement vector  $\mathbf{U}_{n+1}$

$$\left( \frac{1}{\Delta t^2\beta}\mathbf{M} + \frac{\gamma}{\Delta t\beta}\mathbf{C} \right) \mathbf{U}_{n+1} + \mathbf{F}^{\text{int}}(\mathbf{U}_{n+1}) = \mathbf{F}^{\text{ext}}(t_{n+1}) + \left( \frac{1}{\Delta t^2\beta}\mathbf{M} + \frac{\gamma}{\Delta t\beta}\mathbf{C} \right) \tilde{\mathbf{U}}_{n+1} - \mathbf{C}\dot{\tilde{\mathbf{U}}}_{n+1}. \quad (2.115)$$

The latter equation is usually solved with the NEWTON-RAPHSON algorithm. Having  $\mathbf{U}_{n+1}$  at hand, the acceleration and velocity at  $t_{n+1}$  are updated. The algorithm is presented in Figure 2.18.

Instabilities for non-linear problems are common for dynamic contact problems. Certain modifications to the algorithm should be made, if contact condition are included. This question is covered in PANDOLFI ET AL. (2002); LAURSEN (2002); HARTMANN AND RAMM (2008); DEUFLHARD ET AL. (2008); SUWANNACHIT ET AL. (2012).

## 2.5 Assessment of quality of space and time discretization

### 2.5.1 Temporal discretization

A good time integration scheme is crucial for accurate and reliable solution of dynamic problems. The analysis of one-step and multi-step time discretization schemes for linear systems of ODE is available in HUGHES (2000); SAMARSKII (2001). This analysis considers amplification matrices on a single step and provides results for numerical damping, period elongation (dispersion), convergence and stability. Yet, it is difficult to conduct such an analysis for non-linear systems or systems with constraints.

### DAE systems and differential index

A differential-algebraic equation is an equation involving an unknown function and its derivatives, see CAMPBELL ET AL. (2008). The properties and solution methods for a DAE depend on its mathematical structure. In case the system of equations can be solved with respect to highest derivative, the DAE reduces to an ODE. This usually can not be done for constrained mechanical systems discussed here, see equation (2.83). For these problems, the semi-explicit class of DAE arises, which is possible to be solved with respect to the highest derivatives only for a part of unknowns, and for the rest of unknowns algebraic equations are provided. These types of equations are called HESSENBERG forms (ASCHER AND PETZOLD 1998). These DASs can be interpreted as a system of ODEs coupled with algebraic constraint equations. Thus, variables for these DAEs can be distinguished by the type of defining equations between *algebraic and differential variables* (ASCHER AND PETZOLD 1998). For example, the following equation

$$\ddot{\mathbf{U}} = \mathbf{M}^{-1} \left( \mathbf{F}^{\text{ext}}(t) - \mathbf{F}^{\text{int}}(t, \mathbf{U}, \dot{\mathbf{U}}) - \mathbf{G}\mathbf{Z} \right) \quad (2.116a)$$

$$\mathbf{0} = \mathbf{G}^T \mathbf{U} - \mathbf{g}_0 \quad (2.116b)$$

includes differential unknowns  $\mathbf{U}$  and algebraic unknowns  $\mathbf{Z}$ . The algebraic unknowns can be eliminated from system (2.116) using three subsequent differentiation. Thus, this system is classified as HESSENBERG index-3 DAE (ASCHER AND PETZOLD 1998).

The high-index of DAE implies that this DAE includes *hidden constraints*. In case of having system (2.116), the solution  $[\mathbf{U}, \mathbf{Z}]$  must also satisfy two derivatives of (2.116b). The equation (2.116b) is a constraint on the position level. In mechanics, the two derivatives of equations (2.116b) are called constraint on velocity and acceleration level.

High index of DAE indicates higher complexity and higher numerical effort. For the mechanical system, energy conservation, noise in algebraic variables and bad conditioning are usual issues connected with solution of index-3 DAE (ASCHER AND PETZOLD 1998). The common approaches to resolve these issues are discussed in Subsection 2.3.4.

### 2.5.2 Spatial discretization

The standard analysis of the error for elliptical problems is done e.g. in BABUŠKA ET AL. (2010). Static and dynamic unilateral contact problems are analysed in KIKUCHI AND ODEN (1988). The error analysis in hyperbolic problems is more complicated. Some approaches are used for this, e.g. HUGHES ET AL. (1976); IDESMAN (2011); HUGHES (2000). Among these approaches, spectral analysis provide valuable information about quality of the solution.

The basic results on spectral relation FE is given in BELYTSCHKO (1978). This paper considers 2-node and 3-node truss elements with consistent and lumped mass matrices. For the 3-node truss the acoustic and optical branches of the dispersion relation are obtained. For wave propagation in 2D meshes of linear triangular and bilinear quadrilateral elements see MULLEN AND BELYTSCHKO (1982). In this paper is shown that mass lumping and under-integration of a stiffness matrix increase the dispersive error. Dispersion relations in pFEM and isogeometric FE are investigated in THOMPSON AND PINSKY (1995) and AURICCHIO ET AL. (2012); KOLMAN ET AL. (2012).

### 2.5.3 Assessment of dynamic behavior of semi-discretized equations using Fourier analysis

The overall accuracy of inertia and stiffness discretization can be evaluated using a FOURIER analysis of an infinite mesh of equal-sized elements, see Figure 2.19. The results of such an analysis provides an estimate of the error in the eigenfrequencies needed for free vibration problems and it gives an exact dispersion relation relevant to wave propagation problems.

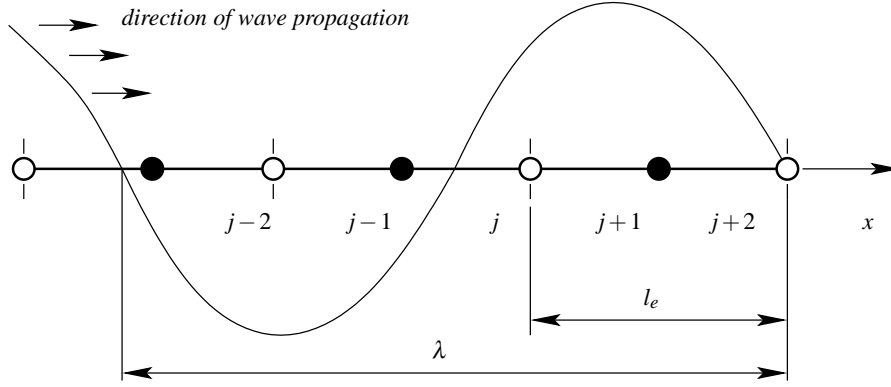


**Figure 2.19:** An infinite mesh of quadratic elements and a harmonic wave.

The wave propagation in the mesh is governed by semi-discrete equations  $\mathbf{M}\ddot{\mathbf{U}} + \mathbf{K}\mathbf{U} = \mathbf{0}$ , which has an infinite number of unknowns  $\mathbf{u} = [\dots, u_{j-2}, u_{j-1}, u_j, u_{j+1}, u_{j+2}, \dots]$ . This system has an infinite number of solutions. These solutions are travelling harmonic waves (FELIPPA 2001, 2010) of wavenumber  $k = 2\pi/\lambda$ , wavelength  $\lambda$ , phase velocity  $c$  and circular frequency  $\omega = 2\pi c/\lambda$ . The displacement vector as a function of time is

$$\mathbf{U}(t) = \tilde{\mathbf{U}}e^{i\omega t} \quad (2.117)$$

with  $\tilde{\mathbf{U}}$  standing for the complex-valued vector of nodal phases and amplitudes and  $i$  being  $\sqrt{-1}$ . Substitution of the latter into the equation of motion results in a system of linear algebraic equations

$$(-\omega^2\mathbf{M} + \mathbf{K})\tilde{\mathbf{U}} = \mathbf{0}. \quad (2.118)$$

As the elements in the infinite mesh have equal size and the coefficients in Equations (2.118) are periodically repeated, the general solution of it can be obtained for a representative sample (patch) with a finite number of degrees of freedom. Consider a typical patch of three elements as

$$(-\omega^2\mathbf{M}_{rep} + \mathbf{K}_{rep})\tilde{\mathbf{U}}_{rep} = \mathbf{0}. \quad (2.119)$$

The determinant of this system provides a characteristic equation, from which the dispersion relation  $k(\omega)$  can be found. Note, that multiple solutions, or branches, of the characteristic equation correspond to physically different waves and/or numerical artifacts. For the elements discussed here we distinguish physical longitudinal, shear and bending waves. The meshes of the finite elements can have optical and acoustic branches (FELIPPA (2001); HUGHES ET AL. (1976)). For convenience, the dispersion relations are presented in dimensionless quantities with wavenumber  $\kappa = k/l_e$  and frequency  $\Omega = \omega l_e/c$ .

### 2.5.4 Participation factor for classification of load cases

Consider an undamped system of  $n$ -degrees under an arbitrary force

$$\begin{aligned}\mathbf{M}\ddot{\mathbf{U}} + \mathbf{K}\mathbf{U} &= \mathbf{F}^{\text{ext}}(t), \\ \mathbf{U}(t=0) &= \mathbf{U}_0, \\ \dot{\mathbf{U}}(t=0) &= \mathbf{V}_0.\end{aligned}\tag{2.120}$$

The system (2.120) gives rise to a generalized eigenvalue problem

$$(\mathbf{K} - \omega^2\mathbf{M})\boldsymbol{\phi} = \mathbf{0}.\tag{2.121}$$

The eigenvalues and eigenvectors for large sparse systems can be extracted with LANCZOS, KRYLOV subspace or QR methods (SAAD 1992).

Let us denote eigenvalues for the system (2.121) sorted in ascending order as  $\omega_i$  and corresponding eigenvectors  $\boldsymbol{\phi}_i$ . Herein, we use only eigenvectors orthonormalized with respect to mass matrix, i.e.  $\boldsymbol{\phi}_i^T \mathbf{M} \boldsymbol{\phi}_j = \delta_{ij}$  with  $\delta_{ij}$  being Kronecker delta. The mode participation factors  $\Gamma_i$  for the given load  $\mathbf{F}^{\text{ext}}$  are defined as

$$\Gamma_i = \boldsymbol{\phi}_i^T \mathbf{F}^{\text{ext}} / \boldsymbol{\phi}_i^T \mathbf{K} \boldsymbol{\phi}_i.\tag{2.122}$$

### 2.5.5 Harmonic analysis

The driven harmonic oscillation for a linear system of  $n$ -degrees with viscous damping is described by

$$\mathbf{M}\ddot{\mathbf{U}} + \mathbf{C}\dot{\mathbf{U}} + \mathbf{K}\mathbf{U} = \mathbf{F}^{\text{ext}}(t),\tag{2.123}$$

with  $\mathbf{C}$  being the damping matrix. The RAYLEIGH model of damping, also called proportional damping, assumes matrix  $\mathbf{C}$  in the form of

$$\mathbf{C} = a_0\mathbf{M} + a_1\mathbf{K},\tag{2.124}$$

where  $a_0$  and  $a_1$  are mass and stiffness proportional damping coefficients. For harmonic excitation the external force can be presented as

$$\mathbf{F}^{\text{ext}}(t) = \tilde{\mathbf{F}}e^{i\omega t}\tag{2.125}$$

where  $\omega$  is the angular frequency of the excitation and  $\tilde{\mathbf{F}}$  is the global vector of forces that includes information about phases and amplitudes. Substitution of the time-harmonic ansatz

$\mathbf{U} = \tilde{\mathbf{U}}e^{i\omega t}$  leads to an equation with respect to steady amplitudes  $\tilde{\mathbf{U}}$

$$(-\omega^2\mathbf{M} + i\omega\mathbf{C} + \mathbf{K})\tilde{\mathbf{U}} = \tilde{\mathbf{F}}. \quad (2.126)$$

Solution of the latter equation for an identity matrix in right hand side at results in frequency response function

$$\mathbf{H}(\omega) = (-\omega^2\mathbf{M} + i\omega\mathbf{C} + \mathbf{K})^{-1}. \quad (2.127)$$

This means, that the amplitude of response in the  $i^{\text{th}}$  DOF caused by a harmonic force with unit amplitude at the  $j^{\text{th}}$  DOF is component  $H_{ij}(\omega)$ . Generally, frequency response function  $\mathbf{H}$  is a rational complex function of  $\omega$ , for details see THOMSON (1993).

### Frequency response assurance criterion

Any two frequency response functions that represent the same input-output relationship (obtained experimentally or numerically) can be compared via a technique known as Frequency Response Assurance Criterion (FRAC), see HEYLEN AND AVITABILE (1998) and ALLEMANG (2003). FRAC is computed for two response functions  $H_{1,ij}(\omega)$  and  $H_{2,ij}(\omega)$  for a given set of sampling frequencies  $[\omega_s]_{s=1}^{sampler}$  with

$$\text{FRAC}_{ij} = \frac{|\sum_{k=1}^{sampler} H_{1,ij}^*(\omega_k)H_{2,ij}(\omega_k)|^2}{\sum_{k=1}^{N_s} H_{1,ij}^*(\omega_k)H_{1,ij}(\omega_k) \sum_{k=1}^{N_s} H_{2,ij}^*(\omega_k)H_{2,ij}(\omega_k)}, \quad (2.128)$$

with *sampler* being number of sampling points and the super-script \* being a complex conjugate. FRAC is one for two linearly dependent response functions. Closeness to one assures similarity in response for a given sampling range, but it does not guaranties the amplitude of response is equal.

### Modal assurance criterion

According to ALLEMANG (2003), a Modal Assurance Criterion (MAC) can be defined as degree of correlation between one modal vector  $\phi_i^1$  and another reference modal vector  $\phi_j^2$  as follows

$$\text{MAC}_{ij} = \frac{\phi_i^1 \cdot \phi_j^2}{|\phi_i^1| |\phi_j^2|}. \quad (2.129)$$

Values of MAC close to one indicate similarity of the modes. Here, as a measure of the distortion due to selective mass scaling, an angle between the original mode  $\phi_i$  and the mode of the scaled system  $\phi_i^\circ$  can be introduced as

$$\varphi_i = \arccos \left( \frac{\phi_i \cdot \phi_i^\circ}{|\phi_i| |\phi_i^\circ|} \right). \quad (2.130)$$

---

## Variational principles of elasto-dynamics

The benefits of singular and selectively scaled mass matrices are presented in Sections 2.3.4 and 2.3.5. Here, a *unified variational approach* for both singular and selectively scaled mass matrices is proposed. It is based on a new penalized HAMILTON's principle that uses displacement, velocity and momentum as variables. Relations between the variables are weakly imposed via a penalty method. This results in a template variational principle<sup>1</sup> of elasto-dynamics depending on the free penalty parameters. The canonical one-, two- and three-field principles are recovered as special instances of the template. In addition, the three-field canonical principle is reformulated by introduction of an incompatible velocity field, which provides another useful variational form.

An in-depth overview on non-parametric variational principles of rigid body dynamics and elasto-dynamics can be found in LANZCOS (1970) and WASHIZU (1975, Appendix I), respectively. An overview on the application of variational principles of elasto-dynamics in FE discretization is given in GERADIN (1980). Among the presented principles, the most important principle for FE applications is HUGHES's principle<sup>2</sup> depending on two independent fields of displacement and velocity (HUGHES ET AL. 1976). This overview also includes dual/reciprocal variational principles of elasto-dynamics, e.g. REISSNER's, TOUPIN's and PIAN's principles. A distinguishing feature of TOUPIN's principle is the introduction of an *impulse field*<sup>3</sup>, that is defined as integral of the stress tensor in time. Other versions of re-

---

<sup>1</sup>In this thesis "parametric", "template" and "penalized" HAMILTON's principle are used as synonyms. The name penalized is preferred because the penalty approach is used here in the derivation and the idea of the derivation is the synthesis of inertial penalties given in ASKES ET AL. (2011) and the rigorous variational basis of template variational principles given in FELIPPA (1994).

<sup>2</sup>It is also called here HELLINGER-REISSNER type II or two-field canonical principle.

<sup>3</sup> $\mathbf{h} := \mathbf{h}_0 + \int_0^t \boldsymbol{\sigma} d\tau$ , impulse and momentum field are related with  $\mathbf{p} = \text{div } \mathbf{h}$  for a zero bodyload  $\hat{\mathbf{b}}$ .

reciprocal forms of HAMILTON's principle are given in REISSNER (1948) and ELIAS (1973). The GURTIN's family of variational principles based on convolutions is thoroughly investigated in GURTIN (1964). For re-parametrization of the three-field functional of elasticity (VEUBEKE-HU-WASHIZU) with incompatible strains, see SIMO AND RIFAI (1990).

Parametric variational principles originate from Beijing school of mechanics. Two one-parametric families of *generalized variational principles* for linear elasto-statics are proposed in WEI-ZANG (1983). In this paper, a so-called method of high-order LAGRANGE multipliers is used to impose the constitutive relation. Based on the same approach, parametric extensions of GURTIN's convolution principle and HAMILTON's principle for elasto-dynamics are proposed in SHIKUI (1992a) and SHIKUI (1992b), respectively. Generalized variational principles with *several arbitrary parameters* are proposed in YU-QIU (1987) and developed further in HUANDING AND DONGBU (1990). They are based on adding quadratic integrals of constitutive, kinematic and equilibrium equations and displacement and force boundary conditions<sup>4</sup>. Another method for establishing *generalized variational principles* is proposed in DAH-WEI (1985). It uses a so-called semi-inverse method, where the form of the functional is not assumed beforehand, but recovered in the process of derivation using an IBVP<sup>5</sup>. This method allows also the derivation of variational principles with free parameters (HE 2000). In this case, the free parameters can be interpreted as integration constants.

Further development and applications of parametric variational principles are connected to template variational principles. For the definition of template variational principles for POISSON's equation, classical, incompressible and micro-polar elasticity, see FELIPPA (1994). High performance plate and shell elements based on these ideas are presented in FELIPPA AND MILITELLO (1989). For further references on the topic, see FELIPPA (2000).

The usage of parametric and generalized variational principles are not limited to elasto-dynamics. Parametric variational principles for elasto-plasticity using complementary and potential energy are presented in ZHONG AND ZHANG (1988). Generalized variational principles for micromorphic thermo-elasticity and micromorphic magneto-electro-elasto-dynamics are given in HE (2005) and ZHENG ET AL. (2011), respectively.

The short overview given above, may be an illustration of the fact that *the inverse problem of variational calculus*<sup>6</sup> has neither a unique solution nor a general method of solution. An extensive study on the subject can be found in FINLAYSON (1972). The high-order LAGRANGE multipliers, semi-inverse and template methods may be recommended as the most powerful techniques.

---

<sup>4</sup>A similar approach is used here.

<sup>5</sup>See Appendix B for an example of derivation.

<sup>6</sup>Given a system of differential equation, find the Lagrangians that have that system as EULER-LAGRANGE equations. These set of Lagrangians embody the variational form of the problem. Usually the PVP results in linear spaces of Lagrangians.

### 3.1 Penalized Hamilton's principle

Recall the strong form of the IBVP for linearized elasto-dynamics from Subsection 2.2.5 with

$$\left\{ \begin{array}{ll} \rho \ddot{\mathbf{u}} = \mathbf{L}^* \boldsymbol{\sigma}_{\text{lin}}(\mathbf{u}) + \hat{\mathbf{b}} & \text{in } \mathcal{I} \times \mathcal{B}_0 \\ \boldsymbol{\sigma}_{\text{lin}} = \mathbf{D}\boldsymbol{\varepsilon} & \text{in } \mathcal{I} \times \mathcal{B}_0 \\ \boldsymbol{\varepsilon} = \mathbf{L}\mathbf{u} & \text{in } \mathcal{I} \times \mathcal{B}_0 \\ \mathbf{u} = \mathbf{0} & \text{in } \mathcal{I} \times \partial\mathcal{B}_u \\ \boldsymbol{\sigma}_{\text{lin}}\mathbf{n} = \hat{\mathbf{t}} & \text{in } \mathcal{I} \times \partial\mathcal{B}_{t,0} \\ \mathbf{u}(0, \cdot) = \mathbf{u}_0 & \text{in } \mathcal{B}_0 \\ \dot{\mathbf{u}}(0, \cdot) = \mathbf{v}_0 & \text{in } \mathcal{B}_0. \end{array} \right. \quad (3.1)$$

Now, a problem is posed to setup a variational framework which allows a parametric family of consistent mass matrices and at the same time is equivalent to the non-parametric IBVP given in equation (3.1). The following considerations are used for the derivation of the new principle. In order to get maximum flexibility, a multi-field approach with independent variables for displacement, velocity and momentum is used. The fields are linked in a weak sense using the penalty method. The penalty factors then naturally define the free parameters. Finally, only symmetric terms for inertia should enter the principle, which guarantees symmetric mass matrices by design.

Let us introduce notations for a scalar product in the domain, the bilinear forms of potential and kinetic energy and the linear form for external work, respectively, with

$$(\mathbf{w}, \mathbf{z}) = \int_{\mathcal{B}_0} \mathbf{w} \cdot \mathbf{z} dV, \quad \mathbf{w}, \mathbf{z} \in [L^2(\mathcal{B}_0)]^{\dim}, \quad (3.2a)$$

$$\Pi^{\text{int}}(\mathbf{u}) = \frac{1}{2} \mathbf{a}(\mathbf{u}, \mathbf{u}) = \frac{1}{2} \int_{\mathcal{B}_0} \boldsymbol{\varepsilon}(\mathbf{u}) \cdot \mathbf{D}\boldsymbol{\varepsilon}(\mathbf{u}) dV, \quad \mathbf{u} \in [H^1(\mathcal{B}_0)]^{\dim}, \quad (3.2b)$$

$$T(\dot{\mathbf{u}}) = \frac{1}{2} \mathbf{m}(\dot{\mathbf{u}}, \dot{\mathbf{u}}) = \frac{1}{2} (\rho \dot{\mathbf{u}}, \dot{\mathbf{u}}) = \frac{1}{2} \int_{\mathcal{B}_0} \rho \dot{\mathbf{u}} \cdot \dot{\mathbf{u}} dV, \quad \dot{\mathbf{u}} \in [L^2(\mathcal{B}_0)]^{\dim}, \quad (3.2c)$$

$$\Pi^{\text{ext}}(\mathbf{u}) = \mathbf{f}(\mathbf{u}) = \int_{\mathcal{B}_0} \hat{\mathbf{b}} \cdot \mathbf{u} d\mathcal{B} + \int_{\partial\mathcal{B}_{t,0}} \hat{\mathbf{t}} \cdot \mathbf{u} d\partial\mathcal{B}. \quad (3.2d)$$

Starting point for the derivation of the alternative formulation is HAMILTON's principle stating that among all admissible displacements that satisfy the prescribed geometrical boundary conditions and the prescribed conditions at the time limits, the actual solution makes the following functional stationary

$$H(\mathbf{u}) = \int_{\mathcal{I}} \left( T - \Pi^{\text{int}} + \Pi^{\text{ext}} \right) dt \rightarrow \text{stat}, \quad (3.3a)$$

$$H(\mathbf{u}) = \int_{\mathcal{I}} \left( \frac{1}{2} (\rho \dot{\mathbf{u}}, \dot{\mathbf{u}}) - \frac{1}{2} \mathbf{a}(\mathbf{u}, \mathbf{u}) + \mathbf{f}(\mathbf{u}) \right) dt \rightarrow \text{stat}. \quad (3.3b)$$

HAMILTON's principle imposes relations between velocity, momentum and displacements in strong form with

$$\mathbf{v} = \dot{\mathbf{u}}, \quad \mathbf{p} = \rho \mathbf{v}, \quad \mathbf{p} = \rho \dot{\mathbf{u}}. \quad (3.4)$$

These conditions enter equation (3.3b) using the penalty method. To construct the penalty term for the kinematic equation  $\mathbf{v} - \dot{\mathbf{u}} = 0$ , the difference  $\mathbf{v} - \dot{\mathbf{u}}$  is squared and weighted with the density  $\rho$  and a dimensionless penalty factor  $\frac{1}{2}C_3$ . In this way, the physical dimension of the term is energy. Finally, it is integrated over the domain, resulting in

$$\int_{\mathcal{B}_0} \frac{1}{2} C_3 \rho (\mathbf{v} - \dot{\mathbf{u}})^2 dV = \frac{1}{2} C_3 (\rho(\dot{\mathbf{u}} - \mathbf{v}), \dot{\mathbf{u}} - \mathbf{v}) = 0. \quad (3.5)$$

Analogous considerations for the other two relations of equation (3.4) lead to two terms with penalty factors  $C_1$  and  $C_2$ . Summing up all terms provides a new expression for the kinetic energy

$$T^\circ = \frac{1}{2} (\rho \dot{\mathbf{u}}, \dot{\mathbf{u}}) + \frac{C_1}{2} \left( \rho \dot{\mathbf{u}} - \mathbf{p}, \dot{\mathbf{u}} - \frac{\mathbf{p}}{\rho} \right) + \frac{C_2}{2} \left( \rho \mathbf{v} - \mathbf{p}, \mathbf{v} - \frac{\mathbf{p}}{\rho} \right) + \frac{C_3}{2} (\rho(\dot{\mathbf{u}} - \mathbf{v}), \dot{\mathbf{u}} - \mathbf{v}). \quad (3.6)$$

The penalized Hamilton's principle uses  $T^\circ$  as

$$H^\circ(\mathbf{u}, \mathbf{v}, \mathbf{p}, C_1, C_2, C_3) = \int_{\mathcal{I}} \left( T^\circ - \Pi^{\text{int}} + \Pi^{\text{ext}} \right) dt \rightarrow \text{stat}. \quad (3.7)$$

Here, dependency of the penalized Hamiltonian on the free parameters  $C_{1,2,3}$  is explicitly stated. For simplicity, it is dropped from the list of arguments below.

In the following, the weak form and EULER-LAGRANGE equations for functional (3.7) are derived. The first variation of equation (3.7) gives

$$\begin{aligned} \delta H^\circ(\mathbf{u}, \mathbf{v}, \mathbf{p}) &= \int_{\mathcal{I}} \left( \delta \mathbf{p}, (C_1 + C_2) \frac{\mathbf{p}}{\rho} - C_1 \dot{\mathbf{u}} - C_2 \mathbf{v} \right) dt \\ &+ \int_{\mathcal{I}} (\delta \mathbf{v}, (C_2 + C_3) \rho \mathbf{v} - C_3 \rho \dot{\mathbf{u}} - C_2 \mathbf{p}) dt \\ &+ \int_{\mathcal{I}} [(\delta \dot{\mathbf{u}}, (1 + C_1 + C_3) \rho \dot{\mathbf{u}} - C_3 \rho \mathbf{v} - C_1 \mathbf{p}) - \delta \Pi] dt. \end{aligned} \quad (3.8)$$

Integrating the term  $(\delta \dot{\mathbf{u}}, (1 + C_1 + C_3) \rho \dot{\mathbf{u}} - C_3 \rho \mathbf{v} - C_1 \mathbf{p})$  by parts in time yields

$$- \int_{\mathcal{I}} \left( \delta \mathbf{u}, \frac{d}{dt} \{ (1 + C_1 + C_3) \rho \dot{\mathbf{u}} - C_3 \rho \mathbf{v} - C_1 \mathbf{p} \} \right) dt. \quad (3.9)$$

Substitution of equation (3.9) into equation (3.8) gives a weak formulation, proposed herein. The EULER-LAGRANGE equations of the weak form (3.8) compose a system of equations

$$\begin{cases} \frac{d}{dt} \{(1 + C_1 + C_3) \rho \dot{\mathbf{u}} - C_3 \rho \mathbf{v} - C_1 \mathbf{p}\} = \mathbf{L}^* \boldsymbol{\sigma}_{\text{lin}} + \hat{\mathbf{b}} & \text{in } \mathcal{I} \times \mathcal{B} \\ \boldsymbol{\sigma}_{\text{lin}} \mathbf{n} = \hat{\mathbf{t}} & \text{in } \mathcal{I} \times \partial \mathcal{B}_t \\ (C_1 + C_2) \mathbf{p} - C_2 \rho \mathbf{v} = C_1 \rho \dot{\mathbf{u}} & \text{in } \mathcal{I} \times \mathcal{B} \\ -C_2 \mathbf{p} + (C_2 + C_3) \rho \mathbf{v} = C_3 \rho \dot{\mathbf{u}} & \text{in } \mathcal{I} \times \mathcal{B}. \end{cases} \quad (3.10)$$

Consider the two last equations in (3.10). They are a system of two linear equations with respect to  $\mathbf{p}$  and  $\mathbf{v}$ . If the determinant of the coefficient matrix is non-zero, i.e.  $C_1 C_2 + C_2 C_3 + C_1 C_3 \neq 0$ , then we can solve for  $\mathbf{p}$  and  $\mathbf{v}$ , leading to

$$\mathbf{v} = \dot{\mathbf{u}}, \quad \mathbf{p} = \rho \dot{\mathbf{u}}. \quad (3.11)$$

Thus, the subsidiary conditions (3.4) are recovered as EULER-LAGRANGE equations. Substitution of the latter in the first equation of (3.10) gives the equation of motion in the form (3.1<sub>1</sub>). This proves the equivalence of the penalized HAMILTON's principle to the IBVP (3.1). Hence, the free parameters in the functional (3.7) do neither change the extreme value of the functional nor the solution of the variational problem (FELIPPA 1994). At an extremal, where the EULER-LAGRANGE equations (3.11) are satisfied, the fields  $\dot{\mathbf{u}}$ ,  $\mathbf{v}$  and  $\mathbf{p}/\rho$  coalesce. Actually, the free parameters can be interpreted as weights on the field equation in the weak form, see equation (3.10). Therefore, these parameters are also called high-order LAGRANGE multipliers. Generally, these parameters can be second order tensors for vector fields, like velocity  $\mathbf{v}$ , or fourth order tensor for second order tensors, like  $\boldsymbol{\varepsilon}$ , for details see WEI-ZANG (1983) and LAMICHHANE ET AL. (2013). According to this point of view, the penalty term can be interpreted as

$$\frac{1}{2} C_1 \rho \left( \dot{\mathbf{u}} - \frac{\mathbf{p}}{\rho} \right)^2 = \frac{1}{2} \left( \dot{\mathbf{u}} - \frac{\mathbf{p}}{\rho} \right) \cdot \rho C_1 \mathbf{I} \left( \dot{\mathbf{u}} - \frac{\mathbf{p}}{\rho} \right) = \frac{1}{2} \left( \dot{\mathbf{u}} - \frac{\mathbf{p}}{\rho} \right) \cdot \mathbf{Q}_1 \left( \dot{\mathbf{u}} - \frac{\mathbf{p}}{\rho} \right), \quad (3.12a)$$

$$\frac{1}{2} C_2 \rho \left( \mathbf{v} - \frac{\mathbf{p}}{\rho} \right)^2 = \frac{1}{2} \left( \mathbf{v} - \frac{\mathbf{p}}{\rho} \right) \cdot \rho C_2 \mathbf{I} \left( \mathbf{v} - \frac{\mathbf{p}}{\rho} \right) = \frac{1}{2} \left( \mathbf{v} - \frac{\mathbf{p}}{\rho} \right) \cdot \mathbf{Q}_2 \left( \mathbf{v} - \frac{\mathbf{p}}{\rho} \right), \quad (3.12b)$$

$$\frac{1}{2} C_3 \rho (\mathbf{v} - \dot{\mathbf{u}})^2 = \frac{1}{2} (\mathbf{v} - \dot{\mathbf{u}}) \cdot \rho C_3 \mathbf{I} (\mathbf{v} - \dot{\mathbf{u}}) = \frac{1}{2} (\mathbf{v} - \dot{\mathbf{u}}) \cdot \mathbf{Q}_3 (\mathbf{v} - \dot{\mathbf{u}}), \quad (3.12c)$$

where  $\mathbf{Q}_{1,2,3} = C_{1,2,3} \mathbf{I}$  are second order tensors for high-order LAGRANGE multipliers. A possible usage of anisotropic matrices for the multipliers  $\mathbf{Q}_{1,2,3}$  is outlined in the outlook in Section 8.2.

Note, that the form  $T^\circ$  is quadratic and symmetric with respect to the triple  $[\dot{\mathbf{u}}, \mathbf{v}, \mathbf{p}]$

$$T^\circ = \frac{1}{2} \int_{\mathcal{B}} \begin{bmatrix} \rho \dot{\mathbf{u}} \\ \rho \mathbf{v} \\ \mathbf{p} \end{bmatrix}^T \begin{bmatrix} (1 + C_1 + C_3) \mathbf{I} & -C_3 \mathbf{I} & -C_1 \mathbf{I} \\ -C_3 \mathbf{I} & (C_2 + C_3) \mathbf{I} & -C_2 \mathbf{I} \\ -C_1 \mathbf{I} & -C_2 \mathbf{I} & (C_1 + C_2) \mathbf{I} \end{bmatrix} \begin{bmatrix} \dot{\mathbf{u}} \\ \mathbf{v} \\ \mathbf{p} \end{bmatrix} d\mathcal{B}. \quad (3.13)$$

The vector  $[\dot{\mathbf{u}}, \mathbf{v}, \mathbf{p}]$  is called *the generalized field vector* in the literature and the matrix in the quadratic form is called as *functional generating matrix*.

The positive definiteness of the form is verified by SYLVESTER's criterion. If the leading principal minors of the functional generating matrix of the quadratic form are all positive, then the form is positive definite. These conditions read as follows

$$\begin{cases} C_1 + C_3 > -1 \\ C_2 + C_3 > 0 \\ C_1 C_2 + C_2 C_3 + C_1 C_3 > 0. \end{cases} \quad (3.14)$$

Thus, the form fulfills the requirement for the new variational formulation given in the problem statement.

The formulation (3.8) can be interpreted as a parametrized (template) variational principle according to FELIPPA (1994). The formulation contains all canonical variational principles of linear elasto-dynamics as particular cases. The standard HAMILTON's principle is obtained for  $C_1 = C_2 = C_3 = 0$ . The modified HAMILTON's principle is recovered for  $C_1 = -C_2 = -1$  and  $C_3 = 0$ . The HELLINGER-REISSNER principle with the variables  $[\mathbf{u}, \mathbf{p}]$  is recovered for  $C_1 = -1$  and  $C_2 = C_3 = 0$ . Setting  $C_1 = -1$ ,  $C_2 = 1/2$  and  $C_3 = 0$  yields LIANG-FU principle (GUO-PING AND ZI-CHI 1982). These examples imply completeness of the parametrization. Moreover, the form  $T^\circ$  satisfies the consistency conditions for a template stated in FELIPPA (1994). The row sums of the functional generating matrix are one for the primary variable  $\mathbf{u}$  and zero for the dual variables  $\mathbf{v}$  and  $\mathbf{p}$ .

Note, that a straightforward extension of the derived parametrized principle to a finite deformation regime is possible, see TKACHUK AND BISCHOFF (2013a). In case of non-conservative systems, the parametric version of the principle of virtual work must be used.

## 3.2 Canonical two-field principles

The penalized HAMILTON's principle (3.7) can be reduced to canonical HELLINGER-REISSNER principles of two types. Type I and II use as variables  $[\mathbf{u}, \mathbf{p}]$  and  $[\mathbf{u}, \mathbf{v}]$ , respectively. Type I is

obtained for  $C_1 = -1$  and  $C_2 = C_3 = 0$ , leading to a weak form

$$\delta H(\mathbf{u}, \mathbf{p}) = \int_{\mathcal{I}} ((\delta \mathbf{p}, \mathbf{p}/\rho - \dot{\mathbf{u}}) + (\dot{\mathbf{p}}, \delta \mathbf{u}) - \mathbf{a}(\mathbf{u}, \delta \mathbf{u}) + \mathbf{f}(\delta \mathbf{u})) dt = 0. \quad (3.15)$$

Type II is obtained for  $C_1 = C_2 = 0$  and  $C_3 = -1$ , leading to a weak form

$$\delta H(\mathbf{u}, \mathbf{v}) = \int_{\mathcal{I}} (m(\delta \mathbf{v}, \mathbf{v} - \dot{\mathbf{u}}) + m(\dot{\mathbf{v}}, \delta \mathbf{u}) - \mathbf{a}(\mathbf{u}, \delta \mathbf{u}) + \mathbf{f}(\delta \mathbf{u})) dt = 0. \quad (3.16)$$

Both weak forms stated above can be used for discretization, see for examples HUGHES ET AL. (1976) and GERADIN (1980). More detailed theory on these variational principles is given in WASHIZU (1975, Appendix I).

### 3.3 Canonical three-field principle

The canonical three-field principle is referred to modified HAMILTON's principle in the literature. It is obtained from the penalized principle (3.7) for  $C_1 = -C_2 = -1$  and  $C_3 = 0$  resulting in the following variational principle

$$H(\mathbf{u}, \mathbf{v}, \mathbf{p}) = \int_{\mathcal{I}} \left( \frac{1}{2} m(\mathbf{v}, \mathbf{v}) - (\mathbf{p}, \mathbf{v} - \dot{\mathbf{u}}) - \frac{1}{2} \mathbf{a}(\mathbf{u}, \mathbf{u}) + \mathbf{f}(\mathbf{u}) \right) dt \rightarrow \text{stat.} \quad (3.17)$$

This principle will later be used for the derivation of singular mass matrices. Note, that the quadratic template for the kinetic energy  $T^*$  reduces to

$$T^* = \frac{1}{2} \int_{\mathcal{B}} \begin{bmatrix} \rho \dot{\mathbf{u}} \\ \rho \mathbf{v} \\ \mathbf{p} \end{bmatrix}^T \begin{bmatrix} \mathbf{0} & \mathbf{0} & \mathbf{I} \\ \mathbf{0} & \mathbf{I} & -\mathbf{I} \\ \mathbf{I} & -\mathbf{I} & \mathbf{0} \end{bmatrix} \begin{bmatrix} \dot{\mathbf{u}} \\ \mathbf{v} \\ \frac{\mathbf{p}}{\rho} \end{bmatrix} d\mathcal{B}. \quad (3.18)$$

The template matrix has two zero blocks on its diagonal and it is not positive definite. Hence, special considerations are necessary for stable discretization. These details are presented in Section 4.3.

### 3.4 A principle using an incompatible velocity field

Starting point for this principle is the canonical three-field principle. Re-parametrization of the velocity field  $\mathbf{v}$  is done according to the original idea of EAS elements for elasticity (WILSON ET AL. 1973; SIMO AND RIFAI 1990; ROMERO AND BISCHOFF 2007). There, the kinematic variable  $\varepsilon$  is split into a part  $\mathbf{L}\mathbf{u}$ , which is compatible with the displacement  $\mathbf{u}$ , and an incom-

patible part  $\tilde{\varepsilon} = \varepsilon - \mathbf{L}\mathbf{u}$ . Here, the velocity  $\mathbf{v}$  is split in a part  $\dot{\mathbf{u}}$ , which is compatible with the displacement  $\mathbf{u}$  and an incompatible part  $\tilde{\mathbf{v}}$ , leading to the following expression

$$\mathbf{v} = \dot{\mathbf{u}} + \tilde{\mathbf{v}}. \quad (3.19)$$

Substitution of the expression (3.19) in the equation (3.3b) yields the re-parametrized modified HAMILTON's principle

$$\tilde{H}(\mathbf{u}, \tilde{\mathbf{v}}, \mathbf{p}) = \int_{\mathcal{I}} \left( \frac{1}{2} m(\dot{\mathbf{u}} + \tilde{\mathbf{v}}, \dot{\mathbf{u}} + \tilde{\mathbf{v}}) - (\mathbf{p}, \tilde{\mathbf{v}}) - \frac{1}{2} a(\mathbf{u}, \mathbf{u}) + f(\mathbf{u}) \right) dt \rightarrow \text{stat}. \quad (3.20)$$

The re-parametrization procedure can be viewed as a linear transformation of the independent variables from  $[\mathbf{u}, \mathbf{v}, \mathbf{p}]$  to  $[\mathbf{u}, \tilde{\mathbf{v}}, \mathbf{p}]$ . The quadratic form for the kinetic energy modifies accordingly with the transformation. Thus, the quadratic form  $\tilde{T}^*$  reads

$$\tilde{T}^* = \frac{1}{2} \int_{\mathcal{B}} \begin{bmatrix} \rho \dot{\mathbf{u}} \\ \rho \tilde{\mathbf{v}} \\ \mathbf{p} \end{bmatrix}^T \begin{bmatrix} \mathbf{I} & \mathbf{I} & \mathbf{0} \\ \mathbf{I} & \mathbf{I} & -\mathbf{I} \\ \mathbf{0} & -\mathbf{I} & \mathbf{0} \end{bmatrix} \begin{bmatrix} \dot{\mathbf{u}} \\ \tilde{\mathbf{v}} \\ \frac{\mathbf{p}}{\rho} \end{bmatrix} d\mathcal{B}. \quad (3.21)$$

If the orthogonality  $(\mathbf{p}, \tilde{\mathbf{v}})$  holds, then only two variables  $[\mathbf{u}, \tilde{\mathbf{v}}]$  are present in the principle and it reduces to

$$\tilde{H}(\mathbf{u}, \tilde{\mathbf{v}}) = \int_{\mathcal{I}} \left( \frac{1}{2} m(\dot{\mathbf{u}} + \tilde{\mathbf{v}}, \dot{\mathbf{u}} + \tilde{\mathbf{v}}) - \frac{1}{2} a(\mathbf{u}, \mathbf{u}) + f(\mathbf{u}) \right) dt \rightarrow \text{stat}. \quad (3.22)$$

Corresponding to this variational form, the template for kinetic energy further reduces to

$$\tilde{T}^* = \frac{1}{2} \int_{\mathcal{B}} \rho \begin{bmatrix} \dot{\mathbf{u}} \\ \tilde{\mathbf{v}} \end{bmatrix}^T \begin{bmatrix} \mathbf{I} & \mathbf{I} \\ \mathbf{I} & \mathbf{I} \end{bmatrix} \begin{bmatrix} \dot{\mathbf{u}} \\ \tilde{\mathbf{v}} \end{bmatrix} d\mathcal{B}. \quad (3.23)$$

This variational principle is very useful if the inertia of a few modes need to be removed. The latter formulation can also be used for the derivation of a one-parametric variational principle with incompatible velocity field. Blending the standard HAMILTON's principle with the form (3.22) with the coefficients  $(1 + C_1)$  and  $(-C_1)$  yields

$$\tilde{H}^\circ(\mathbf{u}, \tilde{\mathbf{v}}) = \int_{\mathcal{I}} \left( \frac{1 + C_1}{2} m(\dot{\mathbf{u}}, \dot{\mathbf{u}}) - \frac{C_1}{2} m(\dot{\mathbf{u}} + \tilde{\mathbf{v}}, \dot{\mathbf{u}} + \tilde{\mathbf{v}}) - \frac{1}{2} a(\mathbf{u}, \mathbf{u}) + f(\mathbf{u}) \right) dt \rightarrow \text{stat}, \quad (3.24)$$

with the kinetic energy template

$$\tilde{T}^* = \frac{1}{2} \int_{\mathcal{B}} \rho \begin{bmatrix} \dot{\mathbf{u}} \\ \tilde{\mathbf{v}} \end{bmatrix}^T \begin{bmatrix} \mathbf{I} & -C_1 \mathbf{I} \\ -C_1 \mathbf{I} & -C_1 \mathbf{I} \end{bmatrix} \begin{bmatrix} \dot{\mathbf{u}} \\ \tilde{\mathbf{v}} \end{bmatrix} d\mathcal{B}. \quad (3.25)$$

The latter formulation illustrates the flexibility of the methods of variational calculus. The methods applied for linear and non-linear static problems are easily applied to elasto-dynamics. From these variational forms families of mass matrices with desired properties can be derived.

### 3.5 Variational principles with contact conditions

There are many ways to include contact conditions in a weak form, see e.g. equation (2.60). Here, the contact conditions are included via adding an indicator function to any of the variational principles mentioned above. An example for such a derivation can be found in PANDOLFI ET AL. (2002). Here, more rigorous solution spaces are introduced. Vector-valued spaces are denoted by bold letters, e.g.,  $\mathbf{L}_2(\mathcal{B}) = [L_2(\mathcal{B})]^{dim}$ . The test space for the displacements is defined as

$$\mathcal{V} := \{ \mathbf{u} \in \mathbf{H}^1 : \mathbf{u} = \mathbf{0} \text{ in } \partial\mathcal{B}_u \}. \quad (3.26)$$

The dual spaces are denoted with a prime sign, e.g.  $\mathcal{V}'$ . A convex subset of  $\mathcal{V}$  that satisfies the kinematic contact constraints is denoted as  $\mathcal{K}$ . The definition of  $\mathcal{K}$  depends on the structural theory behind the contact problem. Usually, it is a set of inequalities that should be satisfied on the contact boundary or inside the domain. For truss and beam models discussed in Subsection 2.2.6, the admissible set reads

$$\mathcal{K} := \{ \mathbf{u} \in \mathcal{V} : \mathbf{u} \cdot \mathbf{n} \leq g_{\mathcal{B}} \text{ in } \mathcal{B} \text{ and } \mathbf{u} \cdot \boldsymbol{\tau} \leq g_{\partial\mathcal{B}_c} \text{ in } \partial\mathcal{B}_c \}. \quad (3.27)$$

The indicator function  $I_K(\mathbf{u})$  for the admissible space can be written as

$$\begin{aligned} I_{\mathcal{B}}(\mathbf{u}, \mathbf{x}) &= \begin{cases} \infty & \text{if } \mathbf{u} \cdot \mathbf{n} > g_{\mathcal{B}}, \mathbf{x} \in \mathcal{B} \\ 0 & \text{otherwise,} \end{cases} & I_{\partial\mathcal{B}_c}(\mathbf{u}, \mathbf{x}) &= \begin{cases} \infty & \text{if } \mathbf{u} \cdot \boldsymbol{\tau} > g_{\partial\mathcal{B}_c}, \mathbf{x} \in \partial\mathcal{B}_c \\ 0 & \text{otherwise,} \end{cases} \\ I_K(\mathbf{u}) &= \int_{\mathcal{B}} I_{\mathcal{B}}(\mathbf{u}, \mathbf{x}) d\mathcal{B} + I_{\partial\mathcal{B}_c}(\mathbf{u}, \mathbf{x})|_{\partial\mathcal{B}_c}, \end{aligned} \quad (3.28)$$

with  $I_{\mathcal{B}}(\mathbf{u}, \mathbf{x})$  and  $I_{\partial\mathcal{B}_c}(\mathbf{u}, \mathbf{x})$  being the indicator functions for the contact constraints inside the domain and the boundary, respectively. Let us consider here an extension to the contact problem of the three-field canonical principle given in equation (3.17). The extended variational formulation reads

$$H(\mathbf{u}, \mathbf{v}, \mathbf{p}) = \int_{\mathcal{I}} \left( \frac{1}{2} \mathbf{m}(\mathbf{v}, \mathbf{v}) - (\mathbf{p}, \mathbf{v} - \dot{\mathbf{u}}) - \frac{1}{2} \mathbf{a}(\mathbf{u}, \mathbf{u}) + \mathbf{f}(\mathbf{u}) + I_K(\mathbf{u}) \right) dt \rightarrow \text{stat}, \quad (3.29)$$

with  $\mathbf{u} \in L^2(\mathcal{I}, \mathcal{V})$ ,  $\mathbf{v} \in L^2(\mathcal{I}, \mathbf{L}_2)$ ,  $\mathbf{p} \in L^2(\mathcal{I}, \mathbf{L}_2)$ ,  $\dot{\mathbf{u}} \in L^2(\mathcal{I}, \mathbf{L}_2)$ . Variation of (3.29) gives

$$\delta H = \int_{\mathcal{I}} (m(\mathbf{v}, \delta \mathbf{v}) - (\delta \mathbf{p}, \mathbf{v} - \dot{\mathbf{u}}) - (\mathbf{p}, \delta \mathbf{v} - \delta \dot{\mathbf{u}}) - a(\mathbf{u}, \delta \mathbf{u}) + f(\delta \mathbf{u}) + \delta I_K(\mathbf{u})) dt. \quad (3.30)$$

If we additionally assume  $\dot{\mathbf{p}} \in L^2(\mathcal{I}, \mathcal{V}')$  and integrate by parts  $(\mathbf{p}, \delta \dot{\mathbf{u}})$ , we get

$$\delta H = \int_{\mathcal{I}} ((\delta \mathbf{p}, \dot{\mathbf{u}} - \mathbf{v}) - (\mathbf{p} - \rho \mathbf{v}, \delta \mathbf{v}) - (\dot{\mathbf{p}}, \delta \mathbf{u}) - a(\mathbf{u}, \delta \mathbf{u}) + f(\delta \mathbf{u}) + \delta I_K(\mathbf{u})) dt. \quad (3.31)$$

This formulation is the starting point for an alternative formulation for the elasto-dynamic contact method proposed herein. The EULER-LAGRANGE equations of the weak form (3.31) are a system of equations

$$\begin{cases} -\dot{\mathbf{p}} + \mathbf{L}^* \boldsymbol{\sigma}_{\text{in}}(\mathbf{u}) + \hat{\mathbf{b}} \in N_{\mathcal{B}}(\mathbf{u}) & \text{in } \mathcal{I} \times \mathcal{B}_0 \\ \boldsymbol{\sigma}_{\text{in}} - \hat{\mathbf{t}} \in N_{\Gamma}(\mathbf{u}) & \text{in } \mathcal{I} \times \partial \mathcal{B}_c \\ \dot{\mathbf{u}} = \mathbf{v} & \text{in } \mathcal{I} \times \mathcal{B}_0 \\ \mathbf{p} = \rho \mathbf{v} & \text{in } \mathcal{I} \times \mathcal{B}, \end{cases} \quad (3.32)$$

with  $N_{\mathcal{B}}(\mathbf{u})$  and  $N_{\Gamma}(\mathbf{u})$  being subdifferentials of the indicator functions  $I_{\mathcal{B}}(\mathbf{u}, \mathbf{x})$  and  $I_{\partial \mathcal{B}}(\mathbf{u}, \mathbf{x})$ , respectively, and  $\in$  denotes the inclusion. Thus, from the equation (3.32<sub>4</sub>) the field  $\mathbf{p}$  can be identified as a momentum field. Also using the properties of differential inclusion, it can be shown that equation (3.32) is equivalent to the IBVP given in equations (2.66<sub>1-3</sub>). The initial condition given in equations (2.66<sub>4-5</sub>) can be introduced in equation (3.30) by the correct boundary terms  $BT$  at the time limits  $t = 0$  and  $t = t_{\text{end}}$ , e.g. according to CANNAROZZI AND MANCUSO (1995),

$$\int_{\mathcal{I}} \delta \left( \frac{1}{2} m(\mathbf{v}, \mathbf{v}) - (\mathbf{p}, \mathbf{v} - \dot{\mathbf{u}}) - \frac{1}{2} a(\mathbf{u}, \mathbf{u}) + f(\mathbf{u}) + I_K(\mathbf{u}) \right) dt = BT,$$

$$BT = (\delta \mathbf{p}|_0, \mathbf{u}|_0 - \mathbf{u}_0) + (\delta \mathbf{u}|_0, \rho \mathbf{v}_0) - (\delta \mathbf{u}, \mathbf{p})|_{t_{\text{end}}}.$$

The first term in the expression for  $BT$  weakly imposes the displacement initial condition, while the second and third term are responsible for the velocity initial condition. However, addition of  $BT$  leads to a non-integrable differential in contrast to modified Hamilton's principle (3.30). Such treatment of the initial conditions is necessary for space-time finite element discretizations. Here, classical time integration rules are used and the initial conditions are merely interpolated at the nodes.

The correct boundary terms can be found also for the parametric variational principle given in equation (3.8). Such a formulation can be used as the starting point for a parametric family of space-time finite elements. However, this question is out of scope of this thesis.

### 3.6 Summary of variational methods for elasto-dynamics

This chapter is the core part of this thesis and its main scientific advance. The unified variational approach presented in this thesis enables an elegant derivation of useful variational formulations, which is the basis for the following description of different elasto-dynamic problems.

The chapter includes quite technical derivations of parametric and mixed principles for elasto-dynamics. The relations between the derived methods are presented in Figure 3.1. The variational principles with their independent variables and their free parameters are shown in rectangular boxes with grey filling. The arrows depict the derivation steps. The text in ellipses attached to the arrows denotes the methods used in the derivations<sup>7</sup>.

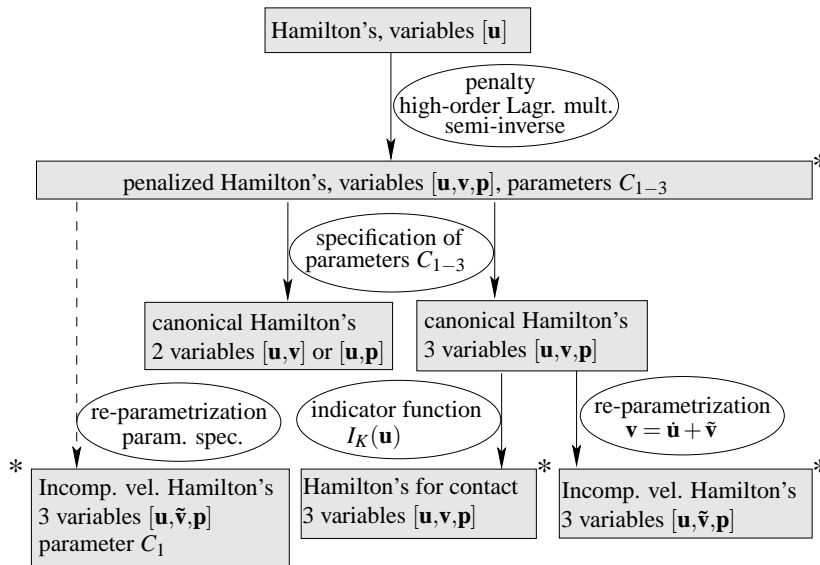


**Figure 3.1:** Relations between variational formulations of elasto-dynamics. The novel principles are marked with an asterisk \*.

The basis for all derivations is one-field HAMILTON's principle. The penalized HAMILTON's principle is derived using the penalty method for kinematic and material equations. Three canonical principles are recovered upon specification of the free parameters. Then, the contact constraints may be included in three-field HAMILTON's principle by adding an indicator function  $I_K(\mathbf{u})$ . Introduction of incompatible velocity allows to derive two further variational principles.

<sup>7</sup>For alternative derivation of the penalized HAMILTON's principle using the semi-inverse method, see Appendix B.



# 4

---

## Spatial discretization of inertial terms

In this chapter, a semi-discretization for the inertial terms is given based on the weak forms presented in Chapter 3. The most general expression for a three-parametric family of mass matrices is derived and analyzed. Three specializations of the three-parametric family relevant for selective mass scaling are given. Then, Hybrid-Singular Mass Matrices (HSMM) are derived with focus on dynamic contact problems. It is shown that nodal mass vanishes, if only a special orthogonality condition is fulfilled. Expressions for incompatible velocity mode mass matrices (EAS-like) conclude the chapter.

### 4.1 Three-parameteric template for mass matrix

In the previous section, a weak formulation for elasto-dynamics (3.8) was derived. This formulation has three independent variables  $[\mathbf{u}, \mathbf{v}, \mathbf{p}]$  and contains three scalar penalty parameters  $(C_1, C_2, C_3)$ . Spatial semi-discretization of the free variables can be written as

$$\mathbf{u}^h = \mathbf{N}\mathbf{U}, \quad \mathbf{v}^h = \mathbf{\Psi}\mathbf{V}, \quad \mathbf{p}^h = \mathbf{\chi}\mathbf{P}, \quad (4.1a)$$

$$\delta\mathbf{u}^h = \mathbf{N}\delta\mathbf{U}, \quad \delta\mathbf{v}^h = \mathbf{\Psi}\delta\mathbf{V}, \quad \delta\mathbf{p}^h = \mathbf{\chi}\delta\mathbf{P}. \quad (4.1b)$$

Here,  $\mathbf{N}$  contains shape functions for interpolation of  $n_d$  nodal displacements, given by the vector  $\mathbf{U}$ . The default physical dimension of the vector  $\mathbf{U}$  is length, or m. Matrices  $\mathbf{\Psi}$  and  $\mathbf{\chi}$  interpolate velocity and momentum from vectors of parameters  $\mathbf{V}$  and  $\mathbf{P}$ . The lengths of  $\mathbf{V}$  and  $\mathbf{P}$  are denoted as  $n_v$  and  $n_p$ . The physical dimensions of  $\mathbf{V}$  and  $\mathbf{P}$  are velocity, or m/s, and linear momentum, or kg·m/s, respectively. Note, that variational indices of variables  $\mathbf{v}$  and  $\mathbf{p}$  for spatial derivatives are zero. This means that inter-element continuity of  $\mathbf{v}^h$  and  $\mathbf{p}^h$  is not required for convergence. Therefore, parameters  $\mathbf{V}$  and  $\mathbf{P}$  are not necessarily nodal values

in contrast to the displacement vector  $\mathbf{U}$ . Later, this property is used for local elimination of these parameters. Herein, the shape functions for the variations are the same as for the variables (BUBNOV-GALERKIN type of discretization). This guarantees symmetry of the obtained mass matrices.

Substitution of the equation (4.1) in equation (3.8) with (3.9) yields a semi-discrete expression of penalized Hamiltonian

$$\begin{aligned} \delta H^{\circ,h}(\mathbf{U}, \mathbf{V}, \mathbf{P}) = & \int_{\mathcal{I}} \delta \mathbf{P} (-C_1 \mathcal{C}^T \dot{\mathbf{U}} - C_2 \mathcal{G}^T \mathbf{V} + (C_1 + C_2) \mathcal{H} \mathbf{P}) dt \\ & + \int_{\mathcal{I}} \delta \mathbf{V} (-C_3 \mathcal{A}^T \dot{\mathbf{U}} + (C_2 + C_3) \mathcal{Y} \mathbf{V} - C_2 \mathcal{G} \mathbf{P}) dt \\ & + \int_{\mathcal{I}} \delta \mathbf{U} ((1 + C_1 + C_3) \mathbf{M} \ddot{\mathbf{U}} - C_3 \mathcal{A} \dot{\mathbf{V}} - C_1 \mathcal{C} \dot{\mathbf{P}} + \mathbf{K} \mathbf{U} - \mathbf{F}^{\text{ext}}) dt. \end{aligned} \quad (4.2)$$

Here,  $\mathbf{K}$  and  $\mathbf{F}^{\text{ext}}$  are the global stiffness matrix and the nodal vector of external forces. Furthermore, the following matrices are defined:

$$\mathbf{M} = \int_{\mathcal{B}_0} \rho_0 \mathbf{N}^T \mathbf{N} d\mathcal{B}, \quad \mathcal{A} = \int_{\mathcal{B}_0} \rho_0 \mathbf{N}^T \Psi d\mathcal{B}, \quad \mathcal{C} = \int_{\mathcal{B}} \mathbf{N}^T \chi d\mathcal{B}, \quad (4.3a)$$

$$\mathcal{Y} = \int_{\mathcal{B}_0} \rho_0 \Psi^T \Psi d\mathcal{B}, \quad \mathcal{G} = \int_{\mathcal{B}} \Psi^T \chi d\mathcal{B}, \quad \mathcal{H} = \int_{\mathcal{B}_0} \rho_0^{-1} \chi^T \chi d\mathcal{B}, \quad (4.3b)$$

where  $\mathbf{M}$  is the consistent mass matrix. Note, that the matrices  $\mathcal{C}$  and  $\mathcal{G}$  are independent of material properties and play the role of projection between discrete spaces. The physical dimension of the matrices  $\mathcal{C}$  and  $\mathcal{G}$  is volume, or  $\text{m}^3$ . Matrices  $\mathcal{Y}$  and  $\mathcal{H}$  are mass matrices on discrete spaces  $\mathbf{V}$  and  $\mathbf{P}$ . Matrix  $\mathcal{A}$  is a weighted projection between discrete spaces. The usage of projections is explained and illustrated in Figures 4.1 and 4.2. The physical dimension of matrices  $\mathbf{V}$  and  $\mathcal{A}$  is mass, or kg. The physical dimension of  $\mathcal{H}$  is volume squared divided over mass, or  $\text{m}^6/\text{kg}$ .

Using independence of the variations  $\delta \mathbf{U}$ ,  $\delta \mathbf{V}$  and  $\delta \mathbf{P}$ , the following system of DAE is obtained

$$\begin{cases} (1 + C_1 + C_3) \mathbf{M} \ddot{\mathbf{U}} - C_3 \mathcal{A} \dot{\mathbf{V}} - C_1 \mathcal{C} \dot{\mathbf{P}} + \mathbf{K} \mathbf{U} = \mathbf{F}^{\text{ext}} \\ (C_2 + C_3) \mathcal{Y} \mathbf{V} - C_2 \mathcal{G} \mathbf{P} = C_3 \mathcal{A}^T \dot{\mathbf{U}} \\ -C_2 \mathcal{G}^T \mathbf{V} + (C_1 + C_2) \mathcal{H} \mathbf{P} = C_1 \mathcal{C}^T \dot{\mathbf{U}}. \end{cases} \quad (4.4)$$

The variables  $\mathbf{V}$  and  $\mathbf{P}$  are collected in the left hand side of the second and the third equation of (4.4). Elimination of  $\mathbf{V}$  and  $\mathbf{P}$  yields the following equations of motion

$$\mathbf{M}^{\circ} \ddot{\mathbf{U}} + \mathbf{K} \mathbf{U} = \mathbf{F}^{\text{ext}}, \quad (4.5)$$

with the new consistent mass matrix  $\mathbf{M}^\circ$ . This mass matrix is important for the variational mass scaling. Therefore, it is called here *the scaled mass matrix*. The artificially added mass is defined analogously to the expression of the algebraic mass scaling in equation (2.88)  $\lambda^\circ = \mathbf{M}^\circ - \mathbf{M}$ , which leads to the expression

$$\lambda^\circ = (C_1 + C_3)\mathbf{M} - \begin{bmatrix} C_3\mathcal{A} \\ C_1\mathcal{C} \end{bmatrix} \begin{bmatrix} (C_2 + C_3)\mathcal{Y} & -C_2\mathcal{G} \\ -C_2\mathcal{G}^\top & (C_1 + C_2)\mathcal{H} \end{bmatrix}^{-1} \begin{bmatrix} C_3\mathcal{A}^\top \\ C_1\mathcal{C}^\top \end{bmatrix}. \quad (4.6)$$

The latter expression can be further expanded using the formula for inversion of block matrices, see e.g. (STRANG 1986, Exercise 1.3.12) to

$$\lambda^\circ = (C_1 + C_3)\mathbf{M} - \frac{C_3^2}{C_2 + C_3}\mathcal{A}^\top\mathcal{Y}^{-1}\mathcal{A} + \frac{C_2^2C_3^2}{(C_2 + C_3)^2}\mathcal{A}^\top\mathcal{Y}^{-1}\mathcal{G}\mathcal{S}\mathcal{G}^\top\mathcal{Y}^{-1}\mathcal{A} - \quad (4.7)$$

$$- \frac{C_1C_2C_3}{C_2 + C_3}(\mathcal{A}\mathcal{Y}^{-1}\mathcal{G}\mathcal{S}\mathcal{C}^\top + \mathcal{C}\mathcal{S}\mathcal{G}^\top\mathcal{Y}^{-1}\mathcal{A}^\top) + C_1^2\mathcal{C}\mathcal{S}\mathcal{C}^\top, \quad (4.8)$$

assuming that  $\mathcal{Y}$  is invertible and with  $\mathcal{S}$  defined as

$$\mathcal{S} = \left( (C_1 + C_2)\mathcal{H} - \frac{C_2^2}{C_2 + C_3}\mathcal{G}^\top\mathcal{Y}^{-1}\mathcal{G} \right)^{-1}. \quad (4.9)$$

Formula (4.6) provides the most general expression for a three-parametric family of mass matrices. From an algebraic point of view, the artificially added mass  $\lambda^\circ$ , entering equation (4.5), is a rational function of the parameters  $(C_1, C_2, C_3)$ . It is not practical to use expression (4.6) directly, as the influence of the individual parameters on the mass matrix is unclear. Below, three important cases are discussed, where the expression (4.6) substantially simplifies.

## 4.2 Variational selective mass scaling

### 4.2.1 Case 1: one-parametric u-v-p-formulation

Let us set the free parameters  $C_1 = -C_2$  and  $C_3 = 0$  and assume that  $C_1$  is positive. In this case, the general expression for the added mass matrix  $\lambda^\circ$  reduces to

$$\lambda^\circ = C_1\mathbf{M} - C_1 \begin{bmatrix} \mathbf{0} \\ \mathcal{C} \end{bmatrix} \begin{bmatrix} -\mathcal{Y} & \mathcal{G} \\ \mathcal{G}^\top & \mathbf{0} \end{bmatrix}^{-1} \begin{bmatrix} \mathbf{0} \\ \mathcal{C}^\top \end{bmatrix}. \quad (4.10)$$

This expression can be further simplified, if the matrices  $\mathcal{Y}$  and  $\mathcal{G}^T \mathcal{Y}^{-1} \mathcal{G}$  are invertible. Finally, this leads to the expression for a one-parametric family of scaled mass matrices in the form

$$\boldsymbol{\lambda}^\circ = C_1 \left( \mathbf{M} - \mathcal{C} (\mathcal{G}^T \mathcal{Y}^{-1} \mathcal{G})^{-1} \mathcal{C}^T \right). \quad (4.11)$$

Note, that in this case  $C_2$  is negative and the conditions for positivity of template principle (3.14) are not fulfilled. This leads to a zero block matrix in expression (4.10), which is not positive definite. Therefore, special stability conditions must be fulfilled, which is discussed in detail in below, see equations (4.17) and (4.22).

### 4.2.2 Case 2: two-parametric u-v-p-formulation

Let us set the free parameter  $C_2 = 0$  and assume positivity of the parameters  $C_1$  and  $C_3$ . The added mass matrix  $\boldsymbol{\lambda}^\circ$  reduces then to

$$\boldsymbol{\lambda}^\circ = (C_1 + C_3) \mathbf{M} - \begin{bmatrix} C_3 \mathcal{A} \\ C_1 \mathcal{C} \end{bmatrix} \begin{bmatrix} C_3 \mathcal{Y} & \mathbf{0} \\ \mathbf{0} & C_1 \mathcal{H} \end{bmatrix}^{-1} \begin{bmatrix} C_3 \mathcal{A}^T \\ C_1 \mathcal{C}^T \end{bmatrix}. \quad (4.12)$$

The matrices  $\mathcal{Y}$  and  $\mathcal{H}$  are positive definite by construction. Hence, the block matrix in expression (4.12) is positive definite and invertible. This leads to a two-parametric added mass matrix in the form

$$\boldsymbol{\lambda}^\circ = C_1 (\mathbf{M} - \mathcal{C} \mathcal{H}^{-1} \mathcal{C}^T) + C_3 (\mathbf{M} - \mathcal{A} \mathcal{Y}^{-1} \mathcal{A}^T). \quad (4.13)$$

Note, that physical dimension of the product  $\mathcal{C} \mathcal{H}^{-1} \mathcal{C}^T$  in equation (4.13) is kg, i.e. dimension of  $\mathcal{H}$ ,  $\text{m}^6/\text{kg}$ , complies with dimension of the projection matrix  $\mathcal{C}$ ,  $\text{m}^3$ .

### 4.2.3 Case 3: one-parametric u-v-formulation

Let us set the free parameters  $C_1 = C_2 = 0$  and assume positivity of  $C_3$ . This case is just a further simplification of case 2 with  $C_1 = 0$ . The added mass matrix  $\boldsymbol{\lambda}^\circ$  is reduced from (4.13) to the expression

$$\boldsymbol{\lambda}^\circ = C_3 (\mathbf{M} - \mathcal{A} \mathcal{Y}^{-1} \mathcal{A}^T). \quad (4.14)$$

In cases 1, 2 and 3, linear families of mass matrices are obtained, which clarifies the meaning of the penalty parameters  $C_1$  and  $C_3$  as scaling factors for the artificially added mass, see Figure 4.1. The penalty factor  $C_2$  that is responsible for the coupling of the dual variables

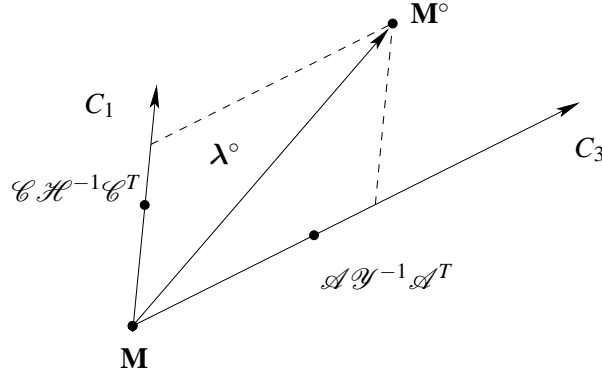


**Figure 4.1:** Linear two-parametric template of mass matrices obtained with equation (4.13)

$\mathbf{v}$  and  $\mathbf{p}$  plays only an auxiliary role in the cases discussed above. The matrices  $\mathcal{A}\mathcal{Y}^{-1}\mathcal{A}^T$ ,  $\mathcal{C}\mathcal{H}^{-1}\mathcal{C}^T$  and  $\mathcal{C}(\mathcal{G}^T\mathcal{Y}^{-1}\mathcal{G})^{-1}\mathcal{C}^T$  present in equations (4.11-4.14) are on the basis of a *consistent hybrid-mixed mass matrices* computed on mixed Hamilton's principle with the variables  $[\dot{\mathbf{u}}, \mathbf{v}]$ ,  $[\dot{\mathbf{u}}, \mathbf{p}]$  and  $[\dot{\mathbf{u}}, \mathbf{v}, \mathbf{p}]$ , respectively. Such mass matrices were defined in HUGHES ET AL. (1976) and used in GERADIN (1980). Thus, the proposed families (4.11-4.14) are weighted sums of known consistent mass matrices and the proposed variational formulation (3.8) justifies such a construction. In addition,  $\lambda^\circ$  is semi-positive by construction. This property follows for the cases 1 to 3 from a matrix generalization of the CAUCHY-SCHWARZ inequality. Thus, positive definiteness of  $\mathbf{M}^\circ$  is guaranteed if the penalty parameters  $C_1$  and  $C_3$  are positive.

The structure of  $\lambda^\circ$  given in (4.11-4.14) explains the way the proposed mass scaling works. The consistent mass matrix and hybrid-mixed mass matrices are equal, if only the ansatz space for  $\mathbf{v}$  and  $\mathbf{p}$  are taken equal to the ansatz space for  $\mathbf{u}$ . This results in  $\lambda^\circ$  being equal to zero. If the ansatz spaces for  $\mathbf{v}$  and  $\mathbf{p}$  are chosen poorer than the ansatz space for  $\mathbf{u}$ , the hybrid-mixed mass matrix produces less inertia than a consistent mass matrix. Thus, the artificially added mass increases inertia for modes orthogonal to the ansatz space of  $\mathbf{v}$  and  $\mathbf{p}$ . The appropriate ansatz spaces are discussed in the subsequent chapter.

## 4.3 Hybrid-mixed mass matrices

### 4.3.1 Discretization of two-field canonical principles

The Hellinger-Reissner principle of type I and II is obtained from the template (3.8) by specification of the penalty factors. In the same manner, the discrete mass matrices are obtained. This question is not considered here in detail.

### 4.3.2 Discretization of three-field canonical principle

The starting point for the discretization of the modified Hamiltonian principle is the weak form given in equation (3.17). Ansatz (4.1) is used for the discretization of independent fields. The projection matrices between fields are denoted according to equation (4.3). Substitution of the discretization yields the following algebraic system

$$\begin{cases} \mathcal{G}\mathbf{P} = \mathcal{Y}\mathbf{V} \\ \mathcal{C}^T\dot{\mathbf{U}} = \mathcal{G}^T\mathbf{V} \\ \mathcal{C}\dot{\mathbf{P}} + \mathbf{K}\mathbf{U} = \mathbf{F}^{\text{ext}}, \end{cases} \quad (4.15)$$

which can be identified as a discretized counterpart of the material, kinematic and kinetic equation, respectively. If the matrix  $\mathcal{Y}$  is invertible, the velocity vector  $\mathbf{V}$  can be eliminated from equations (4.15<sub>1</sub>) and (4.15<sub>2</sub>) resulting in

$$\mathcal{G}^T\mathcal{Y}^{-1}\mathcal{G}\mathbf{P} = \mathcal{C}^T\dot{\mathbf{U}}. \quad (4.16)$$

For linearly independent  $\Psi$  and a positive density  $\rho$ , the matrix  $\mathcal{Y}$  is positive definite and invertible. The matrix product  $\mathcal{G}^T\mathcal{Y}^{-1}\mathcal{G}$  is at least positive semi-definite, if  $\mathcal{Y}$  is positive definite. It is positive definite, if  $\mathcal{G}$  has full rank, and its number of rows is less or equal to the size of  $\mathcal{Y}$ , i.e.

$$n_p \leq n_v. \quad (4.17)$$

Let us assume that  $\mathcal{G}$  satisfies these two conditions. The matrix  $\bar{\mathcal{H}} = (\mathcal{G}^T\mathcal{Y}^{-1}\mathcal{G})^{-1}$  is then well defined. Using this matrix, the relation between displacement and momentum can be written as

$$\bar{\mathcal{H}}\mathcal{C}^T\dot{\mathbf{U}} = \dot{\mathbf{P}}. \quad (4.18)$$

Substitution of the latter in equation (4.15<sub>3</sub>) allows to eliminate  $\mathbf{P}$  from the equation of motion leading to

$$\mathcal{C}\bar{\mathcal{H}}\mathcal{C}^T\dot{\mathbf{U}} + \mathbf{K}\mathbf{U} = \mathbf{F}^{\text{ext}} + \mathbf{Z}. \quad (4.19)$$

That delivers an expression for hybrid-mixed consistent mass matrix

$$\mathbf{M}^* = \mathcal{C}\bar{\mathcal{H}}\mathcal{C}^T = \mathcal{C}(\mathcal{G}^T\mathcal{Y}^{-1}\mathcal{G})^{-1}\mathcal{C}^T. \quad (4.20)$$

The formula (4.20) can be illustrated with Figure 4.2. The kinetic energy in the modified Hamilton's principle (3.17) is computed on the discrete velocity  $\mathbf{v}^h$  producing the matrix  $\mathcal{Y}$ .

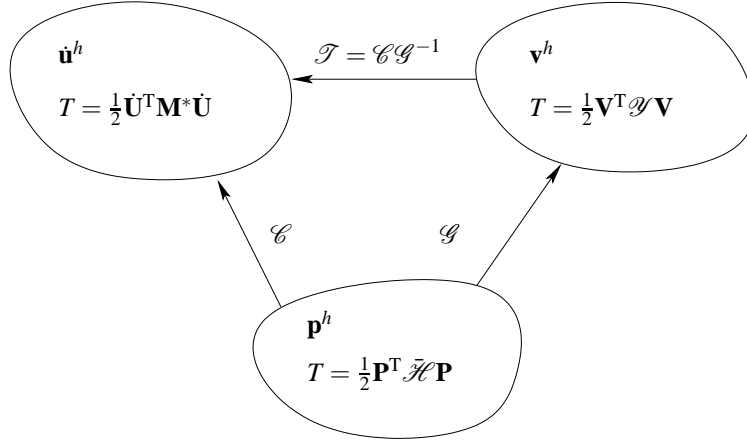


**Figure 4.2:** Approximation spaces for  $\mathbf{u}$ ,  $\mathbf{v}$  and  $\mathbf{p}$ , quadratic forms for kinetic energy and discrete projection between approximation spaces.

Then, it is projected via the Lagrange multiplier  $\mathbf{p}^h$  on  $\mathbf{u}^h$  in terms of the matrices  $\mathcal{C}$  and  $\mathcal{G}$  resulting in the matrix  $\mathbf{M}^*$ . If the matrix  $\mathcal{G}$  is square and non-singular, an auxiliary matrix  $\mathcal{T} = \mathcal{C}\mathcal{G}^{-1}$  may be introduced to combine both projections. In this case, the expression for the matrix  $\mathbf{M}^*$  simplifies to

$$\mathbf{M}^* = \mathcal{C}\mathcal{G}^{-1}\mathcal{Y}\mathcal{G}^{-\text{T}}\mathcal{C}^{\text{T}} = \mathcal{T}\mathcal{Y}\mathcal{T}^{\text{T}}. \quad (4.21)$$

It is identical to the transformation of a quadratic form  $\mathcal{Y}$  under linear transformation  $\mathcal{T}^{\text{T}} : \mathbf{V} \rightarrow \mathbf{U}$ . The variational index in the spatial dimensions of  $\mathbf{p}$  and  $\mathbf{v}$  in the weak form (3.17) is equal to 0. Thus, the inter-element continuity of the shape functions  $\Psi$  and  $\chi$  is not required for convergence and  $\mathbf{V}$  and  $\mathbf{P}$  can be eliminated on the element level provided that the basis functions are element-wise supported. Then, the global matrix  $\mathbf{M}^*$  can be assembled from the local element mass matrices, and  $\mathcal{Y}$  has a block diagonal structure (HUGHES ET AL. 1976).

The second condition for stability of this three-field method is that the intersection of the null-spaces of the mass and stiffness matrices must be empty (cf. (ZIENKIEWICZ AND TAYLOR 2006, p. 371) and (RENARD 2010, Theorem 1, condition (7)) for VEUBEKE-HU-WASHIZU  $\sigma - \varepsilon - \mathbf{u}$  elements),

$$\ker \mathbf{K} \cap \ker \mathbf{M}^* = \emptyset, \quad (4.22)$$

with  $\ker$  being kernel or null-space. This condition automatically provides that  $\mathbf{K} + r\mathbf{M}^*$  is not singular for any  $r > 0$ , and thus, most time integration schemes are well-defined.

### 4.3.3 Orthogonality and stability conditions

$\mathbf{M}^*$  is at least semi-definite by construction. In order to impose 0 at the  $i^{th}$  diagonal component of  $\mathbf{M}^*$ ,  $\mathcal{C}$  and  $\bar{\mathcal{H}}$  have to satisfy the condition

$$\mathbf{M}_{ii}^* = \mathbf{e}_i^T \mathcal{C} \bar{\mathcal{H}} \mathcal{C}^T \mathbf{e}_i = 0. \quad (4.23)$$

with  $\mathbf{e}_i$  being the  $i^{th}$  unit vector. As  $\bar{\mathcal{H}}$  is positive definite, this condition can hold only if  $\mathcal{C}^T \mathbf{e}_i = \mathbf{0}$ , i.e.,

$$\mathcal{C}^T \mathbf{e}_i = \int_{\mathcal{B}} \boldsymbol{\chi}(\mathbf{N}\mathbf{e}_i) d\mathcal{B} = 0. \quad (4.24)$$

Automatically, with the condition (4.24) the entire  $i^{th}$  row and column of the mass matrix  $\mathbf{M}_{ij}^*$  vanish,

$$\mathbf{M}_{ij}^* = \mathbf{e}_i^T \mathcal{C} \bar{\mathcal{H}} \mathcal{C}^T \mathbf{e}_j = \underbrace{(\mathbf{e}_i^T \mathcal{C})}_{\mathbf{0}} \bar{\mathcal{H}} \mathcal{C}^T \mathbf{e}_j = 0. \quad (4.25)$$

The condition (4.23) automatically satisfies the inf-sup condition given in RENARD (2010) that is sufficient for the index reduction of the DAE system (2.83). But it restricts the mass matrix to fit into the form given in (2.84). Such an approach is more complicated because it requires specially constructed shape functions for the displacement field. The advantage of the proposed approach is that massless nodes and nodes with mass are split by the structure of the mass matrix, and they can be treated separately.

The mass matrix  $\mathbf{M}^*$  is computed from the product of  $\bar{\mathcal{H}}$  and  $\mathcal{C}$ . The rank of  $\bar{\mathcal{H}}$  is  $n_p$ , therefore the rank of  $\mathbf{M}^*$  is less or equal to  $n_p$ . At the same time from condition (4.22) it follows that the rank of  $\mathbf{M}^*$  must be greater than or equal to the number of zero eigenvalues of  $\mathbf{K}$ , which is equal to the number of rigid body modes of the element  $n_{rbm}$ . If we want to make the number of massless nodes to be  $n_{d0}$ , then the rank of  $\mathbf{M}^*$  is less or equal to  $n_d - n_{d0}$ . It is pointless to take more than  $n_d - n_{d0}$  momentum shape functions, because  $\mathcal{C}$  in this case does not have a full rank. Its columns are linearly dependent, which means we can use only those shape functions of  $\boldsymbol{\chi}$  that provide linearly independent columns. This delivers the same mass matrix with less computational effort. Thus, the number of momentum shape functions  $n_p$  should satisfy the following conditions

$$n_{rbm} \leq n_p \leq n_d - n_{d0}. \quad (4.26)$$

## 4.4 Incompatible velocity method for mass matrices

The discretization of the variational principle (3.22) requires shape functions for the incompatible velocity  $\tilde{\mathbf{v}}$ . Let us denote these shape functions as  $\tilde{\mathbf{N}}$  and incompatible velocity parameters as  $\tilde{\mathbf{V}}$ . This leads to the following discrete equation of motion with subsidiary conditions

$$\begin{cases} \tilde{\mathbf{L}}\dot{\mathbf{U}} = \tilde{\mathbf{D}}\tilde{\mathbf{V}} \\ \mathbf{M}\ddot{\mathbf{U}} + \tilde{\mathbf{L}}^T\dot{\tilde{\mathbf{V}}} + \mathbf{K}\mathbf{U} = \mathbf{F}^{\text{ext}}, \end{cases} \quad (4.27)$$

where matrices  $\tilde{\mathbf{L}}$  and  $\tilde{\mathbf{D}}$  are defined as

$$\tilde{\mathbf{L}} = \int_{\mathcal{B}_0} \rho_0 \tilde{\mathbf{N}}^T \mathbf{N} d\mathcal{B}, \quad \tilde{\mathbf{D}} = \int_{\mathcal{B}_0} \rho_0 \tilde{\mathbf{N}}^T \tilde{\mathbf{N}} d\mathcal{B}. \quad (4.28)$$

As in the previous cases, the matrices  $\tilde{\mathbf{L}}$  and  $\tilde{\mathbf{D}}$  do not explicitly depend on time. If the rows of the shape function matrix  $\tilde{\mathbf{N}}$  are linearly independent, then the matrix  $\tilde{\mathbf{D}}$  is invertible. Static elimination of incompatible velocity parameters  $\tilde{\mathbf{V}}$  leads to the equation of motion

$$\tilde{\mathbf{M}}\ddot{\mathbf{U}} + \mathbf{K}\mathbf{U} = \mathbf{F}^{\text{ext}}, \quad (4.29)$$

with an EAS-like mass matrix  $\tilde{\mathbf{M}}$  defined as

$$\tilde{\mathbf{M}} = \mathbf{M} - \tilde{\mathbf{L}}^T \tilde{\mathbf{D}}^{-1} \tilde{\mathbf{L}}. \quad (4.30)$$

Conditions for its consistency are described in Subsection 5.4.

The one-parametric family of mass matrices can also be obtained from the discretization of formulation (3.24). The discretization procedure in this case is identical to the one given in equations (4.27-4.30) above. The resulting scaled mass matrix and the artificially added mass matrix read

$$\mathbf{M}^\circ = \mathbf{M} + C_1 \tilde{\mathbf{L}}^T \tilde{\mathbf{D}}^{-1} \tilde{\mathbf{L}}, \quad \boldsymbol{\lambda}^\circ = C_1 \tilde{\mathbf{L}}^T \tilde{\mathbf{D}}^{-1} \tilde{\mathbf{L}}. \quad (4.31)$$

This structure provides symmetry and positive definiteness of the added mass.



---

## Good ansatz spaces

This chapter focuses on ansatz spaces for the proposed formulations. Choosing the right ansatz spaces is crucial for accuracy and consistency of these formulations. First, the patch test for inertia terms is discussed. Passing patch the test is necessary for consistency. Secondly, shape functions for singular mass matrices for formulation (4.20) are derived. The key requirement for the shape functions is completeness of the basis and satisfaction of the orthogonality condition (4.24), which is required for an efficient discretization of dynamic contact problems. Thirdly, appropriate ansatz spaces for selective mass scaling formulation according to equation (4.14) are built. Finally, an example of ansatz spaces for an incompatible velocity formulation according to equation (4.30) is given.

### 5.1 Patch test for inertia terms

The patch test is a useful tool in FE technology for the assessment of crucial discretization properties like consistency, stability, robustness and the asymptotic convergence rate. It was initially proposed to test the performance of FEs with incompatible modes and numerical integration (BAZELEY ET AL. 1966; IRONS AND RAZZAQUE 1972), i.e. the patch test is a simple test for verification of consistency. Later, it was used as an equivalent of BABUŠKA-BREZZI criteria for mixed and hybrid-mixed elements (ZIENKIEWICZ AND TAYLOR 1997), which involved stability (solvability) requirements. The higher order patch test was introduced in TAYLOR ET AL. (1986) and it provides information about the asymptotic convergence rate. Another important application of patch tests is finding implementation errors in FE programs. For a comprehensive overview on the topic, see ZIENKIEWICZ AND TAYLOR (2006).

Here, patch tests for inertia terms (mass matrix) are described. They are described by corresponding numerical experiments and limited to hybrid-mixed and displacement formulations.

Consider a discretized body in a stress-free configuration. The following patch tests are designated by roman capital letters from 'A' to 'E'

- A: prescribed nodal acceleration  $\hat{\mathbf{b}}$  results in an inertia force vector  $\mathbf{MA}$  that is equal to the consistent nodal force  $\int_{\mathcal{B}_e} \mathbf{N}^T \rho_0 \hat{\mathbf{b}} dV$  for the uniform external body load  $\rho_0 \hat{\mathbf{b}}$
- B: an abrupt uniform external body load  $\rho_0 \hat{\mathbf{b}}$  in the domain and a nodal acceleration  $\hat{\mathbf{b}}$  applied at all boundary nodes result in a uniform acceleration at inner nodes
- C: an abrupt uniform external body load  $\rho_0 \hat{\mathbf{b}}$  to an unconstrained body results in uniform acceleration at inner nodes
- D: prescribed nodal acceleration  $\hat{\mathbf{b}}$  results in a translational acceleration of the center of gravity  $\hat{\mathbf{b}}$  and zero rotational acceleration w.r.t the center of gravity
- E: an abrupt uniform body load  $\rho_0 \hat{\mathbf{b}}$  results in a translational acceleration of the center of gravity  $\hat{\mathbf{b}}$  and zero rotational acceleration w.r.t the center of gravity.

Note, that patch tests 'C' and 'E' require non-singular mass matrices. Patch test 'B' requires an appropriate rank of the mass matrix. Patch tests 'A' and 'E' imply no conditions on the singularity of the mass matrix. Singularity of the mass matrix does not imply instability of dynamic solutions (for details see condition (4.17) and COOK ET AL. (2007); HAURET (2010)). Actually, the patch tests 'A' and 'C' correspond to two physical experiments. In the test 'A', the reference frame gets an abrupt acceleration  $\rho_0 \hat{\mathbf{b}}$ . In the test 'C', the gravity force is abruptly "turned on". In both cases, an arbitrary body without constraints is expected to move as a rigid body, and the nodal inertial forces must be consistent with  $\rho_0 \hat{\mathbf{b}}$ . Test 'B' can be regarded as the mixture of 'A' and 'C'. Tests 'D' and 'E' are weaker. These tests check only in an average sense.

For higher order patch tests, the uniform vector  $\hat{\mathbf{b}}$  should be substituted by

$$\hat{\mathbf{b}} = \hat{\mathbf{b}}_0 + \hat{\mathbf{b}}_{0x}x + \hat{\mathbf{b}}_{0y}y + \hat{\mathbf{b}}_{0xx}x^2 + \hat{\mathbf{b}}_{0xy}xy + \hat{\mathbf{b}}_{0yy}y^2 + \dots \quad (5.1)$$

The exact acceleration vector  $\mathbf{A}$  should interpolate the corresponding values of  $\hat{\mathbf{b}}$ . A special case of a higher order patch test is referred here as a rigid body rotation. It can be obtained for the 2D case as

$$\hat{\mathbf{b}}_{\text{ROTZ}} = \begin{bmatrix} 0 \\ 0 \end{bmatrix} + \begin{bmatrix} 0 \\ 1 \end{bmatrix} x + \begin{bmatrix} -1 \\ 0 \end{bmatrix} y. \quad (5.2)$$

An alternative approach for consistency of hybrid-singular mass matrices is given in HUGHES ET AL. (1976). It is based on the completeness of the bases and provides a theoretical estimate of the convergence rate for the lowest eigenfrequencies and eigenmodes.

Note, that the patch tests discussed above do not affect rotary degrees of freedom. Patch tests for elements with rotary DOFs are not discussed here.

One important consequence of all patch tests is that the ansatz spaces for all discretized fields must contain at least a constant mode. This argument is often used for construction of ansatz spaces herein.

## 5.2 Shape functions for singular mass matrices

This section is organized as follows. First, the shape functions for a one-dimensional three-node element are derived. This derivation mainly follows the ideas of RENARD (2010). Secondly, the derivation is extended to arbitrary number of nodes for 1D elements and some quadratic TIMOSHENKO beams. These three bases are given in TKACHUK ET AL. (2013). Thirdly, the ansatz spaces on the basis of tensor-products are derived for 2D and 3D cases, which were presented in TKACHUK ET AL. (2012) and ECK ET AL. (2013).

### 5.2.1 Derivation of shape functions in 1D

Here, the shape functions for 1D elements are constructed that satisfy the orthogonality condition (4.24) at the corner nodes<sup>1</sup>, where later contact conditions are collocated. It is natural to take  $n_d - 2 = n_v = n_p$ , which automatically satisfies the stability conditions (4.17) and (4.26). This choice is also optimal with respect to computational costs for the element-wise computation of the singular mass matrix.

#### Three-node element

Consider a three-node 1D element ( $dim = 1, n_d = 3$ ). The goal is to obtain massless left and right nodes. First, for a consistent approximation of the momentum and the kinetic energy at least constant shape functions are required for the velocity (see Figure 5.2). This also guarantees that the element passes the inertia patch tests. The momentum shape functions  $\chi$  enter into the zero mass condition (4.24). In order to avoid complications in the case of a non-uniform Jacobian, the momentum shape functions  $\chi$  are modified by multiplication with the factor  $|J_0|/|J|$ .

$$\Psi_1 = 1 \quad \chi_1 = |J_0|/|J| \quad n_v = n_p = 1, \quad (5.3)$$

---

<sup>1</sup>This construction prohibits use of linear elements for HSMM.

where  $|J|$  is the determinant of the Jacobian, and  $|J_0|$  is evaluated at the center of the element  $\xi = 0$ .

Secondly, it is assumed that the new displacement shape functions have the same linear span as the standard quadratic shape functions and that each shape function is a linear combination with so far the unknown coefficients  $\alpha_i$

$$\text{Span}[N_1, N_2, N_3] = \text{Span}[1, \xi, \xi^2], \quad (5.4)$$

with Span denoting the linear span.

Thirdly, it is assumed that the interpolation condition is satisfied only at corner nodes with

$$\begin{aligned} N_1(-1) &= 1, & N_2(-1) &= 0, & N_3(-1) &= 0, \\ N_1(1) &= 0, & N_2(1) &= 0, & N_3(1) &= 1. \end{aligned} \quad (5.5)$$

Finally, satisfying the condition (4.24) with  $N_1 = \alpha_0 + \alpha_1 \xi + \alpha_2 \xi^2$  leads to a system of equations

$$\begin{cases} N_1(-1) = 1 \\ N_1(1) = 0 \\ \int_{-1}^1 N_1 \chi_1 |J| d\xi = \int_{-1}^1 N_1 |J_0| d\xi = 0. \end{cases} \quad (5.6)$$

The solution is  $N_1 = -\frac{1}{4} - \frac{1}{2}\xi + \frac{3}{4}\xi^2$ . Due to symmetry, the other corner shape function reads  $N_3 = -\frac{1}{4} + \frac{1}{2}\xi + \frac{3}{4}\xi^2$ . There are only two conditions for the three coefficients to define  $N_2$ . To obtain a unique  $N_2$ , it is additionally required that  $N_1, N_2, N_3$  form a partition of unity with

$$N_2 = 1 - N_1 - N_3 = \frac{3}{2}(1 - \xi^2). \quad (5.7)$$

Summarizing the results (see Figures 5.1 and 5.2 for an illustration), we get

$$\begin{cases} n_d = 3 : & N_1 = -\frac{1}{4} - \frac{1}{2}\xi + \frac{3}{4}\xi^2 \\ & N_2 = \frac{3}{2}(1 - \xi^2) \\ & N_3 = -\frac{1}{4} + \frac{1}{2}\xi + \frac{3}{4}\xi^2 . \\ n_v = 1 : & \psi_1 = 1 \\ n_p = 1 : & \chi_1 = |J_0|/|J| \end{cases} \quad (5.8)$$

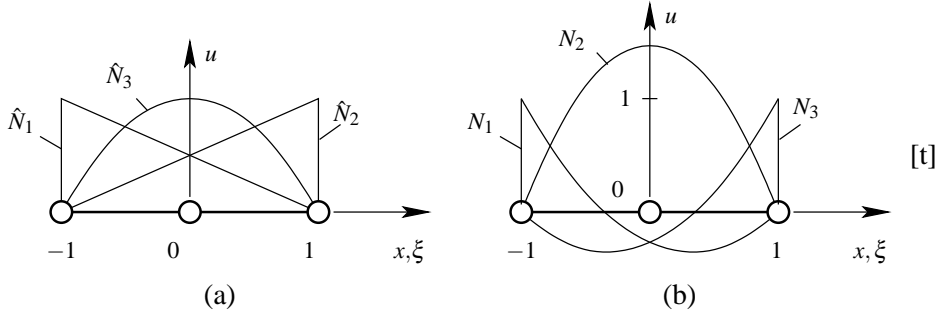


**Figure 5.1:** Hierarchical (left) and modified (right) shape functions for a quadratic truss element.

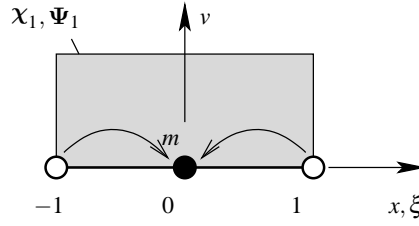


**Figure 5.2:** Velocity shape function for quadratic truss element.

### General case ( $n_d$ -node element)

Consider a 1D element with arbitrary number of nodes  $n_d > 2$ . There is more than one possibility to construct shape functions that satisfy the interpolation condition at the corner nodes and the orthogonality condition (4.24). Here, an option with closed form expressions for the shape functions is presented. It uses GAUSS-LOBATTO quadrature points as node locations and partially follows the idea of construction of biorthogonal bases proposed in LAMICHANE AND WOHLMUTH (2007).

Let us denote  $\{\xi_i\}_{i=1}^{n_d}$  and  $\{w_i\}_{i=1}^{n_d}$  as locations and weights for the GAUSS-LOBATTO quadrature of order  $n_d$  for the interval  $[-1; 1]$ , see (ABRAMOWITZ ET AL. 1964, p. 887). The special feature of the GAUSS-LOBATTO quadrature is that the integration points include the end points of the interval ( $\xi_1 = -1$  and  $\xi_{n_d} = 1$ ). The inner points are the roots of the derivative of the Legendre polynomial  $\mathcal{P}'_{n_d-1}(\xi) = 0$ , and the weights are equal to  $w_i = \frac{2}{n_d(n_d-1)(\mathcal{P}'_{n_d-1}(\xi_i))^2}$ .

Then, two LAGRANGE bases are defined using the quadrature points as interpolation points

$$\bar{N}_j = \prod_{\substack{i=1 \\ j \neq i}}^{n_d} \frac{\xi - \xi_i}{\xi_j - \xi_i}, \quad j = \overline{1, n_d} \quad \bar{\chi}_j = \prod_{\substack{i=2 \\ j \neq i}}^{n_d-1} \frac{\xi - \xi_i}{\xi_j - \xi_i}, \quad j = \overline{2, (n_d - 1)}. \quad (5.9)$$

$\bar{\chi}$  and  $\bar{N}$  are complete polynomials of order  $n_d - 2$  and  $n_d$ , respectively. Moreover,  $\bar{\chi}$  and  $\bar{N}$  satisfy the interpolation condition at  $\{\xi_i\}_{i=2}^{(n_d-1)}$  and  $\{\xi_i\}_{i=1}^{n_d}$ , respectively.

The shape functions for momenta  $\xi_i$  are defined as complete polynomials of order  $n_d - 2$  multiplied with  $|J_0|/|J|$

$$\chi_i = |J_0|/|J| \bar{\chi}_{i+1} \quad j = \overline{2, (n_d - 1)}. \quad (5.10)$$

The left corner shape function can be constructed as a linear combination of  $\bar{N}_i$  with

$$N_1 = \bar{N}_1 - \sum_{i=2}^{n_d-1} a_i \bar{N}_i. \quad (5.11)$$

The orthogonality condition for  $N_1$  and  $\chi_k$  reads as

$$\int_{-1}^1 N_1 \chi_k |J| d\xi = |J_0| \int_{-1}^1 \left( \bar{N}_1 - \sum_{i=2}^{n_d-1} a_i \bar{N}_i \right) \bar{\chi}_k d\xi, \quad k = \overline{2, (n_d - 1)}. \quad (5.12)$$

The integrand is a polynomial of order  $(2n_d - 4)$  and thus, the integral can be evaluated exactly in terms of the GAUSS-LOBATTO quadrature formula with  $n_d$  nodes. Next, the interpolation property of  $\bar{\chi}$  and  $\bar{N}$  is used to simplify the expression

$$\begin{aligned} |J_0| \int_{-1}^1 \left( \bar{N}_1 - \sum_{i=2}^{n_d-1} a_i \bar{N}_i \right) \bar{\chi}_k d\xi &= |J_0| \sum_{j=1}^{n_d} \left[ \left( \bar{N}_1(\xi_j) - \sum_{i=2}^{n_d-1} a_i \bar{N}_i(\xi_j) \right) \bar{\chi}_k(\xi_j) \right] w_j = \\ &= |J_0| (\bar{\chi}_k(-1) w_1 - a_k w_k), \quad k = \overline{2, (n_d - 1)}. \end{aligned} \quad (5.13)$$

Then, the orthogonality relation (5.12) gives

$$a_k = \frac{w_1 \bar{\chi}_k(-1)}{w_k} = \frac{\bar{\chi}_k(-1)}{(\mathcal{P}_{n_d-1}(\xi_k))^2}. \quad (5.14)$$

Due to symmetry, the right corner shape function can be constructed as

$$N_{n_d} = \bar{N}_{n_d} - \sum_{i=2}^{n_d-1} b_i \bar{N}_i, \quad b_i = \frac{w_{n_d} \bar{\chi}_i(1)}{w_i} = \frac{\bar{\chi}_i(1)}{(\mathcal{P}_{n_d-1}(\xi_i))^2}. \quad (5.15)$$

Note, that the corner shape functions do not satisfy the interpolation condition at inner nodes.

The inner shape functions are not uniquely defined. They may be constructed such that  $\{N_i\}_{i=1}^{n_d}$  form a partition of unity

$$N_i = (1 + a_i + b_i)\bar{N}_i = \left(1 + \frac{\bar{\chi}_i(-1) + \bar{\chi}_i(1)}{(\mathcal{P}_{n_d-1}(\xi_i))^2}\right)\bar{N}_i, \quad i = \overline{2, (n_d - 1)}. \quad (5.16)$$

The functions  $\{\bar{N}_i\}_{i=1}^{n_d}$  form a complete polynomial basis, and it is easy to check that it is the same case for the basis  $\{N_i\}_{i=1}^{n_d}$ . The basis  $\{\bar{N}_i\}_{i=1}^{n_d}$  is built from  $\{N_i\}_{i=1}^{n_d}$  via a linear transformation  $\mathbf{T}_N$ , which has a nice block structure

$$N_i = \sum_{j=1}^{n_d} T_{N,ij}\bar{N}_j \quad \text{or} \quad \mathbf{N} = \mathbf{T}_N\bar{\mathbf{N}}, \quad (5.17)$$

with

$$\mathbf{T}_N = \begin{pmatrix} 1 & -a_2 & \cdots & -a_{n_d-1} & 0 \\ 0 & (1 + a_2 + b_2) & \cdots & 0 & 0 \\ \vdots & \vdots & \ddots & \vdots & \vdots \\ 0 & 0 & \cdots & (1 + a_{n_d-1} + b_{n_d-1}) & 0 \\ 0 & -b_2 & \cdots & -b_{n_d-1} & 1 \end{pmatrix}. \quad (5.18)$$

Note, that the determinant of the transformation matrix  $\mathbf{T}_N$  can be computed as follows

$$\det(\mathbf{T}_N) = \prod_{i=2}^{n_d-1} (1 + a_i + b_i). \quad (5.19)$$

The absolute values of  $a_i$  and  $b_i$  are less than 0.5, which implies that  $(1 + a_i + b_i) > 0$ . Thus, the determinant of the matrix  $\mathbf{T}_N$  is non-zero and the transformation matrix is regular.

In the case  $n_d = 3$ , the functions are identical to the ones in equation (5.8). In the case  $n_d = 4$ , the basis reduces to

$$\left\{ \begin{array}{l} \xi_{1,4} = \pm 1; \quad \xi_{2,3} = \pm \frac{1}{\sqrt{5}} \\ n_d = 4: \quad N_1 = -\frac{1}{4} + \frac{3}{4}\xi + \frac{3}{4}\xi^2 - \frac{5}{4}\xi^3 \\ \quad \quad N_2 = \frac{3}{4} + \frac{3\sqrt{5}}{4}\xi - \frac{3}{4}\xi^2 - \frac{3\sqrt{5}}{4}\xi^3 \\ \quad \quad N_3 = \frac{3}{4} - \frac{3\sqrt{5}}{4}\xi - \frac{3}{4}\xi^2 + \frac{3\sqrt{5}}{4}\xi^3 \\ \quad \quad N_4 = -\frac{1}{4} - \frac{3}{4}\xi + \frac{3}{4}\xi^2 + \frac{5}{4}\xi^3 \\ n_v = 2: \quad \psi_1 = 1; \quad \psi_2 = \xi \\ n_p = 2: \quad \chi_1 = \frac{|J_0|}{2|J|}(\sqrt{5}\xi + 1); \quad \chi_2 = \frac{|J_0|}{2|J|}(-\sqrt{5}\xi + 1). \end{array} \right. \quad (5.20)$$

The shape functions (5.20) are illustrated in Figure 5.3.

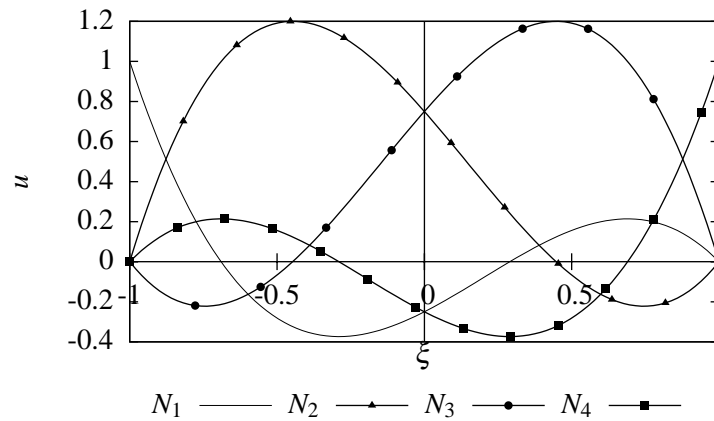


**Figure 5.3:** Modified shape functions for the cubic 1D element.

This method can be easily extended for multiple dimensions in case of tensor product structure, see Subsections 5.2.3 and 5.2.4.

The formulation and shape functions developed above enable us to construct finite elements for thin-walled structures that significantly reduce artificial oscillations of contact forces in dynamic problems and show sufficient accuracy for modal and wave propagation analysis. Herein, the discussion is restricted to 1D truss and 2D TIMOSHENKO beam elements, quadratic nine-node quadrilaterals and 27-node hexahedrals. In addition, only formulations with equal number of velocity and momentum parameters  $n_v = n_p$  are considered.

Now, a notation for the two discussed truss elements is introduced:

- Tr2-0: a three-node truss with quadratic shape functions for displacements and constant ansatz for velocity, according to (5.8)
- Tr3-1: a four-node truss with cubic shape functions for displacements and linear ansatz for velocity, according to (5.20).

In the denomination (TrX-Y) for the elements, X and Y are the order of the displacement and velocity interpolation, respectively. For these elements, contact may occur at the end of the domain  $\partial\mathcal{B}_c$ , i.e., at the left or right node. The shape functions for some TIMOSHENKO beam elements are given below.

### 5.2.2 Special shape functions for three-node Timoshenko beam element

For a beam element, a lateral contact inside the domain  $\mathcal{B}$  may occur. It is collocated at the corner nodes of the elements herein. Only three-node TIMOSHENKO beam elements are presented

- Ti2-2-2-2: standard Lagrange formulation with CMM (used for reference computations)
- Ti2-2-0-0: quadratic shape functions (5.8) for displacement and rotation
- Ti2-2-0-1: quadratic shape functions (5.8) for displacement and rotation, but angular velocity is linear
- Ti2-2-0-2: quadratic shape functions (5.8) for displacement and rotation, but angular velocity is quadratic
- Ti2\*-2-1-2: cubic linked interpolation (5.21), see discussion below.

In the element notation (TiX-Y-Z-W), the four numbers stand for the order of displacement, rotation, translational and angular velocity, respectively. The latter four elements have singular mass matrices with zero masses at the corner nodes. They differ in the computation of the rotational inertia. Ti2-2-0-1 and Ti2-2-0-2 use a higher order ansatz for angular velocity. The linked interpolation Ti2\*-2-1-2 allows the element to yield an exact stiffness matrix for static problems. The shape functions reads

$$\mathbf{N} = \begin{bmatrix} -1/4 + 3/4\xi + 3/4\xi^2 - 5/4\xi^3 & 0 \\ -5/8\xi(1-\xi^2)le & 1/2 - 1/2\xi \\ 3/2 - 3/2\xi^2 & 0 \\ 0 & 1 - \xi^2 \\ -1/4 - 3/4\xi + 3/4\xi^2 + 5/4\xi^3 & 0 \\ -5/8\xi(1-\xi^2)le & 1/2 + 1/2\xi \end{bmatrix}^T, \quad \Psi = \begin{bmatrix} 1 & 0 \\ \xi & 0 \\ 0 & 1 \\ 0 & \xi \\ 0 & \xi^2 \end{bmatrix}^T. \quad (5.21)$$

Moreover, the corner displacement shape functions are orthogonal to linear velocities. The linear translational velocity  $\psi_{22}$  allows exact computation of the polar inertia, which is beneficial for flexural dominated problems.

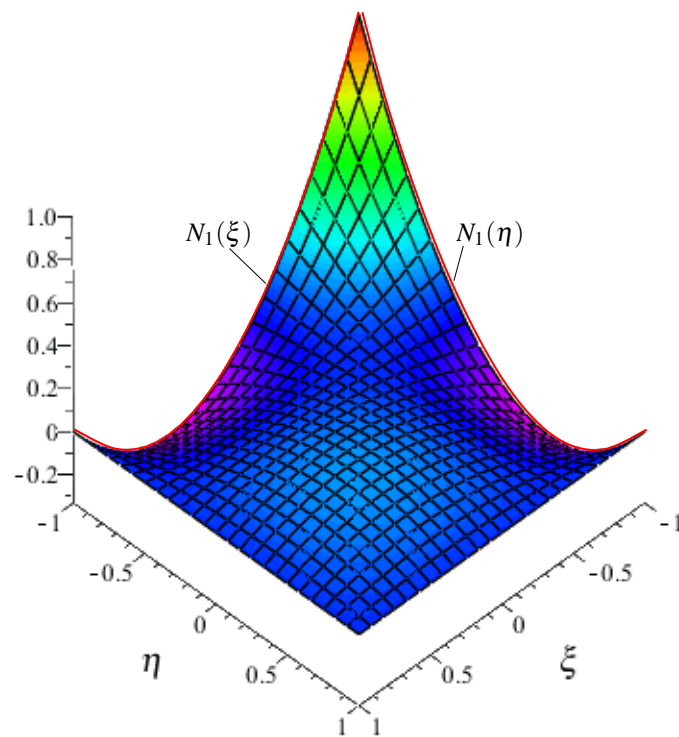


**Figure 5.4:** Shape function  $N_1(\xi, \eta)$  of a nine-node quadrilateral element (Q2).

### 5.2.3 Shape functions for 2D

The shape functions for the 2D case may be obtained by means of tensor product rule, see Figure 5.4. The shape functions for a nine-node quadrilateral element are constructed with the help of the shape functions for three-node element according to equation(5.8).

The orthogonality condition for displacement and momentum shape functions given in equation (4.24) requires the multiplier  $\frac{|J_0|}{|J|}$  for  $\chi$ . Moreover, mixed products of monomials  $\xi$  and  $\eta$  must be avoided for  $\chi$ , which limits the maximal number of momentum shape functions  $n_p$  to 10. The number of velocity parameters is assigned to  $n_v = 10$ . This leads to shape functions

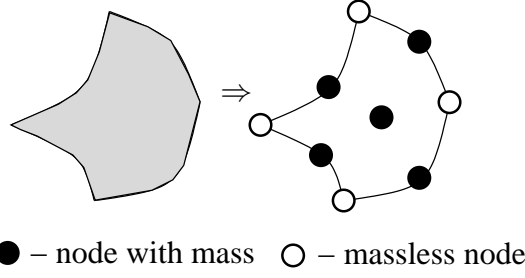


**Figure 5.5:** Nine-node quadrilateral element (Q2).

in the form

$$\mathbf{N} = \begin{bmatrix} N_1(\xi)N_1(\eta) & 0 & N_3(\xi)N_1(\eta) & 0 & \dots \\ 0 & N_1(\xi)N_1(\eta) & 0 & N_3(\xi)N_1(\eta) & \dots \end{bmatrix}, \quad (5.22)$$

$$\Psi = \begin{bmatrix} 1 & 0 & X^h & 0 & Y^h & 0 & \xi^2 & \eta^2 & 0 & 0 \\ 0 & 1 & 0 & X^h & 0 & Y^h & 0 & 0 & \xi^2 & \eta^2 \end{bmatrix}, \quad (5.23)$$

$$\chi = \frac{|J_0|}{|J|} \begin{bmatrix} 1 & 0 & \xi & 0 & \eta & 0 & \xi^2 & \eta^2 & 0 & 0 \\ 0 & 1 & 0 & \xi & 0 & \eta & 0 & 0 & \xi^2 & \eta^2 \end{bmatrix}. \quad (5.24)$$

This element is denoted as Q2V10P10, i.e. it is a quadratic Lagrange element with ten velocity and momentum modes (parameters). This element has massless corner nodes, see Figure 5.5. The inertia is consistently redistributed between the center node and the mid-edge nodes.

### 5.2.4 Shape functions for 3D

The derivation of the shape functions for a 27-node Lagrange element follows the procedure for the element Q2V10P10. The shape functions are constructed with the help of the shape functions for three-node element (5.8). In this case, the maximum number of the momentum shape functions is 57 including 19 monomials for each direction

$$\Theta = [1, \xi, \eta, \zeta, \xi^2, \eta^2, \zeta^2, \xi\eta, \xi\zeta, \eta\zeta, \xi^2\eta, \xi^2\zeta, \xi\eta^2, \eta^2\zeta, \xi\zeta^2, \eta\zeta^2, \xi^2\eta^2, \eta^2\zeta^2, \xi^2\zeta^2]. \quad (5.25)$$

The orthogonality condition for displacement and momentum shape functions given in equation (4.24) requires the multiplier  $\frac{|J_0|}{|J|}$  for momentum shape functions  $\chi$ . This leads to shape

functions in the form

$$\mathbf{N} = [N_1(\xi)N_1(\eta)N_1(\zeta)\mathbf{I} \quad N_1(\xi)N_3(\eta)N_1(\zeta)\mathbf{I} \quad N_3(\xi)N_3(\eta)N_1(\zeta)\mathbf{I} \quad \dots], \quad (5.26)$$

$$\Psi = \mathbf{I}\Theta, \quad (5.27)$$

$$\chi = \frac{|J_0|}{|J|}\mathbf{I}\Theta, \quad (5.28)$$

where  $\mathbf{I}$  is the identity matrix of size three by three and  $\Theta$  is defined above defined above vector of monomials. The element is denoted as Hexa27V57P57.

### 5.3 Variational selective mass scaling

Justification of the existing methods for SMS is not the primary goal of the derivation. Flexibility of the mass matrices (4.11-4.14) facilitates the construction of SMS that does not have some of the disadvantages of existing techniques. For example, some mass scaling technique do not preserve rotational inertia of a single element. This leads to large errors for problems where substantial rotations of a structure occur. If the ansatz space for velocities contains all rigid body modes (RBM), then the mass matrix (4.14) gives the exact values for translational and rotational inertia. For 1D, 2D and 3D cases the following  $\Psi$  is required:

$$\Psi_{1D} = [1], \quad \Psi_{2D} = \begin{bmatrix} 1 & 0 & -Y^h \\ 0 & 1 & X^h \end{bmatrix}, \quad (5.29)$$

$$\Psi_{3D} = \begin{bmatrix} 1 & 0 & 0 & -Y^h & Z^h & 0 \\ 0 & 1 & 0 & X^h & 0 & -Y^h \\ 0 & 0 & 1 & 0 & -X^h & Z^h \end{bmatrix}. \quad (5.30)$$

Here,  $X^h(\xi, \eta, \zeta)$ ,  $Y^h(\xi, \eta, \zeta)$  and  $Z^h(\xi, \eta, \zeta)$  are approximations of the reference geometry of an element obtained from the isoparametric approach. However, such velocity shape functions  $\Psi$  lead to a mass matrix  $\mathbf{M}^\circ$  with coupled terms between  $x$ -,  $y$ - and  $z$ - direction. This is a rather undesired property. In order to decouple inertia, each column of  $\Psi$  should contain only one non-zero entry. This leads to a different ansatz  $\Psi$  with

$$\Psi_{2D} = \begin{bmatrix} 1 & 0 & Y^h & 0 \\ 0 & 1 & 0 & X^h \end{bmatrix}, \quad (5.31)$$

$$\Psi_{3D} = \begin{bmatrix} 1 & 0 & 0 & Y^h & Z^h & 0 & 0 & 0 & 0 \\ 0 & 1 & 0 & 0 & 0 & 0 & X^h & 0 & Y^h \\ 0 & 0 & 1 & 0 & 0 & X^h & 0 & Z^h & 0 \end{bmatrix}. \quad (5.32)$$

For high-order elements a complete linear ansatz may be used with

$$\Psi_{1D} = [1 \quad X^h], \quad \Psi_{2D} = \begin{bmatrix} 1 & 0 & X^h & 0 & Y^h & 0 \\ 0 & 1 & 0 & X^h & 0 & Y^h \end{bmatrix}, \quad (5.33)$$

$$\Psi_{3D} = \begin{bmatrix} 1 & 0 & 0 & X^h & Y^h & Z^h & 0 & 0 & 0 & 0 & 0 & 0 \\ 0 & 1 & 0 & 0 & 0 & 0 & X^h & Y^h & Z^h & 0 & 0 & 0 \\ 0 & 0 & 1 & 0 & 0 & 0 & 0 & 0 & 0 & X^h & Y^h & Z^h \end{bmatrix}. \quad (5.34)$$

For some low order elements, such as T1 or Tetra4, constant ansatz space for  $\Psi$  may be used with

$$\Psi_{2D} = \begin{bmatrix} 1 & 0 \\ 0 & 1 \end{bmatrix}, \quad \Psi_{3D} = \begin{bmatrix} 1 & 0 & 0 \\ 0 & 1 & 0 \\ 0 & 0 & 1 \end{bmatrix}. \quad (5.35)$$

Note, usage of current geometry for velocity ansatz is possible. Some aspects of such treatment are discussed in TKACHUK AND BISCHOFF (2013a).

The elements using variational mass scaling are denoted with the suffix 'MS' and  $n_v$ , the number of columns in the matrix  $\Psi$ , e.g. 8-node hexahedral element using ansatz (5.35) with three velocity shape functions is denoted Hexa8MS3. The value of scaling factor  $C_1$  is specified separately.

In the following section, some examples demonstrate the efficiency of the proposed techniques.

### 5.3.1 Three-node triangle

A simple example is discussed to clarify this approach. Consider a three-node membrane element with two DOFs per node with constant density  $\rho_0$ , described also in Figure 2.12. Let us stick to the case with  $C_2 = C_3 = 0$ , leading to  $\mathbf{M}^\circ = \mathbf{M} + \lambda_e^\circ$  with the mass augmentation matrix in the form  $\lambda_e^\circ = C_1 (\mathbf{M} - \mathcal{C} \mathcal{H}^{-1} \mathcal{C}^T)$ . Standard shape functions for displacements and constant functions for momenta are used with

$$\mathbf{N} = \begin{bmatrix} 1 - \xi - \eta & 0 & \xi & 0 & \eta & 0 \\ 0 & 1 - \xi - \eta & 0 & \xi & 0 & \eta \end{bmatrix}, \quad \mathcal{X} = \begin{bmatrix} 1 & 0 \\ 0 & 1 \end{bmatrix}. \quad (5.36)$$

This corresponds to an element T1MS2 in the notation of the thesis. Substitution of shape functions lead to

$$\mathbf{M} = \frac{\rho_0 A_0}{12} \begin{bmatrix} 2 & 0 & 1 & 0 & 1 & 0 \\ 0 & 2 & 0 & 1 & 0 & 1 \\ 1 & 0 & 2 & 0 & 1 & 0 \\ 0 & 1 & 0 & 2 & 0 & 1 \\ 1 & 0 & 1 & 0 & 2 & 0 \\ 0 & 1 & 0 & 1 & 0 & 2 \end{bmatrix}, \mathcal{C}^T = \frac{A_0}{3} \begin{bmatrix} 1 & 0 \\ 0 & 1 \\ 1 & 0 \\ 0 & 1 \\ 1 & 0 \\ 0 & 1 \end{bmatrix}, \mathcal{H} = \frac{A_0}{\rho_0} \begin{bmatrix} 1 & 0 \\ 0 & 1 \end{bmatrix}, \quad (5.37)$$

$$\lambda_e^\circ = C_1 \frac{\rho_0 A_0}{18} \begin{bmatrix} 2 & 0 & -1 & 0 & -1 & 0 \\ 0 & 2 & 0 & -1 & 0 & -1 \\ -1 & 0 & 2 & 0 & -1 & 0 \\ 0 & -1 & 0 & 2 & 0 & -1 \\ -1 & 0 & -1 & 0 & 2 & 0 \\ 0 & -1 & 0 & -1 & 0 & 2 \end{bmatrix}. \quad (5.38)$$

The latter expression is identical to the mass scaling matrix  $\lambda_e^\circ$  given by equation (2.90) up to a factor three, see also OLOVSSON ET AL. (2005).

Ansatz (5.30) can be used for more accurate computations, where exact value for the element's rotational moment is needed. The basis  $\chi$  reads

$$\chi = \begin{bmatrix} 1 & 0 & -Y^h \\ 0 & 1 & X^h \end{bmatrix}. \quad (5.39)$$

This results in the following projection matrices  $\mathcal{C}$  and  $\mathcal{H}$  for the element T1MS3 with

$$\mathcal{H} = \frac{A_0}{\rho_0} \begin{bmatrix} 1 & 0 & -y_G \\ 0 & 1 & x_G \\ -y_G & x_G & I_{xx} + I_{yy} + x_G^2 + y_G^2 \end{bmatrix}, \quad (5.40)$$

$$\mathcal{C}^T = \frac{A_0}{12} \begin{bmatrix} 4 & 0 & -2Y_1 - Y_2 - Y_3 \\ 0 & 4 & 2X_1 + X_2 + X_3 \\ 4 & 0 & -Y_1 - 2Y_2 - Y_3 \\ 0 & 4 & X_1 + 2X_2 + X_3 \\ 4 & 0 & -Y_1 - Y_2 - 2Y_3 \\ 0 & 4 & X_1 + X_2 + 2X_3 \end{bmatrix}. \quad (5.41)$$

The obtained mass scaling matrix  $\lambda_e^\circ$  for an element T1MS3 is identical to the one obtained in Subsection 2.3.5.

### 5.3.2 Bilinear quadrilateral element

In Chapters 6 and 7, the elements Q1MS2, Q1MS3 and Q1MS4 are tested. For comparison of these formulations, see also TKACHUK AND BISCHOFF (2013c). The most efficient element among the proposed ones is Q1MS3 leading to accurate results in bending dominated transient and eigenvalue problems. The conditioning of the mass matrix obtained with Q1MS3 is comparable with ASMS. This element is also found to be less sensitive to element distortion w.r.t. ASMS (TKACHUK AND BISCHOFF 2013b). For wave propagation example the dispersion produced by Q1MS3 is substantially larger than for ASMS (TKACHUK AND BISCHOFF 2013b).

### 5.3.3 Quadratic Serendipity and Lagrange elements

Q2MS6 and S2MS6 elements are proposed in TKACHUK AND BISCHOFF (2013a). They may be considered as very good alternatives to LMM. They produce accurate results and enable calculation with large time-step sizes. However, conditioning of mass matrices obtained with S2MS6 prohibits large values for the selective mass scaling factor  $C_1$ . Conditioning of mass matrices obtained with Q2MS6 is by factors smaller. Thus, VSMS with six velocity modes can be used for broad ranges of the selective mass scaling factor  $C_1$ .

### 5.3.4 Linear tetrahedral element

Tetra4MS3 and Tetra4MS6 elements were proposed in ECK ET AL. (2014). These elements yield accurate results. They can be recommended for bulk structures free-meshed with tetrahedral meshes. Thus, it may be used in various areas like biomechanics and forging. More examples can be found in Sections 7.2 and 6.3. Ten-node quadratic tetrahedral elements (like *LS-Dyna* ELFORM=16 or *ANSYS SOLID92*) and composite ten-node tetrahedral elements (like *LS-Dyna* ELFORM=17) are not considered here. Extension of variational selective mass scaling for these elements is outlined in the outlook in Section 8.2.

### 5.3.5 Trilinear hexahedral element

The element formulation Hexa8MS3, Hexa8MS6, Hexa8MS9 and Hexa8MS12 are proposed and tested in TKACHUK AND BISCHOFF (2013b) and ECK ET AL. (2014). Hexa8MS6 is chosen for efficiency and accuracy, see for examples Section 7.2. The influence of number of velocity modes on accuracy and efficiency is given in ECK ET AL. (2014) and Subsections 6.3.3, 7.2.2, 7.2.3, 7.2.5. Further extensions of variational selective mass scaling for 20- and 27-node hexahedral element are outlined in the outlook in Section 8.2.

## 5.4 Mass matrices using incompatible velocity formulations

The shape functions for a nine-node quadrilateral element are constructed with the help of the shape functions for a three-node element according to equation (5.8). In this case, consistency of the mass matrix requires that the shape functions for incompatible velocity  $\tilde{\mathbf{N}}$  is orthogonal to at least constant velocity. A possible ansatz reads

$$\tilde{\mathbf{N}} = \frac{|J_0|}{|J|} \begin{bmatrix} N_1(\xi)N_1(\eta) & 0 & N_3(\xi)N_1(\eta) & 0 & \cdots \\ 0 & N_1(\xi)N_1(\eta) & 0 & N_3(\xi)N_1(\eta) & \cdots \end{bmatrix}, \quad (5.42)$$

where each function is product of corner shape functions for the three-node truss element Tr2-0. This element has eight incompatible velocity modes (parameters) and it is denoted as Q2IVM8. The consistency of the element Q2IVM8 is checked in Appendix A and eigenfrequency benchmark in Section 6.3. The same ansatz may be used for the discretization of the one-parametric family (4.31). This element is not considered here.

# 6

---

## Spectral analysis

In this section, the most important results for spectral and dispersion analysis are given. The details of the dispersion analysis are presented in Subsection 2.5.3. Here, examples from TKACHUK ET AL. (2013); TKACHUK AND BISCHOFF (2013b, c) are collected. New results for dispersion relations of VSMS are given in Section 6.2.

### 6.1 Dispersion relations for selected hybrid-mixed singular mass matrices

#### 6.1.1 Three-node truss element: Tr2-0

The dispersion analysis is performed on the basis of the patch equation and the local stiffness and mass matrices. In case of the truss element Tr2-0, these matrices read

$$\mathbf{k}^e = \frac{EA}{l_e} \begin{bmatrix} 4 & -6 & 2 \\ -6 & 12 & -6 \\ 2 & -6 & 4 \end{bmatrix}, \quad \mathbf{m}^{*,e} = \rho A l_e \begin{bmatrix} 0 & 0 & 0 \\ 0 & 1 & 0 \\ 0 & 0 & 0 \end{bmatrix}, \quad (6.1)$$

with  $l_e$  being the element length. The solution of the equation of motion is a harmonic wave, and the corresponding ansatz for it at the  $j^{\text{th}}$  node reads

$$U_j(t) = U_c \exp(i(\kappa j/2 - \Omega ct/l_e)) \quad \text{for } j \text{ odd}, \quad (6.2)$$

$$U_j(t) = U_m \exp(i(\kappa j/2 - \Omega ct/l_e)) \quad \text{for } j \text{ even}, \quad (6.3)$$

with  $U_c$  and  $U_m$  being the complex-valued amplitudes at the corner and middle nodes, respectively, and  $c = \sqrt{E/\rho}$  being the speed of sound. The amplitudes  $U_c$  and  $U_m$  form an unknown

patch amplitude vector  $\tilde{\mathbf{U}}_{rep} = [U_m, U_c]$ . Substitution of the ansatz in the equation of motion leads to a homogeneous system with the two unknowns  $U_c$  and  $U_m$

$$\left( -\Omega^2 \begin{bmatrix} 0 & 1 & 0 & 0 & 0 \\ 0 & 0 & 0 & 0 & 0 \end{bmatrix} + \begin{bmatrix} -6 & 12 & -6 & 0 & 0 \\ 2 & -6 & 8 & -6 & 2 \end{bmatrix} \right) \begin{bmatrix} U_c e^{-i\kappa} \\ U_m \\ U_c \\ U_m e^{i\kappa} \\ U_c e^{i\kappa} \end{bmatrix} = \mathbf{0}, \quad (6.4)$$

$$\begin{bmatrix} -6e^{-i\kappa} - 6 & -\Omega^2 + 12 \\ 4\cos(\kappa) + 8 & -6 - 6e^{i\kappa} \end{bmatrix} \begin{bmatrix} U_c \\ U_m \end{bmatrix} = \mathbf{0}. \quad (6.5)$$

A non-trivial solution of (6.5) only exists, if the determinant of the system is zero. This condition yields the characteristic equation, from which the dispersion relation is obtained with

$$\Omega^2 = \frac{6(1 - \cos(\kappa))}{\cos(\kappa) + 2}. \quad (6.6)$$

In the case of a 1D problem, the analytical solution predicts non-dispersive wave propagation  $\Omega_0 = \kappa$ , i.e., the wave speed is constant for all wave numbers (see Figure 6.1). The semi-discrete solutions are dispersive. The TAYLOR expansion of the dispersion relation (6.6) at  $\kappa = 0$  is

$$\Omega^2 = \kappa^2 + \frac{1}{12}\kappa^4 + \frac{1}{360}\kappa^6 + O(\kappa^8), \quad (6.7)$$

and coincides with the expression for the continuum problem  $\Omega_0^2 = \kappa^2$  up to the fourth order term.

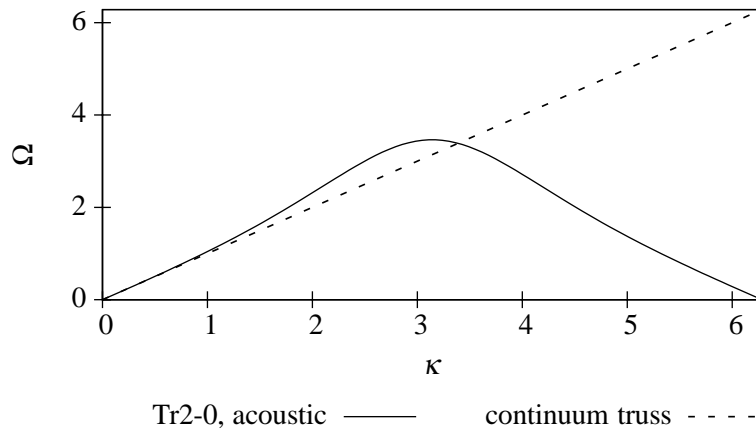


**Figure 6.1:** Dispersion for a quadratic truss element with constant velocities, Tr2-0.

Thus, the phase velocity for long waves ( $\kappa \rightarrow 0$ ) and the values of the lowest eigenfrequencies converge uniformly to the exact solution. Surprisingly, the dispersion relation of the element Tr2-0 coincides with the dispersion relation of a two-node truss element with CMM, see BELYTSCHKO (1978). Moreover, the dispersion relation of the element Tr3-1 (see below (6.16)) coincides with the dispersion relation of a three-node truss element with CMM, refer to BELYTSCHKO (1978).

### 6.1.2 Four-node truss element: Tr3-1

The spectral analysis for the element Tr3-1 is performed analogously to the element Tr2-0. The stiffness matrix and HSMM read

$$\mathbf{k}^e = \frac{3EA}{l_e} \begin{bmatrix} 3 & -\sqrt{5}-1 & \sqrt{5}-1 & -1 \\ -\sqrt{5}-1 & 4 & -2 & \sqrt{5}-1 \\ \sqrt{5}-1 & -2 & 4 & -\sqrt{5}-1 \\ -1 & \sqrt{5}-1 & -\sqrt{5}-1 & 3 \end{bmatrix}, \quad \mathbf{m}^e = \frac{\rho A l_e}{10} \begin{bmatrix} 0 & 0 & 0 & 0 \\ 0 & 4 & 1 & 0 \\ 0 & 1 & 4 & 0 \\ 0 & 0 & 0 & 0 \end{bmatrix}. \quad (6.8)$$

The solution is assumed in the form of harmonic waves with

$$U_j(t) = U_c \exp(i(\kappa j/3 - \Omega ct/l_e)) \quad \text{for } j \bmod 3 = 0, \quad (6.9)$$

$$U_j(t) = U_{m1} \exp(i(\kappa j/3 - \Omega ct/l_e)) \quad \text{for } j \bmod 3 = 1, \quad (6.10)$$

$$U_j(t) = U_{m2} \exp(i(\kappa j/3 - \Omega ct/l_e)) \quad \text{for } j \bmod 3 = 2, \quad (6.11)$$

with  $U_c$ ,  $U_{m1}$  and  $U_{m2}$  being the corner and the two midnode amplitudes.

The reduced matrices for the patch equation given in (2.119) read

$$\mathbf{M}^{red} = -\frac{\Omega^2}{10} \begin{bmatrix} 0 & 1 & 4 & 0 & 0 & 0 & 0 \\ 0 & 0 & 0 & 0 & 0 & 0 & 0 \\ 0 & 0 & 0 & 0 & 4 & 1 & 0 \end{bmatrix}, \quad (6.12)$$

$$\mathbf{K}^{red} = 3 \begin{bmatrix} \sqrt{5}-1 & -2 & 4 & -\sqrt{5}-1 & 0 & 0 & 0 \\ -1 & \sqrt{5}-1 & -\sqrt{5}-1 & 6 & -\sqrt{5}-1 & \sqrt{5}-1 & -1 \\ 0 & 0 & 0 & -\sqrt{5}-1 & 4 & -2 & \sqrt{5}-1 \end{bmatrix}, \quad (6.13)$$

$$\tilde{\mathbf{U}}^{red} = [U_c e^{-i\kappa} \quad U_{m1} \quad U_{m2} \quad U_c \quad U_{m1} e^{i\kappa} \quad U_{m2} e^{i\kappa} \quad U_c e^{i\kappa}]^T. \quad (6.14)$$

The characteristic equation finally results in

$$\begin{bmatrix} -18e^{-i\kappa} + 12 & 1/2\Omega^2 - 42 & -\Omega^2 + 48 \\ -6\cos(\kappa) + 18 & -18 + 12e^{i\kappa} & 12 - 18e^{i\kappa} \\ 12 - 18e^{i\kappa} & -e^{i\kappa}(\Omega^2 - 48) & 1/2e^{i\kappa}(\Omega^2 - 84) \end{bmatrix} \begin{bmatrix} U_{m2} \\ U_c \\ U_{m1} \end{bmatrix} = \mathbf{0}. \quad (6.15)$$

The spectral analysis offers two branches for the dispersion relation. These branches may be classified as acoustic and optical branches according to FELIPPA (2001) with the following expressions for dispersion

$$\Omega_{aco}^2 = 4 \frac{13 + 2 \cos(\kappa) - R_1}{3 - \cos(\kappa)}, \quad \Omega_{opt}^2 = 4 \frac{13 + 2 \cos(\kappa) + R_1}{3 - \cos(\kappa)}, \quad (6.16)$$

with  $R_1 = \sqrt{124 + 112 \cos(\kappa) - 11 \cos^2(\kappa)}$ . The TAYLOR expansion of the acoustic branch  $\Omega_{aco}^2$  is exact up to  $O(\kappa^6)$ , i.e. the first eigenvalue converges with sixth order, see Figure 6.2.

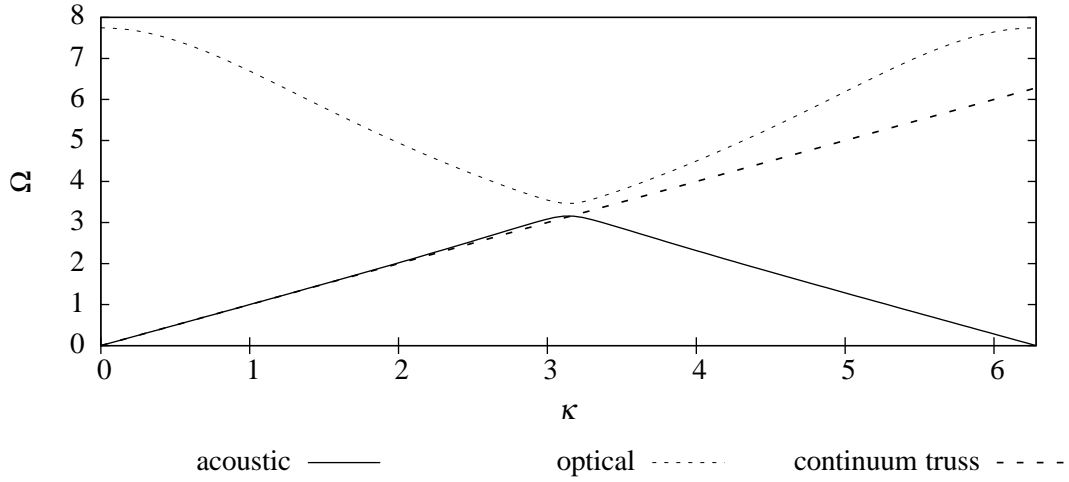


**Figure 6.2:** Dispersion for a cubic truss element with linear velocities, Tr3-1.

### 6.1.3 Quadratic Timoshenko element

The exact dispersion relation for a TIMOSHENKO beam is given in FELIPPA (2010) and FELIPPA (2001). It can be found from the characteristic equation

$$\kappa^4 - \Omega^2 - \left( \frac{EI}{GA_s l_e^2} + \frac{r_g^2}{l_e^2} \right) \kappa^2 \Omega^2 + \frac{EI r_g^2}{GA_s l_e^4} \Omega^4 = 0. \quad (6.17)$$

This characteristic equation yields solution with two branches, i.e. flexural (bending) and shear. The TAYLOR expansions of these solutions for rectangular cross-section and  $\nu = 0.0$ , no shear correction (i.e.  $GA_s = GA$ ) are given here as a reference

$$\Omega_{bend}^2 = \kappa^4 - 1/4 \Lambda^2 \kappa^6 + \frac{11}{144} \Lambda^4 \kappa^8 - \frac{5}{192} \Lambda^6 \kappa^{10} + O(\kappa^{12}), \quad (6.18a)$$

$$\Omega_{shear}^2 = \frac{72}{\Lambda^4} + 18 \frac{\kappa^2}{\Lambda^2} - \kappa^4 + 1/4 \Lambda^2 \kappa^6 - \frac{11}{144} \Lambda^4 \kappa^8 + \frac{5}{192} \Lambda^6 \kappa^{10} + O(\kappa^{12}), \quad (6.18b)$$

| Instance   | Description   | Dispersion behavior   |
|------------|---|---|
| Ti2-2-2-2  | Standard shape functions for displacements and rotations                    | Four branches. Flexural and shear branches match the analytical expressions for continuum beam up to $O(\kappa^8)$ and $O(\kappa^6)$ . Third branch is the continuation of flexural branch without gap. Fourth branch is optical with a gap above the shear branch. |
| Ti2-2-0-0  | Constant ansatz for translational and angular velocities                    | Two branches. Flexural and shear branches match the analytical expressions for a continuum beam up to $O(\kappa^6)$ and $O(\kappa^2)$ , respectively.   |
| Ti2-2-0-1  | Constant ansatz for translational velocity and linear angular velocities    | Three branches. Flexural and shear branches match the analytical expressions for continuum beam up to $O(\kappa^6)$ and $O(\kappa^2)$ , respectively. Third branch is optical with a gap above the shear branch.  |
| Ti2-2-0-2  | Constant ansatz for translational velocity and quadratic angular velocities | Three branches. Flexural and shear branches match the analytical expressions for a continuum beam up to $O(\kappa^6)$ and $O(\kappa^4)$ , respectively. Third branch is optical lying between flexural and shear branches.  |
| Ti2*-2-1-2 | Linked interpolation formulation according to (5.21)                        | Three branches. Flexural and shear branches match the analytical expressions for a continuum beam up to $O(\kappa^8)$ and $O(\kappa^0)$ , respectively. Third branch is the continuation of the flexural branch without a gap.                                      |

**Table 6.1:** Comparison of dispersion properties of TIMOSHENKO beam element formulations (TKACHUK ET AL. 2013).

where  $\Lambda = \frac{h}{t_e}$  is the length-to-thickness ratio of an individual element.

The spectral analysis for quadratic TIMOSHENKO beam is quite technical. The length of representative amplitude vector  $\tilde{\mathbf{U}}^{red}$  is four, i.e. the corner and midnode displacements and rotations. The resulting characteristic equation is cubic or quartic for singular and consistent mass matrix, respectively. Expressions for dispersion relations are found and analyzed with the help of the computer algebra system *Maple*. The number of branches for dispersion relations and their properties are summarized in Table 6.1.

The dispersion curves for a Ti2-2-0-2 element in the case of shear-to-bending ratio  $l_e^2 GA = 100EI$  are given in Figure 6.3. Note, that the shear acoustic branch for short waves ( $k \rightarrow 0$ ) gives correct values for the phase velocity  $96\sqrt{2}$ . The errors for short shear and flexural waves with  $k \rightarrow \pi$  are 1.3 % and 23.8 %, respectively. The smaller accuracy of the flexural branch is caused by the poorer ansatz space chosen for the translational velocity (only constant). The larger relative error in the flexural branch leads to higher dispersive ripples in the flexural part of the solution in the wave propagation benchmark, see Figure 7.6.

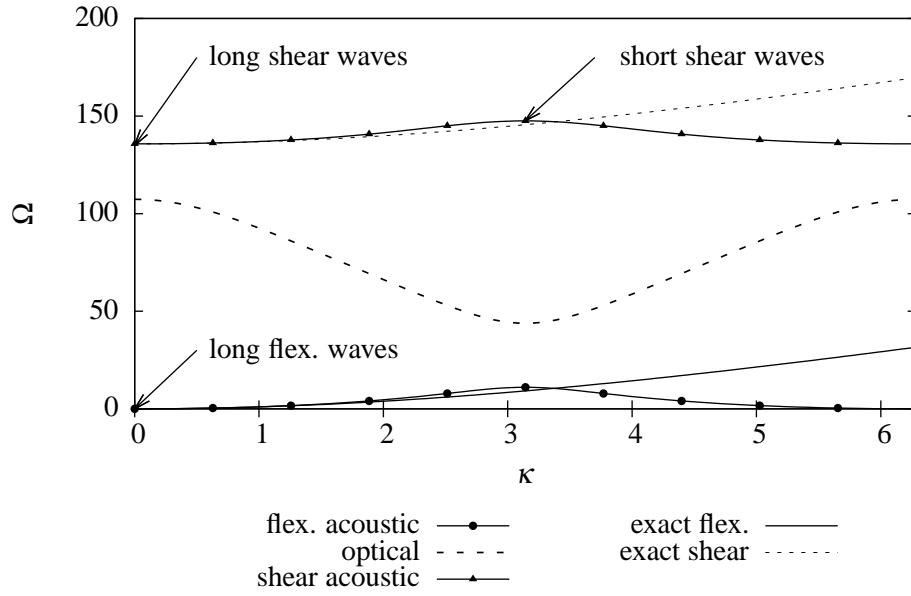


**Figure 6.3:** Dispersion of a TIMOSHENKO Tr2-2-0-2 element vs. dispersion of continuum TIMOSHENKO beam model,  $\Lambda = 1/4$ .

## 6.2 Dispersion relations for selected SMS templates

### 6.2.1 Truss elements

#### Two-node truss element

Consider a two-node truss element with constant velocity shape functions and one parametric mass matrix template. The dispersion relation is computed following the standard procedure. The element matrices read

$$\mathbf{N} = \left[ \frac{1}{2}(1 - \xi) \quad \frac{1}{2}(1 + \xi) \right], \quad \boldsymbol{\Psi} = [1], \quad (6.19)$$

$$\mathbf{k}_e = \frac{EA}{l_e} \begin{bmatrix} 1 & -1 \\ -1 & 1 \end{bmatrix}, \quad \mathbf{m}_e = \frac{\rho A l_e}{6} \begin{bmatrix} 2 & 1 \\ 1 & 2 \end{bmatrix}, \quad \mathcal{Y} = \rho A l_e [1], \quad (6.20)$$

$$\mathcal{A} = \frac{\rho A l_e}{2} [1 \quad 1], \quad \mathcal{A} \mathcal{Y}^{-1} \mathcal{A}^T = \frac{\rho A l_e}{4} \begin{bmatrix} 1 & 1 \\ 1 & 1 \end{bmatrix}, \quad \boldsymbol{\lambda}_e^\circ = \frac{\rho A l_e}{12} \begin{bmatrix} 1 & -1 \\ -1 & 1 \end{bmatrix}. \quad (6.21)$$

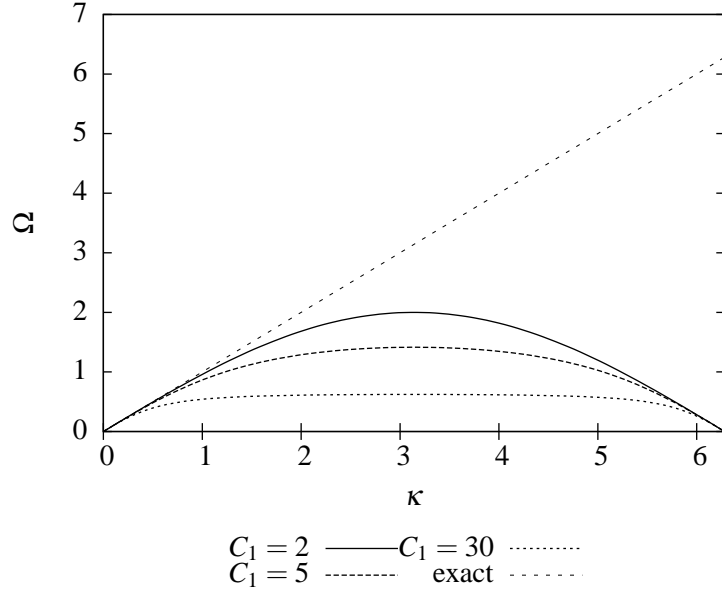


**Figure 6.4:** Dispersion of Tr2MS1 element vs. continuum truss model.

Note, the hybrid mixed mass matrix  $\mathbf{m}_e^\circ$  satisfies the velocity patch tests A,B,C,D and E. The solution for the dynamic equation is assumed in the form of a harmonic wave

$$U_j(t) = U_c \exp(i(\kappa j - \Omega ct/l_e)) \quad \text{for all } j. \quad (6.22)$$

Substitution of latter ansatz in the equation of motion leads to a patch equation with two elements and one unknown

$$\left( \frac{-\Omega^2}{12} [[2 \ 4 \ 2] + C_1 [-1 \ 2 \ -1]] + [-1 \ 2 \ -1] \right) \begin{bmatrix} \exp(-i\kappa) \\ 1 \\ \exp(i\kappa) \end{bmatrix} U_c = 0. \quad (6.23)$$

The latter equation may be solved for  $\Omega^2$ , yielding the dispersion relation for the acoustic branch

$$\Omega_{aco}^2 = \frac{12(1 - \cos \kappa)}{4 + 2 \cos \kappa + C_1(1 - \cos \kappa)}. \quad (6.24)$$

The spectral relations for  $C_1 = [2,5,30]$  are shown in Figure 6.4.

The TAYLOR expansion of the acoustic branch  $\Omega_{aco}^2$  at  $\kappa = 0$  reads

$$\Omega^2 = \kappa^2 + \frac{1 - C_1}{12} \kappa^4 + \frac{1 + 4C_1 + 5C_1^2}{720} \kappa^6 + O(\kappa^8). \quad (6.25)$$

If the mass scaling factor is chosen to be  $C_1 = 1$ , then the TAYLOR expansion is exact up to the sixth order and up to the fourth order, otherwise. The maximum frequency may be obtained from the acoustic branch. The extreme values of the dimensionless frequency may be obtained for very short ( $\kappa = \pi$ ) waves with

$$\Omega_{\max}^2 = \frac{12}{C_1 + 1}. \quad (6.26)$$

Thus, the critical time-step for the element in dependence of  $C_1$  can be computed as

$$dt_{\text{crit}} = \frac{2}{\omega_{\max}} = \frac{2}{\Omega_{\max}} \frac{l_e}{c} = \sqrt{\frac{C_1 + 1}{3}} \frac{l_e}{c}. \quad (6.27)$$

For reference, CMM and RSL result in  $dt_{\text{crit}} = \frac{l_e}{\sqrt{3}c}$  and  $dt_{\text{crit}} = \frac{l_e}{c}$ , respectively (BELYTSCHKO ET AL. 2001). The growth of the time-step size is conform with other SMS methods with  $\sqrt{1 + C_1}$ .

### Three-node truss element

Consider a three-node truss element with standard LAGRANGE shape functions and velocity shape functions according to equation (5.33). Here, constant Jacobian  $|J| = \frac{l_e}{2}$  and constant section properties are assumed. The dispersion relation can be derived as follows. Shape functions and element matrices read

$$\mathbf{N} = \left[ \frac{1}{2}(\xi^2 - \xi) \quad 1 - \xi^2 \quad \frac{1}{2}(\xi^2 + \xi) \right], \quad \Psi = [1 \quad x^h] \equiv \left[ 1 \quad \frac{l_e}{2}\xi \right], \quad (6.28)$$

$$\mathbf{k}_e = \frac{EA}{3l_e} \begin{bmatrix} 7 & -8 & 1 \\ -8 & 16 & -8 \\ 1 & -8 & 7 \end{bmatrix}, \quad \mathbf{m}_e = \frac{\rho A l_e}{30} \begin{bmatrix} 4 & 2 & -1 \\ 2 & 16 & 2 \\ -1 & 2 & 4 \end{bmatrix}, \quad (6.29)$$

$$\mathcal{Y} = \frac{\rho A l_e}{12} \begin{bmatrix} 12 & 0 \\ 0 & l_e^2 \end{bmatrix}, \quad \mathcal{A} = \frac{\rho A l_e}{12} \begin{bmatrix} 2 & 8 & 2 \\ -l_e & 0 & l_e \end{bmatrix}, \quad (6.30)$$

$$\mathcal{A} \mathcal{Y}^{-1} \mathcal{A}^T = \frac{\rho A l_e}{18} \begin{bmatrix} 2 & 2 & -1 \\ 2 & 8 & 2 \\ -1 & 2 & 2 \end{bmatrix}, \quad \boldsymbol{\lambda}_e^\circ = \frac{\rho A l_e}{45} \begin{bmatrix} 1 & -2 & 1 \\ -2 & 4 & 2 \\ 1 & -2 & 1 \end{bmatrix}. \quad (6.31)$$

Note, that the hybrid mixed mass matrix  $\mathbf{m}_e^\circ$  satisfies the velocity patch tests A,B,C,D and E. The solution for the dynamic equation is assumed in the same form as for the element Tr2-0 in equation (6.3). The representative patch contains two elements and the length of the

representative amplitude vector  $\tilde{\mathbf{U}}$  is two. The dynamic equation of motion reads

$$\left(\frac{-\Omega^2}{30} \begin{bmatrix} 6 & 48 & 6 & 0 & 0 \\ -3 & 6 & 24 & 6 & -3 \end{bmatrix} + C_1 \begin{bmatrix} -4 & 8 & 4 & 0 & 0 \\ 2 & -4 & 4 & -4 & 2 \end{bmatrix} + \begin{bmatrix} -8 & 16 & -8 & 0 & 0 \\ 1 & -8 & 14 & -8 & 1 \end{bmatrix}\right) \tilde{\mathbf{U}} = \mathbf{0}. \quad (6.32)$$

The latter equation leads to the biquadratic characteristic equation

$$\tilde{a}_4 \Omega^4 + \tilde{a}_2 \Omega^2 + \tilde{a}_0 = 0, \quad (6.33)$$

where the coefficients of the equation are defined as

$$\tilde{a}_4 = 3 \cos \kappa - 9 - 2C_1(2 + \cos \kappa), \quad \tilde{a}_2 = 48 \cos \kappa + 312 + 12C_1(1 - \cos \kappa) \quad (6.34)$$

$$\tilde{a}_0 = 720(\cos \kappa - 1). \quad (6.35)$$

Solving equation (6.33) for  $\Omega^2$  results in two branches for the spectral relation with

$$\Omega_{aco}^2 = \frac{-\tilde{a}_2 + \sqrt{\tilde{a}_2^2 - 4\tilde{a}_0\tilde{a}_4}}{2\tilde{a}_4}, \quad \Omega_{opt}^2 = \frac{-\tilde{a}_2 - \sqrt{\tilde{a}_2^2 - 4\tilde{a}_0\tilde{a}_4}}{2\tilde{a}_4}, \quad (6.36a)$$

The spectral relations for  $C_1 = [2, 10]$  are shown in Figure 6.5.

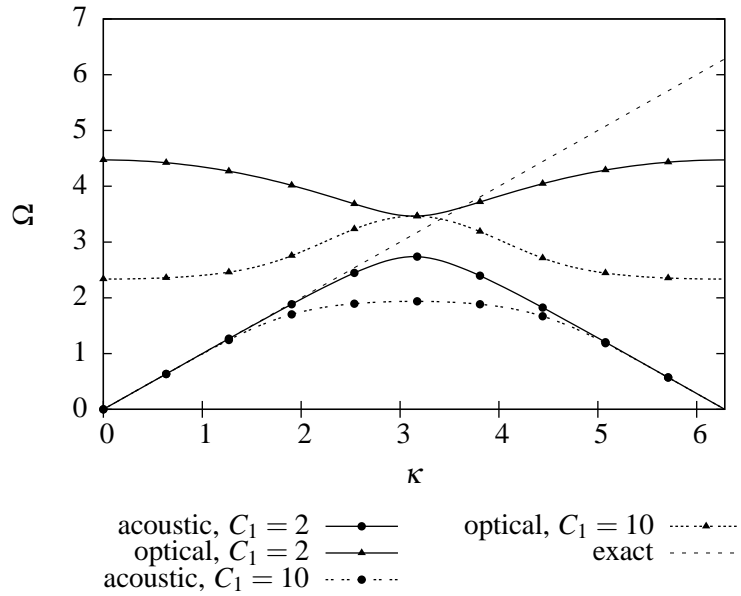


**Figure 6.5:** Dispersion of Tr3MS2 element vs. continuum truss model.

The TAYLOR expansion of the acoustic branch  $\Omega_{aco}^2$  at  $\kappa = 0$  reads

$$\Omega^2 = \kappa^2 + \frac{1 - C_1}{720} \kappa^6 + \frac{-22 + 21C_1 - 7C_1^2}{302400} \kappa^8 + O(\kappa^{10}). \quad (6.37)$$

If the mass scaling factor is chosen to be  $C_1 = 1$ , then the TAYLOR expansion is exact up to the eighth order and up to the sixth order, otherwise. The maximum frequency may be obtained from the optical branch. The extreme values of the dimensionless frequency may be obtained for very short ( $\kappa = \pi$ ) or long waves ( $\kappa = 0$ ) with

$$\Omega_{\max}^2 = \max \left( 12, \frac{60}{C_1 + 1} \right). \quad (6.38)$$

Thus, the critical time-step size for the element in dependence of  $C_1$  can be computed as

$$dt_{\text{crit}} = \frac{2}{\omega_{\max}} = \frac{2}{\Omega_{\max}} \frac{l_e}{c} = \min \left( \sqrt{\frac{1}{3}}, \sqrt{\frac{C_1 + 1}{15}} \right) \frac{l_e}{c}. \quad (6.39)$$

For reference, CMM and RSL result in  $dt_{\text{crit}} = \frac{l_e}{\sqrt{15}c}$  and  $dt_{\text{crit}} = \frac{l_e}{\sqrt{6}c}$ , respectively, see BE-LYTSCHKO ET AL. (2001). This means that for  $C_1 > 4$  the critical time-step size is limited by the first argument in the min function and does not decrease any further for greater values of  $C_1$ . The critical time-step size can be maximally increased by a factor  $\sqrt{2}$  w.r.t. RSL.

A stronger reduction of the maximum frequency requires a poorer ansatz space for velocity  $\Psi$ , e.g.  $\Psi = [1]$ . Derivation of element matrices and dispersion relations for this mass scaling is omitted. The resulting critical time-step size is  $\sqrt{\frac{C_1 + 1}{15}} \frac{l_e}{c}$ . Thus, the time-step size is proportional to  $\sqrt{1 + C_1}$  like at other SMS techniques. However, the acoustic branch for this ansatz is exact up to the fourth order.

## 6.2.2 Two-node Timoshenko element

Consider a two-node TIMOSHENKO beam with rectangular cross-section  $GA_s = GA$ ,  $\nu = 0.0$  and exact stiffness, see ZIENKIEWICZ AND TAYLOR (2006). Now, the dispersion analysis is performed for a one parametric family of matrices, corresponding to case 1. The velocity shape functions read

$$\Psi = [1 \quad 0]^T, \quad (6.40)$$

i.e. a constant translational velocity and no rotary velocity functions are assumed.

The main results are reported here, omitting the intermediate steps. Only two branches are obtained, an acoustic flexural and an acoustic shear. TAYLOR expansion of the flexural branch

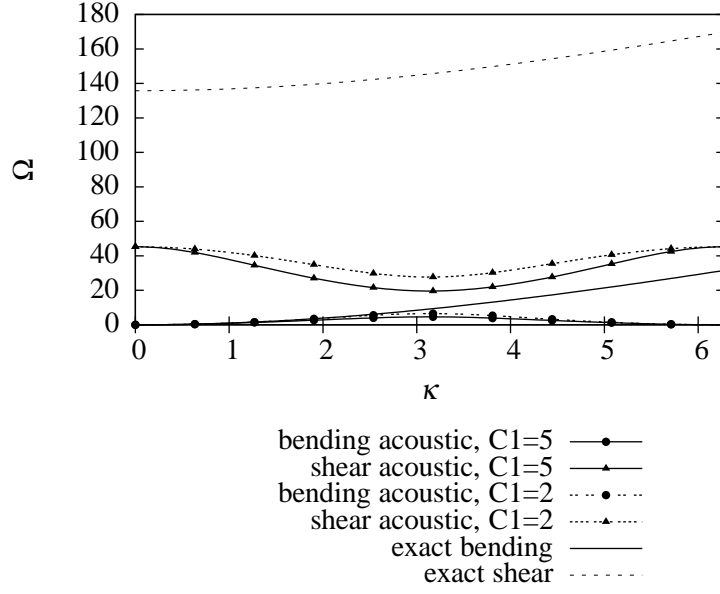


**Figure 6.6:** Dispersion of Timoshenko Ti1-1-1-1MS2 element vs. continuum beam model,  $\Lambda = 1/4$ . VSMS with constant ansatz for velocity.

reads

$$\omega_{bend}^2 = \kappa^4 - (1/4\Lambda^2 + 1/12C_1 - 1/12\Lambda^2C_1 - 1/6) \kappa^6 + O(\kappa^8). \quad (6.41)$$

This means only fourth order accuracy is attained. The extreme values of the dimensionless frequency are obtained for very short ( $\kappa = \pi$ ) shear waves. The maximum dimensionless frequency is

$$\Omega_{\max}^2 = \frac{144}{\Lambda^2(C_1 + 1)}. \quad (6.42)$$

Thus, the critical time-step size for the element dependant of  $C_1$  can be computed as

$$dt_{\text{crit}} = \frac{2}{\omega_{\max}} = \frac{2}{\Omega_{\max}} \frac{l_e}{c} = \sqrt{\frac{h(C_1 + 1)}{12l_e}} \frac{l_e}{c} = \frac{h}{6c} \sqrt{C_1 + 1}. \quad (6.43)$$

Note, that if  $\Psi$  contains linear translational velocity, then the shear branch for long waves is unaffected by mass scaling. In this case, the critical time-step is defined as

$$\Omega_{\max}^2 = \max \left( \frac{144}{\Lambda^2(C_1 + 1)}, \frac{144}{\Lambda^2(2\Lambda^2 + 1)} \right). \quad (6.44)$$

The second term of the latter expression does not depend on the mass scaling parameter  $C_1$ . Hence, for such an ansatz  $\Psi$ , VSMS is not efficient. This is illustrated in Figure 6.6, where two shear acoustic branches for  $C_1 = 2$  and 5 intersect the axis with  $\kappa = 0$  at values independent of  $C_1$ . This value depends only on the slenderness  $\Lambda$  and can be evaluated as

$$\Omega_{\max}(\Lambda = 1/4) = \frac{12}{\Lambda\sqrt{2\Lambda^2 + 1}} \Big|_{\Lambda=1/4} = 32\sqrt{2} \approx 45.25. \quad (6.45)$$

### 6.2.3 Three-node Timoshenko element

Consider a three-node TIMOSHENKO beam. The stiffness matrix of the element is computed using two-point reduced integration and the mass matrix is computed with VSMS for a complete linear ansatz of  $\Psi$ .

The main results are reported here, omitting the intermediate steps. In this case, four branches are observed: acoustic flexural, optical flexural, acoustic shear and optical shear. TAYLOR expansion of the acoustic flexural branch reads

$$\begin{aligned} \omega_{bend}^2 &= \kappa^4 - \left( \frac{1}{4}\Lambda^2 + \frac{1}{12}C_1 \right) \kappa^6 \\ &+ \left( \frac{1}{180}C_1 + \frac{1}{144}C_1^2 + \frac{1}{48}\Lambda^2 C_1 + \frac{1}{240} + \frac{11}{144}\Lambda^4 \right) \kappa^8 + O(\kappa^{10}). \end{aligned} \quad (6.46)$$

This means that only the fourth order accuracy is attained if  $C_1 \neq 0$ . The extreme values of the dimensionless frequency are obtained for very long waves ( $\kappa = 0$ ), for the optical shear branch, or very short waves ( $\kappa = \pi$ ), for the acoustic bending branch

$$\Omega_{\max}^2 = \max \left( \frac{720}{\Lambda^2(C_1 + 1)}, \frac{72}{\Lambda^4} \right). \quad (6.47)$$

The mass scaling is efficient only if shear the branch is not consistently approximated (spoiled). Otherwise, the maximum frequency depends on the slenderness  $\Lambda$ . This also implies that VSMS in the form used here is not efficient for rotational DOF's. So, further research is needed in this direction.

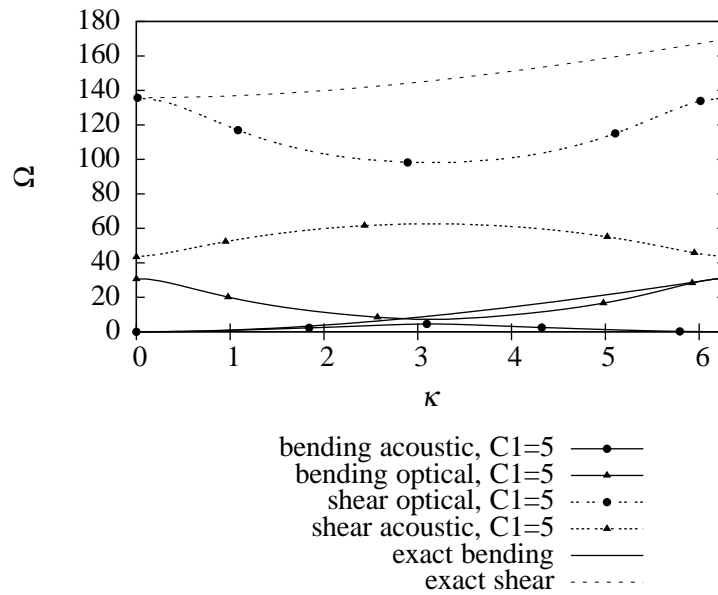


**Figure 6.7:** Dispersion of a Timoshenko Tr2-2-2-2MS2 element vs. continuum model,  $\Lambda = 1/4$ . VSMS with a linear ansatz for translational velocity.

## 6.3 Eigenvalue benchmarks

### 6.3.1 NAFEMS FV32

As an example of a two-dimensional problem, the eigenfrequency benchmark FV32 of NAFEMS (NAFEMS 1990) is considered. Geometry, mesh and material properties of the model are presented in Figure 6.8. Boundary conditions  $u_x = u_y = 0$  are imposed along the y-axis. Here, Q1, Q2 and S2 types of elements are tested. For the bilinear 4-node element Q1, enhanced assumed strains formulation with four EAS modes is used for stiffness calculation and  $3 \times 3$  quadrature rule is used for mass computation. For S2 and Q2 elements, pure displacement formulation with  $3 \times 3$  quadrature is used for stiffness computation, and  $4 \times 4$  quadrature rule is used for mass matrix computation. The six lowest modes are shown in Figure 6.9. The reference values to the frequencies are given in Table 6.2. Note, that modes 1, 2, 4 and 6 are bending dominated modes, while modes 3 and 5 are longitudinal modes.

### Hybrid-Singular Mass Matrices

Consistency of hybrid singular mass matrix formulations of Q2P10V10 and Q2E8 is tested here. Results for the six lowest eigenfrequencies are presented in Table 6.2. Computed frequencies agree with the reference values.

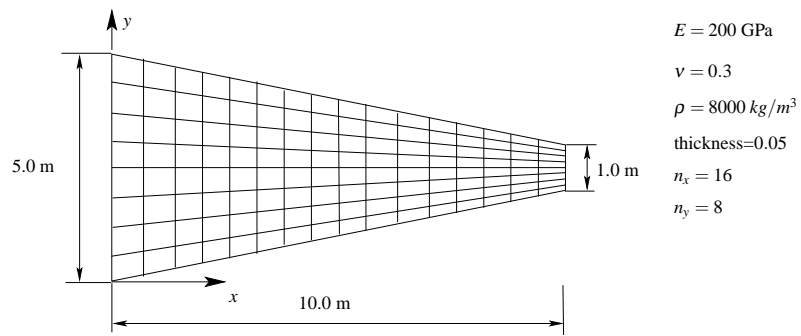


**Figure 6.8:** Setup of FV32 NAFEMS benchmark.

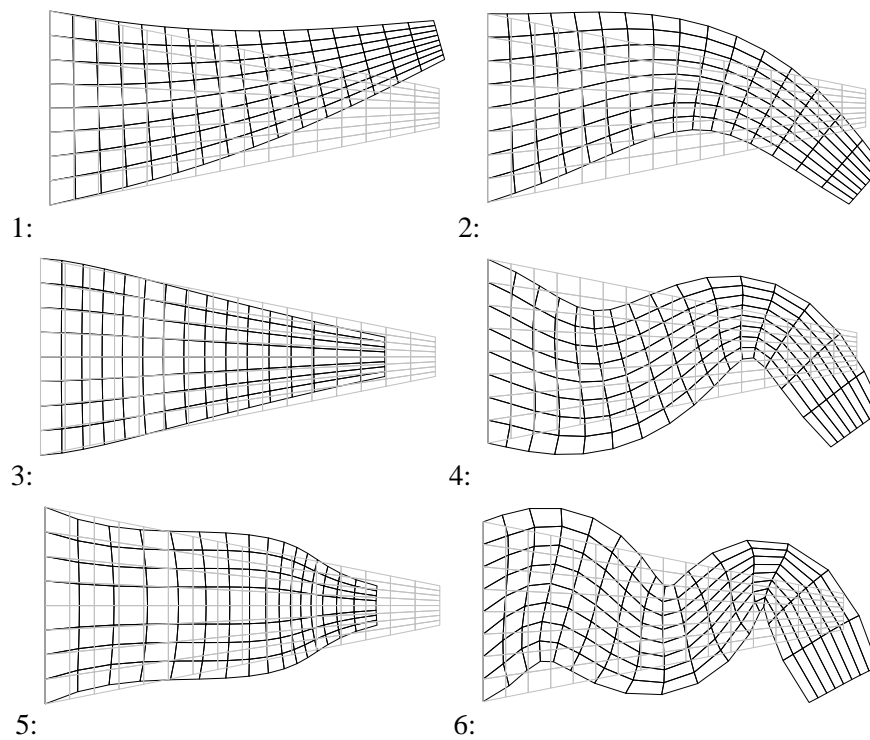


**Figure 6.9:** The six lowest modes for FV32 NAFEMS benchmark computed with Q1 element and CMM.

|           | $f_1$ , Hz | $f_2$ , Hz | $f_3$ , Hz | $f_4$ , Hz | $f_5$ , Hz | $f_6$ , Hz |
|-----------|------------|------------|------------|------------|------------|------------|
| Reference | 44.623     | 130.03     | 162.70     | 246.05     | 379.90     | 391.44     |
| Q2P10V10  | 44.630     | 130.14     | 162.71     | 246.76     | 382.01     | 391.54     |
| Q2E8:     | 44.630     | 130.12     | 162.71     | 246.81     | 382.03     | 391.54     |

**Table 6.2:** Six lowest frequencies for FV32 benchmark computed with hybrid singular mass matrices.

| $\Psi$ from                                 | Q1MS2 | Q1MS3 | Q1MS4 | Q1ASMS, $\beta = 2$ |
|---|-------|-------|-------|---------------------|
| $f_{max}$ , Hz                              | 4036  | 4045  | 7198  | 4459                |
| $f_{max}/f_{max}^{LMM}$                     | 0,35  | 0.35  | 0.63  | 0.39                |
| $\text{cond}(\mathbf{P}_j\mathbf{M}^\circ)$ | 14.1  | 26.9  | 39.3  | 11.0                |
| error in lowest 10% freq., %                | 56    | 38    | 31    | 49                  |

**Table 6.3:** Comparison of different mass scaling formulations for FV32,  $C_1 = 30$ .

### Selective Mass Scaling

The proposed family of mass matrices is obtained from the novel variational formulations. The influence of the proposed mass scaling techniques on eigenvalues of structures is studied. These problems are small enough so that the full spectra can be obtained and analyzed. Efficiency of mass scaling is estimated by the reduction of the maximum frequency  $f_{max}$ . The spectrum computed for a LMM is taken as a reference. Additionally, the comparison is done by the condition number of mass matrices and the maximum error in the lowest 10% range of the spectra, which is important for the structural response.

The reduction of eigenfrequencies for Q1MS3 with different values of the scaling parameter  $C_1$  are shown in Figure 6.10. Increase of  $C_1$  decreases the maximum frequency. For  $C_1 < 5$  the maximum frequency of the scaled mass matrix is higher than for the LMM. For  $C_1 = 20$  the maximum frequency is halved and for  $C_1 = 30$  decreased by a factor of three. Comparable reduction of maximum frequency can be obtained with Q1ASMS with  $\beta = 2$ , however the error in lowest eigenfrequencies for the proposed method is smaller. Performance of the proposed method for a set of ansatz function for velocity  $\Psi$  with fixed penalty value  $C_1 = 30$  is examined and results are presented in Table 6.3. As a reference, performance of the element Q1ASMS is also given.

A similar study is done for S2MS6 and Q2MS6 elements. Results for the six lowest eigenfrequencies computed with S2MS6 are presented in Table 6.4. Variational mass scaling is capable of accurate approximation of these six lowest frequencies. The error for S2ASMS with scaling factor  $\beta = 2$  is much larger. Dependency of the critical time-step on scaling parameter  $C_1$  and  $\beta$  is given in Table 6.5. The following observations can be made from the table. The values of conditioning of mass matrix for variational selective mass scaling are larger than for ASMS. Conditioning for S2MS6 is by a factor two larger than for Q2MS6. Similar observation are made for larger model of an arch bridge, see Table 7.1.

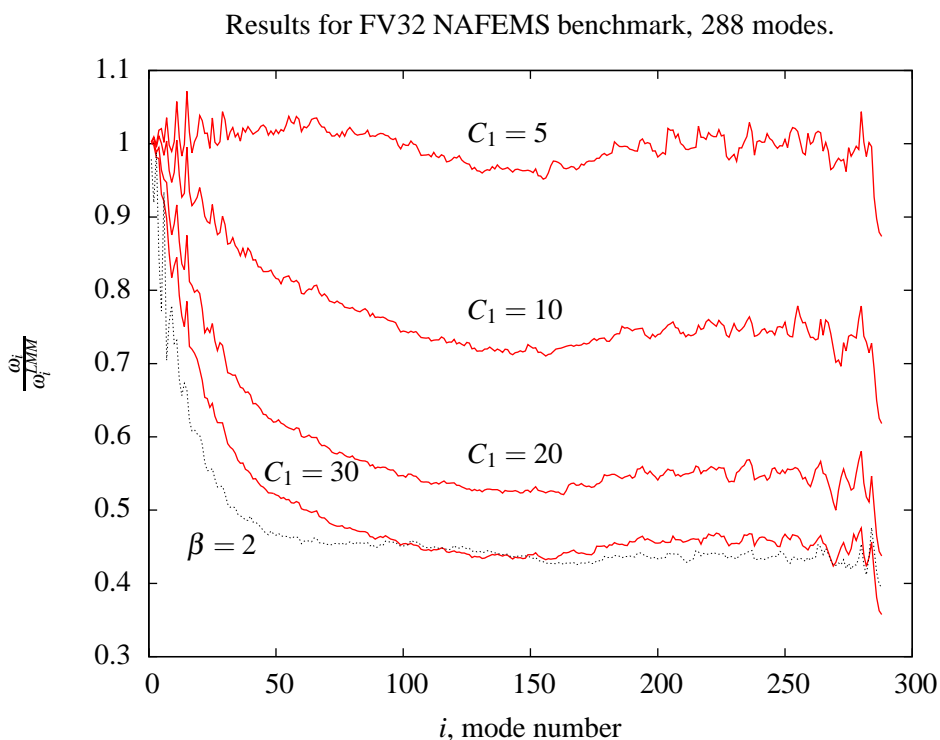


**Figure 6.10:** Ratio of eigenfrequencies for different values of selective mass scaling parameters.  $C_1$  - proposed in paper with  $\Psi$  from (5.30),  $\beta$  - method II OLOVSSON ET AL. (2005).

|                     | $f_1$ , Hz | $f_2$ , Hz | $f_3$ , Hz | $f_4$ , Hz | $f_5$ , Hz | $f_6$ , Hz |
|---------------------|------------|------------|------------|------------|------------|------------|
| reference           | 44.623     | 130.03     | 162.70     | 246.05     | 379.90     | 391.44     |
| CMM                 | 44.626     | 130.06     | 162.70     | 246.15     | 380.23     | 391.46     |
| $C_1 = 10$          | 44.625     | 130.01     | 162.70     | 245.72     | 378.04     | 391.30     |
| $C_1 = 30$          | 44.622     | 129.93     | 162.69     | 244.83     | 373.05     | 390.95     |
| $C_1 = 60$          | 44.618     | 129.79     | 162.68     | 243.36     | 363.58     | 390.31     |
| S2ASMS, $\beta = 2$ | 43.943     | 122.99     | 161.50     | 220.18     | 317.47     | 375.50     |

**Table 6.4:** Six lowest eigenfrequencies  $f_{1-6}$  computed with S2MS6 elements for FV32 benchmark.

### 6.3.2 2D square membrane with distorted mesh

Consider a modal problem for a square unconstrained membrane. Dimensions, material properties and mesh are shown in Figure 6.11. The stiffness matrix is computed with  $2 \times 2$  quadrature rule and four enhanced assumed strain modes. The CMM and VSMS are computed with  $4 \times 4$  quadrature rule. Row sum lumping is used for LMM. A moderate distortion is introduced to the mesh in order to find which mass scaling techniques are sensitive to mesh distortion.

| Mass type    | S2MS6                           |                         | Q2MS6                           |                         |
|--------------|---------------------------------|-------------------------|---------------------------------|-------------------------|
|              | $dt_{\text{crit}}, \mu\text{s}$ | $\text{cond}\mathbf{M}$ | $dt_{\text{crit}}, \mu\text{s}$ | $\text{cond}\mathbf{M}$ |
| LMM          | 14.8                            | 49                      | 13.4                            | 79                      |
| CMM          | 8.7                             | 219                     | 8.4                             | 128                     |
| $\beta = 10$ | 34.5                            | 184                     | 38.5                            | 72                      |
| $\beta = 30$ | 50.1                            | 236                     | 64.8                            | 153                     |
| $\beta = 60$ | 61.0                            | 348                     | 91.0                            | 247                     |
| $C_1 = 30$   | 31.4                            | 299                     | 31.7                            | 149                     |
| $C_1 = 60$   | 36.7                            | 537                     | 37.1                            | 275                     |
| $C_1 = 100$  | 41.9                            | 857                     | 42.4                            | 444                     |

**Table 6.5:** Critical time-step and conditioning of mass matrix for FV32 benchmark. S2 and Q2 element families.

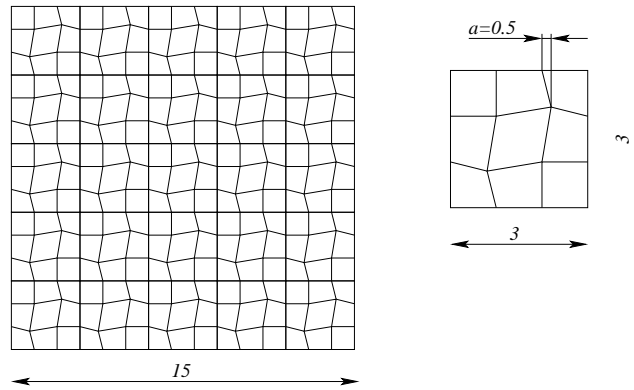


**Figure 6.11:** The model of a square membrane (left) and sub-model (right) with mesh distortion  $a = 0.5$  m (right). Material properties:  $E = 207$  GPa,  $\nu = 0.3$ ,  $\rho = 7800$  kg/m<sup>3</sup>. Mesh:  $15 \times 15$  elements.

The results of the eigenvalue analysis are summarized in Table 6.6. The values obtained for consistent and lumped mass matrix are given in the first and second row, respectively. These values can be used as reference. Algebraic mass scaling based on OLOVSSON ET AL. (2005) is performed with  $\beta=2$ , VSMS with  $C_1=30$ . The following data is presented in the columns: the three lowest non-zero eigenfrequencies, the maximum eigenfrequency, conditioning and average fill-in of the mass matrices and the distortion angle  $\varphi_4$  for mode four computed with equation (2.130). The condition number is computed for the product  $\mathbf{P}_1\mathbf{M}$ . The following observation may be made from Table 6.6. The maximum frequency for LMM is about half of the one for CMM and the lowest frequencies are slightly smaller. All given mass scaling methods reduce the maximum frequency by a factor two to three compared to LMM.

Only algebraic mass scaling changes the order of the presented lowest eigenmodes, see Figures 6.12 and 6.13. Modes four and six are interchanged. Moreover, the structure has four

|                    | $f_4$ , Hz | $f_5$ , Hz | $f_6$ , Hz | $f_{max}$ , Hz | $\text{cond}(\mathbf{P}_J\mathbf{M})$ | Average bandwidth | mode 4 distortion $\varphi_4$ |
|--------------------|------------|------------|------------|----------------|---------------------------------------|-------------------|-------------------------------|
| LMM                | 133.105    | 140.466    | 140.731    | 1928.99        | 1                                     | 1                 | -                             |
| CMM                | 133.807    | 142.709    | 142.752    | 3707.33        | 12.39                                 | 8.3               | -                             |
| ASMS,<br>$\beta=2$ | 124.824    | 126.598    | 127.716    | 873.97         | 12.35                                 | 8.3               | 1.32°                         |
| VSMS,<br>$C_1=30$  | 128.123    | 136.495    | 136.958    | 762.06         | 21.91                                 | 16.5              | 0.59°                         |

**Table 6.6:** Comparison of different mass matrices for 2D square membrane example

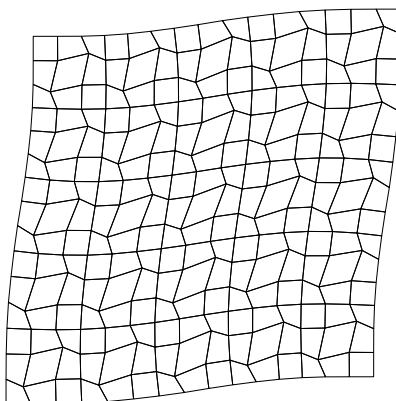


**Figure 6.12:** Eigenmode four for a square plate computed with algebraic selective mass scaling with  $\beta = 2, f = 127.716$  Hz.

symmetry planes and its eigenmodes four and five are mirrored. Thus, the corresponding frequencies must be equal. The difference between the frequencies of the two symmetric modes is the largest for the algebraic mass scaling among discussed methods (1.774 Hz). Algebraic mass scaling leads also to the largest distortion angle  $\varphi_4$ . Thus, the algebraic mass scaling after OLOVSSON ET AL. (2005) should be carefully used for distorted meshes.

Further observations can be made from the modes for the highest frequency, see Figure 6.14. In case of the lumped mass matrix the mode is localized. Application of SMS with off-diagonal terms yields the highest mode that propagate over the model.

### 6.3.3 NAFEMS FV52

As an example of a three-dimensional problem, the eigenfrequency benchmark FV52 of NAFEMS (1990) is considered. Geometry and mesh of the model are shown in Figure 6.15. Material properties of the benchmark FV52 are identical to FV32, see Figure 6.8. Boundary

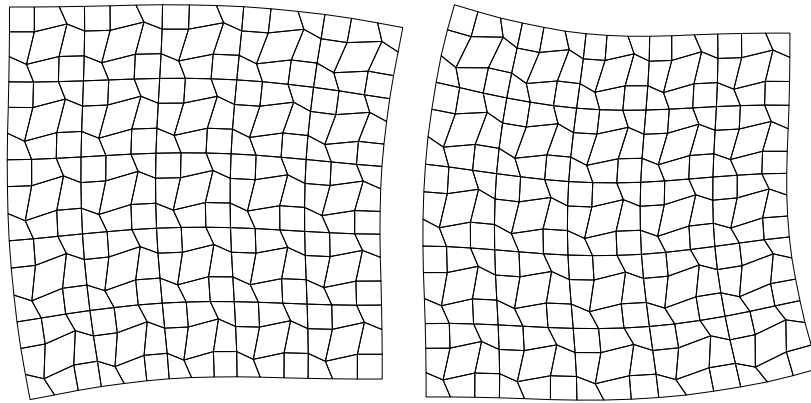


**Figure 6.13:** Eigenmodes five (left) and six (right) for a square plate computed with algebraic selective mass scaling with  $\beta = 2$ ,  $f_5 = 124.824$  Hz and  $f_6 = 126.598$  Hz.

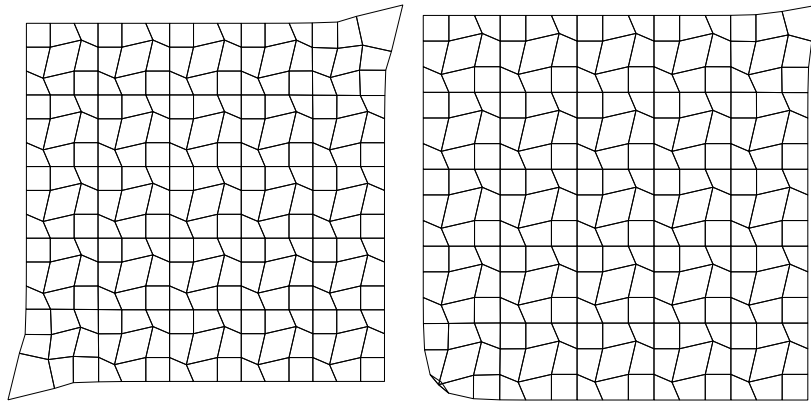


**Figure 6.14:** Eigenmodes 256 for lumped mass matrix (left) and for algebraic selective mass scaling (right) with  $\beta = 2$ ,  $f_{\max}^{\text{LMM}} = 1928.99$  Hz and  $f_{\max}^{\text{ASMS}} = 873.97$  Hz.

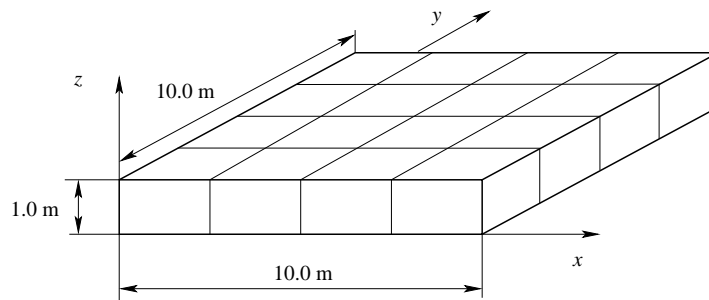


**Figure 6.15:** Setup of FV52 NAFEMS benchmark.

conditions  $u_z = 0$  are imposed along all four lower edges ( $z = -0.5$ ). For stiffness calculation, eight-node solid elements with nine enhanced strains are used.

The reductions of the eigenfrequencies obtained for Hexa8MS6 element with different values of scaling parameters are shown in Figure 6.16. A reduction of 40%, 55% and 65% is ob-

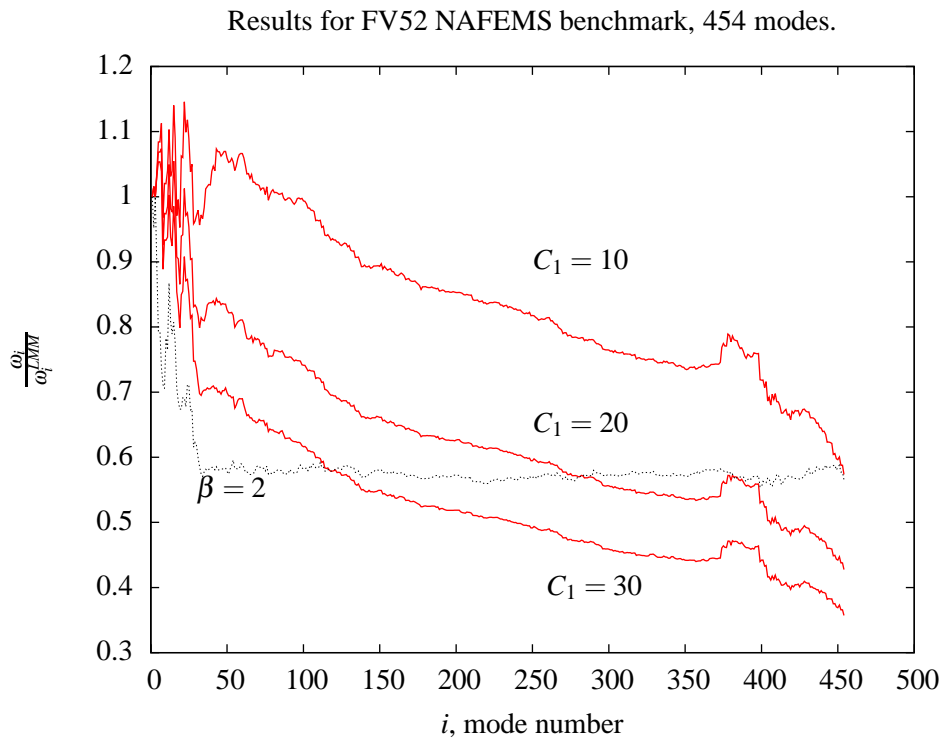


**Figure 6.16:** Ratio of eigenfrequencies for different values of selective mass scaling parameters.  $C_1$  for element Hexa8MS6,  $\beta$  for algebraic selective mass scaling.

tained for  $C_1 = 10, 20$  and  $30$ , respectively. The accuracy of the lowest eigenfrequencies is compared with ASMS. For  $\beta = 2$ , the error in the lowest 10% range of eigenfrequencies is 40% compared to an error of 13% for  $C_1 = 10$ .

## 6.4 Summary of spectral analysis

In this chapter dispersion and modal analyses for HSMM and VSMS are carried out. Dispersion analysis provided important results about the number of branches of the dispersion relation and their quality (optical vs. acoustic, longitudinal, shear or flexural). Information about these branches allowed to find the convergence rate for different modes. For the discussed examples of truss and beam elements, HSMM reduces the order of accuracy with respect to CMM at least by two. VSMS may preserve the order of accuracy, but then it is not efficient in the reduction of the highest frequencies. This means that the two alternative mass formulations lead to higher dispersion error than LMM or CMM. In addition, the proposed version of VSMS for elements with rotary DOF is not efficient.

Influence of HSMM and VSMS on the lowest eigenmodes is studied for three modal benchmarks (NAFEMS FV32 and FV53, 2D square membrane). From results of these benchmarks the following conclusions can be made. The proposed formulations for HSMM, i.e. Q2V10P10 and Q2IVM8, give good results for NAFEMS FV32 benchmark. The accuracy of the lowest modes computed with Q1MS2, Q1MS3, Q1MS4, Q2MS6, S2MS6 and S2ASMS are satisfactory for NAFEMS FV32 benchmark. The lowest modes computed with Hexa8ASMS and Hexa8MS6 give satisfactory results in benchmark NAFEMS FV52. Comparing the two competing mass scaling techniques (ASMS and VSMS), it is observed, that ASMS is more sensitive to mesh distortions than VSMS (2D square membrane benchmark). The conditioning of mass matrix for VSMS is higher than for ASMS. However, VSMS shows better accuracy of the frequencies.

The spectral analysis for linearized equations cannot give complete properties of VSMS and HSMM. In the next chapter transient examples are studied, that include contact and finite deformations.



# 7

---

## Transient examples

In the previous chapters, the theory of hybrid-singular mass matrices and variational selective mass scaling is developed and an error analysis for harmonic waves is carried out. In this chapter, the proposed methods are tested for several dynamic problems of three types (wave propagation, impact and structural dynamics). In wave propagation problems, the dispersion error can be separately studied. The reduction of the spurious contact pressure oscillation is studied in unilateral dynamic contact problems. In structural dynamics problems, the behavior of the system is studied for simple load cases. Time integration is done with trapezoidal rule (examples 7.1.1-7.1.4 and 7.2.1), NEWMARK  $\beta$  method (examples 7.1.5 and 7.1.6) and the central difference method (examples 7.2.2-7.2.5). Numerical tests are conducted using the implementation of the elements in the computer algebra package *Maple* or the in-house FE code *NumPro*. For the examples 7.2.5 and 7.2.6, a comparison with the solutions obtained in the commercial code *LS-Dyna* is done. Advantages, disadvantages and limitations of the proposed methods are summarized at the end of the chapter.

### 7.1 Examples with hybrid singular mass matrices

#### 7.1.1 Wave propagation in truss

To illustrate the capabilities of the element for the wave propagation problem, a problem with a sharp shock front is considered. The initial conditions correspond to a rectangular wave packet moving from the left side of a finite truss to the right, see Figure 7.1. The length of the packet is 20 % of the total truss length. The length of the truss is large enough to avoid reflections within the simulation time. The analytical solution predicts that the particle velocity  $v_0$  in the packet is preserved during the wave propagation. Snapshots of the velocity profile are presented in

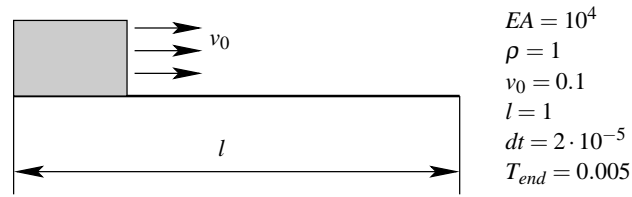


**Figure 7.1:** Wave propagation benchmark for trusses.

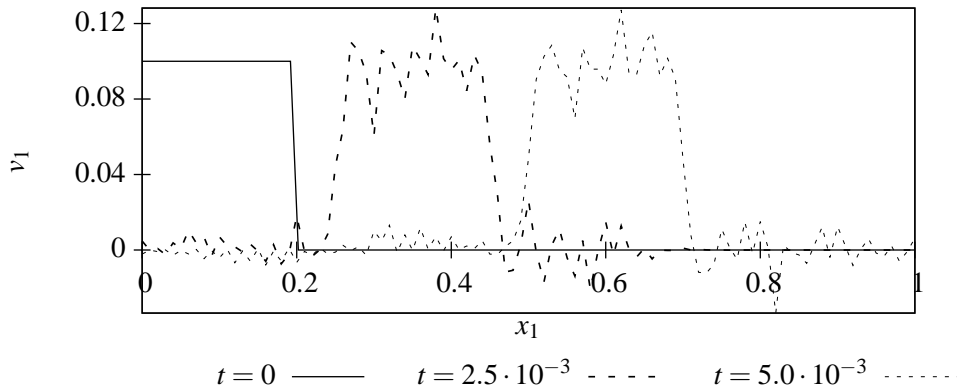


**Figure 7.2:** Velocity profiles at different time points for a quadratic truss element with constant velocities, Tr2-0.

Figures 7.2 and 7.3 for Tr2-0 and Tr3-1 elements<sup>1</sup>, respectively. It shows reasonably small dispersion, however dispersive ripples are present. The velocity profiles obtained with Tr3-1 are less dispersive than the ones obtained with Tr2-0. This is due to the higher accuracy of the dispersion curve (6.16), see Figures 6.2 and 7.3.

### 7.1.2 Projectile in rigid wall

The proposed finite element formulations for truss elements Tr2-0 and Tr3-1 are tested in a rigid wall impact problem. The setup for this test is analogous to the wave propagation test apart from the fact that the initial velocity is uniform in the truss. The contact condition is applied on the node at the right end. The exact analytical solution predicts a constant contact force  $F_c^{\text{exact}} = v_0 A \sqrt{\rho E}$  and a total impact duration of  $T_c = 2l \sqrt{\frac{\rho}{E}}$ . For the specified data, the numeric values are  $F_c^{\text{exact}} = 10$  and  $T_c = 0.02$ . The time history of the computed contact force for different time step sizes is presented in Figures 7.4 and 7.5 for the element Tr2-0 and Tr3-1, respectively. The contact persists during the entire impact for both element formulations,

<sup>1</sup>Three-node truss element with constant velocity and four-node truss element with linear velocity, respectively. Shape functions are given in equations (5.8) and (5.20). For further details of element naming convention, see page xviii.

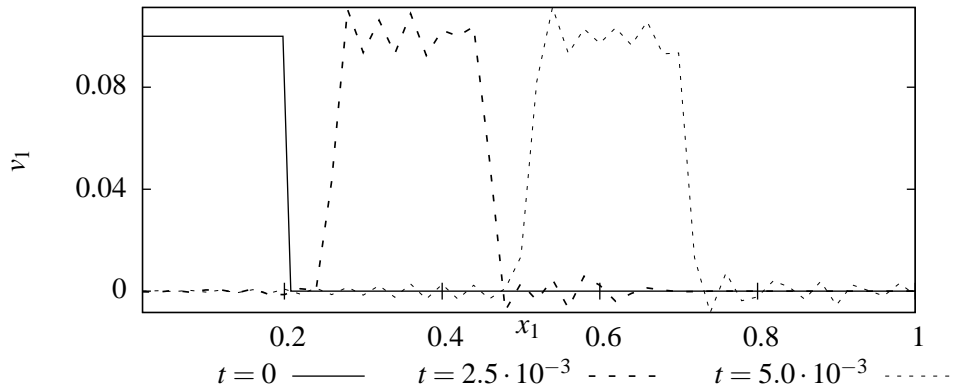


**Figure 7.3:** Velocity profiles for a cubic truss element with linear velocities, Tr3-1, at different time points.

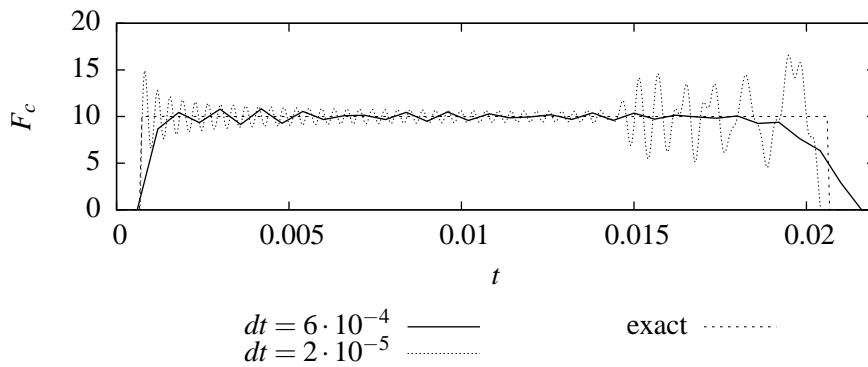


**Figure 7.4:** Contact force at a rigid wall impact problem for a quadratic truss element, Tr2-0

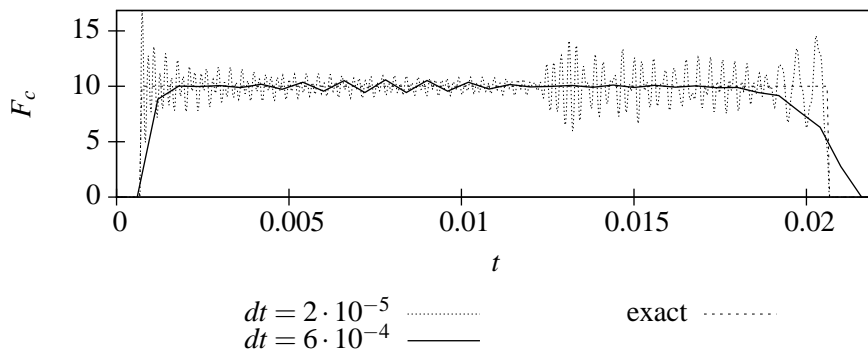


**Figure 7.5:** Contact force at a rigid wall impact problem for a cubic truss element with linear velocities, Tr3-1.

and the computed durations of the impact are close to the theoretical one, which is not the case for the standard mass matrix approach.

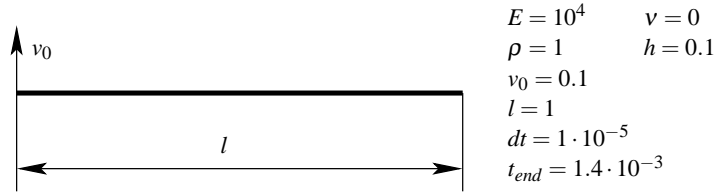


**Figure 7.6:** Timoshenko beam wave propagation benchmark for 40 elements mesh. Constant velocity  $v_0$  is prescribed at left end of the beam.

The maximum overshoot of the contact force  $t_c/F_c$  for an element Tr2-0 is by a factor of around 1.8 in the range of the studied time-steps, and the overshoot reduces with the increasing size of the time step sizes. The reason for that is as follows: time integration with larger time-steps  $dt > 3l_e/c$  cuts off the highest modes in the solution. The phase velocity for the higher modes possesses a larger error (see Figure 6.1). This shows up also in the history of the contact force, where spurious irregular oscillations in the second half of the impact are caused by reflected higher modes. It also means, that the resolution of space and time discretization should match. The choice of the time step  $dt$  in the range from  $2l_e/c$  to  $5l_e/c$  provides the most accurate results in the contact force for this benchmark. The maximum overshoot  $t_c/F_c$  produced with Tr3-1 element is around 1.7, see Figure 7.5.

The maximum overshoot of the contact force computed with CMM or LMM grows as  $dt^{-1}$  with  $dt \rightarrow 0$ . Values for the overshoot of 1.7, 5.0 and 8.0 are obtained for the problem with quadratic elements and CMM for  $l_e/(c dt)$  values of 0.25, 0.5 and 1.0, respectively. A similar behavior is also reported for MOREAU-JEAN's scheme in ACARY (2013). The overshoots of the contact force for  $l_e/(c dt)$  values of 0.963, 9.63 and 96.3 are 1.07, 2.75 and 27.5, respectively.

### 7.1.3 Wave propagation in a Timoshenko beam

The dispersion properties of the element may also be evaluated from the following test problem. Consider a semi-infinite beam with a free left end. A constant velocity  $v_0$  is prescribed at the free end. We model this problem with a beam of finite length taking it long enough to avoid spurious reflections from the right end (see Figure 7.6). A regular mesh with slenderness  $\Lambda = 7.0$  is used.

The numerical solutions are compared with an analytical solution obtained in BOLEY AND CHAO (1955). Figure 7.7 compares the profiles of at a given time for the four different element formulations. We plot the velocity the velocity in transverse direction normalized with  $v_0$  by connecting values at the midpoints of the elements, however the distribution for the formulation Ti2\*-2-1-2 is actually piecewise linear and discontinuous. The analytical solution is dispersive, i.e., shear and flexural wave propagate through the beam with a velocity de-

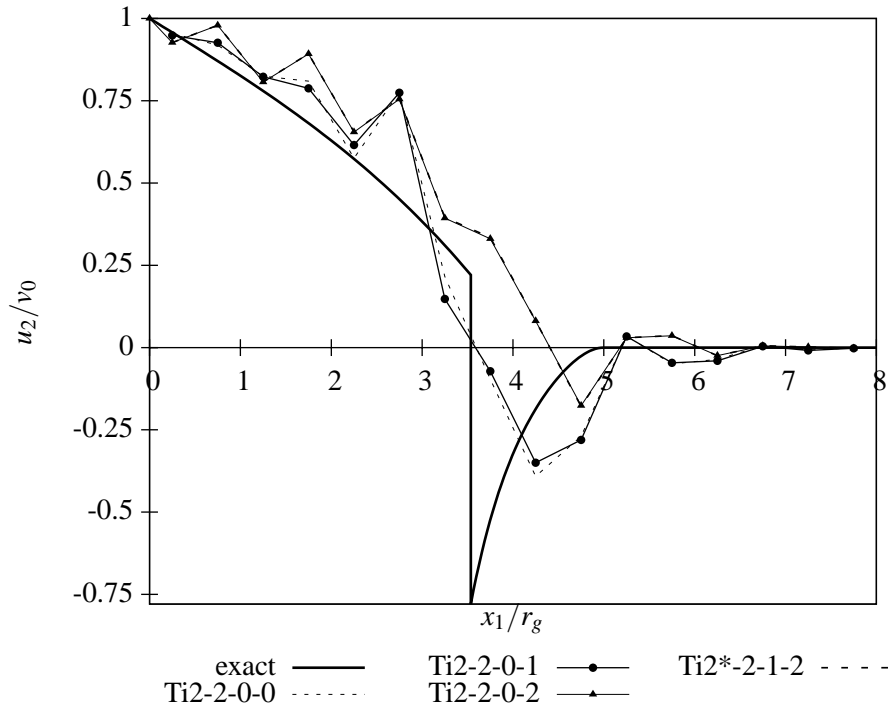


**Figure 7.7:** Profiles of normalized transverse velocity  $u_2/v_0$  for a wave propagation test for a Timoshenko beam at  $t_{end} = 1.4 \cdot 10^{-3}$ .

pending on the wave number  $k$ . The maximum velocity of flexural waves is smaller than the maximum velocity of shear waves by a factor of  $\sqrt{EA/GA_s} \approx 1.4$ , for details see BOLEY AND CHAO (1955). Therefore, a sharp front is predicted between shear and flexural wave packages (see Figure 7.7 at the location  $x_1/r_g \approx 3.5$  with  $r_g = \sqrt{I/A}$  being the radius of gyration). The formulations Ti2-2-0-0 and Ti2-2-0-1 can follow the front much better than Ti2-2-0-2 and Ti2\*-2-1-2. The results for Ti2-2-0-2 and Ti2\*-2-1-2 are almost identical, because the difference in their mass matrices reduces with large slenderness. Furthermore, the height of the spurious oscillations of the velocity profile around the front is comparable with the ones obtained in an identical wave propagation test for two-node Timoshenko beam elements in BELYTSCHKO AND MINDLE (1980).

#### 7.1.4 Lateral impact of a Timoshenko beam

The performance in the case of elasto-dynamic contact is tested using a bounce problem (Figure 7.8). A beam hinged on both ends with a sine profile for the initial velocity is considered. There is a rigid obstacle with initial gap  $g_{\mathcal{B}}$ . We use a coarse mesh with four elements, such that contact occurs only in the middle node, which is a massless node. The time interval is big enough for one impact.

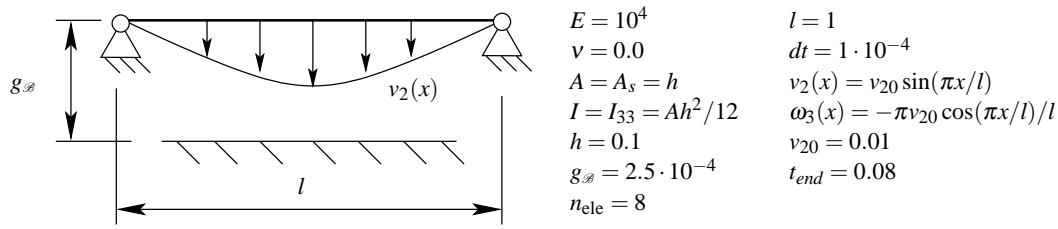


**Figure 7.8:** Setup of TIMOSHENKO bounce benchmark.

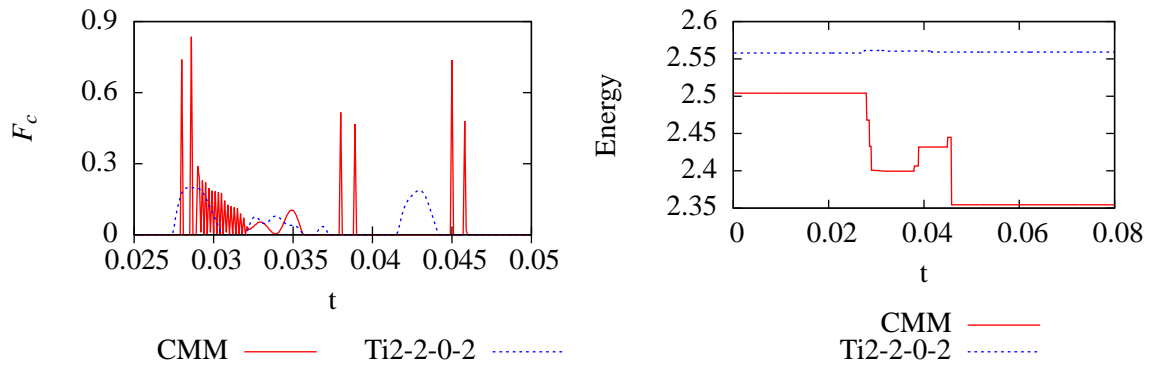


**Figure 7.9:** Contact force at the center of the beam and evolution of the total energy. TIMOSHENKO bounce benchmark.

The numerical results for the contact force at the middle node are given in Figure 7.9. The results for the standard mass matrix consist of several impacts with duration of one time step each. In the case of HSMM, spurious oscillations of the contact force are eliminated. All the formulations proposed herein provide almost similar results, since rotational inertia – which makes the difference between the formulations – are not very significant in this test problem. A similar behavior for the impact of a beam with an obstacle is reported in POZZOLINI AND SALAUN (2011) and POZZOLINI ET AL. (2013), where small differences have been obtained for linear and constant velocity field approximations in the case of the Euler-Bernoulli beam model.

### 7.1.5 Lateral impact of beam modeled with solid elements

The previous problem described in Figure 7.8 can be solved using 2D solid elements. The model setup is shown in Figure 7.10. No friction between the rigid obstacle and the beam is assumed. Two meshes are used for computation. Both meshes have one element in thickness direction. Eight or 16 elements are used in axial direction. For the transient simulation, NEWMARK  $\beta$  method with time-step size  $dt = 1.25 \cdot 10^{-4}$  is used.

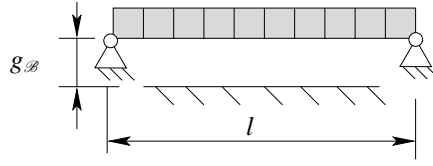


**Figure 7.10:** Setup of bounce benchmark modeled with solid elements Q2P10V10.

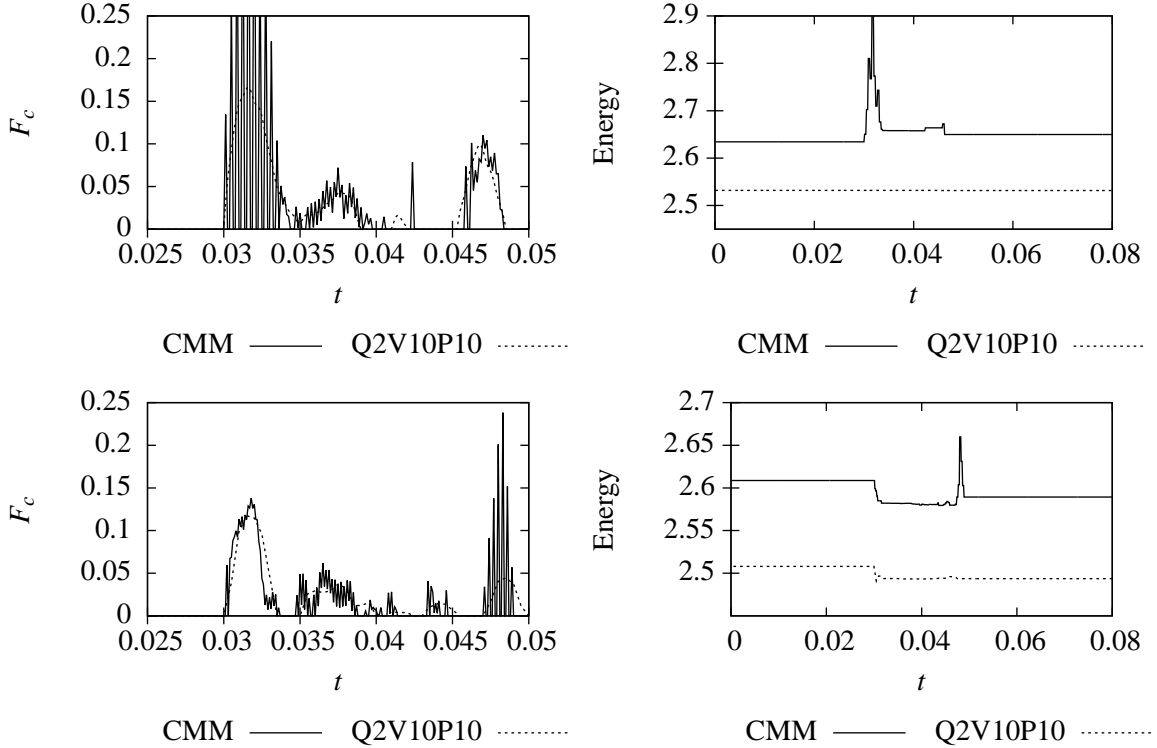


**Figure 7.11:** Contact force at the center of a beam (left) and total energy evolution (right) for impact problem of beam modeled with solid elements (Q2 vs. Q2P10V10). Results for  $1 \times 8$  (above) and  $1 \times 16$  (below) meshes.

The results of the simulation are presented in Figure 7.11. Here, standard nine-node quadrilateral elements Q2 and the element formulation Q2P10V10 are compared. The history of the contact force at the center of the beam computed with HSMM exhibits less spurious oscillations and allows persistent contact. Energy losses and gains due to activation or release from contact in case of standard mass matrix are much higher.

Although all numerical results of the newly proposed approach are at least as good and quite often superior to results in the standard case, there is one drawback. The condition number of the time integration matrix of the mid-point rule  $\left(\frac{4}{dt^2}\mathbf{M}^* + \mathbf{K}\right)$  starts growing for very small time-steps ( $dt < \frac{l_e}{100c}$ ), see Figure 7.12. The reason to this is that the singular term  $\frac{4}{dt^2}\mathbf{M}^*$  for

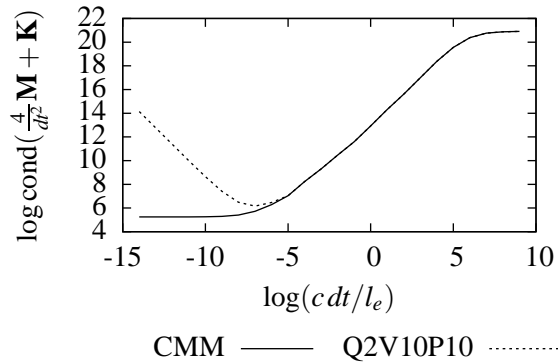


**Figure 7.12:** Dependency of conditioning of algorithmic tangent on relative time-step for a beam modeled with solid elements Q2P10V10.

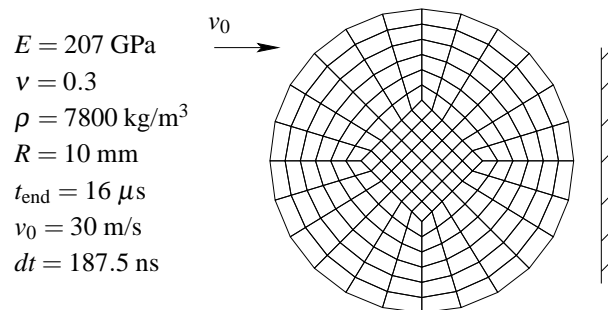


**Figure 7.13:** Impact of a circular disk onto a rigid obstacle modeled with 125 solid elements Q2P10V10.

such small time-step sizes, dominates the term  $\mathbf{K}$ . However, a simple JACOBI preconditioner solves this problem for all examples considered here.

### 7.1.6 Impact of a disk onto rigid wall

Another example computed with Q2V10P10 elements is presented below. Consider a frictionless impact of a thin circular disc onto a rigid obstacle. The setup of the problem is shown in Figure 7.13. It is expected that the disk bounces within a short period of time. The disk has a smooth surface. Hence, the contact force – in contrast to the projectile problem 7.1.2 – should be smooth in time. In addition, the total energy must be preserved in the absence of internal or external friction and external forces.

Solutions with NEWMARK  $\beta$  method for three time-steps sizes  $0.5 \mu\text{s}$ ,  $0.25 \mu\text{s}$  and  $0.1825 \mu\text{s}$  are carried out. The histories of the contact force and total energy are presented in Figure 7.14. Standard Q2 elements with CMM show stable results for a time-step size  $0.5 \mu\text{s}$  ( $dt > 2L_e/c$ ). No clear advantage in the history of the contact force at the middle node or in the evolution of

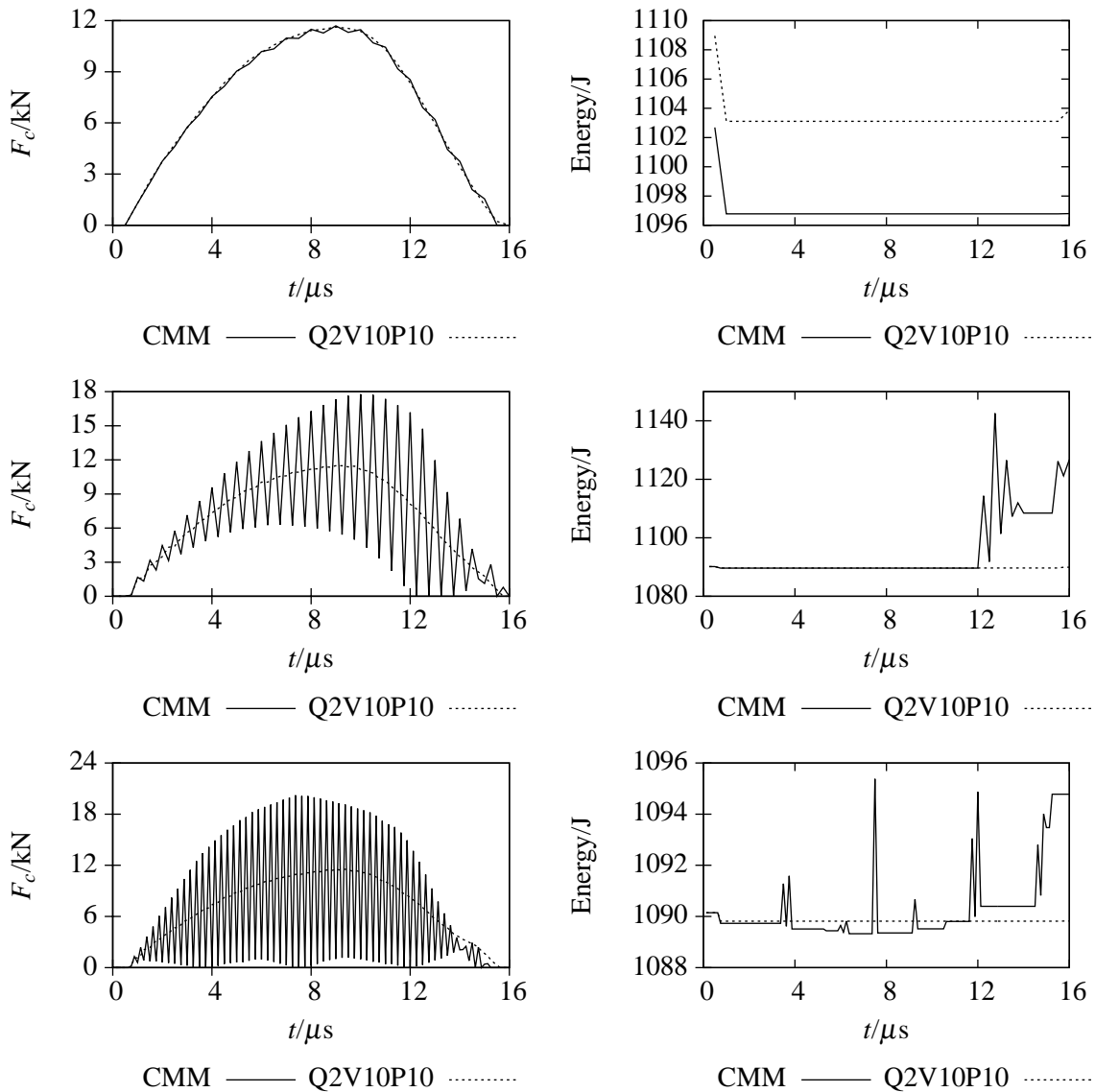


**Figure 7.14:** Contact force and energy evolution for impact of a circular disk on a rigid obstacle (Q2 vs. Q2P10V10).  $dt = 0.5 \mu s$  (above),  $dt = 0.25 \mu s$  (middle) and  $dt = 0.1825 \mu s$  (below).

the total energy can be seen for HSMM. For time-steps  $0.25 \mu s$  and  $0.1825 \mu s$  ( $dt < 2L_e/c$ ), HSMM shows superior results. The contact force is smooth, and the contact is persistent during the whole impact. The change of the total energy is significantly less than for CMM.

The method of hybrid-singular mass matrices can be viewed as a regularization of dynamic contact problems. Like in a penalty method a certain stiffness is assigned between nodes with mass and locations where contact is collocated. In contrast to a penalty method, contact constraints are fulfilled exactly (no penetration allowed). As only the massless nodes are

subject to contact constraints, the distance between "contact nodes" and "mass nodes" plays the role of springs in a penalty method (typically one half or one third of an element's length). For example, in the case of the impact of a one-dimensional three-node element, contact occurs at the corner node, but inertia is condensed in the middle node. An attractive feature of this sort of regularization is that the equivalent penalty stiffness is automatically adjusted, in case of lateral and edge contact, to bending/shear and membrane stiffness of the element, respectively.

## 7.2 Examples with selective mass scaling

### 7.2.1 Wave propagation in a Timoshenko beam

The artificial dispersion brought by selective mass scaling can be demonstrated by a wave propagation example for a long TIMOSHENKO beam. The problem setup is identical to the setup from Subsection 7.1.3. The results are presented in Figure 7.15 for Ti2-2-2-2MS1 and Ti2-2-2-2MS2 elements. The velocity profile obtained for CMM ( $C_1 = 0$ ) contains less dispersion. The flexural part of the wave for  $x_1/r_g < 3.5$  is presented accurately and the shear part of the wave for  $x_1/r_g > 3.5$  shows moderate oscillations. Application of VSMS with constant velocity ansatz (Ti2-2-2-2MS1) leads to substantial dispersion, especially in the shear part of the solution. The velocity jump between the two parts of the waves is not clear. Moreover, for  $C_1 = 20$ , the maximum value of velocity is attained inside the domain, which is unphysical. Results with linear ansatz space are more accurate. However, the potential for increasing the critical time-step size with this ansatz is limited, see Subsection 6.2.3.

### 7.2.2 Tip loaded cantilever beam

The model for a transient problem is shown in Figure 7.16. Initial zero displacements and velocities are assumed. The beam is loaded at the tip by an abrupt force  $F$ . The structural response is compared using the history of the tip displacement  $w$ , see Figure 7.17. The deflections obtained with a LMM and the proposed SMS are almost identical even for high scaling values. For the same reduction of time step size, the method OLOVSSON ET AL. (2005) yields a greater error.

Computation with a regular LMM requires 12900 time steps. For the number of time steps for different mass matrices, the following results are obtained. The consistent mass matrix requires 21106 time steps, which is almost twice as much as for LMM. The method proposed herein adds inertia to the consistent mass matrix (4.14). Therefore, after mass scaling, the required number of time steps is always less. The application of the ansatz  $\Psi$  from (5.32)

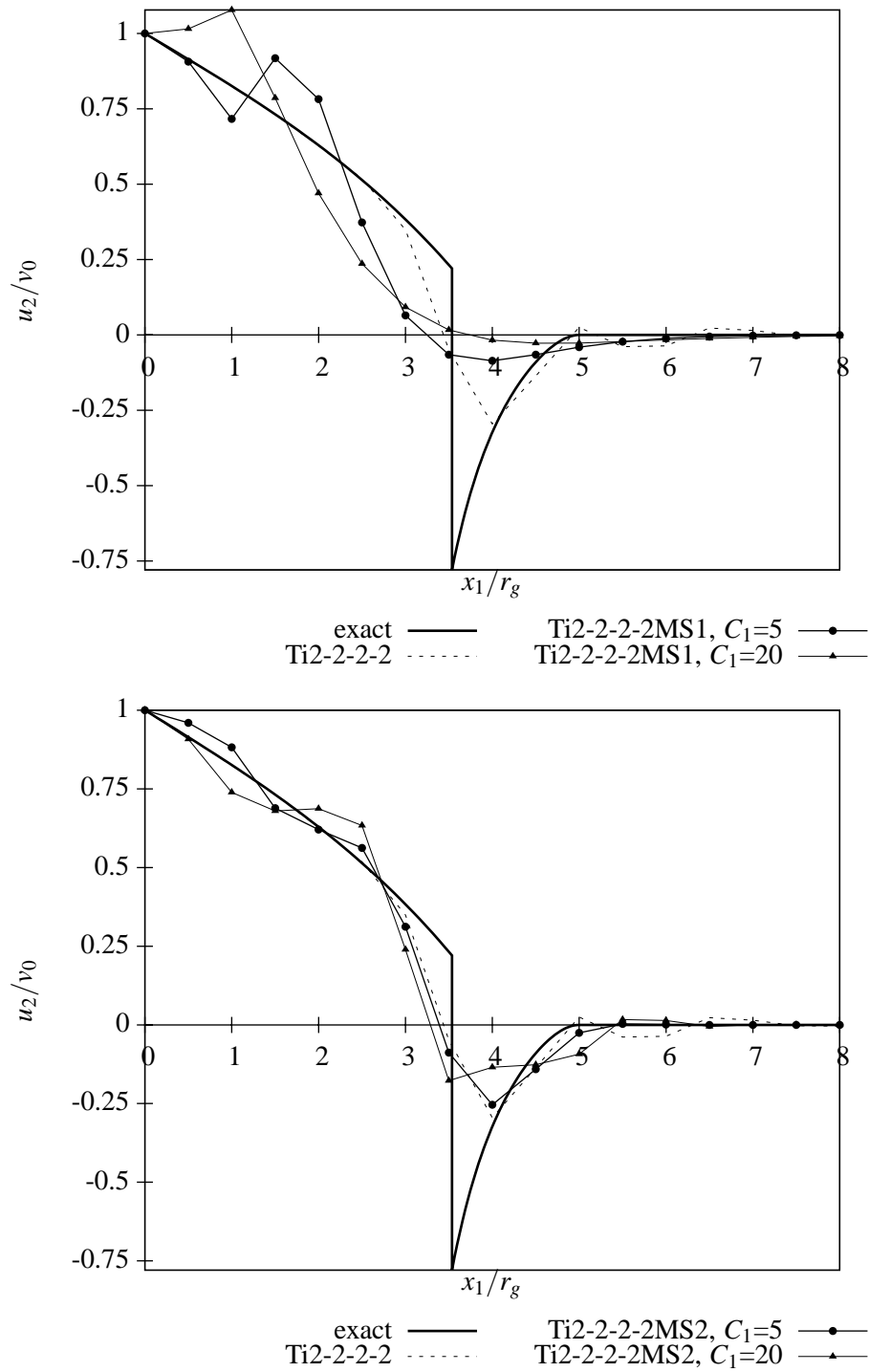


**Figure 7.15:** Profiles of normalized transverse velocity  $u_2/v_0$  for wave propagation test for TIMOSHENKO beam at  $t_{end} = 1.4 \cdot 10^{-3}$ . VSMS with constant velocity ansatz space (above) and linear ansatz space (below).

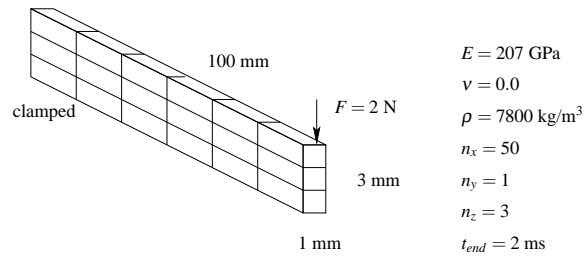


**Figure 7.16:** The model of tip loaded beam (OLOVSSON ET AL. 2005).

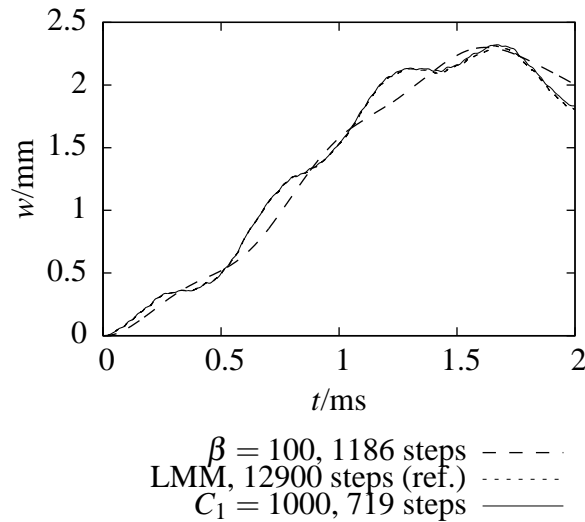


**Figure 7.17:** Tip deflection  $w$  of a cantilever beam.

does not decrease the time step substantially; it is even more than for LMM, therein ansatz (5.32) is not pursued further. Ansatz (5.35) and (5.30) lead to a comparable reduction of the number of the steps, e.g. 2248 and 2392 for  $C_1=100$ , 717 and 719 for  $C_1 = 1000$ , respectively. For comparison, mass scaling with  $\beta = 100$  from OLOVSSON ET AL. (2005) cuts down the number of steps to 1186.

The accuracy of SMS can be monitored by the kinetic energy stored in the artificially added mass  $T^\circ - T = \frac{1}{2} \dot{\mathbf{u}} \boldsymbol{\lambda}^\circ \dot{\mathbf{u}}$ . The small ratio of the artificially added kinetic energy to the total energy indicates a small change in the structural response, for more elaborate error estimators using parametrized variational principles see KEATING ET AL. (1993), FELIPPA ET AL. (1995) and CASTRO (2011). For the problem at hand, the ratio of the artificial energy to the total energy is presented in Figure 7.18. It is clear from the figure that the proposed method accumulates much less artificially added energy than the method proposed in OLOVSSON ET AL. (2005).

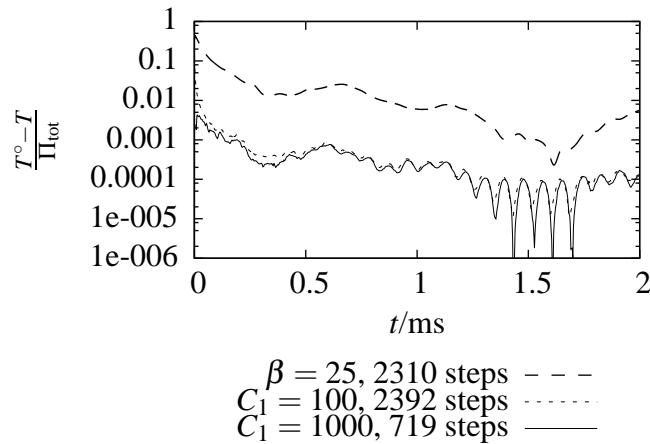


**Figure 7.18:** Ratio of kinetic energy stored in artificially added mass to total energy.

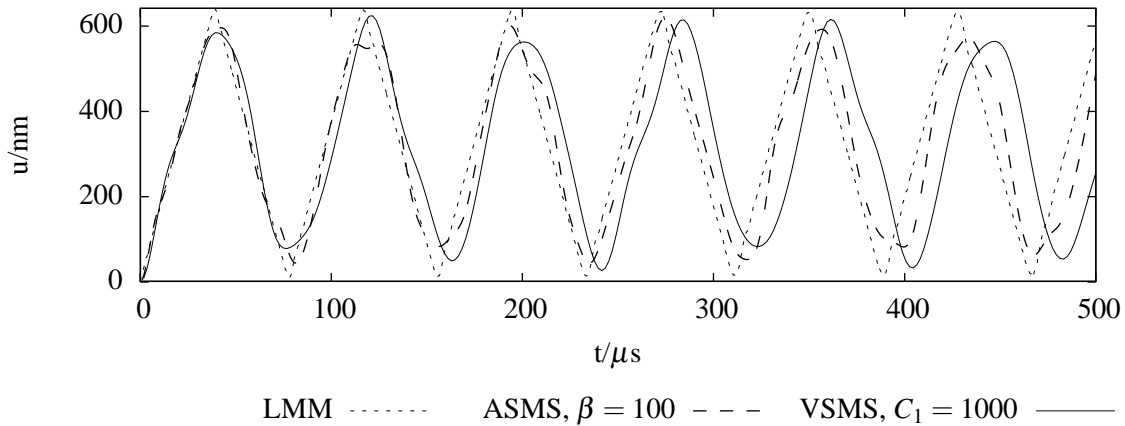


**Figure 7.19:** Axial tip displacement for the compression wave benchmark.

### 7.2.3 Cantilever beam under a longitudinal load

Consider the beam from the previous subsection under abruptly applied longitudinal load  $F = 2 \text{ N}$ . The axial displacement during  $0.5 \text{ ms}$  is given in Figure 7.19. The analytical solution predicts a standing wave in the beam and the axial tip displacement is a staggered line with the amplitude  $\Delta u = 2Fl/EA \approx 645 \text{ nm}$  and the period  $T_{\text{long}} = 2l/\sqrt{E/\rho} \approx 77 \mu\text{s}$ . The LMM catches the behavior of the problem very good. The algebraic mass scaling produces reasonable error. The result obtained with VSMS is acceptable.

The difference in the performance for a transverse and longitudinal load can be explained by different distribution of mode participation factors, see Figure 7.20. Structurally significant modes must have relative participation factors greater than  $10^{-3}$ . The transverse and longitudinal loads actuate the modes from a cluster in the beginning and the middle of the

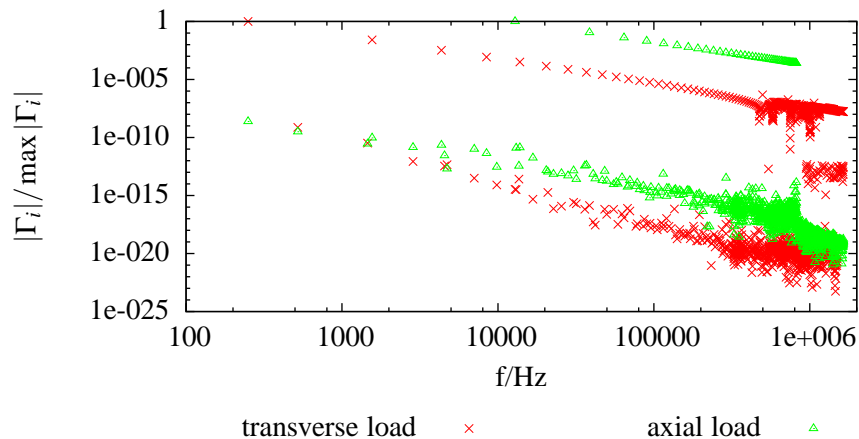


**Figure 7.20:** Normalized mode participation factors.

spectrum, respectively. Thus, the choice of optimal SMS requires the knowledge of the mode participation distribution.

#### 7.2.4 Arch bridge under point load

Consider an example for a 2D model of an arch bridge discussed in TKACHUK AND BISCHOFF (2013a). The model for a transient problem is shown in Figure 7.21. Initial zero displacements and velocities are assumed. The model is loaded in the middle of the left arch by an abrupt point load  $F$ . The structural response is compared using the history of the vertical displacement  $w$  under the applied load, see Figure 7.22.

Computation with lumped mass matrices required 3691 and 2634 time-steps for S2 and Q2 elements, respectively. For S2 element, the following observations can be made. The application of a small variational mass scaling factor  $C_1 = 10$  with 1693 steps leads to very accurate results. Larger values of mass scaling factor result in larger conditioning of the mass matrix without substantial reduction of the time-step size and they are not recommended. Usage of algebraic mass scaling with  $\beta = 10$  with 832 steps increases inertia and results in phase shift of the displacement. For Q2 elements, a similar behavior is observed. However, the conditioning of the mass matrix for variational mass scaling is better.

The conditioning of the mass matrix reflects on the number of necessary iterations for computation of the acceleration vector. The preconditioned conjugate gradient method with Jacobi preconditioner is used for the numerical experiments. The relative error of residual norm is taken as  $10^{-6}$ . For the Q2 element with values of algebraic mass scaling factor  $\beta = 10, 30$  and  $100$ , the average number of iterations is 25, 41 and 60, respectively. For values of variational mass scaling factors  $C_1 = 30, 100$  and  $300$ , the average number of iterations is 37, 65

and 111. These numbers perfectly correlate with the expected number of iterations, which is proportional to the square root of the condition number.

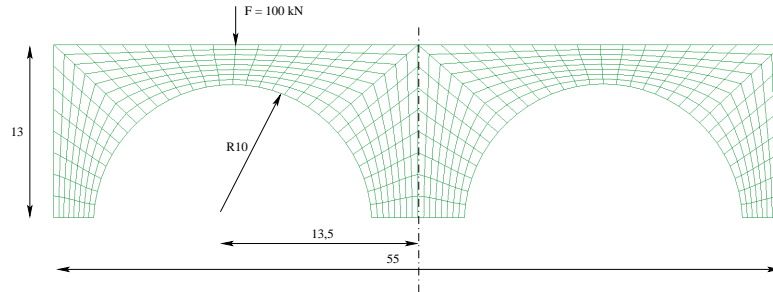


**Figure 7.21:** A model of an arch bridge. Material properties:  $E = 30$  GPa,  $\nu = 0.2$ ,  $\rho = 2400$  kg/m<sup>3</sup>, plane stress, thickness = 1 m. Mesh: 512 elements (eight- or nine-node quadrilaterals). Load: point force  $F = 100$  kN applied in the middle of left arch. Duration:  $t_{\text{end}} = 0.1$  s.

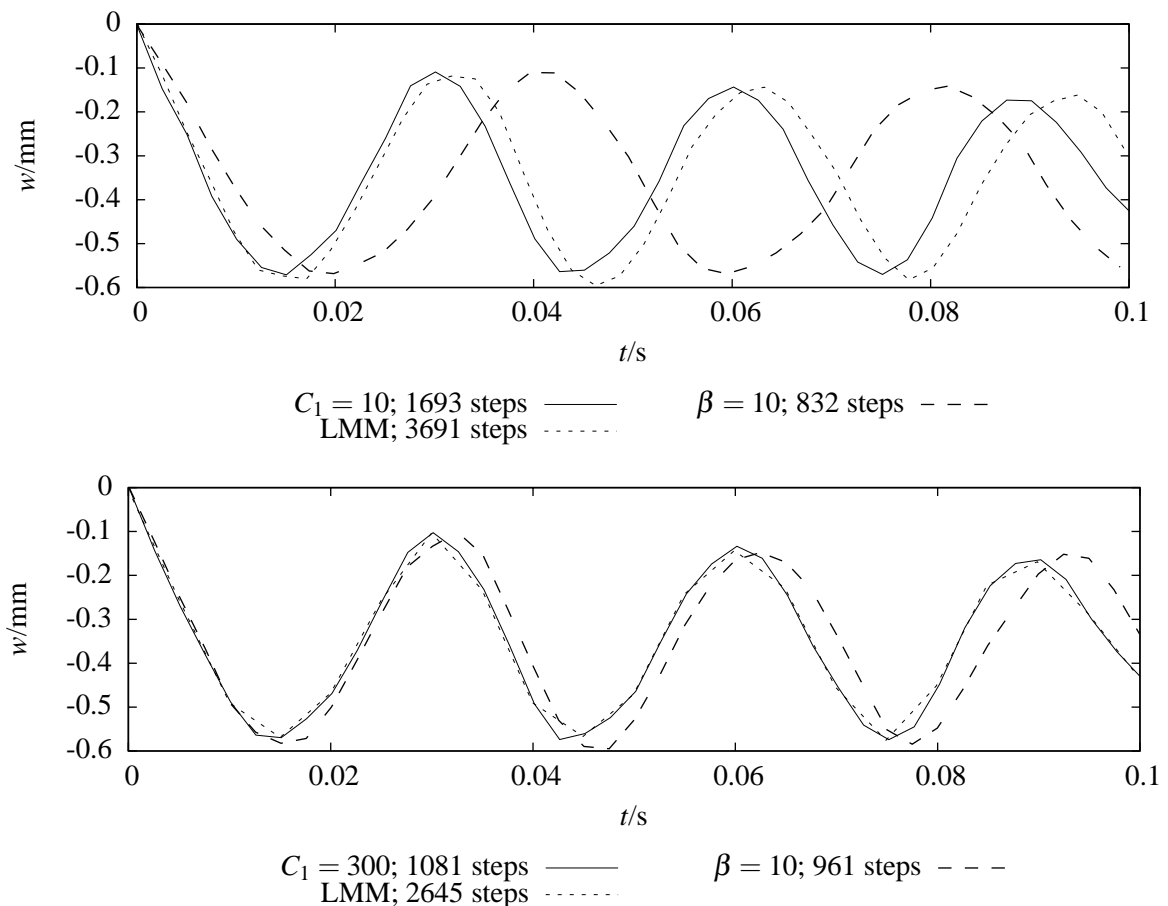


**Figure 7.22:** Displacement under external load. Results for S2 (above) and Q2 (below) element families.

| Mass type     | S2                              |                               | Q2                              |                               |
|---------------|---------------------------------|-------------------------------|---------------------------------|-------------------------------|
|               | $dt_{\text{crit}}, \mu\text{s}$ | $\text{cond}\mathbf{M}^\circ$ | $dt_{\text{crit}}, \mu\text{s}$ | $\text{cond}\mathbf{M}^\circ$ |
| LMM           | 26.8                            | 19                            | 42.0                            | 29                            |
| CMM           | 42.4                            | 93                            | 26.5                            | 62                            |
| $\beta = 10$  | 134.9                           | 43                            | 115.5                           | 51                            |
| $\beta = 30$  | 227.1                           | 98                            | 194.5                           | 115                           |
| $\beta = 100$ | 410.3                           | 190                           | 351.7                           | 303                           |
| $C_1 = 30$    | 71.8                            | 159                           | 71.5                            | 77                            |
| $C_1 = 100$   | 85.2                            | 372                           | 84.7                            | 191                           |
| $C_1 = 300$   | 103.6                           | 903                           | 103.0                           | 470                           |

**Table 7.1:** Critical time-step and conditioning of mass matrix for the arch bridge model.

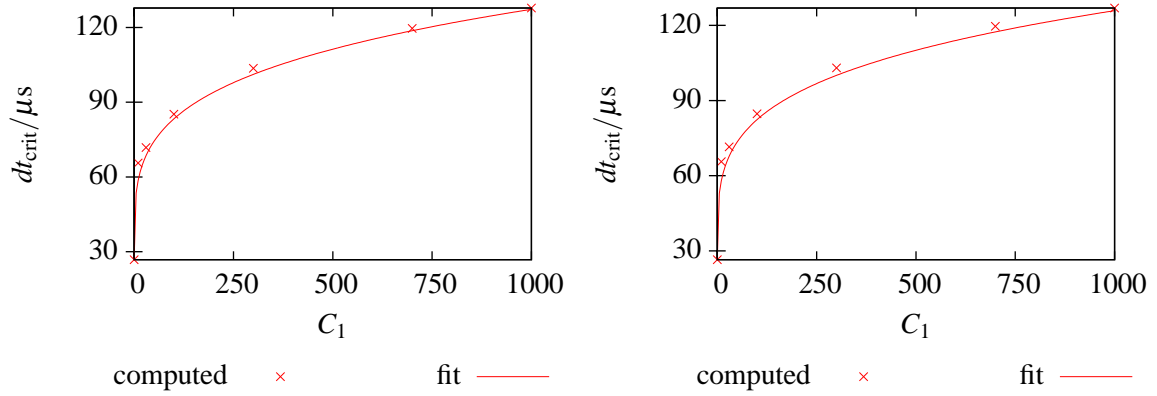


**Figure 7.23:** Dependence of the critical time-step size on mass scaling factor  $C_1$  for S2 (left) and Q2 (right) element families. Computed values vs. fitted curve.

It was found that the critical time-step and conditioning of mass matrix grows with  $C_1$ , see Table 7.1. Least square fit of the data yields the following approximated relations

$$\text{S2MS6:} \quad \frac{dt_{\text{crit}}^\circ}{dt_{\text{crit}}} \approx 1 + \frac{2}{3} \sqrt[4]{C_1} \quad \text{cond}\mathbf{M}^\circ \approx \text{cond}\mathbf{M}_{\text{CMM}} + 3C_1, \quad (7.1)$$

$$\text{Q2MS6:} \quad \frac{dt_{\text{crit}}^\circ}{dt_{\text{crit}}} \approx 1 + \frac{2}{3} \sqrt[4]{C_1} \quad \text{cond}\mathbf{M}^\circ \approx \text{cond}\mathbf{M}_{\text{CMM}} + \frac{4}{3}C_1. \quad (7.2)$$

The quality of this fit is illustrated in Figure 7.23. One can see that the rise of the critical time-step is the same for eight- and nine-node elements. At the same time, conditioning of scaled mass matrix  $\mathbf{M}^\circ$  for an eight-node element is much larger. Thus, it can prohibit its usage for large mass scaling values  $C_1$ .

Another approach to evaluate the mass scaling methods is comparing response curves for a harmonic analysis or computing the frequency response assurance criterion (ALLEMANG

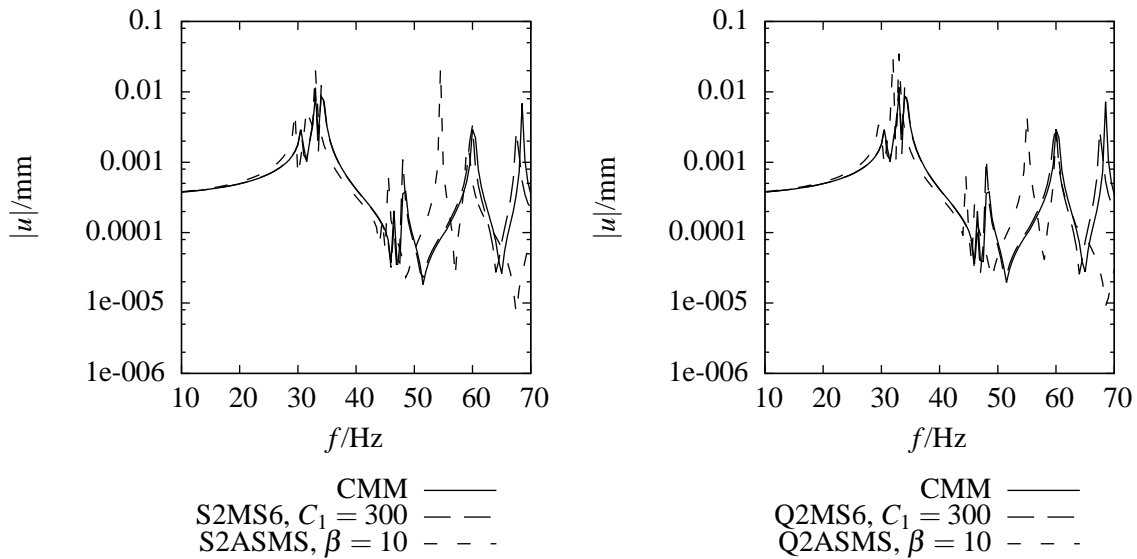


**Figure 7.24:** Spectral response of the arch bridge evaluated at the excitation point computed with S2 (left) and Q2 (right) element families.

2003). The boundary conditions and loading is identical to the transient analysis. The frequency range is chosen from 10 to 20 Hz. In this range, the reference system computed with CMM has the five lowest eigenfrequencies, see Figure 7.24. Uniform sampling for frequency response is used with 121 sampling points. A RAYLEIGH model for damping is used. The stiffness proportional damping coefficient is assumed to be zero. The coefficient of mass proportional damping is set to  $0.05 \text{ s}^{-1}$ .

Frequency response curves for consistent, algebraically and variationally scaled mass matrices for S2 and Q2 element families are shown in Figure 7.24. Values for mass scaling factors  $\beta$  and  $C_1$  are chosen to produce approximately equal critical time-steps of 110 ms. Algebraic mass scaling leads to larger errors in spectral response curves, which confirms with results of the transient computations, see Figure 7.22. The error in the frequency response function is evaluated using the frequency response assurance criterion (FRAC) given in equation (2.128). As a reference response, the values obtained with CMM are used. FRACs computed for Q2ASMS with  $\beta = 10$  and Q2MS6 with  $C_1 = 300$  are 0.50 and 0.90, respectively. FRACs computed for S2ASMS with  $\beta = 10$  and S2MS6 with  $C_1 = 10$  is 0.46 and 0.91, respectively.

### 7.2.5 Six-throw crankshaft

Previous examples use simple geometric domains, regular meshes and comparably small numbers of well-shaped elements. Here, the proposed methods for SMS are tested for an example with real-life geometry. The tetrahedral meshes are produced with free mesh generators and

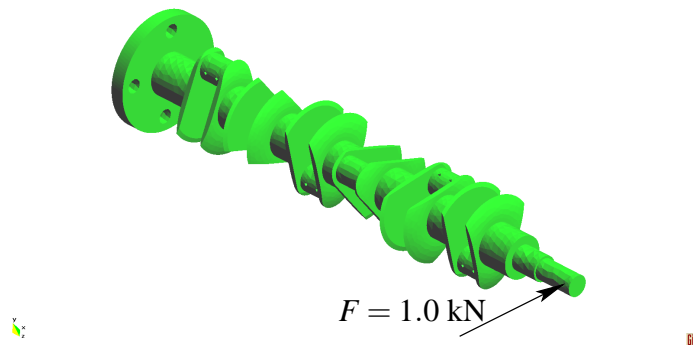


**Figure 7.25:** Mesh of six-throw crankshaft.

the model has more than  $10^5$  DOFs. However, boundary conditions and the load case are still rather academic.

A one-piece, six-throw crankshaft shown in Figure 7.25<sup>2</sup> is considered. The material of the crankshaft is assumed to be steel with YOUNG's modulus  $E = 210$  GPa, POISSON coefficient  $\nu = 0.3$  and density  $\rho = 7850$  kg/m<sup>3</sup>. The part's length is 750 mm and the weight is approximately 17.9 kg. The diameter of the flywheel is 160 mm.

The geometric model of the crankshaft is prepared in *SolidWorks*®2012 and exported as a surface model via IGES format to the pre- and postprocessor *GiD 10.0.9*. In *GiD*, a single volume is created, which includes 504 points, 798 lines and 289 surfaces. Small features like oil drilled holes with diameter 1-3 mm are kept in the geometric model.

For simulation purposes, several linear tetrahedral meshes with target element sizes of 7 mm and 8.5 mm are built. These models include 120450 and 110238 DOF's, 193218 and 181720 finite elements, respectively. The distribution of the smallest edges of finite elements and the mesh quality factor are shown in Figure 7.26. The mesh quality factor for tetrahedra is measured in *GiD* as

$$q = \frac{6\sqrt{2}V}{\sum_{i=1}^6 l_i^3}, \quad (7.3)$$

where  $V$  is the volume of the element,  $l_i$  are the lengths of tetrahedron's edges, see CIMNE (2013).

An harmonic analysis is performed with 8.5 mm mesh. Additionally, the rim of the flywheel is fixed in all the three directions. A point load is applied at the free end of the crankshaft along the x-direction as shown in Figure 7.25. The frequency ranges are chosen from 15 to 45 Hz and from 150 to 180 Hz, respectively. These ranges correspond to the four lowest bending

<sup>2</sup>The model is kindly provided by SUDHIR GILL and can be downloaded from <http://grabcad.com/library/crankshaft-37>.

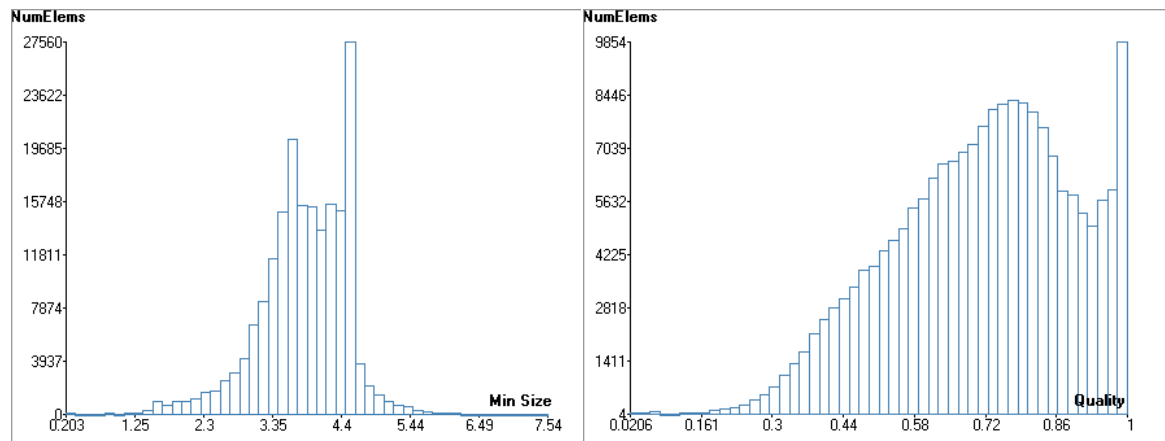


**Figure 7.26:** Crankshaft mesh built in GiD with target mesh size 7 mm.

modes in x- and y-directions, see Figure 7.28. Uniform sampling for the frequency response is used with 61 sampling points. A RAYLEIGH model for damping is used. The stiffness proportional damping coefficient is set to zero. The coefficient of mass proportional damping is assumed to be  $0.01 \text{ s}^{-1}$ .

Frequency response curves for consistent, algebraically and variationally scaled mass matrices are shown in Figure 7.27. The values for the mass scaling factors  $\beta$  and  $C_1$  are chosen to produce equal critical time-step of 187 ns. Note, that the response curves for variational mass scaling lies behind the curves for CMM. This illustrates the accuracy of the approach. Algebraic mass scaling produces substantial error for the frequencies 162 and 168 Hz already for  $\beta = 30$ , which confirms earlier observations about deficiency of algebraic mass scaling for bending dominated problems. The error in the frequency response function is evaluated using the frequency response assurance criterion given in equation (2.128). As a reference response, the values obtained with CMM are used. FRAC computed for range [15-45] Hz for Tetra4ASMS with  $\beta = 30$  and TetraMS6 with  $C_1 = 300$  are 0.87 and 1.00 (exact up to the sixth digit), respectively. FRAC computed for range [150-180] Hz for Tetra4ASMS with  $\beta = 30$  and TetraMS6 with  $C_1 = 300$  are 0.18 and 0.9998, respectively.

The 7 mm model is used for an explicit transient analysis. In this case, no displacement boundary conditions are applied. Duration of the analysis is 1 ms. Estimation of the critical time-steps for LMM in *LS-Dyna*<sup>3</sup> and *NumPro* are 14.3 and 33.5 ns. *LS-Dyna* uses a local estimation of the critical time-step size, whereas *NumPro* uses the global estimate. A local estimate is conservative, which explains the difference.

Dependency of the added mass diagonal terms and the speed-up via conventional mass scaling is presented in Table 7.2. As the model contains small number of short elements, the CMS is very efficient for increasing the time-step by a factor of ten. Then, less than 1 % of mass is

<sup>3</sup>Herein smp version 971 release 5.1.1 for win64 is used.

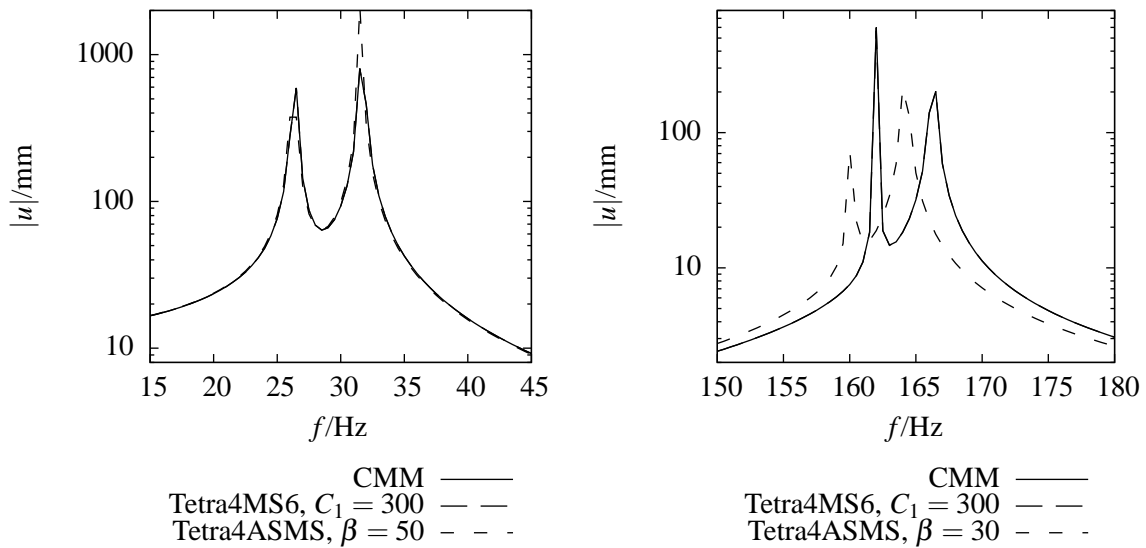


**Figure 7.27:** Spectral response of crankshaft evaluated at excitation point for different mass matrices (for range [15-45] Hz left and [150-180] Hz right).

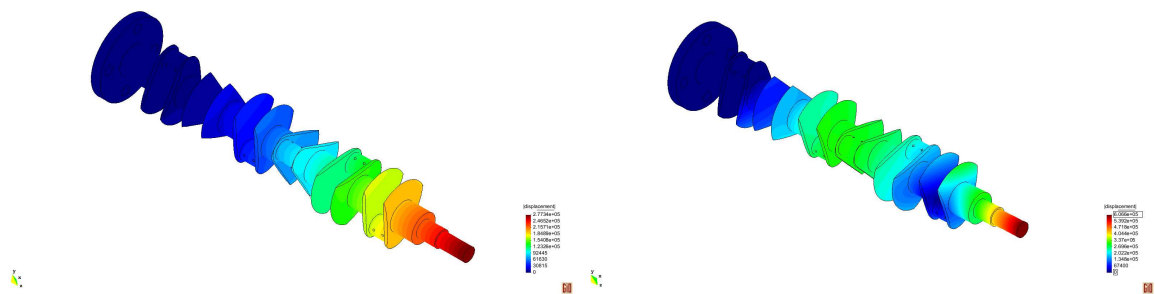


**Figure 7.28:** Absolute displacement amplitudes of crankshaft at excitation frequency 26 Hz (left) and 162 Hz (right).

added to the model which in most engineering applications is acceptable. However, increase of the critical time-step to 360 ns leads to 16 % of added mass, which is unacceptable.

In *NumPro* implementation, uniform values of mass scaling parameter for the whole model are used. Dependency of the critical time-step on the scaling parameters is presented in Table 7.3. Efficient increasing of the time-step is obtained for both mass scaling techniques. However, VSMS requires twice as much PCG iterations and produces twice as much non-zero entries in the mass matrix. Thus, the overhead for linear system solution in case of VSMS is by a factor of four greater than for ASMS, see the estimate of speed-up given in equation (2.110).

Resulting displacements are given in Figure 7.29. Comparison of displacements is given in Figure 7.30. VSMS gives result which are in good correspondence with LMM.

| Mass type | $dt_{\text{crit}}$ , ns | $\Delta m/m$ , % | speed-up |
|-----------|-------------------------|------------------|----------|
| LMM       | 14.3                    | 0                | 1 (ref)  |
| CMS       | 50.0                    | 0.006            | 3.5      |
| CMS       | 100.0                   | 0.035            | 7.0      |
| CMS       | 187.0                   | 0.2              | 11.8     |
| CMS       | 360.0                   | 16.21            | 22.5     |
| SMS       | 187.0                   | 0.2              | 9.8      |

**Table 7.2:** Added mass and speed-up for conventional mass scaling applied the 7 mm crankshaft model. Value of added mass  $\Delta m$  for SMS is given in sense of equation (2.88).

| Mass type    | $dt_{\text{crit}}$ , ns | # iter |
|--------------|-------------------------|--------|
| LMM          | 33.5                    | 1      |
| CMM          | 21.0                    | 10     |
| $\beta = 5$  | 82.0                    | 12     |
| $\beta = 10$ | 111                     | 18     |
| $\beta = 30$ | 187                     | 27     |
| $\beta = 50$ | 240                     | 33     |
| $C_1 = 30$   | 62.3                    | 10     |
| $C_1 = 100$  | 109                     | 28     |
| $C_1 = 300$  | 187                     | 54     |
| $C_1 = 1000$ | 339                     | 64     |

**Table 7.3:** Critical time-step size and average number of PCG iterations with JACOBI preconditioner for the mass matrix for the 7 mm crankshaft model.

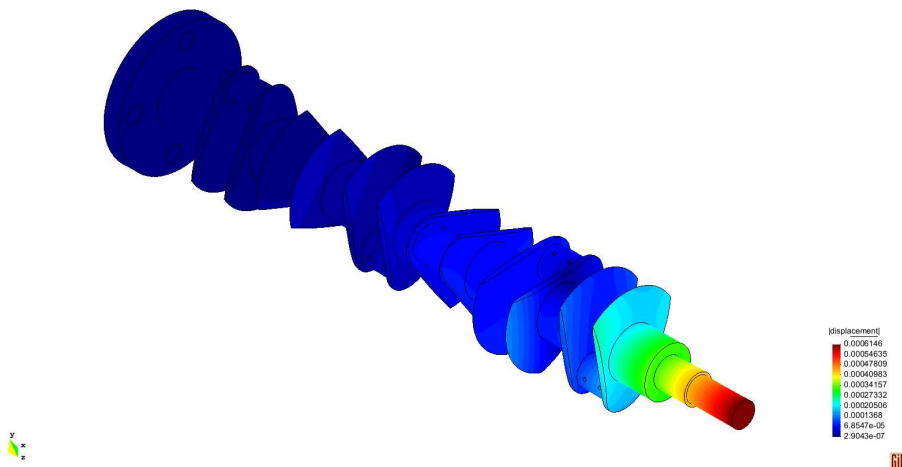


**Figure 7.29:** Absolute displacement of crankshaft at time 1 ms. Tetra4MS6,  $C_1 = 300$ .

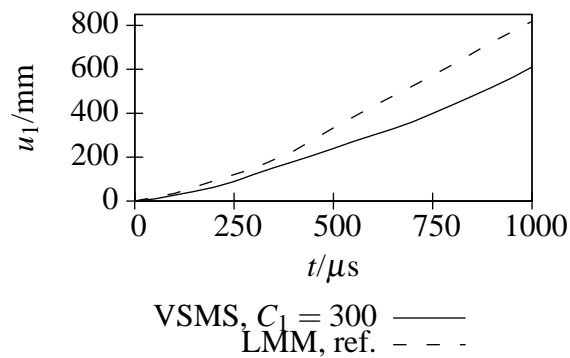


**Figure 7.30:** Evolution of displacements at the tip of crankshaft (node 1) computed with Tetra4MS6,  $C_1 = 300$  and LMM.

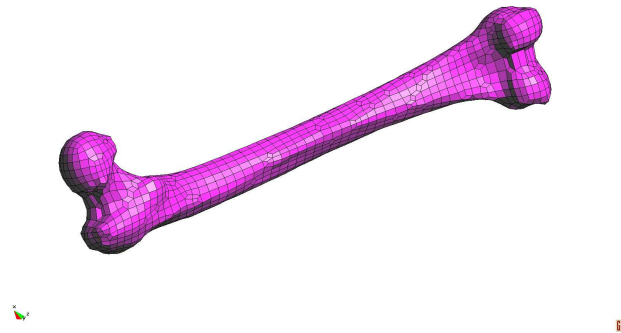


**Figure 7.31:** Model of a femur bone.

## 7.2.6 Femur bone

So far, SMS is not tested on real-life examples with hexahedral meshes. A free model of human femur bone is used for this purpose<sup>4</sup>.

The length of the femur bone model is approximately 395 mm. The mesh contains 6714 nodes and 5702 trilinear hexahedral elements, see Figure 7.31. The mesh quality is evaluated with internal tools of *GiD*, see Figure 7.32. The mesh quality for the femur model is better than the mesh quality for the six-throw crankshaft, as it was produced with *HEXAR* mesher (Cray Research, USA). However, the shortest edge is 1.47 mm (2.5 times smaller than the average) and the smallest angle is  $9.4^\circ$ .

*LS-Dyna* and *NumPro* are employed for simulation. The default *LS-Dyna* formulation with one point quadrature (ELFORM=1) and the implementation in *NumPro* with  $2 \times 2 \times 2$  are used for internal force computation. The mass matrix in *NumPro* is computed with  $3 \times 3 \times 3$  quadrature.

<sup>4</sup>VAKHUM project, FP5 project 1998–2001, six mesh refinements are available in JAN (2001)

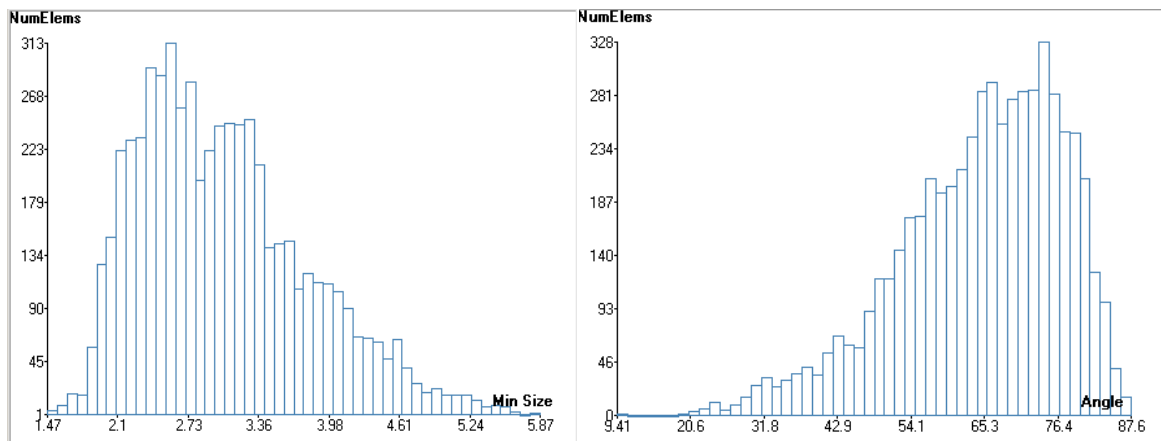


**Figure 7.32:** Mesh properties for the femur bone model.

The original model is available in six mesh refinement grades from coarse to fine. Here, model refinement one (the most coarse) is used. This model has non-uniform materials with 151 grades. It uses for every point an elastic isotropic material law with  $\nu = 0.3$ . The YOUNG's modulus and the density are mapped onto the elements using CT data. Here, the material is assumed to be uniform isotropic with  $E = 5 \text{ GPa}$ ,  $\nu = 0.3$ ,  $\rho = 1.042 \text{ kg/m}^3$  as average values for the provided model. The total mass of the bone is 0.466 kg.

An estimation of the critical time-step sizes for LMM in *LS-Dyna* and *NumPro* are 405 and 15.7 ns. The difference in the critical time-step sizes between the two codes can be explained by different quadrature rules used. The difference is especially pronounced for highly distorted elements. e.g. with the smallest angle between edges  $9.41^\circ$ .

The dependency of the added mass diagonal terms and the speed-up via Conventional mass scaling is presented in Table 7.4. The CMS is quite efficient for increasing the time-step by a factor of 1.5. Further scaling of mass leads to a large added translational mass. This is usual for such high-quality meshes.

The dependency of the critical time-step size and conditioning of the mass matrix for a set values  $\beta$  and  $C_1$  are given in Table 7.5.

For such a mesh, CMS can speed-up up to the factor of 1.5 whereas VSMS can speed-up up to the factor of 10 without loss of accuracy.

The harmonic analysis is performed in a range from 100 to 250 Hz with the sampling frequency of 3 Hz. In this range, the second bending mode is situated, see the mode in Figure 7.33 and corresponding a peak of response function in Figure 7.34. A RAYLEIGH model for damping is used. The stiffness proportional damping coefficient is set to zero. The coefficient of mass proportional damping is assumed to be  $0.01 \text{ s}^{-1}$ .

| Mass type | $dt_{\text{crit}}, \mu\text{s}$ | $\Delta m/m, \%$ | speed-up |
|-----------|---------------------------------|------------------|----------|
| LMM       | 0.405                           | 0                | 1 (ref)  |
| CMS       | 0.500                           | 0.0047           | 1.24     |
| CMS       | 0.600                           | 0.142            | 1.48     |
| CMS       | 0.700                           | 1.43             | 1.73     |
| CMS       | 0.800                           | 6.74             | 1.97     |
| CMS       | 1.600                           | 201.59           | 3.92     |
| SMS       | 1.600                           | 201.59           | 3.52     |

**Table 7.4:** Added mass and speed-up for conventional mass scaling applied to the femur bone model, refinement 1. Value of added mass  $\Delta m$  for SMS is given in the sense of equation (2.88).

| Mass type    | $dt_{\text{crit}}, \text{ns}$ | cond $\mathbf{M}$ |
|--------------|-------------------------------|-------------------|
| LMM          | 15.7                          | 24.2              |
| CMM          | 1.2                           | 173               |
| $\beta = 10$ | 47.63                         | 46.2              |
| $\beta = 30$ | 1848                          | 116.1             |
| $\beta = 50$ | 6627                          | 350.7             |
| $C_1 = 30$   | 117                           | 66.7              |
| $C_1 = 100$  | 609                           | 122.4             |
| $C_1 = 235$  | 1853                          | 265.8             |
| $C_1 = 300$  | 2505                          | 333.5             |

**Table 7.5:** Critical time-step and conditioning of mass matrix for the femur bone model.

Frequency response curves for consistent, algebraically and variationally scaled mass matrices are shown in Figure 7.34. The values for the mass scaling factors  $\beta$  and  $C_1$  are chosen to produce an equal critical time-step of 1853 ns. Note, that the response curve for variational mass scaling lies behind the curves for CMM. This illustrates the accuracy of the approach. Algebraic selective mass scaling with  $\beta = 30$  produces substantial error for the frequency of 223 Hz, which is the second bending frequency. The peak of the response function corresponding to the second bending mode is shifted to 202 Hz. FRAC computed for the range [100-250] Hz for Hexa8ASMS with  $\beta = 30$  and Hexa6MS6 with  $C_1 = 235$  are 0.245 and 0.99956, respectively.

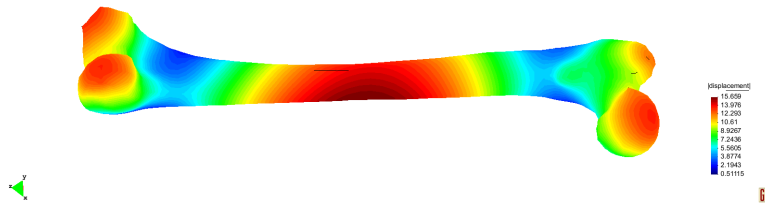


**Figure 7.33:** Absolute displacement amplitudes of femur at excitation frequency 223 Hz.

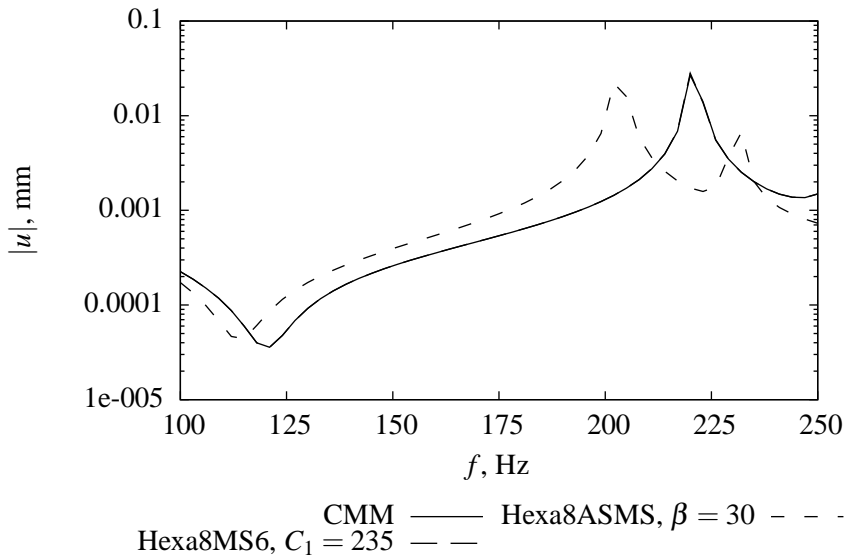


**Figure 7.34:** Spectral response of crankshaft evaluated at excitation point for different mass matrices for range [100-150] Hz.

## 7.3 Summary for transient examples

In this chapter numerical examples for elasto-dynamic contact with HSMM and dynamic problems for VSMS are considered. From the results of the benchmarks carried out, the following conclusions can be made. The proposed formulations for HSMM, i.e. Tr2-0, Tr3-1, Timo2-2-0-2 and Q2V10P10, significantly reduce spurious oscillation of contact forces. Besides, the evolution of the total energy shows much smaller artificial gain/loss for these elements. The advantages of HSMM are specially pronounced for time-step values of  $dt < 2l_e/c$ . Based on this observations, the newly developed elements can be recommended for use in impact modeling.

Proposed formulations for VSMS for solid elements, i.e. Q1MS3, Q2MS6 and S2MS6, Tetra4MS6 and Hexa8MS6, are competitive with ASMS. VSMS yields more accurate results especially for bending dominated problems modelled with solid elements or on distorted meshes. However, ASMS is more accurate for wave propagation problems and ASMS re-

quires from 30 to 50% less iterations for computation of acceleration with PCG. Besides, an example for TIMOSHENKO beam elements Ti2-2-2-2MS1 and Ti2-2-2-2MS2 shows that the current formulation of VSMS is not efficient.

---

## Conclusions and outlook

### 8.1 Conclusions

In this thesis, a unified approach for singular and selectively-scaled mass matrices is proposed. This is a powerful theoretical framework that provides families of consistent mass matrices. They can be used in elasto-dynamical contact problems and explicit dynamics. Moreover, novel techniques are used for the evaluation of the accuracy of these mass matrices, like inertial patch tests and the frequency response assurance criterion. Together with a set of benchmarks, these techniques prove the efficiency and accuracy of the proposed approach. Detailed conclusions for singular and selectively scaled matrices are given below.

#### Hybrid singular mass matrices

An alternative spatial discretization of elasto-dynamic contact problems that uses hybrid singular mass matrices is proposed. It is based on the three-field modified HAMILTON's principle with independent fields of velocity, momentum and displacement. This approach allows to reduce the differential index of the semi-discretized system from three to one. As result, it efficiently reduces spurious temporal oscillations of the contact pressure and allows precise energy preservation during impact. The formulation does not increase the total number of unknowns, as the discretization parameters for velocity and momentum are eliminated locally.

The first major result of the thesis is the proposed discretization of the three-field modified HAMILTON's principle for contact problems. It combines a novel expression for a hybrid singular mass matrix, a condition for vanishing of mass at certain nodes and a new class of polynomial shape functions. It was shown that a diagonal entry of the element mass matrix

vanishes if the shape function belonging to the corresponding node is orthogonal to all momentum shape functions. New shape functions that fulfill the orthogonality condition have been proposed. The elements use GAUSS-LOBATTO quadrature points as node location (see also LAMICHHANE AND WOHLMUTH (2007)) and fulfill the interpolation condition only at the corner (vertex) nodes. It has been verified that the discretization satisfies the conditions for computability and stability needed within the framework of a hybrid-mixed approach.

The main advantage of the approach w.r.t. standard mass matrices is significant reduction of spurious temporal oscillations of the contact pressure. Persistent contact was obtained for all considered benchmarks. There is still some overshoot of contact pressure; most importantly, it stays finite for very small time steps ( $dt \rightarrow 0$ ), in contrast to formulations with a standard consistent mass matrix. The maximum contact pressure converges quickly to the analytical value for time steps  $dt \approx l_e/c$  and stays close to it for larger time steps.

One limitation of the concept of hybrid singular mass matrices is the need of implicit time integration. Further studies are necessary to check competitiveness and efficiency of the method for various contact-impact applications (crash, deep-drawing, robot dynamics, etc.). Another approach for time integration is an explicit/implicit scheme where all *inner* nodes can be still handled explicitly. Another issue is that the proposed method requires at least quadratic shape functions and a re-parametrization of the shape functions is needed. Elements with quadratic shape functions are not very popular for strongly non-linear problems, because of their lack of stability. However, some very stable high-order elements are coming to the market (see *Impetus AFEA* code with quadratic and cubic elements for blast and impact). The interest for element technology for high-order elements will grow and this type of elements may find its niche.

The conducted spectral analysis proves that the order of convergence of the proposed method for the lowest eigenfrequencies is lower than when using standard consistent and lumped mass matrices. This is due to the poorer function spaces used for velocity and momentum. Moreover, the number and physics of the spectral branches obtained with HSMM is different from the ones obtained with LMM or CMM. Usually, the application of HSMM allows to eliminate one or two optical branches. The behavior of elements in wave propagation problems is acceptable. Dispersive ripples are observed for sharp shock waves, but the size of these ripples is comparable with LMM. They can be almost eliminated after using special filtering techniques, but this question lies too far outside the scope of this thesis. A separate study is conducted on the satisfaction of the inertial patch test. The results of this study are summarized in Appendix A. The element Q2V10P10 passes the weak patch test 'D' and 'E' for any shapes, but, unfortunately, the element Q2V10P10 passes the patch test of type 'A', 'B' and 'C' only for trapezoidal shapes. The element Hexa27V57P57 shows similar properties. This question should be studied further.

The method can be easily extended to shells and membranes as well as 2D and 3D bulk structures. The derived shape functions may be extended by means of a tensor product structure. Well tuned ansatz spaces are given for the 2D nine-node element Q2V10P10 and the 3D 27-node solid element Hexa27V57P57. The element Q2V10P10 is tested with eigenvalue benchmark FV32 and two impact benchmarks. The results of these benchmarks show that all theoretical results from 1D elements are transferred to higher dimensions. Namely, the spurious temporal oscillations of contact forces are substantially reduced for an arbitrary relation between time-step and element size and preservation of the total energy during the multiple impacts is better satisfied for HSMM, especially for  $l_e/(c dt) > 2$ . However, conditioning of the algorithmic tangent may cause problems for  $l_e/(c dt) > 10^8$ , but such time-step sizes are outside of practical interest.

### Variational selective mass scaling

Variational methods for selective mass scaling are the second major result of this thesis. It is proposed to use a new penalized HAMILTON's principle as the starting point of spatial discretization. Together with appropriate ansatz spaces for velocity and momentum, the proposed approach results in parametric families of *consistent* mass matrices. The usage of these mass matrices decreases the maximum eigenfrequency of the system and increases the critical time step. At the same time the lowest eigenfrequencies in the range of interest and structural response are not significantly changed.

The theoretical basis of this part of the thesis is the new parametric principle for elastodynamics. It is a modification of HAMILTON's principle where kinematic and kinetic equations are satisfied via a penalty method. Its discretization yields a general expression for mass matrices depending on three free parameters. Three sub-families that are efficient for numerical implementation are chosen and evaluated. It is also shown that the mass scaling technique presented in OLOVSSON ET AL. (2005) can be obtained as a special case of the present formulation and thus, it is variationally justified. The main practical result is a study of several instances of proposed mass scaling. Ansatz spaces for velocity are constructed that preserve rotational inertia. The numerical examples show that the best results are obtained with a formulation with the velocity field just containing the rigid body modes. This formulation also outperforms the method presented in OLOVSSON ET AL. (2005) in the investigated examples.

For the first time, the spectral analysis for elements with SMS is performed and the dispersion relations are obtained. A dispersion analysis provides important result about the number of branches of dispersion and their quality (optical vs. acoustic, longitudinal, shear or flexural). Information about these branches allows to find the convergence rate for different modes. For the discussed examples, VSMS may preserve the order of accuracy, but then it is not efficient in reduction of the highest frequencies. This means that the variational selective

mass scaling formulation increases artificial dispersion. Influence of VSMS on the lowest eigenmodes is studied for several modal benchmarks. Comparing the two competing mass scaling techniques (ASMS and VSMS), it is observed, that ASMS is more sensitive to mesh distortions than VSMS. The conditioning of the mass matrix for VSMS is higher than for ASMS. However, VSMS shows better accuracy of the frequencies.

All proposed mass matrices for VSMS pass the patch test, which is a solid basis for the usage of this method. Unfortunately, ASMS passes the patch test only for the translation modes.

An efficient SMS requires good conditioning of the mass matrix. Such studies are performed for different variants of VSMS. Generally, conditioning with VSMS is worse than for ASMS for an equal time-step size. But for the same reduction of the computational time, the VSMS provides more accurate results.

Variational selective mass scaling can also be applied for high-order elements. Here it is proposed to use the new formulation in 2D: eight- and nine-node quadrilateral elements. Choice of ansatz spaces for velocity with complete linear ansatz allows an efficient implementation for selective mass scaling. This selective mass scaling works efficiently even after finite rotations. The accuracy is higher than for ASMS. High values of speed-up are obtained for the nine-node element. However, conditioning mass matrix for eight-node prohibits high values of the mass scaling factor.

## 8.2 Outlook

This thesis is dedicated to a variational framework of singular and selectively scaled matrices and initial testing of the proposed approach. Further developments and tests are needed.

New developments regarding the *element types* may be carried out. For hybrid singular mass matrices more testing of nine-node quadrilateral and 27-node hexahedral element is required. Further, ten-node quadratic tetrahedral elements, cubic quadrilateral Q3 and quadratic shells can be studied. For selectively scaled mass matrices, high-order elements for 3D, like Tetra10MS12 and Hexa27MS12, should be evaluated. Variational selective mass scaling may also be developed for thick shells, where anisotropy of element's geometry requires non-isotropic penalty factors for in-plane and out-of-plane directions. Besides, VSMS can be applied to NURBS based elements. Static elimination of the dual variables is not easy for patches with large number of degrees of freedom. Hence, alternative ansatz spaces must be developed in this case.

New developments regarding the *formulations* may be suggested. The orthogonality condition (4.23) for shape functions in HSMM approach may be relaxed. This would allow singular mass matrices for standard LAGRANGE shape functions. VSMS can be developed for po-

lar/micromorphic continua. This may provide large savings for explicit simulations of granular/polymeric materials, biomechanics or MEMSs. The same approach may be also used for shell theories with rotational degrees of freedom.

New developments regarding *time integration* may be proposed. The domains with SMS and HSMM can be united in an explicit-implicit time integration scheme in order to get a stable, accurate and efficient method for crash simulation. Moreover, the penalized HAMILTON's principle can be directly discretized with space-time elements.

New developments regarding *alternative field problems* and *multi-physics* are also possible. Singular mass and heat capacity matrices have potential application for coupled thermo-elasto-dynamic contact problems, where numerical instabilities and oscillation of contact pressures are common. Selective scaling of heat capacities can be applied for hyperbolic (non-FOURIER's) heat conductance equations in order to increase the critical time-step sizes for the explicit integration schemes.

Finally, I am looking forward for industrial applications, which expose more issues connected to the variational methods for consistent singular and scaled mass matrices. Remarks, suggestions and ideas are welcomed at *tkachuk-anton@rambler.ru*.



---

# Appendix

## A Patch test for selected elements

The definition and notation for an inertial patch test are given in Section 5.1. Here, the patch test is conducted for Q1, S2, Q2 and Hexa8 element families. Hexagonal shaped patches of elements are used for 2D elements. An assembly of six distorted elements is used for 3D element, see Figure A.3. The nodes in a patch are placed such that the Jacobian of the individual elements is a polynomial of the highest possible order. Exact locations of nodes are given in Figures A.1 and A.2 for Q1 and S2 elements, respectively. The mesh of Q2 elements is completed with mid-element nodes for S2 elements.

The patch test is conducted automatically in a specially programmed *Maple* worksheet. Results of these tests are given in Tables A.1, A.2, A.3 and A.4.

| Mass type | Constant velocity |   |   |   |   | Rigid rotation |   |   |   |   | Linear velocity |   |   |   |   |
|-----------|-------------------|---|---|---|---|----------------|---|---|---|---|-----------------|---|---|---|---|
|           | A                 | B | C | D | E | A              | B | C | D | E | A               | B | C | D | E |
| CMM       | ✓                 | ✓ | ✓ | ✓ | ✓ | ✓              | ✓ | ✓ | ✓ | ✓ | ✓               | ✓ | ✓ | ✓ | ✓ |
| LMM (RSL) | ✓                 | ✓ | ✓ | ✓ | ✓ | -              | - | - | - | - | -               | - | - | - | - |
| Q1ASMS    | ✓                 | ✓ | ✓ | ✓ | ✓ | -              | - | - | - | - | -               | - | - | - | - |
| Q1MS2     | ✓                 | ✓ | ✓ | ✓ | ✓ | -              | - | - | - | - | -               | - | - | - | - |
| Q1MS3     | ✓                 | ✓ | ✓ | ✓ | ✓ | ✓              | ✓ | ✓ | ✓ | ✓ | -               | - | - | - | - |

**Table A.1:** Patch test for the inertia term with the Q1 family.

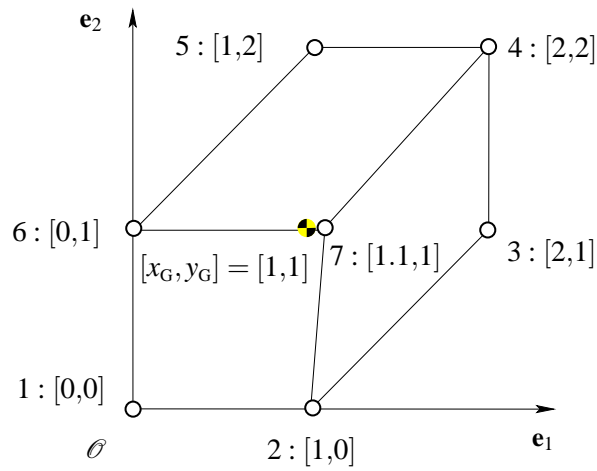


**Figure A.1:** Setup for an inertia patch test. Q1 element. Density  $\rho = 1.0$ .

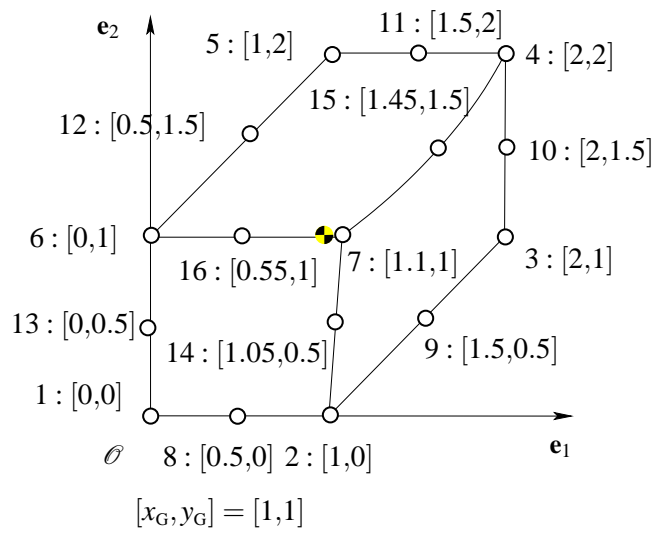


**Figure A.2:** Setup for an inertia patch test. S2 element. Density  $\rho = 1.0$ .

| Mass type | Constant velocity |   |   |   |   | Rigid rotation |   |   |   |   | Linear velocity |   |   |   |   |
|-----------|-------------------|---|---|---|---|----------------|---|---|---|---|-----------------|---|---|---|---|
|           | A                 | B | C | D | E | A              | B | C | D | E | A               | B | C | D | E |
| CMM       | ✓                 | ✓ | ✓ | ✓ | ✓ | ✓              | ✓ | ✓ | ✓ | ✓ | ✓               | ✓ | ✓ | ✓ | ✓ |
| LMM (HRZ) | -                 | - | - | ✓ | ✓ | -              | - | - | - | - | -               | - | - | - | - |
| S2ASMS    | ✓                 | ✓ | ✓ | ✓ | ✓ | -              | - | - | - | - | -               | - | - | - | - |
| S2MS6     | ✓                 | ✓ | ✓ | ✓ | ✓ | ✓              | ✓ | ✓ | ✓ | ✓ | ✓               | ✓ | ✓ | ✓ | ✓ |

**Table A.2:** Patch test for the inertia term with the S2 family.

| Mass type                       | Constant velocity |   |   |   |   | Rigid rotation |   |   |   |   | Linear velocity |   |   |   |   |
|---------------------------------|-------------------|---|---|---|---|----------------|---|---|---|---|-----------------|---|---|---|---|
|                                 | A                 | B | C | D | E | A              | B | C | D | E | A               | B | C | D | E |
| CMM                             | ✓                 | ✓ | ✓ | ✓ | ✓ | ✓              | ✓ | ✓ | ✓ | ✓ | ✓               | ✓ | ✓ | ✓ | ✓ |
| LMM (RSL)                       | ✓                 | ✓ | ✓ | ✓ | ✓ | -              | - | - | - | - | -               | - | - | - | - |
| ASMS                            | ✓                 | ✓ | ✓ | ✓ | ✓ | -              | - | - | - | - | -               | - | - | - | - |
| Q2MS6                           | ✓                 | ✓ | ✓ | ✓ | ✓ | ✓              | ✓ | ✓ | ✓ | ✓ | ✓               | ✓ | ✓ | ✓ | ✓ |
| Q2V10P10                        | -                 | - | - | ✓ | ✓ | -              | - | - | ✓ | ✓ | -               | - | - | ✓ | ✓ |
| Q2V10P10<br>(trapezoidal shape) | ✓                 | ✓ | ✓ | ✓ | ✓ | ✓              | ✓ | ✓ | ✓ | ✓ | ✓               | ✓ | ✓ | ✓ | ✓ |
| Q2IVM8                          | ✓                 | ✓ | ✓ | ✓ | ✓ | -              | - | - | ✓ | ✓ | -               | - | - | ✓ | ✓ |

**Table A.3:** Patch test for the inertia term with the Q2 family.

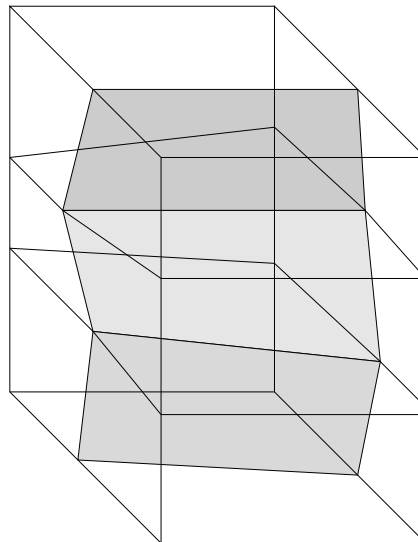


**Figure A.3:** Setup for the inertia patch test in 3D with Hexa8 element. Density  $\rho = 1.0$ .

| Mass type | Constant velocity |   |   |   |   | Rigid rotation |   |   |   |   | Linear velocity |   |   |   |   |
|-----------|-------------------|---|---|---|---|----------------|---|---|---|---|-----------------|---|---|---|---|
|           | A                 | B | C | D | E | A              | B | C | D | E | A               | B | C | D | E |
| CMM       | ✓                 | ✓ | ✓ | ✓ | ✓ | ✓              | ✓ | ✓ | ✓ | ✓ | ✓               | ✓ | ✓ | ✓ | ✓ |
| LMM (HRZ) | -                 | - | - | ✓ | ✓ | -              | - | - | - | - | -               | - | - | - | - |
| Hexa8ASMS | ✓                 | ✓ | ✓ | ✓ | ✓ | -              | - | - | - | - | -               | - | - | - | - |
| Hexa8MS6  | ✓                 | ✓ | ✓ | ✓ | ✓ | ✓              | ✓ | ✓ | ✓ | ✓ | -               | - | - | - | - |

**Table A.4:** Patch test for the inertia term with the Hexa8 element family.

## B Derivation of the penalized Hamilton's principle of elasto-dynamics using a semi-inverse method

The semi-inverse method is one of the most powerful methods for the derivation of weak forms. For details of the semi-inverse method, see DAH-WEI (1985) and HE (2000). Here, the penalized HAMILTON's principle given in equation (3.8) is derived using this method as an alternative to penalty method. The motivation for this derivation is to show that the high-order LAGRANGE multipliers, semi-inverse and template methods have comparable capabilities for problems, where at least one non-parametric variational principle is known. The advantage of the semi-inverse method w.r.t. the high-order LAGRANGE multipliers or penalty methods is that the semi-inverse method enables derivation of parametric variational principles even for problems without known variational principles. This issue is important for coupled problems (more concrete goals are set in Outlook, Chapter 8.2).

The starting point for the derivation is the equation (2.66). Here, the displacement, the velocity and the linear momentum are assumed to be independent. This leads to a following IBVP

$$\left\{ \begin{array}{ll} \dot{\mathbf{p}} = \mathbf{L}^* \boldsymbol{\sigma}_{\text{lin}}(\mathbf{u}) + \hat{\mathbf{b}} & \text{in } \mathcal{I} \times \mathcal{B}_0 \\ \mathbf{p} = \rho \mathbf{v} & \text{in } \mathcal{I} \times \mathcal{B}_0 \\ \mathbf{v} = \dot{\mathbf{u}} & \text{in } \mathcal{I} \times \mathcal{B}_0 \\ \mathbf{u} = \mathbf{0} & \text{in } \mathcal{I} \times \partial \mathcal{B}_u \\ \boldsymbol{\sigma}_{\text{lin}} \mathbf{n} = \hat{\mathbf{t}} & \text{in } \mathcal{I} \times \partial \mathcal{B}_{t,0} \\ \mathbf{u}(0, \cdot) = \mathbf{u}_0 & \text{in } \mathcal{B}_0 \\ \dot{\mathbf{u}}(0, \cdot) = \mathbf{v}_0 & \text{in } \mathcal{B}_0. \end{array} \right. \quad (\text{B.1})$$

Now comes a crucial step of the semi-inverse approach. The Hamiltonian functional  $H^{\text{GEN}}$  is assumed in the most general form using a *free function*, the generalized Lagrangian  $L^{\text{GEN}}$  and the generalized boundary terms  $BT^{\text{GEN}}$ . Then, using the system (B.1) and equivalent transformations, the shape of the functional is recovered. Thus, step one reads

$$H^{\text{GEN}}(\mathbf{u}, \mathbf{v}, \mathbf{p}) = \int_{\mathcal{I}} L^{\text{GEN}}(\mathbf{u}, \dot{\mathbf{u}}, \mathbf{v}, \mathbf{p}) dt + BT^{\text{GEN}}(\mathbf{u}, \dot{\mathbf{u}}, \mathbf{v}, \mathbf{p}) \rightarrow \text{stat.} \quad (\text{B.2})$$

In contrast to SHIKUI (1992b), here the boundary term is allowed to depend on the velocity  $\mathbf{v}$ . This makes the difference in the derivation, increasing the number of free parameters in the final expression of generalized Lagrangian  $L^{\text{GEN}}$  from one to three. The second step of the derivation is to take first variation of equation (B.2)

$$\delta H^{\text{GEN}} = \int_{\mathcal{I}} \left( \frac{\partial L^{\text{GEN}}}{\partial \mathbf{u}} \delta \mathbf{u} + \frac{\partial L^{\text{GEN}}}{\partial \dot{\mathbf{u}}} \delta \dot{\mathbf{u}} + \frac{\partial L^{\text{GEN}}}{\partial \mathbf{v}} \delta \mathbf{v} + \frac{\partial L^{\text{GEN}}}{\partial \mathbf{p}} \delta \mathbf{p} \right) dt + \delta BT^{\text{GEN}} = 0. \quad (\text{B.3})$$

In the third step, the weak form (B.3) is simplified using equation (B.1). In order to do this, the term  $\partial L^{\text{GEN}}/\partial \mathbf{v}$  is assumed to be null-Lagrangian, i.e. to be functionally dependent on a system of equations (B.1). Here, it is assumed in the form

$$\frac{\partial L^{\text{GEN}}}{\partial \mathbf{v}} = \tilde{C}_1(\mathbf{p} - \rho \dot{\mathbf{u}}) + (\mathbf{p} - \rho \mathbf{v}) + \tilde{C}_3 \rho (\dot{\mathbf{u}} - \mathbf{v}), \quad (\text{B.4})$$

where  $\tilde{C}_{1,3}$  are free parameters.

In the fourth step, a partial integration of the term  $\partial L^{\text{GEN}}/\partial \mathbf{v}$  is performed, leading to

$$L^{\text{GEN}} = \tilde{C}_1(\mathbf{p} - \rho \dot{\mathbf{u}}) \cdot \mathbf{v} + \left( \mathbf{p} \cdot \mathbf{v} - \frac{\rho \mathbf{v}^2}{2} \right) + \tilde{C}_3 \rho \left( \dot{\mathbf{u}} \cdot \mathbf{v} - \frac{\mathbf{v}^2}{2} \right) + \tilde{g}_1(\mathbf{u}, \dot{\mathbf{u}}, \mathbf{p}), \quad (\text{B.5})$$

with  $\tilde{g}_1$  being an integration constant function independent on  $\mathbf{v}$ . The function  $\tilde{g}_1$  depends only on three parameters  $(\mathbf{u}, \dot{\mathbf{u}}, \mathbf{p})$ .

In the fifth step, the generalized Lagrangian  $L^{\text{GEN}}$  is further specified by exploitation of  $\partial L^{\text{GEN}}/\partial \mathbf{p}$ . The term  $\partial L^{\text{GEN}}/\partial \mathbf{p}$  reads

$$\frac{\partial L^{\text{GEN}}}{\partial \mathbf{p}} = \tilde{C}_1 \mathbf{v} + \mathbf{v} + \frac{\partial \tilde{g}_1}{\partial \mathbf{p}}. \quad (\text{B.6})$$

The latter equation must be zero up to null-Lagrangian. However, the term  $\partial \tilde{g}_1/\partial \mathbf{p}$  is independent of  $\mathbf{v}$ . It reduces to zero only in case of a special form of boundary terms. Here, following combination of null-Lagrangian is used

$$\tilde{C}_1 \mathbf{v} + \mathbf{v} + \frac{\partial \tilde{g}_1}{\partial \mathbf{p}} = (1 + \tilde{C}_1) \left( \mathbf{v} - \frac{\tilde{C}_2 \mathbf{p}}{\rho} - (1 - \tilde{C}_2) \dot{\mathbf{u}} \right) + \left[ \frac{\partial \tilde{g}_1}{\partial \mathbf{p}} + (1 + \tilde{C}_1) \left( \frac{\tilde{C}_2 \mathbf{p}}{\rho} + (1 - \tilde{C}_2) \dot{\mathbf{u}} \right) \right] = \mathbf{0}. \quad (\text{B.7})$$

From equation (B.7), the integration function  $\tilde{g}_1$  can be expressed. Partial integration of  $\partial \tilde{g}_1/\partial \mathbf{p}$  yields the expression

$$\tilde{g}_1 = -(1 + \tilde{C}_1) \left( \frac{\tilde{C}_2 \mathbf{p}^2}{2\rho} + (1 - \tilde{C}_2) \dot{\mathbf{u}} \cdot \mathbf{p} \right) + \tilde{g}_2(\mathbf{u}, \dot{\mathbf{u}}), \quad (\text{B.8})$$

where  $\tilde{g}_2$  is an integration constant function. Thus, the expression of the generalized Lagrangian further reduces to

$$L^{\text{GEN}} = \tilde{C}_1(\mathbf{p} - \rho \dot{\mathbf{u}}) \cdot \mathbf{v} + \left( \mathbf{p} \cdot \mathbf{v} - \frac{\rho \mathbf{v}^2}{2} \right) + \tilde{C}_3 \rho \left( \dot{\mathbf{u}} \cdot \mathbf{v} - \frac{\mathbf{v}^2}{2} \right) - (1 + \tilde{C}_1) \left( \frac{\tilde{C}_2 \mathbf{p}^2}{2\rho} + (1 - \tilde{C}_2) \dot{\mathbf{u}} \cdot \mathbf{p} \right) + \tilde{g}_2(\mathbf{u}, \dot{\mathbf{u}}). \quad (\text{B.9})$$

In the sixth step, the terms  $\frac{\partial L^{\text{GEN}}}{\partial \mathbf{u}}$  and  $\frac{\partial L^{\text{GEN}}}{\partial \dot{\mathbf{u}}}$  are computed and exploited in the equilibrium equation as follows

$$\frac{\partial L^{\text{GEN}}}{\partial \mathbf{u}} = \frac{\partial \tilde{g}_2}{\partial \mathbf{u}}, \quad \frac{\partial L^{\text{GEN}}}{\partial \dot{\mathbf{u}}} = \rho \mathbf{v}(\tilde{C}_3 - \tilde{C}_1) - (1 + \tilde{C}_1)(1 - \tilde{C}_2)\mathbf{p} + \frac{\partial \tilde{g}_2}{\partial \dot{\mathbf{u}}}. \quad (\text{B.10})$$

As the next step, integration by parts of the term  $\frac{\partial L^{\text{GEN}}}{\partial \dot{\mathbf{u}}}$  is performed and the latter expression is substituted in equation (B.3). This yield an equation of motion in the form

$$-\rho \dot{\mathbf{v}}(\tilde{C}_3 - \tilde{C}_1) + (1 + \tilde{C}_1)(1 - \tilde{C}_2)\dot{\mathbf{p}} - \frac{\partial^2 \tilde{g}_2}{\partial \dot{\mathbf{u}}^2} \ddot{\mathbf{u}} - \frac{\partial^2 \tilde{g}_2}{\partial \dot{\mathbf{u}} \partial \mathbf{u}} \dot{\mathbf{u}} + \frac{\partial \tilde{g}_2}{\partial \mathbf{u}} = \mathbf{0}. \quad (\text{B.11})$$

Assuming independence of  $\frac{\partial \tilde{g}_2}{\partial \dot{\mathbf{u}}}$  on  $\dot{\mathbf{u}}$ , the following expression for  $\tilde{g}_2$  is obtained

$$\tilde{g}_2 = \Pi(\mathbf{u}) - (\tilde{C}_3 - 2\tilde{C}_1 + \tilde{C}_2 - \tilde{C}_1\tilde{C}_2) \frac{\rho \dot{\mathbf{u}}^2}{2}, \quad (\text{B.12})$$

with  $\Pi(\mathbf{u})$  being the full potential energy of the system. Thus, from the complete expression of  $L^{\text{GEN}}$  and kinetic energy in the form

$$L^{\text{GEN}} = \Pi(\mathbf{u}) - T^\circ, \quad (\text{B.13})$$

$$T^\circ = \frac{1}{2} \int_{\mathcal{B}} \begin{bmatrix} \rho \dot{\mathbf{u}} \\ \rho \mathbf{v} \\ \mathbf{p} \end{bmatrix} \begin{bmatrix} (\tilde{C}_3 - 2\tilde{C}_1 + \tilde{C}_2 - \tilde{C}_1\tilde{C}_2)\mathbf{I} & (\tilde{C}_3 - \tilde{C}_1)\mathbf{I} & -(1 + \tilde{C}_1)(1 - \tilde{C}_2)\mathbf{I} \\ (\tilde{C}_3 - \tilde{C}_1)\mathbf{I} & (-1 - \tilde{C}_3)\mathbf{I} & -(1 - \tilde{C}_1)\mathbf{I} \\ -(1 + \tilde{C}_1)(1 - \tilde{C}_2)\mathbf{I} & -(1 - \tilde{C}_1)\mathbf{I} & (\tilde{C}_1 + 1)\tilde{C}_2\mathbf{I} \end{bmatrix} \begin{bmatrix} \dot{\mathbf{u}} \\ \mathbf{v} \\ \frac{\mathbf{p}}{\rho} \end{bmatrix} d\mathcal{B}. \quad (\text{B.14})$$

is obtained. This template for kinetic energy  $T^\circ$  has three free parameters  $\tilde{C}_{1-3}$ . It can be shown, that it is equivalent to the equation (3.8) with free parameters  $C_{1-3}$ .

---

# Bibliography

- Abramowitz, M. E., Stegun, I. A., et al. (1964). *Handbook of mathematical functions: with formulas, graphs, and mathematical tables*. Dover Publications, New York.
- Acary, V. (2013). Projected event-capturing time-stepping schemes for nonsmooth mechanical systems with unilateral contact and Coulomb's friction. *Computer Methods in Applied Mechanics and Engineering*, 256:224 – 250.
- Alexandrov, V. and Pozharskii, D. (2002). *Three-Dimensional Contact Problems*. Solid Mechanics and Its Applications Series. Springer London, Limited.
- Allemang, R. J. (2003). The modal assurance criterion – twenty years of use and abuse. *Sound and Vibration*, 37(8):14–23.
- Arnaudeau, F. (2010). Faster realistic crash simulations. In *4th ETHC, Versailles, France*.
- Ascher, U. M. and Petzold, L. R. (1998). *Computer Methods for Ordinary Differential equations and Differential-Algebraic equations*. SIAM, Philadelphia.
- Askes, H., Nguyen, D., and Tyas, A. (2011). Increasing the critical time step: micro-inertia, inertia penalties and mass scaling. *Computational Mechanics*, 47:657–667.
- Auricchio, F., Beirão da Veiga, L., Hughes, T., Reali, A., and Sangalli, G. (2012). Isogeometric collocation for elastostatics and explicit dynamics. *Computer methods in applied mechanics and engineering*, 249-252:2–14.
- Babuška, I., Whiteman, J., and Strouboulis, T. (2010). *Finite Elements: An Introduction to the Method and Error Estimation*. OUP Oxford.
- Bathe, K. (2006). *Finite Element Procedures*. Prentice Hall, Upper Saddle River, New Jersey.

- Baumgarte, J. (1972). Stabilization of constraints and integrals of motion in dynamical systems. *Computer Methods in Applied Mechanics and Engineering*, 1:1–16.
- Bazeley, G., Cheung, Y. K., Irons, B. M., and Zienkiewicz, O. (1966). Triangular elements in plate bending-conforming and non-conforming solutions. In *Proc. 1st Conf. Matrix Methods in Structural Mechanics*, volume AFFDL-TR-66-80, pages 547–576.
- Belytschko, T.B.; Mullen, R. (1978). On dispersive properties of finite element solutions. In Miklowitz, J., editor, *Modern problems in elastic wave propagation*, pages 67–82. John Wiley & Sons, Inc.
- Belytschko, T. and Lin, J. I. (1985). Eigenvalues and stable time steps for the bilinear Mindlin plate element. *International Journal for Numerical Methods in Engineering*, 21(9):1729–1745.
- Belytschko, T., Liu, W. K., and Moran, B. (2001). *Nonlinear Finite Element for Continua and Structures*. Wiley.
- Belytschko, T. and Mindle, W. L. (1980). Flexural wave propagation behavior of lumped mass approximations. *Computers and Structures*, 12(6):805 – 812.
- Benson, D., Bazilevs, Y., Hsu, M., and Hughes, T. (2010). Isogeometric shell analysis: The Reissner-Mindlin shell. *Computer Methods in Applied Mechanics and Engineering*, 199(58):276 – 289.
- Benson, D. J. and Hallquist, J. O. (1990). A single surface contact algorithm for the post-buckling analysis of shell structures. *Computer Methods in Applied Mechanics and Engineering*, 78(2):141–163.
- Betsch, P. and Hesch, C. (2007). Energy-momentum conserving schemes for frictionless dynamic contact problems. In Wriggers, P. and Nackenhorst, U., editors, *IUTAM Symposium on Computational Methods in Contact Mechanics*, volume 3 of *IUTAM Bookseries*, pages 77–96. Springer Netherlands.
- Boley, D. and Chao, C. (1955). Some solutions of the timoshenko beam equations. *Journal of Applied Mechanics. Transactions of ASME*, 75:579–586.
- Bonet, J. (2008). *Nonlinear mechanics for finite element analysis*. Cambridge University Press, New York, 2<sup>nd</sup> edition.
- Borrvall, T. (2011). Selective mass scaling in LS-DYNA to reduce non-physical inertia effects. In *Developers' forum, DYNAMORE, Stuttgart, Germany, 2011*.
- Campbell, S. L., Linh, V. H., and Petzold, L. R. (2008). Differential-algebraic equations. *Scholarpedia*, 3(8):2849.

- Cannarozzi, M. and Mancuso, M. (1995). Formulation and analysis of variational methods for time integration of linear elastodynamics. *Computer methods in applied mechanics and engineering*, 127(1):241–257.
- Carpenter, N. J., Taylor, R. L., and Katona, M. G. (1991). Lagrange constraints for transient finite element surface contact. *International Journal for Numerical Methods in Engineering*, 32(1):103–128.
- Castro, F. J. B. (2011). Dispersion analysis of an energy-orthogonal thin plate finite element. *International Journal of Computational Methods*, 8(03):425–462.
- Chen, Q. and Babuška, I. (1996). The optimal symmetrical points for polynomial interpolation of real functions in the tetrahedron. *Computer Methods in Applied Mechanics and Engineering*, 137(1):89 – 94.
- Cichosz, T. and Bischoff, M. (2011). Consistent treatment of boundaries with mortar contact formulations using dual Lagrange multipliers. *Computer Methods in Applied Mechanics and Engineering*, 200:1317 – 1332.
- CIMNE (2013). *GiD help, version 11*.
- Cocchetti, G., Pagani, M., and Perego, U. (2013). Selective mass scaling and critical time-step estimate for explicit dynamics analyses with solid-shell elements. *Computers & Structures*, 157:39–52.
- Cook, R. D., Malkus, D. S., Plesha, M. E., and Witt, R. E. (2007). *Concepts and Applications of Finite Element*. Wiley India Pvt. Limited, 4<sup>th</sup> edition.
- Curnier, A., He, Q., and Klabring, A. (1995). *Continuum mechanics modelling of large deformation contact with friction*. in Contact mechanics / edited by M. Raous, M. Jean, and J.J. Moreau. New York;London:Plenum Press.
- Dah-wei, H. (1985). A method for establishing generalized variational principle. *Applied Mathematics and Mechanics (English Ed)*, 6(6):501–509.
- Deuffhard, P., Krause, R., and Ertel, S. (2008). A contact-stabilized Newmark method for dynamical contact problems. *International Journal for Numerical Methods in Engineering*, 73(9):1274–1290.
- Eck, C., Kovalenko, Y., Mangold, O., Prohl, R., Tkachuk, A., and Trickov, V. (2014). Reduction of numerical sensitivities in crash simulations on HPC-computers (HPC-10). In Nagel, W. E., Kröner, D. H., and Resch, M. M., editors, *High Performance Computing in Science and Engineering '13*, pages 679–697. Springer Berlin / Heidelberg.
- Eck, C., Mangold, O., Prohl, R., and Tkachuk, A. (2013). Reduction of numerical sensitivities in crash simulations on HPC-computers (HPC-10). In Nagel, W. E., Kröner, D. H., and

- Resch, M. M., editors, *High Performance Computing in Science and Engineering '12*, pages 547–560. Springer Berlin / Heidelberg.
- Elias, Z. (1973). On the reciprocal form of Hamilton's principle. *Journal of Applied Mechanics*, 40:93–94.
- Felippa, C. A. (1994). A survey of parametrized variational principles and applications to computational mechanics. *Computer Methods in Applied Mechanics and Engineering*, 113:109 – 139.
- Felippa, C. A. (2000). Recent advances in finite element templates. In Topping, B. H. V., editor, *Computational Mechanics for the Twenty-First Century*, pages 71–98. Saxe-Coburn Publications.
- Felippa, C. A. (2001). Customizing high performance elements by fourier methods. In Wall, W., Bletzinger, K., and Schweizerhof, K., editors, *Trends in computational structural mechanics*, pages 283–296. International Center for Numerical Methods in Engineering (CIMNE).
- Felippa, C. A. (2006). Construction of customized mass-stiffness pairs using templates. *Journal of Aerospace Engineering*, 19(4):241–258.
- Felippa, C. A. (2010). Customized mass matrices of 1D elements, IFEM lecture notes, Chapter 33. [Online; accessed 07-November-2011].
- Felippa, C. A., Haugen, B., and Militello, C. (1995). From the individual element test to finite element templates: evolution of the patch test. *International journal for numerical methods in engineering*, 38(2):199–229.
- Felippa, C. A. and Militello, C. (1989). Developments in variational methods for high performance plate and shell elements. *Analytical and computational models of shells*, pages 191–215.
- Finlayson, B. (1972). *The Method of Weighted Residuals and Variational Principles: With Applications in Fluid Mechanics, Heat and Mass Transfer*. Mathematics in Science and Engineering Series. Academic Press.
- Flanagan, D. and Belytschko, T. (1981). A uniform strain hexahedron and quadrilateral with orthogonal hourglass control. *International Journal for Numerical Methods in Engineering*, 17(5):679–706.
- Francavilla, A. and Zienkiewicz, O. (1975). A note on numerical computation of elastic contact problems. *Int. Journal for Numerical Methods in Engineering*, 9:913–924.

- Fried, I. and Malkus, D. S. (1975). Finite element mass matrix lumping by numerical integration with no convergence rate loss. *International Journal of Solids and Structures*, 11(4):461–466.
- Fu, Y. and Ogden, R. (2001). *Nonlinear Elasticity: Theory and Applications*. London Mathematical Society Lecture Note Series. Cambridge University Press.
- Galín, L. and Gladwell, G. (2008). *Contact Problems: The Legacy of L.A. Galin*. Solid Mechanics and Its Applications Series. Springer.
- Gavoille, S. (2013). Enrichissement modal du selective mass scaling (in French). In *Proceedings of 11e Colloque National en Calcul des Structures by Calcul des Structures et Modélisation (CSMA 2013)*.
- Gear, C. W., Leimkuhler, B., and Gupta, G. K. (1985). Automatic integration of Euler-Lagrange equations with constraints. *Journal of Computational and Applied Mathematics*, 12-13:77–90.
- Gee, M. (2004). *Effiziente Lösungsstrategien in der nichtlinearen Schalenmechanik*. PhD thesis, Institut für Baustatik und Baudynamik, Universität Stuttgart.
- Geradin, M. (1980). Variational methods of structural dynamics and their finite element implementation. In Donéa, J., editor, *Advanced structural dynamics*, pages 1–42. Applied Science Publishers.
- Gitterle, M., Popp, A., Gee, M. W., and Wall, W. A. (2010). Finite deformation frictional mortar contact using a semi-smooth Newton method with consistent linearization. *International Journal for Numerical Methods in Engineering*, 84(5):543–571.
- Grigolyuk, E. and Tolkachev, V. (1987). *Contact Problems in the Theory of Plates and Shells*. Mir Publishers, Moscow.
- Guo, Q. (2012). Developing optimal mass matrices for membrane triangles with corner drilling freedoms. Master thesis, University of Colorado at Boulder.
- Guo-ping, L. and Zi-chi, F. (1982). Finite element method with mixed/hybrid penalty functions and their applications. In *Dalian International Symposium on Mixed/Hybrid Finite Element Method*.
- Gurtin, M. (1964). Variational principles for linear elastodynamics. *Archive for Rational Mechanics and Analysis*, 16(1):34–50.
- Gurtin, M. (1981). *An Introduction to Continuum Mechanics (Mathematics in Science and Engineering)*. Academic Press.
- Hager, C. (2010). *Robust numerical algorithms for dynamic frictional contact problems with different time and space scales*. PhD thesis, Universität Stuttgart.

- Hager, C., Hüeber, S., and Wohlmuth, B. (2008). A stable energy-conserving approach for frictional contact problems based on quadrature formulas. *International Journal for Numerical Methods in Engineering*, 73:205–225.
- Hallquist, J. O. et al. (2006). LS-DYNA theory manual. *Livermore Software Technology Corporation*, 3.
- Hartmann, S., Brunssen, S., Ramm, E., and Wohlmuth, B. (2007). Unilateral non-linear dynamic contact of thin-walled structures using a primal-dual active set strategy. *International Journal for Numerical Methods in Engineering*, 70:883–912.
- Hartmann, S. and Ramm, E. (2008). A mortar based contact formulation for non-linear dynamics using dual Lagrange multipliers. *Finite element analysis and design*, 44:245–248.
- Hauret, P. (2010). Mixed interpretation and extensions of the equivalent mass matrix approach for elastodynamics with contact. *Computer Methods in Applied Mechanics and Engineering*, 199(45-48):2941 – 2957.
- He, J.-H. (2000). Semi-inverse method and generalized variational principles with multi-variables in elasticity. *Applied Mathematics and Mechanics*, 21(7):797–808.
- He, J.-H. (2005). A generalized variational principle in micromorphic thermoelasticity. *Mechanics Research Communications*, 32(1):93–98.
- Heylen, W. and Avitabile, P. (1998). Correlation considerations, part 5. In *Proceedings of the 16th International Modal Analysis Conference*, pages 2–5.
- Hinton, E., Rock, T., and Zienkiewicz, O. C. (1976). A note on mass lumping and related processes in the finite element method. *Earthquake Engineering & Structural Dynamics*, 4(3):245–249.
- Holzapfel, G. (2000). *Nonlinear Solid Mechanics: A Continuum Approach for Engineering*. Wiley, Chichester (u.a.).
- Huanding, W. and Dongbu, C. (1990). Generalized variational principles with several selectable parameters. *Journal of Harbin University of Civil Engineering and Architecture*, pages 30–38.
- Hueber, S., Stadler, G., and Wohlmuth, B. (2006). A primal-dual active set algorithm for three-dimensional contact problems with friction. *SIAM Journal on scientific computing*, 30:572–596.
- Hughes, T. (2000). *The finite element method: linear static and dynamic finite element analysis*. Dover Civil and Mechanical Engineering Series. Dover Publications, New York.
- Hughes, T., Cohen, M., and Haroun, M. (1978). Reduced and selective integration techniques in the finite element analysis of plates. *Nuclear Engineering and Design*, 46:203 – 222.

- Hughes, T., Hilber, H., and Taylor, R. (1976). A reduction scheme for problems of structural dynamics. *International Journal of Solids Structures*, 12(11):749 – 767.
- Idesman, A. (2011). A new exact, closed-form a priori global error estimator for second- and higher-order time-integration methods for linear elastodynamics. *International Journal for Numerical Methods in Engineering*, 88(10):1066–1084.
- Idesman, A., Schmidt, M., and Foley, J. (2011). Accurate finite element modeling of linear elastodynamics problems with the reduced dispersion error. *Computational Mechanics*, 47(5):555–572.
- Irons, B. M. and Razzaque, A. (1972). Experience with the patch test for convergence of finite elements. In *The Mathematical Foundations of the Finite Element Method with Applications to Partial Differential Equations*, pages 557–587. Academic Press, New York.
- JAN, S. V. S. (2001). Vakhum.
- Johnson, K. (2003). *Contact mechanics*. Cambridge University Press, 9<sup>th</sup> edition.
- Keating, S., Felippa, C. A., and Militello, C. (1993). Implementation of a mesh adaptive scheme based on an element-level error indicator. In *34<sup>th</sup> AIAA/ASME/ASCE/AHS/ASC Structures, Structural Dynamics and Materials Conference*, pages 2893–2903.
- Key, S. W. and Beisinger, Z. E. (1971). The transient dynamic analysis of thin shells by the finite element method. In *Proc. of the Third Conference on Matrix Methods in Structural Mechanics*.
- Khenous, H., Laborde, P., and Renard, Y. (2008). Mass redistribution method for finite element contact problems in elastodynamics. *European Journal of Mechanics - A/Solids*, 27:918–932.
- Kikuchi, N. and Oden, J. (1988). *Contact problems in Elasticity: A Study of variational Inequalities and Finite Element Methods*. SIAM Philadelphia.
- Kolman, R., Plešek, J., and Okrouhlik, M. (2012). B-spline finite element method in one-dimensional elastic wave propagation problems. *Engineering Mechanics*, page 24.
- Krause, R. and Walloth, M. (2009). A time discretization scheme based on Rothe’s method for dynamical contact problems with friction. *Computer Methods in Applied Mechanics and Engineering*, 199:1–19.
- Krenk, S. (2001). Dispersion-corrected explicit integration of the wave equation. *Computer Methods in Applied Mechanics and Engineering*, 191(8-10):975–987.
- Lamichhane, B. and Wohlmuth, B. (2007). Biorthogonal bases with local support and approximation properties. *Mathematics of Computation*, 76(257):233–249.

- Lamichhane, B. P., McBride, A., and Reddy, B. (2013). A finite element method for a three-field formulation of linear elasticity based on biorthogonal systems. *Computer Methods in Applied Mechanics and Engineering*, 258(0):109 – 117.
- Lanzcos, C. (1970). *The variational principles of mechanics*. Dover Publications, New York.
- Laursen, T. (2002). *Computational Contact and Impact Mechanics: Fundamentals of Modeling Interfacial Phenomena in Nonlinear Finite Element Analysis*. Springer Verlag: New York.
- Laursen, T. A. and Chawla, V. (1997). Design of energy conserving algorithms for frictionless dynamic contact problems. *International Journal for Numerical Methods in Engineering*, 40(5):863–886.
- Luo, H. and Pozrikidis, C. (2006). A Lobatto interpolation grid in the tetrahedron. *IMA Journal of Applied Mathematics*, 71(2):298–313.
- Macek, R. W. and Aubert, B. H. (1995). A mass penalty technique to control the critical time increment in explicit dynamic finite element analyses. *Earthquake Engineering & Structural Dynamics*, 24(10):1315–1331.
- Makino, M. (2008). The performance of 10-million element car model by MPP version of LS-DYNA® on Fujitsu PrimePower. In *10th International LS-DYNA Users Conference*, pages 5–7.
- Marsden, J. and Hughes, T. (1983). *Mathematical Foundations of Elasticity*. Dover books on mathematics. Dover.
- Mattern, S. (2012). *Hocheffiziente Formulierung und Implementierung finiter Elemente für transiente Analysen mit expliziter Zeitintegration*. PhD thesis, Institut für Mechanik, Karlsruher Institut für Technologie.
- Meng, N., Wang, J., and Pathy, S. (2010). New features in LS-DYNA hybrid version. In *11th International LS-DYNA Users Conference*, pages 8–27.
- Mullen, R. and Belytschko, T. (1982). Dispersion analysis of finite element semidiscretizations of the two-dimensional wave equation. *International Journal for Numerical Methods in Engineering*, 18(1):11–29.
- NAFEMS (1990). *The standard NAFEMS benchmarks, National Agency for Finite Element Methods & Standards (Great Britain)*. NAFEMS.
- Naghdi, P. (1975). On the formulation of contact problems of shells and plates. *Journal of Elasticity*, 5:379–398.
- Newmark, N. M. (1959). A method of computation for structural dynamics. In *Proc. ASCE*, volume 85, pages 67–94.

- Ogden, R. (1997). *Non Linear Elastic Deformations*. Dover Civil and Mechanical Engineering Series. Dover Publication.
- Olovsson, L. and Simonsson, K. (2006). Iterative solution technique in selective mass scaling. *Communications in Numerical Methods in Engineering*, 22(1):77–82.
- Olovsson, L., Simonsson, K., and Unosson, M. (2005). Selective mass scaling for explicit finite element analyses. *International Journal for Numerical Methods in Engineering*, 63(10):1436–1445.
- Olovsson, L., Unosson, M., and Simonsson, K. (2004). Selective mass scaling for thin walled structures modeled with tri-linear solid elements. *Computational Mechanics*, 34:134–136.
- Pagani, M. (2013). *An explicit finite element computational strategy for the simulation of blade cutting of thin shells*. PhD thesis, Politecnico di Milano, Italy.
- Pagani, M. and Perego, U. (2013). Finite element simulations of cutting processes of thin-walled structures. In *The Third International Conference on Computational Modeling of Fracture and Failure of Materials and Structures, 5-7 June, Prague, Czech Republic*.
- Pandolfi, A., Kane, C., Marsden, J. E., and Ortiz, M. (2002). Time-discretized variational formulation of non-smooth frictional contact. *International Journal for Numerical Methods in Engineering*, 53(8):1801–1829.
- Pasquetti, R. and Rapetti, F. (2006). Spectral element methods on unstructured meshes: Comparisons and recent advances. *Journal of Scientific Computing*, 27:377–387.
- Peleh, B. and Suhorolskiy, M. (1980). *Contact Problems in the Theory of Elastic Anisotropic Shells (in Russian)*. Naukova Dumka, Kiev.
- Popp, A. (2012). *Mortar Methods for Computational Contact Mechanics and General Interface Problems*. Dissertation, Technische Universität München.
- Popp, A., Gee, M., and Wall, W. (2009). A finite deformation mortar contact formulation using a primaldual active set strategy. *International Journal for Numerical Methods in Engineering*, 79(11):1354–1391.
- Pozzolini, C., Renard, Y., and Salaun, M. (2013). Vibro-impact of a plate on rigid obstacles: existence theorem, convergence of a scheme and numerical simulations. *IMA Journal of Numerical Analysis*, 33(1):261–294.
- Pozzolini, C. and Salaun, M. (2011). Some energy conservative schemes for vibro-impacts of a beam on rigid obstacles. *Mathematical Modelling and Numerical Analysis*, 45.
- Puso, M. and Laursen, T. (2004a). A mortar segment-to-segment contact method for large deformation solid mechanics. *Computer Methods in Applied Mechanics and Engineering*, 193:601–629.

- Puso, M. and Laursen, T. (2004b). A mortar segment-to-segment frictional contact method for large deformation. *Computer Methods in Applied Mechanics and Engineering*, 193:4891–4913.
- Rajan, M. (2007). Performance analysis in support of capability computing on Red Storm/XT3. Technical report, Sandia National Laboratories.
- Reissner, E. (1948). Note on the method of complementary energy. *J. Math. Phys*, 27(2):159–160.
- Renard, Y. (2010). The singular dynamic method for constrained second order hyperbolic equations: Application to dynamic contact problems. *Journal of Computational and Applied Mathematics*, 234:906–923.
- Romero, I. and Bischoff, M. (2007). Incompatible bubbles: A non-conforming finite element formulation for linear elasticity. *Computer Methods in Applied Mechanics and Engineering*, 196(9-12):1662–1672.
- Roy, S., Morancay, L., Beauchesne, E., and Palaniswamy, H. (2011). Recent innovations in Hyperworks® stamping simulation technology. In *AIP Conference Proceedings*, volume 1383, page 413.
- Saad, Y. (1992). *Numerical methods for large eigenvalue problems*, volume 158. SIAM.
- Samarskii, A. (2001). *The Theory of Difference Schemes*. Monographs and Textbooks in Pure and Applied Mathematics. CRC Press.
- Schmied, C., Mattern, S., and Schweizerhof, K. (2013). Enhanced displacement mode finite elements for explicit transient analysis focussing on efficiency. In *Shell Structures, Theory and Applications, (10th SSTA 2013), October 16 - 18, 2013, Gdańsk (Poland)*.
- Shikui, L. (1992a). Extended Gurtin’s variational principle for linear elastodynamics (in Chinese). *Engineering Mechanics*, 1:1–8.
- Shikui, L. (1992b). Extended Hamilton generalized variational principle for linear elastodynamics (in Chinese). *Journal of Beijing Institute of Civil Engineering and Architecture*, pages 9–17.
- Simo, J., Wriggers, P., and Taylor, R. (1985). A perturbed Lagrangian formulation for the finite element solution of contact problems. *Computer Methods in Applied Mechanics and Engineering*, 50:163–180.
- Simo, J. C. and Rifai, M. (1990). A class of mixed assumed strain methods and the method of incompatible modes. *International Journal for Numerical Methods in Engineering*, 29(8):1595–1638.

- Stein, E., de Borst, R., and Hughes, T. (2004). *Encyclopedia of computational mechanics*. Number V. 2 in *Encyclopedia of Computational Mechanics*. John Wiley.
- Strang, G. (1986). *Introduction to Applied Mathematics*. Wellesley-Cambridge Press, Wellesley MA, USA.
- Suwannachit, A., Nackenhorst, U., and Chiarello, R. (2012). Stabilized numerical solution for transient dynamic contact of inelastic solids on rough surfaces. *Computational Mechanics*, 49(6):769–788.
- Taylor, M. A., Wingate, B. A., and Vincent, R. E. (2001). An algorithm for computing Fekete points in the triangle. *SIAM Journal on Numerical Analysis*, 38(5):1707–1720.
- Taylor, R., Simo, J., Zienkiewicz, O., and Chan, A. (1986). The patch test – a condition for assessing FEM convergence. *International Journal for Numerical Methods in Engineering*, 22(1):39–62.
- Thompson, L. L. and Pinsky, P. M. (1995). A Galerkin least-squares finite element method for the two-dimensional Helmholtz equation. *International Journal for Numerical Methods in Engineering*, 38(3):371–397.
- Thomson, W. (1993). *Theory of Vibration With Applications*. Stanley Thornes (Publishers).
- Tkachuk, A. and Bischoff, M. (2013a). Applications of variationally consistent selective mass scaling in explicit dynamics. In *Proc. of the Fourth ECCOMAS Thematic Conference on Computational Methods in Structural Dynamics and Earthquake Engineering*.
- Tkachuk, A. and Bischoff, M. (2013b). Local and global strategies for optimal selective mass scaling. *Computational Mechanics*. submitted.
- Tkachuk, A. and Bischoff, M. (2013c). Variational methods for selective mass scaling. *Computational Mechanics*, 52:563–570.
- Tkachuk, A., Wohlmuth, B., and Bischoff, M. (2012). Discretization of dynamic contact using singular hybrid mass matrices. In *Proc. of the 6th EUROPEAN CONGRESS ON COMPUTATIONAL METHODS IN APPLIED SCIENCES AND ENGINEERING*.
- Tkachuk, A., Wohlmuth, B., and Bischoff, M. (2013). Hybrid-mixed discretization of elastodynamic contact problems using consistent singular mass matrices. *International Journal for Numerical Methods in Engineering*, 94:473 – 493.
- Vysloukh, V. A., Kandidov, V. P., and Chesnokov, S. S. (1973). Reduction of the degrees of freedom in solving dynamic problems by the finite element method. *International Journal for Numerical Methods in Engineering*, 7(2):185–194.
- Washizu, K. (1975). *Variational Methods in Elasticity and Plasticity*. Pergamon Press, Oxford/London/Edinburgh/New York/Toronto/Sydney/Paris/Braunschweig, 2<sup>nd</sup> edition.

- Wei-zang, C. (1983). Method of high-order Lagrange multiplier and generalized variational principles of elasticity with more general forms of functionals. *Applied Mathematics and Mechanics (English Ed)*, 4(2):143–157.
- Whirley, R. G. and Engelmann, B. E. (1993). *DYNA3D: A nonlinear, explicit, three-dimensional finite element code for solid and structural mechanics, User manual. Revision 1*. Lawrence Livermore National Lab., CA, USA.
- Wilson, E., Taylor, R., Doherty, W., and Ghaboussi, J. (1973). Incompatible displacement models(isoparametric finite elements in solid and thick shell structural analysis). *Numerical and computer methods in structural mechanics.(A 74-17756 06-32)* New York, Academic Press, Inc., 1973, pages 43–57.
- Wriggers, P. (2006). *Computational Contact Mechanics*. Springer Verlag: Heidelberg, 2<sup>nd</sup> edition.
- Yang, B., Laursen, T., and Meng, X. (2005). A mortar segment-to-segment contact method for large deformation solid mechanics. *International Journal for Numerical Methods in Engineering*, 62:1183–1225.
- Yu-qiu, L. (1987). Generalized variational principles with several arbitrary parameters and the variable substitution and multiplier method. *Applied Mathematics and Mechanics*, 8(7):617–629.
- Zheng, C.-B., Liu, B., Wang, Z.-J., and Lü, H.-S. (2011). Generalized variational principles for micromorphic magnetoelectroelastodynamics. *Computers and Mathematics with Applications*, 61(8):2201 – 2204. Advances in Nonlinear Dynamics, The 3<sup>rd</sup> International Symposium on Nonlinear Dynamics.
- Zhong, W. and Zhang, R. (1988). Parametric variational principles and their quadratic programming solutions in plasticity. *Computers & Structures*, 30(4):887–896.
- Zienkiewicz, O. and Taylor, R. (1997). The finite element patch test revisited a computer test for convergence, validation and error estimates. *Computer Methods in Applied Mechanics and Engineering*, 149:223–254.
- Zienkiewicz, O. and Taylor, R. (2006). *The Finite Element Method Set*. Elsevier/Butterworth-Heinemann, Amsterdam, 6<sup>th</sup> edition.

## Lebenslauf

### Persönliche Angaben:

Name: Anton Tkachuk  
Geburtsdatum: 06. Februar 1986  
Geburtsort: Charkiw, Ukraine  
Staatsangehörigkeit: ukrainisch  
Familienstand: ledig

### Schulbildung:

09/1992 - 06/1995 Allgemeinbildende Schule #126, Charkiw, Ukraine  
09/1995 - 06/1996 Akademische Gymnasium #45, Charkiw, Ukraine  
09/1996 - 06/2002 Physische und mathematische Lyzeum #27, Charkiw, Ukraine

### Studium:

09/2002 - 06/2007 Ingenieurwissenschaften an der Nationalen Technischen Universität, Charkiw, Ukraine  
10/2007 - 04/2009 Computational Mechanics of Materials and Structures an der Universität Stuttgart  
09/2009 - 03/2014 Wiss. Assistent am Institut für Baustatik und Baudynamik, Universität Stuttgart



---

## Berichte des Instituts für Baustatik und Baudynamik der Universität Stuttgart

- 1 (1983) **P. Osterrieder:**  
Traglastberechnung von räumlichen Stabwerken bei großen Verformungen mit finiten Elementen.
- 2 (1983) **T.A. Kompfner:**  
Ein finites Elementmodell für die geometrisch und physikalisch nichtlineare Berechnung von Stahlbetonschalen.
- 3 (1983) **A. Diack:**  
Beitrag zur Stabilität diskret längsversteifter Kreiszyinderschalen unter Axialdruck.
- 4 (1984) **A. Burmeister, F.W. Bornscheuer, E. Ramm:**  
Traglasten von Kugelbehältern mit Stutzen und Formabweichungen unter Innendruck und Stützenlängskraft.
- 5 (1985) **H. Stegmüller:**  
Grenzlastberechnungen flüssigkeitsgefüllter Schalen mit "degenerierten" Schalenelementen.
- 6 (1987) **A. Burmeister:**  
Dynamische Stabilität nach der Methode der finiten Elemente mit Anwendungen auf Kugelschalen.
- 7 (1987) **G. Kammler:**  
Ein finites Elementmodell zur Berechnung von Trägern und Stützen mit offenem, dünnwandigem Querschnitt unter Berücksichtigung der Interaktion zwischen globalem und lokalem Versagen.
- 8 (1988) **A. Matzenmiller:**  
Ein rationales Lösungskonzept für geometrisch und physikalisch nichtlineare Strukturberechnungen.

- 9 (1989) D. Tao:**  
Die Technik der reduzierten Basis bei nichtlinearen finiten Element-Berechnungen.
- 10 (1989) K.M. Weimar:**  
Ein nichtlineares Balkenelement mit Anwendung als Längssteifen axialbelasteter Kreiszyylinder.
- 11 (1990) K.-U. Bletzinger:**  
Formoptimierung von Flächentragwerken.
- 12 (1990) S. Kimmich:**  
Strukturoptimierung und Sensibilitätsanalyse mit finiten Elementen.
- 13 (1991) U. Andelfinger:**  
Untersuchungen zur Zuverlässigkeit hybrid-gemischter Finiter Elemente für Flächentragwerke.
- 14 (1992) N. Büchter:**  
Zusammenführung von Degenerationskonzept und Schalentheorie bei endlichen Rotationen.
- 15 (1992) T.J. Hofmann:**  
Beitrag zur verfeinerten Balkentheorie.
- 16 (1994) D. de Mesquita Roehl:**  
Zur Berechnung von großen elastoplastischen Deformationen bei Flächentragwerken und Kontinua.
- 17 (1994) R. Reitinger:**  
Stabilität und Optimierung imperfektionsempfindlicher Tragwerke.
- 18 (1995) R.L.M. Suanno:**  
Ein dreidimensionales Simulationsmodell für Stahlbeton mit Plastizität und Schädigung.
- 19 (1995) M. Braun:**  
Nichtlineare Analysen von geschichteten, elastischen Flächentragwerken.

- 
- 20 (1996) N. Rehle:**  
Adaptive Finite Element Verfahren bei der Analyse von Flächentragwerken.
- 21 (1996) C. Haußer:**  
Effiziente Dreieckselemente für Flächentragwerke.
- 22 (1996) D. Kuhl:**  
Stabile Zeitintegrationsalgorithmen in der nichtlinearen Elastodynamik dünnwandiger Tragwerke.
- 23 (1998) H. Schmidts:**  
Zur effizienten Modellierung und Analyse von Hochhaustragwerken.
- 24 (1998) H. Wang:**  
Interaktion des lokalen und globalen Stabilitätsverhaltens dünnwandiger Stäbe.
- 25 (1998) K. Maute:**  
Topologie- und Formoptimierung von dünnwandigen Tragwerken.
- 26 (1998) B. Maurer:**  
Karl Culmann und die graphische Statik.
- 27 (1998) F. Cirak:**  
Adaptive Finite-Element-Methoden bei der nichtlinearen Analyse von Flächentragwerken.
- 28 (1998) M. Trautz:**  
Zur Entwicklung von Form und Struktur historischer Gewölbe aus der Sicht der Statik.
- 29 (1999) H. Menrath:**  
Numerische Simulation des nichtlinearen Tragverhaltens von Stahlverbundträgern.
- 30 (1999) M. Bischoff:**  
Theorie und Numerik einer dreidimensionalen Schalenformulierung.
- 31 (1999) W.A. Wall:**  
Fluid-Struktur-Interaktion mit stabilisierten Finiten Elementen.

- 32 (2000) E. Kuhl:**  
Numerische Modelle für kohäsive Reibungsmaterialien.
- 33 (2001) A. Maute:**  
Fehlerkontrolle bei Finite-Element-Methoden in der linearen Strukturdynamik.
- 34 (2001) S. Schwarz:**  
Sensitivitätsanalyse und Optimierung bei nichtlinearem Strukturverhalten.
- 35 (2001) A. Haufe:**  
Dreidimensionale Simulation bewehrter Flächentragwerke aus Beton mit der Plastizitätstheorie.
- 36 (2001) D.P. Mok:**  
Partitionierte Lösungsansätze in der Strukturdynamik und der Fluid-Struktur-Interaktion.
- 37 (2002) H. Steeb:**  
Fehlerschätzer für FE-Berechnungen bei entfestigenden Materialien.
- 38 (2002) K. Krausz:**  
Tragverhalten gemauerter Tonnengewölbe mit Stichkappen.
- 39 (2002) M. Hörmann:**  
Nichtlineare Versagensanalyse von Faserverbundstrukturen.
- 40 (2003) V. Gravemeier:**  
The Variational Multiscale Method for Laminar and Turbulent Incompressible Flow.
- 41 (2004) R. Kemmler:**  
Stabilität und große Verschiebungen in der Topologie- und Formoptimierung.
- 42 (2004) G.A. D'Addetta:**  
Discrete Models for Cohesive Frictional Materials.
- 43 (2004) M. Gee:**  
Effiziente Lösungsstrategien in der nichtlinearen Schalenmechanik.

- 44 (2004) T. Erhart:**  
Strategien zur numerischen Modellierung transienter Impaktvorgänge bei nichtlinearem Materialverhalten.
- 45 (2005) M. Leukart:**  
Kombinierte anisotrope Schädigung und Plastizität bei kohäsiven Reibungsmaterialien.
- 46 (2006) F. Huber:**  
Nichtlineare dreidimensionale Modellierung von Beton- und Stahlbetontragwerken.
- 47 (2007) A. Lipka:**  
Verbesserter Materialeinsatz innovativer Werkstoffe durch die Topologieoptimierung.
- 48 (2007) A.S. Hund:**  
Hierarchische Mehrskalenmodellierung des Versagens von Werkstoffen mit Mikrostruktur.
- 49 (2007) S. Hartmann:**  
Kontaktanalyse dünnwandiger Strukturen bei großen Deformationen.
- 50 (2007) T.M. Hettich:**  
Diskontinuierliche Modellierung zur Versagensanalyse von Verbundmaterialien.
- 51 (2007) C. Förster:**  
Robust methods for fluid-structure interaction with stabilised finite elements.
- 52 (2009) M. von Scheven:**  
Effiziente Algorithmen für die Fluid-Struktur-Wechselwirkung.
- 53 (2010) J. Kato:**  
Material Optimization for Fiber Reinforced Composites applying a Damage Formulation.
- 54 (2010) C.F. Hilchenbach:**  
Optimierung von Mehrphasenstrukturen mit lokalem Schädigungsverhalten.

- 55 (2011) I. Bruss:**  
Dreidimensionale Schädigungsmodellierung heterogener Materialien.
- 56 (2012) B.J. Schneider:**  
Polygonale diskrete Elemente zur Modellierung heterogener Materialien.
- 57 (2012) R. Etlender:**  
Modellierung und Simulation der Wellenausbreitung in flexiblen hydraulischen Leitungen.
- 58 (2012) T. Cichocz:**  
Stabile und konsistente Kontaktmodellierung in Raum und Zeit.
- 59 (2013) R. Echter:**  
Isogeometric Analysis of Shells.



**Anton Tkachuk**

This thesis presents a *unified* variational approach for the derivation of alternative mass matrices. Singular mass matrices within implicit dynamics allow substantial reduction of spurious temporal oscillations of contact pressures as well as more accurate preservation of the total energy. Application of selective mass scaling in explicit dynamics increases the critical time step size and results in a substantial speed-up for many practical problems, like deep drawing and drop test simulations. The unified approach is based on a novel mixed parametric HAMILTON's principle with independent variables for displacements, velocities and momenta and free parameters. The independent fields are linked in sense of penalty method with penalty factors free parameters. This provides the necessary flexibility during spatial discretization in choosing ansatz spaces and free parameters. Their skillful tuning results in consistent mass matrices with desired properties.

The presented approach is validated for several eigenvalue problems and transient benchmarks. The proposed alternative mass matrices yield accurate values for the lowest eigenfrequencies. The proposed singular mass matrices significantly reduce the spurious oscillations of contact forces. Variational selective mass scaling yields accurate results especially for bending dominated problems.